THE UNIVERSITY *of* EDINBURGH

Ab initio simulations of reactions occurring in molecular crystals

Michał Andrzej Kochman

Doctor of Philosophy
The University of Edinburgh
2014

Declaration

This thesis has not been submitted, in whole or in part, for any degree at this or any other university. The work is original and my own, carried out under the supervision of Dr Carole A. Morrison and Prof. Benedict Leimkuhler; where this is not so, credit has been duly given.

Acknowledgements

Undertaking this PhD has been a brilliant experience for me and it would not have been possible to do without the support and guidance that I received from many people.

I would like to first thank my Supervisors, Dr Carole A. Morrison from the School of Chemistry and Prof. Benedict Leimkuhler from the School of Mathematics, for giving me this great opportunity to do research in the field of Computational Chemistry, and for their help and guidance throughout these past three years.

An important part of this thesis originated from our collaboration with the group of Prof. Dwayne Miller at the Max Planck Research Department for Structural Dynamics at the University of Hamburg and at the Institute for Optical Sciences at the University of Toronto, whose time-resolved electron diffraction studies into the photocyclisation of diarylethenes in the solid state inspired me to implement and apply the hybrid QM/QM simulation method to model photochemical reactions in molecular crystals.

I thank a great friend and collaborator, Dr Andrzej Bil from the Faculty of Chemistry at the University of Wrocław, who on many occassions shared with me his vast knowledge of *ab initio* methods, and furthermore graciously agreed to carry out the CC2 calculations that were reported in our the paper on the photochemical reaction of *N*-salicylidene-2-chloroaniline in the solid state.

Credit is due to the many members and students of the University of Edinburgh School of Chemistry who encouraged and supported me during my research. I am indebted to Dr Philip J. Camp from the University of Edinburgh School of Chemistry for his insightful comments and questions throughout my PhD course. Dr Patricia Richardson set me up on our computing clusters, and made a huge contribution to the Computational Chemistry workshops that I organised during my PhD course. I also thank Dr David Rogers for his valuable advice concerning excited-state calculations in GAMESS, and for his continuing work to keep our hardware in running condition.

I would like to express my sincere gratitude and appreciation to the Reviewers of this thesis, Dr Michael J. Bearpark from the Imperial College London and

Dr Adam Kirrander from the University of Edinburgh, for the changes and corrections that they suggested, thus helping me greatly to improve its quality.

I am also grateful to the the University of Edinburgh and the Centre for Numerical Algorithms and Intelligent Software (NAIS) for the award of a Principal's Career Development Scholarship which supported me financially throughout my PhD course.

My final acknowledgements are to the numerous people and institutions owing to whose altruistic work I could conduct simulations and analyse results with excellent free and/or open-source software. These include:

- The developers of the *ab initio* simulation program PSI (www.psicode.org): the Center for Computational Quantum Chemistry at the University of Georgia; the research group of Prof. C. David Sherrill at the Georgia Institute of Technology; the research group of Prof. T. Daniel Crawford at Virginia Tech; the research group of Prof. Edward F. Valeev at Virginia Tech; and the research group of Prof. Rollin A. King at Bethel University.
- The research group of Prof. Mark Gordon at the Iowa State University, developers of GAMESS-US.
- Prof. Vladislav A. Blatov, Prof. Alexander P. Shevchenko and Prof. Davide M. Proserpio, authors of the crystal structure analysis program TOPOS 4.0.
- The developers of Jmol, an open-source Java viewer for chemical structures in 3D (www.jmol.org).
- Dr Sean Fleming, the author of molecular visualisation and editing program GDIS.

Abstract

Although the solid state may not usually be thought of as an environment suitable for chemical reactions under mild conditions, a growing number of organic compounds are known to undergo interesting and, in many cases, practically useful chemistry in the molecular crystal phase. Of particular interest are photochemical reactions occurring in molecular crystals, which possess a number of characteristic features that make them attractive to study using the methods of theoretical chemistry.

Firstly, molecular packing and steric effects strongly influence the mechanistic course of reactions in the crystal phase, which in some cases enables clean and controllable chemistry, including synthetic reactions as well as reversibly switchable isomerisations accompanied by a change of the macroscopic properties of the crystal, such as shape and colour. Secondly, in part due to their fast (subpicosecond) timescales and relatively low conversion rates (of the order of a few per cent), many of these reactions present challenges to experimental techniques, which computer simulation methods are uniquely positioned to overcome. Finally, these systems lend themselves well to simulation using a hybrid combination of two *ab initio* electronic structure methods, one of which is used to describe the electronic excitation of a reactive molecule while the other is applied to the surrounding bulk lattice.

This thesis describes the computational modelling of two such reactions: the *syn* → *anti* photoisomerisation of 7-(2-pyridyl)indole and the reversible *cis*-enol ⇄ *trans*-keto photoisomerisation of *N*-salicylidene-2-chloroaniline. The solid-state mechanisms and rates of both reactions are computed using the TD-DFT/DFT hybrid method, in the latter case validating a previously postulated reaction mechanism. Furthermore, the thermal (ground-state) tautomerisation reaction in the photochromic and non-photochromic polymorphs of *N*-salicylidene-2-chloroaniline is investigated through calculations at the DFT level of theory. The results of these calculations indicate that both polymorphs are thermochromic, but tautomeric equilibrium in the non-photochromic polymorph is more sensitive to temperature than in the photochromic polymorph. Additionally, a critical assessment is presented of the accuracy of the various emphab initio methods employed throughout this work.

Lay Summary

Although crystals of organic compounds are not commonly regarded as a medium in which chemical reactions can take place, there are in fact many compounds whose crystals react in interesting and useful ways. Among others, a number of reactions are known which are triggered by exposing a crystal to ultraviolet or visible light. Some yield desirable product compounds, while others may cause the crystal as a whole to change shape or colour, which has potential application in optics. Because reactions of this type happen extremely fast, they are generally difficult to study using experimental methods, but lend themselves very well to computer simulation.

This thesis describes the theoretical simulation of the light-induced reactions of the compounds 7-(2-pyridyl)indole and *N*-salicylidene-2-chloroaniline. A detailed step by step picture of both reactions is presented. In the case of *N*-salicylidene-2-chloroaniline, the sequence of events that take place during the reaction has previously been deduced from experimental data, and agrees closely with our own computer simulations. Also, the processes which cause crystals of *N*-salicylidene-2-chloroaniline to change colour with changing temperature have been studied using theoretical methods.

Contents

List of symbols, terms, abbreviations and acronyms used

7PyIn	7-(2-pyridyl)-indole
Å	Ångstrom
ϕ	torsion angle
ϕ(A-B-C-D)	the torsion angle formed by the four atoms A, B, C and D
BSSE	basis set superposition error
CASSCF	complete active space multiconfigurational self-consistent field
CC2	second-order approximate coupled cluster singles and doubles
CCSD	coupled cluster singles and doubles
CI	conical intersection; also: configuration interaction
DFT	density functional theory
ESIPT	excited-state intramolecular proton transfer
EOM-CC2	the extension of the CC2 method to excited electronic states by means of the equations-of-motion method
E_h	hartree (atomic unit of energy)
eV	electronvolt
FDE	frozen density embedding
fs	femtosecond
GSIPT	ground-state intramolecular proton transfer
GTO	Gaussian-type orbital basis set
HF	the Hartree-Fock method
IC	internal conversion
KEDF	kinetic-energy density functional
LCAO	the linear combination of atomic orbitals method
LSDA	local spin density approximation
MD	molecular dynamics
MP2	the second-order Møller-Plesset perturbation method
NEB	the nudged elastic band method
NVE	the microcanonical ensemble
NVT	the canonical ensemble
OFDFT	orbital-free density functional theory
PBE	the exchange-correlation functional of Perdew, Burke and Ernzerhof
PBE0	the exchange-correlation functional of Perdew, Burke and Ernzerhof as made into a hybrid by Adamo and Barone
PES	potential energy surface
ps	picosecond
PW	plane-wave basis set
QM/MM	the quantum mechanics/molecular mechanics hybrid method
QM/QM	the quantum mechanics/quantum mechanics hybrid method

R(A-B)	the distance between atoms A and B
S_0	the singlet ground state
S_1	the first (lowest) singlet excited state
S_2	the second singlet excited state
SA	*N*-salicylideneaniline
SCA	*N*-salicylidene-2-chloroaniline
T_1	the T_1 diagnostic
TD-DFT	time-dependent density functional theory
TD-DFT/DFT	the subtractive QM/QM method hybridising a TD-DFT description of the reactive molecule with a ground-state DFT description of the surrounding molecules
TS	transition state
VDP	Voronoi-Dirichlet polyhedron

Chapter 1
The QM/QM Hybrid Method

1.1. Introduction

Photochemical reactions occurring within molecular crystals are of major importance for their various technological applications, both existing and prospective. Examples include information storage,[1] photoactuators,[2,3] non-linear optical materials,[4] media for optical amplifiers or lasers,[5] as well as chemical synthesis,[6,7] including asymmetric synthesis.[8,9] A distinguishing characteristic of such systems is the interdependence between the reactivity of individual molecules and the bulk crystal structure, which in many cases exerts a strong directing influence and enables clean and controllable photochemical reactions.[6–9] In computer simulation studies, however, this same feature poses a challenge to the methods of theoretical chemistry. The interplay between crystal architecture and photochemical reactivity necessitates that the simulation method be capable of simultaneously modelling the excited-state process and the interaction of the excited molecule with the surrounding bulk lattice.

Reflecting the inhomogeneity of a system containing a photoexcited molecule surrounded by a number of nonreactive ground-state molecules, it is natural to use a hybrid simulation scheme whereby the two components of the system are treated on an unequal footing. Indeed, simulation techniques combining a quantum-mechanical (*ab initio* or semiempirical) description of the photoexcited molecule and a molecular mechanics treatment of the surrounding lattice (QM/MM) have previously been utilised in studies of photochemical reactions occurring within molecular crystals.[10,11] In the present work, a somewhat different hybrid simulation method is applied, whereby the photoexcited molecule is treated using a quantum-mechanical excited-state method, such as time-dependent DFT (TD-DFT) with a localised basis set, while the bulk lattice is modelled using the ground-state DFT approach. In this manner, the potential energy surface for the entire system is constructed using only *ab initio* methods, without recourse to parameterisation against experimental data. Such a combination of two quantum-mechanical techniques is termed the hybrid QM/QM method, and its theoretical foundation is the subject matter of the present Chapter. Because the mathematical formalism that underlies both the QM/MM and QM/QM methods

Figure 1.1: A diagrammatic illustration of the type of reaction studied in the present work. The black rectangle represents the boundaries of the simulated system, which is understood to be surrounded on all sides by periodic replicas of itself. The grey "bricks" are the ground-state molecules comprising the crystal lattice. The green arrow on the left-hand side represents the absorption of a photon by a single molecule in the system, which is highlighted in green on the right-hand side. The bold letters **S** and **C** denote, respectively, the entire system and the excited molecule.

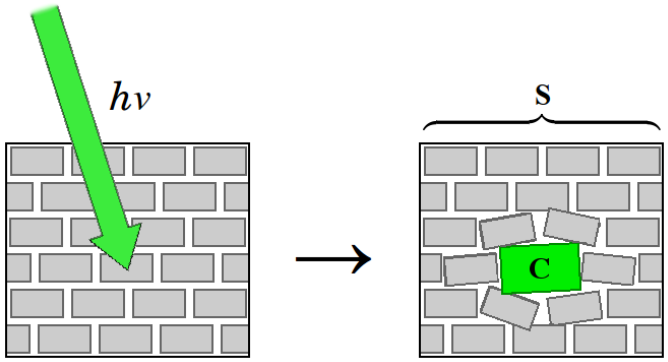

is easier explained in the context of the former, before discussing the QM/QM method we provide a (necessarily) brief review of the QM/MM method.

Let us first provide a formal problem statement and introduce the terminology that will be used throughout this work when discussing either method. Our goal will be to perform simulations of chemical reactions as they happen in the molecular crystal phase. As our model of the bulk crystal lattice in which the reaction takes place, we will use a single unit cell, or several unit cells constituting a supercell, repeated periodically in three dimensions, thus forming an infinite lattice. As illustrated in Figure 1.1 above, the irradiation of the crystal with electromagnetic radiation will result in some molecules absorbing photons and becoming excited from the ground electronic state to a higher electronic state. It will be assumed that the photoexcited molecules are sparsely distributed throughout the bulk crystal lattice, so that in the simulated system, there will be only a single such molecule. Furthermore, it will also be assumed that the electronic excitation is localised on only that molecule. This crucial assumption paves the way for the application of a hybrid simulation scheme in which only the single photoexcited molecule is described using a quantum-mechanical excited-state method, allowing an immense saving of computing time relative to a hypothetical simulation whereby the photoexcitation is permitted to become delocalised over multiple molecules, and the entire system must accordingly be

treated using an excited-state method. Of course, this assumption is only valid in the absence of relatively strong intermolecular interactions such as hydrogen bonding, and only if it is also known *a priori* that the photochemical process does not directly involve multiple molecules (through *e.g.* intermolecular charge transfer).

In the systems that are of interest to us, the photoexcitation triggers substantial structural changes in the excited molecule, such as *cis* to *trans* isomerisation. Naturally, the initial conformation of the photoexcited molecule is determined by the crystal architecture and molecular packing. What is more, although the surrounding ground-state molecules are not directly involved in the photochemical reaction, in the sense that they do not form relatively strong interactions such as hydrogen or covalent bonding with the excited molecule, they nevertheless influence its mechanistic course through steric and polarisation effects. Hence the need to include in the simulated system both the photoexcited molecule and the surrounding non-reactive molecules.

As shown in Figure 1.1, in what follows we will use the bold letter **C** to denote the photoexcited molecule, while **S** will represent the entire system including the photoexcited molecule. Moreover, in the following Figures in this Chapter (with the exception of Figure 1.4), we will use a consistent colour scheme whereby the colour of any region within the simulated system denotes the computational method used to evaluate its energy. Navy blue will always denote a quantum-mechanical excited-state method, yellow will indicate a molecular mechanics ground-state method, and the salmon colour will represent a quantum-mechanical ground-state method.

Also, in this and the following Chapters, for the sake of brevity we will generally refrain from discussing in depth well-known theoretical methods that we have employed in our simulations. For a detailed description of these methods, the Reader is instead referred to Appendices A to E. Appendix A deals with the nudged elastic band (NEB) method, Appendix B covers the Hartree-Fock (HF) method, Appendix C covers coupled cluster methods, Appendix D introduces density functional theory (DFT), and finally Appendix E concerns itself with the application of DFT to the solid state.

1.2. The QM/MM hybrid method

Originally introduced by Warshel and Levitt[12] for the purpose of simulating enzymatic reactions, the QM/MM method is generally applicable to systems that may be partitioned into a reaction site which will be treated using a quantum-mechanical (QM) method and a surrounding region that will be described using a molecular mechanics (MM) force field.

1.2.1. MM force fields

An MM force field is an expression for the potential energy whereby the electronic structure of the system is not considered explicitly, and the potential energy is calculated as a series of terms which describe specific interactions such as covalent bonding, van der Waals interactions, electrostatic interactions between partial charges localised on atoms, *etc.* For instance, a simple force field, whereby the van der Waals interaction is described using the Lennard-Jones potential, bond stretching and bending are both represented using harmonic potentials, and torsions are described using the cosine function, would take the following functional form:

$$E = \sum_{i,j}^{\substack{\text{non-bonded}\\ \text{pairs}}} 4\varepsilon \left[\left(\frac{\sigma}{r_{ij}} \right)^{12} - \left(\frac{\sigma}{r_{ij}} \right)^{6} \right] + \sum_{i<j} \frac{q_i q_j}{r_{ij}} + \sum_{i,j}^{\text{bonds}} \frac{1}{2} k_r \left(r_{ij} - r_0 \right)^2 +$$

$$+ \sum_{i,j,k}^{\substack{\text{bond}\\ \text{angles}}} \frac{1}{2} k_\theta \left(\theta_{ijk} - \theta_0 \right)^2 + \sum_{i,j,k,l}^{\text{dihedrals}} k_\phi \left[1 + \cos(n \phi_{ijkl} - \phi_0) \right] \tag{1.1}$$

The various parameters which appear in the definition of an MM force field are not known *a priori*, and must be derived by fitting to experimental and possibly also theoretical data. In the context of our simulations of photochemical reactions in the solid state, this requirement for parameterisation is unwelcome for two reasons:

Firstly, from a methodological standpoint, it is preferable to rely to the greatest possible extent on first principles. This rules out using an MM force field, which is in essence a function fitted to reproduce experimental data.

Secondly, the construction of a force field sufficiently accurate for the purposes

of the present work is a difficult prospect in its own right. Experimentally, it is known that photochemical reactions in molecular crystals are controlled by many factors, including the packing of molecules in the crystal lattice, the molecular conformation, and steric hindrance to the motions of molecules in the confined environment of crystal. In order for us to be able to make a convincing case that our computer simulations are a realistic model of these reactions, the simulation methodology must be proven to be able to to accurately describe these phenomena.

Pre-existing force fields designed generally for organic and biological molecules do not achieve this degree of accuracy. Literature reports of the application of some such force fields in molecular dynamics (MD) simulations of organic molecular crystals show that they are often incapable of accurately reproducing experimental crystal structures,[13,14] in some cases failing so severely as to predict a partial or complete loss of crystalline ordering, or spurious phase transitions.[14] Crystals of conformationally flexible molecules appear to be especially problematic, because for such molecules the force field must correctly reproduce both the conformational preference of the molecules and the intermolecular interactions. Failure to do so may result in the molecules deforming away from their experimentally-determined conformations, and the molecular packing being predicted incorrectly. Such behaviour appears to manifest itself in the case of the tripeptide L-alanyl-glycyl-L-alanine simulated[14] using the force fields MM3[15–17] and GAFF:[18] in the first case, all molecules in the crystal lattice curl in, while in the latter, half of the molecules curl in and half elongate. Because the anil *N*-salicylidene-2-chloroaniline is known to be able to form two different crystal structures, in one of which the molecules are planar, and non-planar in the other (an instance of polymorphism; the two crystal structures are the non-photochromic and the photochromic polymorphs, respectively), and the loosely packed crystal structure of the photochromic polymorph of that compound is likely to exacerbate a poor description of its conformational preference, we believe that in order to obtain a realistic force field for *N*-salicylidene-2-chloroaniline, it would be necessary to simultaneously refine both intra- and intermolecular interaction parameters of an existing force field.

In summary, without re-parameterisation, a pre-existing force field cannot be relied on to accurately reproduce the crystal structures that are of interest to us. On the other hand, for relatively large molecules such as 7-(2-pyridyl)indole and *N*-salicylidene-2-chloroaniline, the refinement of even only a subset of the

force field parameters (say, the van der Waals interaction parameters) is a daunting task. In the present work, this Gordian knot has been cut by employing a quantum mechanical method, namely, density functional theory (DFT), instead of a force field to describe the region surrounding the reaction site. In this manner, we have circumvented the need for the parameterisation of a force field, while retaining the advantages of a hybrid simulation method. As pointed out in Appendix D, due to the inability of popular DFT exchange-correlation functionals to describe dispersion interactions, the resulting simulation does not rely exclusively on first principles, and dispersion is included as a molecular mechanics-like correction. Nevertheless, we believe that owing to the well-attested ability of DFT to predict molecular conformations and potential energy surface topologies, it is at least as accurate as a tailor-made MM force field, while also being more in line with the idea of *ab initio* simulation.

Presently, in order to provide historical and methodological context for hybrid simulations combining two quantum-mechanical methods (QM/QM), we will discuss the chronologically older QM/MM method. The formalism established in this section will then be extended to the case of the QM/QM method.

For the system consisting of a reactive photoexcited molecule surrounded by a number of non-reactive molecules, the obvious QM/MM partitioning is to treat the photoexcited molecule using an excited-state quantum-mechanical method, and the surrounding ground-state molecules using a suitable MM force field. There are two main ways in which the potential energy function of the entire simulated system may be constructed using a combination of the QM and MM methods: the additive scheme, and the subtractive scheme. We will now discuss in turn both these variants of the QM/MM method.

1.2.2. The additive QM/MM scheme

In the additive scheme, the potential energy of the system is taken as the sum of the energy of the ground-state molecules calculated using the MM method, the energy of the photoexcited molecule calculated at the QM level, and an explicit coupling term which describes the interactions between the photoexcited molecule and the surrounding molecules:

$$E_{\mathrm{QM/MM}}(\mathbf{S}) = E_{\mathrm{MM}}(\mathbf{S}-\mathbf{C}) + E_{\mathrm{QM}}(\mathbf{C}) + E_{\mathrm{coupling}}(\mathbf{S}) \tag{1.2}$$

Figure 1.2: The breakdown of the potential energy within the additive QM/MM scheme. The symbols in this pictorial equation correspond, in the same order, to the terms which appear in equation 1.2.

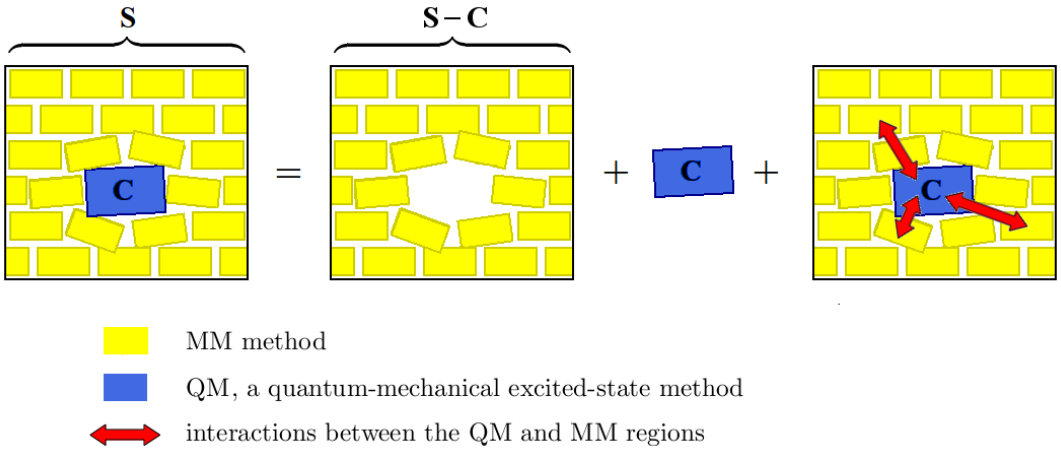

Here, $\mathbf{S}-\mathbf{C}$ denotes the simulated system without the photoexcited molecule. (More formally, if $\mathbf{S}$ and $\mathbf{C}$ are considered as sets of atoms, then $\mathbf{S}-\mathbf{C}$ is the set-theoretic difference of $\mathbf{S}$ and $\mathbf{C}$.) Equation 1.2, which defines the additive QM/MM scheme, is also explained pictorially in Figure 1.2 above.

The coupling term $E_{\text{coupling}}(\mathbf{S})$ includes electrostatic and van der Waals interactions between the quantum and classical subsystems:

$$E_{\text{coupling}}(\mathbf{S}) = E^{\text{vdW}}_{\text{coupling}}(\mathbf{S}) + E^{\text{electrostatic}}_{\text{coupling}}(\mathbf{S}) \tag{1.3}$$

The van der Waals interactions between the photoexcited molecule ($\mathbf{C}$) and the surrounding molecules ($\mathbf{S}-\mathbf{C}$) are usually treated at the MM level. Then, the van der Waals coupling term is simply a sum of pair interactions between atoms belonging to $\mathbf{C}$ and those belonging to $\mathbf{S}-\mathbf{C}$:

$$E^{\text{vdW}}_{\text{coupling}}(\mathbf{S}) = \sum_{i}^{\substack{\text{atoms}\\ \text{in } \mathbf{C}}} \sum_{j}^{\substack{\text{atoms}\\ \text{in } \mathbf{S}-\mathbf{C}}} 4\varepsilon \left[\left(\frac{\sigma}{r_{ij}} \right)^{12} - \left(\frac{\sigma}{r_{ij}} \right)^{6} \right] \tag{1.4}$$

Here, the summation $\sum_{j}^{\substack{\text{atoms}\\ \text{in } \mathbf{S}-\mathbf{C}}}$ is understood to include the MM atoms in the system and all of its periodic replicas.

On the other hand, the electrostatic coupling term may be evaluated by

either the MM method or the QM calculation. In the former case, partial charges q_i must be assigned to the atoms belonging to the photoexcited molecule $\mathbf{C}$, and the electrostatic coupling energy will be calculated as a sum of electrostatic interactions between partial charges on atoms belonging to $\mathbf{C}$ and to $\mathbf{S}-\mathbf{C}$:

$$E_{\text{coupling}}^{\text{electrostatic}}(\mathbf{S}) = \sum_{i}^{\substack{\text{atoms} \\ \text{in } \mathbf{C}}} \sum_{j}^{\substack{\text{atoms} \\ \text{in } \mathbf{S}-\mathbf{C}}} \frac{q_i q_j}{r_{ij}} \tag{1.5}$$

The latter case, whereby the electrostatic coupling is handled by the quantum-mechanical calculation, is much more interesting, as it allows for the electron density of the photoexcited molecule to be polarised by the surrounding molecules. In the simplest implementation, which is known in the literature as electrostatic embedding,[19] this is achieved by including in the QM Hamiltonian operator the electrostatic interaction of the electrons with the point charges of the surrounding molecules. It is worth mentioning that in the case of additive QM/MM calculations for solid-state systems, the calculation of these interactions is complicated by the long range of the electrostatic interaction and the fact that the crystal extends infinitely and periodically in three dimensions. Accordingly, in general it is not possible to accurately describe them by simply including a sum of the form

$$-\sum_{i=1}^{N} \sum_{b=1}^{\substack{\text{atoms} \\ \text{in } \mathbf{S}-\mathbf{C}}} \frac{q_b}{r_{bi}} \tag{1.6}$$

in the quantum-mechanical Hamiltonian, because such a summation converges slowly and conditionally (meaning that the result is dependent on the order in which the terms are added). Instead, these interactions require a more sophisticated treatment such as an Ewald summation-based method.[20] As described in Section 2.3 of Chapter 2, in the present work we have carried out a single-point electrostatic embedding calculation in order to quantify the effects of the polarisation of a photoexcited molecule by the surrounding molecules, and thereby to test the validity of the subtractive QM/QM scheme which neglects this polarisation. In that calculation, a simplistic finite and nonperiodic model of the crystal was used which contained the photoexcited molecule and a surrounding shell of ground-state molecules. Hence, it described only the interactions of the photoexcited molecule with the nearest few surrounding molecules. As such, within that model it was possible to achieve electrostatic embedding by adding the term 1.6 to the quantum-mechanical Hamiltonian.

1.2.3. The subtractive QM/MM scheme

The subtractive QM/MM scheme of Morokuma and coworkers,[21,22] also known in the literature as ONIOM (our own N-layered integrated molecular orbital and molecular mechanics), is defined by equation 1.7, which is an expression of the idea that the potential energy of the system may be evaluated as the sum of the energy of the entire system (**S**) calculated using the MM method and the energy of the photoexcited molecule (**C**) calculated using the QM method, minus a third term that corrects for the double counting of the energy of the photoexcited molecule by the previous two terms. This third term turns out to be simply the energy of the photoexcited molecule calculated using the MM force field as though the photoexcited molecule was in the electronic ground state. The way in which equation 1.7 calculates the total energy is illustrated schematically in Figure 1.3 below.

$$E_{\mathrm{QM/MM}}(\mathbf{S}) = E_{\mathrm{MM}}(\mathbf{S}) + E_{\mathrm{QM}}(\mathbf{C}) - E_{\mathrm{MM}}(\mathbf{C}) \tag{1.7}$$

The term $E_{\mathrm{MM}}(\mathbf{S})$ in equation 1.7 represents the potential energy of the entire system evaluated through an MM calculation. All interactions between the photoexcited molecule and the surrounding bulk lattice are included exclusively in this term, and as such the subtractive QM/MM treats these interactions at the MM level, as though the photoexcited molecule was in the electronic ground state, which is an approximation inherent to this variant of the QM/MM method.

Figure 1.3: A schematic explanation of the subtractive QM/MM scheme. The symbols in this pictorial equation correspond, in the same order, to the terms which appear in equation 1.7.

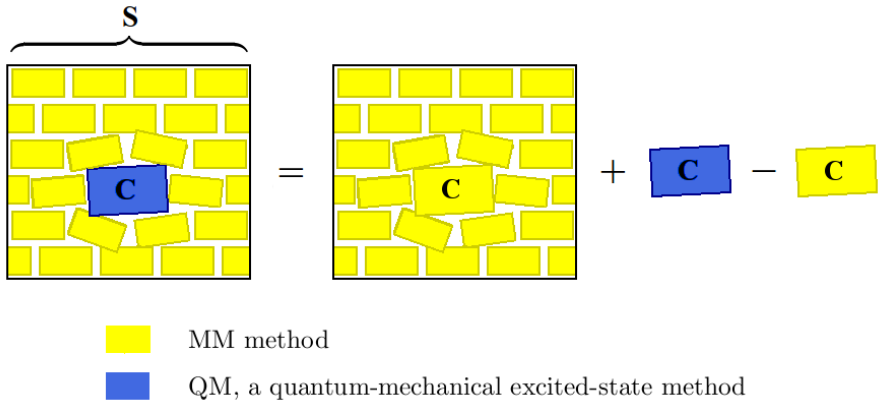

$E_{\mathrm{QM}}(\mathbf{C})$ and $E_{\mathrm{MM}}(\mathbf{C})$ are the potential energies of the photoexcited molecule alone, evaluated respectively at the QM and MM levels. Both these terms are calculated in the absence of the surrounding bulk lattice. As a consequence, in the subtractive QM/MM calculation the electron density of the reactive molecule does not experience the polarising influence of the surrounding bulk lattice. This omission of the polarisation of the photoexcited molecule is another approximation inherent in the subtractive QM/MM scheme.

The term $E_{\mathrm{MM}}(\mathbf{C})$ is subtracted from the sum $E_{\mathrm{MM}}(\mathbf{S}) + E_{\mathrm{QM}}(\mathbf{C})$ in order to correct for the double counting of the intramolecular energy of the photoexcited molecule by these two terms. Because in MM force fields, as exemplified by the force field given by equation 1.1, the energy is expressed as a sum over terms which describe specific bond, three-atom angles, electrostatic interactions and so on, in the subtractive QM/MM scheme the cancellation of the intramolecular energy of the reactive molecule is guaranteed to be exact. For instance, for each covalent bond in the photoexcited molecule, a term of the form $\frac{1}{2}\, k_r\, (r_{ij} - r_0)^2$ will appear in $E_{\mathrm{MM}}(\mathbf{S})$, and an identical term will be found in $E_{\mathrm{MM}}(\mathbf{C})$; these identical terms will cancel each other exactly. In other words, in the subtractive QM/MM scheme, the energy cancellation between the terms $E_{\mathrm{MM}}(\mathbf{S})$ and $E_{\mathrm{MM}}(\mathbf{C})$ is not a source of error.

1.3. The QM/QM hybrid method

Having reviewed the QM/MM hybrid method, we now turn our attention to its more sophisticated analogue: the QM/QM method, in which the system is partitioned into two regions that are treated at different levels of quantum-mechanical theory. We begin with an outline of the frozen density embedding theory, which is a variant of the QM/QM method that is somewhat akin to additive QM/MM. We then proceed to discuss the subtractive QM/QM scheme, which forms the basis of the QM/QM simulations reported in the present work, and finally, we describe its practical implementation.

1.3.1. Frozen density embedding theory

The frozen density embedding (FDE) theory of Wesołowski and Warshel[23] provides a rigorous quantum-mechanical framework for the treatment of the interaction

between two electron densities. We discuss it here to provide methodological context for the approximate subtractive QM/QM scheme which we used in our simulations. The FDE theory has its roots in orbital-free DFT,[24] (OFDFT) which is the variant of DFT that does not take advantage of the Kohn-Sham spinorbitals in order to calculate the kinetic energy of the auxiliary system of non-interacting electrons, and instead attempts to calculate the kinetic energy directly from the electron density. Like the more popular Kohn-Sham DFT scheme, OFDFT is a formally exact ground-state method, and hence its use does not limit the scope of the FDE theory.

As illustrated in Figure 1.4, the total electron density of the system, $\rho_{\mathrm{tot}}(\mathbf{r})$, is expressed as a sum of two component densities $\rho_{\mathrm{I}}(\mathbf{r})$ and $\rho_{\mathrm{II}}(\mathbf{r})$:

$$\rho_{\mathrm{tot}}(\mathbf{r}) = \rho_{\mathrm{I}}(\mathbf{r}) + \rho_{\mathrm{II}}(\mathbf{r}) \tag{1.8}$$

The component densities are allowed to overlap, and furthermore each component density is required to integrate to a fixed integral number of electrons:

$$\int \rho_{\mathrm{I}}(\mathbf{r})\,\mathrm{d}\mathbf{r} = N_{\mathrm{I}} \qquad \int \rho_{\mathrm{II}}(\mathbf{r})\,\mathrm{d}\mathbf{r} = N_{\mathrm{II}}$$

$N_{\mathrm{I}} + N_{\mathrm{II}} = N$ is the total number of electrons in the system. Aside from this constraint, the way that the total density is partitioned is entirely arbitrary. Likewise, the nuclei are also somehow divided into those that "belong" to $\rho_{\mathrm{I}}(\mathbf{r})$ and those that "belong" to $\rho_{\mathrm{II}}(\mathbf{r})$. The electrostatic potential due to the nuclei, $v^{\mathrm{nuc}}(\mathbf{r})$, may therefore be broken down into terms originating from nuclei belonging to $\rho_{\mathrm{I}}(\mathbf{r})$ and to $\rho_{\mathrm{II}}(\mathbf{r})$:

$$v^{\mathrm{nuc}}(\mathbf{r}) = v_{\mathrm{I}}^{\mathrm{nuc}}(\mathbf{r}) + v_{\mathrm{II}}^{\mathrm{nuc}}(\mathbf{r})$$

Within OFDFT, the total energy of the system is written out as follows (*cf.* the energy expression within the Kohn-Sham DFT scheme, equation D.10 in Appendix D):

$$E_{\mathrm{tot}} = E^{\mathrm{nuc}} + \int \rho_{\mathrm{tot}}(\mathbf{r})\, v^{\mathrm{nuc}}(\mathbf{r})\,\mathrm{d}\mathbf{r} + \frac{1}{2}\int\int \frac{\rho_{\mathrm{tot}}(\mathbf{r})\,\rho_{\mathrm{tot}}(\mathbf{r}')}{|\mathbf{r}-\mathbf{r}'|}\,\mathrm{d}\mathbf{r}\,\mathrm{d}\mathbf{r}' +$$

$$+ E_{\mathrm{xc}}[\rho_{\mathrm{tot}}] + T_{\mathrm{s}}[\rho_{\mathrm{tot}}] \tag{1.9}$$

Figure 1.4: A schematic illustration of the QM/QM partitioning within FDE theory, on the example of the hydrogen-bonded $H_2O\cdots HF$ complex. The total density is partitioned into a sum of overlapping component densities $\rho_{\mathrm{I}}(\mathbf{r})$ and $\rho_{\mathrm{II}}(\mathbf{r})$. The corresponding green and red isodensity curves represent the projections of the three-dimensional electron isodensity surfaces onto the xy plane.

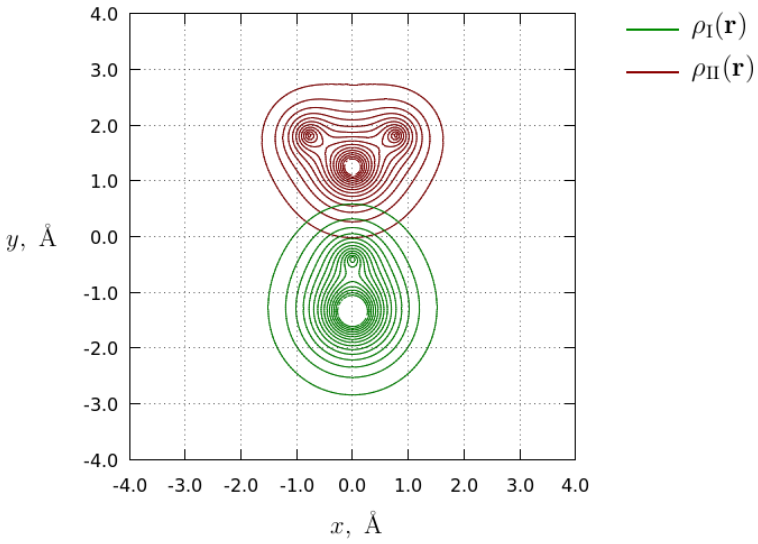

Here,

- E_{nuc} is the nuclear repulsion energy.
- The term $\int \rho_{\mathrm{tot}}(\mathbf{r}) v^{\mathrm{nuc}}(\mathbf{r}) \mathrm{d}\mathbf{r}$ is the interaction of the electron density with the Coulombic potential of the nuclei.
- $\frac{1}{2}\int\int \frac{\rho_{\mathrm{tot}}(\mathbf{r})\rho_{\mathrm{tot}}(\mathbf{r}')}{|\mathbf{r}-\mathbf{r}'|}\mathrm{d}\mathbf{r}\,\mathrm{d}\mathbf{r}'$ is the classical electrostatic self-interaction energy of the electron density.
- $E_{\mathrm{xc}}[\rho_{\mathrm{tot}}]$ represents the exchange-correlation energy.
- Finally, $T_{\mathrm{s}}[\rho_{\mathrm{tot}}]$ is the kinetic energy of the auxiliary system of non-interacting electrons, calculated through a kinetic-energy density functional ($T_{\mathrm{s}}[\rho]$, abbreviated KEDF) without introducing the Kohn-Sham spinorbitals.

Given that the total electron density has been broken down into a sum of two component electron densities, we may rewrite equation 1.9 as follows:

$$E_{\mathrm{tot}} = E^{\mathrm{nuc}}_{\mathrm{I\text{-}I}} + E^{\mathrm{nuc}}_{\mathrm{II\text{-}II}} + E^{\mathrm{nuc}}_{\mathrm{I\text{-}II}} + \int \left[\rho_{\mathrm{I}}(\mathbf{r}) + \rho_{\mathrm{II}}(\mathbf{r})\right]\left[v^{\mathrm{nuc}}_{\mathrm{I}}(\mathbf{r}) + v^{\mathrm{nuc}}_{\mathrm{II}}(\mathbf{r})\right]\mathrm{d}\mathbf{r} +$$

$$+\frac{1}{2}\int\int \frac{\left[\rho_{\mathrm{I}}(\mathbf{r}) + \rho_{\mathrm{II}}(\mathbf{r})\right]\left[\rho_{\mathrm{I}}(\mathbf{r}') + \rho_{\mathrm{II}}(\mathbf{r}')\right]}{|\mathbf{r}-\mathbf{r}'|}\mathrm{d}\mathbf{r}\,\mathrm{d}\mathbf{r}' +$$

$$+ E_{\mathrm{xc}}[\rho_{\mathrm{I}}] + E_{\mathrm{xc}}[\rho_{\mathrm{II}}] + E_{\mathrm{xc}}^{\mathrm{nadd}}[\rho_{\mathrm{I}}, \rho_{\mathrm{II}}] + T_{\mathrm{s}}[\rho_{\mathrm{I}}] + T_{\mathrm{s}}[\rho_{\mathrm{I}}, \rho_{\mathrm{II}}] + T_{\mathrm{s}}^{\mathrm{nadd}}[\rho_{\mathrm{II}}] \tag{1.10}$$

where $E_{\mathrm{xc}}^{\mathrm{nadd}}[\rho_{\mathrm{I}}, \rho_{\mathrm{II}}]$ is the non-additive exchange-correlation energy defined as:

$$E_{\mathrm{xc}}^{\mathrm{nadd}}[\rho_{\mathrm{I}}, \rho_{\mathrm{II}}] = E_{\mathrm{xc}}[\rho_{\mathrm{I}} + \rho_{\mathrm{II}}] - E_{\mathrm{xc}}[\rho_{\mathrm{I}}] - E_{\mathrm{xc}}[\rho_{\mathrm{II}}] \tag{1.11}$$

and $T_{\mathrm{s}}^{\mathrm{nadd}}[\rho_{\mathrm{I}}, \rho_{\mathrm{II}}]$ is the non-additive kinetic energy:

$$T_{\mathrm{s}}^{\mathrm{nadd}}[\rho_{\mathrm{I}}, \rho_{\mathrm{II}}] = T_{\mathrm{s}}[\rho_{\mathrm{I}} + \rho_{\mathrm{II}}] - T_{\mathrm{s}}[\rho_{\mathrm{I}}] - T_{\mathrm{s}}[\rho_{\mathrm{II}}] \tag{1.12}$$

We may furthermore express the total energy as a sum of a term that involves only $\rho_{\mathrm{I}}(\mathbf{r})$, a term that involves only $\rho_{\mathrm{II}}(\mathbf{r})$, and an explicit coupling term $E_{\mathrm{int}}[\rho_{\mathrm{I}}, \rho_{\mathrm{II}}]$ that can be said to describe the interactions between $\rho_{\mathrm{I}}(\mathbf{r})$ and $\rho_{\mathrm{II}}(\mathbf{r})$:

$$E_{\mathrm{tot}}[\rho_{\mathrm{II}}] = E_{\mathrm{I}}[\rho_{\mathrm{I}}] + E_{\mathrm{II}}[\rho_{\mathrm{II}}] + E_{\mathrm{int}}[\rho_{\mathrm{I}}, \rho_{\mathrm{II}}] \tag{1.13}$$

where

$$E_{\mathrm{I}}[\rho_{\mathrm{I}}] = E_{\mathrm{I}}^{\mathrm{nuc}} + \int \rho_{\mathrm{I}}(\mathbf{r})\, v_{\mathrm{I}}^{\mathrm{nuc}}(\mathbf{r})\, \mathrm{d}\mathbf{r} + \frac{1}{2} \int\int \frac{\rho_{\mathrm{I}}(\mathbf{r})\, \rho_{\mathrm{I}}(\mathbf{r}')}{|\mathbf{r} - \mathbf{r}'|}\, \mathrm{d}\mathbf{r}\, \mathrm{d}\mathbf{r}' +$$

$$+ E_{\mathrm{xc}}[\rho_{\mathrm{I}}] + T_{\mathrm{s}}[\rho_{\mathrm{I}}] \tag{1.14}$$

$$E_{\mathrm{II}}[\rho_{\mathrm{II}}] = E_{\mathrm{II}}^{\mathrm{nuc}} + \int \rho_{\mathrm{II}}(\mathbf{r})\, v_{\mathrm{II}}^{\mathrm{nuc}}(\mathbf{r})\, \mathrm{d}\mathbf{r} + \frac{1}{2} \int\int \frac{\rho_{\mathrm{II}}(\mathbf{r})\, \rho_{\mathrm{II}}(\mathbf{r}')}{|\mathbf{r} - \mathbf{r}'|}\, \mathrm{d}\mathbf{r}\, \mathrm{d}\mathbf{r}' +$$

$$+ E_{\mathrm{xc}}[\rho_{\mathrm{II}}] + T_{\mathrm{s}}[\rho_{\mathrm{II}}] \tag{1.15}$$

and the coupling term is given by

$$E_{\mathrm{int}}[\rho_{\mathrm{I}}, \rho_{\mathrm{II}}] = E_{\mathrm{I\text{-}II}}^{\mathrm{nuc}} + \int \rho_{\mathrm{I}}(\mathbf{r})\, v_{\mathrm{II}}^{\mathrm{nuc}}(\mathbf{r})\, \mathrm{d}\mathbf{r} + \int \rho_{\mathrm{II}}(\mathbf{r})\, v_{\mathrm{I}}^{\mathrm{nuc}}(\mathbf{r})\, \mathrm{d}\mathbf{r} +$$

$$+ \int\int \frac{\rho_{\mathrm{I}}(\mathbf{r})\, \rho_{\mathrm{II}}(\mathbf{r}')}{|\mathbf{r} - \mathbf{r}'|}\, \mathrm{d}\mathbf{r}\, \mathrm{d}\mathbf{r}' + E_{\mathrm{xc}}^{\mathrm{nadd}}[\rho_{\mathrm{I}}, \rho_{\mathrm{II}}] + T_{\mathrm{s}}^{\mathrm{nadd}}[\rho_{\mathrm{I}}, \rho_{\mathrm{II}}] \tag{1.16}$$

We note that the form of equation 1.13 is closely reminiscent of equation 1.3 which defines the additive QM/MM scheme. Through further manipulations, it is possible to transform this equation into a form that lends itself to numerical QM/QM calculations. We will minimise the total energy of the system by varying the electron density component $\rho_{\mathrm{I}}(\mathbf{r})$, while imposing the constraint that $\rho_{\mathrm{II}}(\mathbf{r})$ is to be frozen (unchanged everywhere) throughout all calculations. Also, the number N_{I} of electrons in the density component $\rho_{\mathrm{I}}(\mathbf{r})$ is to remain constant. These conditions correspond to $\rho_{\mathrm{I}}(\mathbf{r})$ being embedded in the frozen density $\rho_{\mathrm{II}}(\mathbf{r})$.

The density component $\rho_{\mathrm{I}}(\mathbf{r})$ will from now on be expressed in terms of the Kohn-Sham spinorbitals $\phi_{\mathrm{I}i}(\mathbf{r},\sigma_1)$:

$$\rho_{\mathrm{I}}(\mathbf{r}) = \sum_{i=1}^{N_{\mathrm{I}}} \sum_{\sigma_1} |\,\phi_{\mathrm{I}i}(\mathbf{r},\sigma_1)\,|^2$$

The minimisation of $E_{\mathrm{int}}[\rho_{\mathrm{I}},\rho_{\mathrm{II}}]$ with frozen ρ_{II} and constrained N_{I} leads to the following set of modified Kohn-Sham equations for the spinorbitals $\phi_{\mathrm{I}i}(\mathbf{r},\sigma_1)$:

$$\left[-\frac{1}{2}\nabla^2 + v_{\mathrm{KS}}[\rho_{\mathrm{I}}](\mathbf{r}) + v_{\mathrm{emb}}[\rho_{\mathrm{I}},\rho_{\mathrm{II}}](\mathbf{r})\right]\phi_{\mathrm{I}i}(\mathbf{r},\sigma_1) = \varepsilon_i\phi_{\mathrm{I}i}(\mathbf{r},\sigma_1) \tag{1.17}$$

where the Kohn-Sham potential is given by

$$v_{\mathrm{KS}}[\rho_{\mathrm{I}}](\mathbf{r}) = \frac{\delta E_{\mathrm{I}}[\rho_{\mathrm{I}}]}{\delta\rho_{\mathrm{I}}(\mathbf{r})} = v_{\mathrm{I}}^{\mathrm{nuc}}(\mathbf{r}) + \int \frac{\rho_{\mathrm{I}}(\mathbf{r}')}{|\mathbf{r}-\mathbf{r}'|}\,\mathrm{d}\mathbf{r}' + \frac{\delta E_{\mathrm{xc}}[\rho_{\mathrm{I}}]}{\delta\rho_{\mathrm{I}}(\mathbf{r})} \tag{1.18}$$

and $v_{\mathrm{emb}}[\rho_{\mathrm{I}},\rho_{\mathrm{II}}](\mathbf{r})$ is an embedding potential that describes the interaction of $\rho_{\mathrm{I}}(\mathbf{r})$ with the frozen $\rho_{\mathrm{II}}(\mathbf{r})$:

$$v_{\mathrm{emb}}[\rho_{\mathrm{I}},\rho_{\mathrm{II}}](\mathbf{r}) = \frac{\delta E_{\mathrm{int}}[\rho_{\mathrm{I}},\rho_{\mathrm{II}}]}{\delta\rho_{\mathrm{I}}(\mathbf{r})} = v_{\mathrm{II}}^{\mathrm{nuc}}(\mathbf{r}) + \int \frac{\rho_{\mathrm{II}}(\mathbf{r}')}{|\mathbf{r}-\mathbf{r}'|}\,\mathrm{d}\mathbf{r}' +$$

$$+\frac{\delta E_{\mathrm{xc}}[\rho_{\mathrm{tot}}]}{\delta\rho_{\mathrm{tot}}(\mathbf{r})} - \frac{\delta E_{\mathrm{xc}}[\rho_{\mathrm{I}}]}{\delta\rho_{\mathrm{I}}(\mathbf{r})} + \frac{\delta T_{\mathrm{s}}[\rho_{\mathrm{tot}}]}{\delta\rho_{\mathrm{tot}}(\mathbf{r})} - \frac{\delta T_{\mathrm{s}}[\rho_{\mathrm{I}}]}{\delta\rho_{\mathrm{I}}(\mathbf{r})} \tag{1.19}$$

The triumph of the FDE theory is that the interaction of the variationally minimised $\rho_{\mathrm{I}}(\mathbf{r})$ with the frozen $\rho_{\mathrm{II}}(\mathbf{r})$ has been condensed into the one-electron operator $v_{\mathrm{emb}}[\rho_{\mathrm{I}},\rho_{\mathrm{II}}](\mathbf{r})$. The numerical solution of the modified Kohn-Sham equations 1.17 yields the optimal $\rho_{\mathrm{I}}(\mathbf{r})$ in the presence of the frozen $\rho_{\mathrm{II}}(\mathbf{r})$, thus providing a route to the modelling of a molecule described by the electron density distribution $\rho_{\mathrm{I}}(\mathbf{r})$ embedded in an environment described by $\rho_{\mathrm{II}}(\mathbf{r})$. As yet, this computational scheme includes the polarisation of $\rho_{\mathrm{I}}(\mathbf{r})$ by $\rho_{\mathrm{II}}(\mathbf{r})$, but does not allow for the back-polarisation of $\rho_{\mathrm{II}}(\mathbf{r})$ by $\rho_{\mathrm{I}}(\mathbf{r})$ (since $\rho_{\mathrm{II}}(\mathbf{r})$ is frozen). Having obtained the optimal $\rho_{\mathrm{I}}(\mathbf{r})$ in the presence of the frozen $\rho_{\mathrm{I}}(\mathbf{r})$, we may, however, reverse the roles of $\rho_{\mathrm{I}}(\mathbf{r})$ and $\rho_{\mathrm{II}}(\mathbf{r})$ by freezing $\rho_{\mathrm{I}}(\mathbf{r})$ and unfreezing $\rho_{\mathrm{II}}(\mathbf{r})$, and subsequently minimise the total energy with respect to $\rho_{\mathrm{II}}(\mathbf{r})$. By repeating this "freeze-and-thaw" procedure iteratively until self-consistency between $\rho_{\mathrm{I}}(\mathbf{r})$ and $\rho_{\mathrm{II}}(\mathbf{r})$, we may compute the total electron density and the total energy.[25]

It is furthermore possible to extend the FDE approach to the case where one (or both) of the component electron densities will originate from a wavefunction-based *ab initio* calculation, rather than from a DFT calculation.[26] Within the Hartree-Fock theory, for instance, whereby the wavefunction is approximated as a single Slater determinant, and which provides the starting point for many wavefunction-based methods that include electron correlation, the embedding potential enters the Roothan-Hall equation (equation B.32 in Appendix B) in the form of the so-called matrix representation of the embedding potential, $\mathbf{M}$:

$$(\mathbf{F} + \mathbf{M})\,\mathbf{c} = \mathbf{S}\,\mathbf{c}\,\boldsymbol{\varepsilon} \tag{1.20}$$

where the elements of the matrix $\mathbf{M}$ are given by

$$M_{kj} = \int \chi_k^*(1)\, v_{\mathrm{emb}}[\rho_{\mathrm{I}}, \rho_{\mathrm{II}}](\mathbf{r}_1)\, \chi_j(1)\, \mathrm{d}\tau_1 \tag{1.21}$$

Møller-Plesset perturbational (MPn) and multideterminantal (*e.g.* CASSCF) methods may also be used, in the latter case paving the way for FDE calculations for localised excitations in a ground-state environment.

The FDE theory has been applied to several examples of localised excited states in extended systems, among them the excited states of carbon monoxide adsorbed on a metal surface[26] (modelled using the CI/DFT combination of methods, where CI stands for configuration interaction, and CASSCF/DFT), charge transfer excitations in nucleobase complexes[27] (DFT/DFT), the n, π^* transition of the acetone water complex and a high π, π^* excitation of pyridine adsorbed on a silver nanoparticle[28] (TD-DFT/DFT), and local excited states in magnesium oxide[29] (using a range of correlated wavefunction-based methods in combination with DFT). Raghavachari and coworkers[30–33] have also developed a more approximate QM/QM embedding scheme, whereby only the classical electrostatic interaction between the two component electron densities was included at the quantum-mechanical level. The general form of such a purely electrostatic embedding method may be formally derived from FDE theory by simply eliminating the terms $E_{\mathrm{xc}}^{\mathrm{nadd}}[\rho_{\mathrm{I}}, \rho_{\mathrm{II}}]$ and $T_{\mathrm{s}}^{\mathrm{nadd}}[\rho_{\mathrm{I}}, \rho_{\mathrm{II}}]$ from the coupling term $E_{\mathrm{int}}[\rho_{\mathrm{I}}, \rho_{\mathrm{II}}]$ defined by equation 1.16. Of course, the "missing" part of the interaction energy must then be somehow re-included in the potential energy expression.

These successes notwithstanding, it seems uncertain whether embedding schemes based on the FDE theory are sufficiently reliable to be used for production calculations. The main concern is that the calculation of the coupling term $E_{\mathrm{int}}[\rho_{\mathrm{I}}, \rho_{\mathrm{II}}]$ requires the use of the KEDF ($T_{\mathrm{s}}[\rho]$), the exact form of which is unknown, necessitating the use of an approximate KEDF. A survey of studies which compare the performance of various approximate KEDFs within the framework of the FDE theory[34–38] suggests that existing state-of-the-art approximate KEDFs are not yet accurate enough for our purposes. At the very least, extensive testing and quite likely a reparameterisation of the dispersion correction scheme (see Section 6 of Appendix D) would be required.

On the other hand, the accuracy of purely electrostatic embedding schemes has recently been called into question.[39,40] In particular, it has been demonstrated that the calculated excitation energies of aromatic molecules subjected to purely electrostatic embedding vary strongly and erratically with increasing basis set size, whereas with full FDE theory-based embedding, the excitation energies are considerably more stable.[40] This indicates that neglecting the nonadditive exchange-correlation and kinetic energy terms from the coupling term 1.16 may lead to an overestimation of the polarisation of the electron density of the embedded molecule.

In light of the above, we have elected not to use either of the two explicitly embedded types of calculation (full FDE and purely electrostatic). Instead, in our QM/QM simulations we have used the subtractive QM/QM scheme, which is analogous to the previously considered subtractive QM/MM scheme. As will become clear in the following Section, the QM/QM scheme involves several approximations, the effects of some of which we attempt to quantify in Chapter 2. We believe that for the specific systems that we have studied, these approximations do not seriously impair the accuracy of the subtractive QM/QM scheme, and that the subtractive QM/QM scheme gives rise to realistic potential energy surfaces for reactions in molecular crystals.

1.3.2. The subtractive QM/QM scheme

The QM/QM coupling method used in the present work is a direct adaptation of the subtractive QM/MM scheme to the case where the photoexcited molecule is to be treated using an excited-state electronic structure method (QM2), while the

Figure 1.5: A schematic explanation of the subtractive QM/QM scheme. The symbols in this pictorial equation correspond, in the same order, to the terms which appear in equation 1.22.

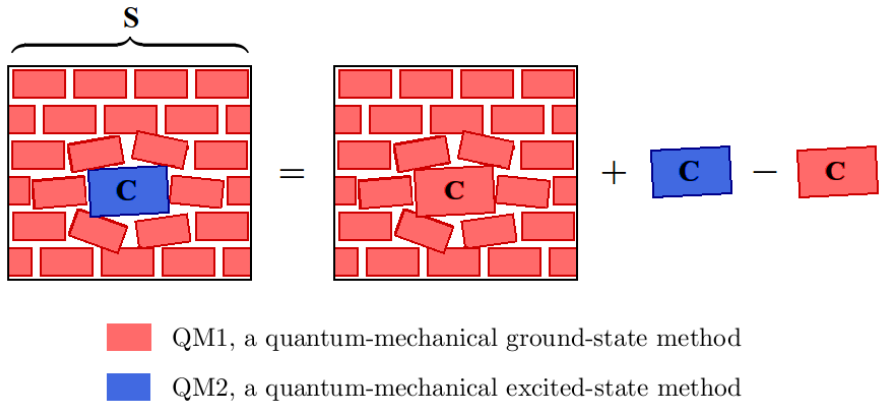

surrounding molecules will be described using a ground-state electronic structure method (QM1). The resulting subtractive hybrid QM/QM potential energy surface is defined by the following equation 1.22; the same idea is also illustrated diagramatically in Figure 1.5 above.

$$E_{\mathrm{QM2/QM1}}(\mathbf{S}) = E_{\mathrm{QM1}}(\mathbf{S}) + E_{\mathrm{QM2}}(\mathbf{C}) - E_{\mathrm{QM1}}(\mathbf{C}) \tag{1.22}$$

Naturally, the subtractive QM/QM scheme is subject to the same approximations as the original subtractive QM/MM scheme. Namely, all interactions between the photoexcited molecule and the surrounding molecules are evaluated within the term $E_{\mathrm{QM1}}(\mathbf{S})$ and are therefore treated at the QM1 level, as if the photoexcited molecule was in the ground electronic state. Clearly, this makes the subtractive QM/QM scheme unsuitable to systems in which the photoexcitation involves a strong change in the electron density, such as a charge-transfer excitation. Also, in the subtractive QM/QM scheme, as in the subtractive QM/MM scheme, the electronic structure of the photoexcited molecule in the term $E_{\mathrm{QM1}}(\mathbf{C})$ is calculated in isolation from the surrounding crystal lattice. As a consequence, the subtractive QM/QM scheme is unable to correctly describe systems which exhibit strong intermolecular interactions such as ionic and zwitterionic molecular crystals. The crystals that we will concern ourselves with are, however, composed of weakly polar molecules, and the excited states of interest will invariably be low-lying π, π^* states. Hence, the approximation that all interactions between the excited molecule and the surrounding molecules are treated using a ground-state method is not expected to lead to significant errors, although this has not been tested explicitly.

Furthermore, there exists another potential source of error that is idiosyncratic to the subtractive QM/QM scheme. Recall that, as explained in Section 1.2.3 of the present Chapter, due to the fact that the MM energy is given by a sum of terms that describe the various interatomic interactions, in the subtractive QM/MM scheme we are guaranteed to achieve exact cancellation between the two ground-state (MM) calculations. Not so in the subtractive QM/QM scheme: in quantum-mechanical methods, the total energy cannot be broken down into a sum of various interatomic (or intermolecular) interaction terms. It follows that in the subtractive QM/QM scheme the cancellation of the intramolecular energy of the photoexcited molecule between the terms $E_{\mathrm{QM1}}(\mathbf{S})$ and $E_{\mathrm{QM1}}(\mathbf{C})$ is not necessarily exact.

Given that quantum mechanics provides no prescription on how to break down the potential energy into an intramolecular part and an intermolecular part, it seems impossible to quantitatively analyse the effects of this inexact cancellation. We have therefore not attempted to do so, but merely draw attention to the fact that such a source of error exists and it may potentially lead to a slight "contamination" of the forces acting on the photoexcited molecule with incompletely cancelled-out ground-state forces originating from the terms $E_{\mathrm{QM1}}(\mathbf{S})$ and $E_{\mathrm{QM1}}(\mathbf{C})$.

1.3.3. Implementation of the subtractive TD-DFT/DFT scheme

For both the photoreactive systems studied in the present work, the electronic excited state of the reactive molecule was described using the linear response TD-DFT method with a Gaussian-type orbital (GTO) basis set, as implemented within the computational chemistry software package Gaussian 09.[41] The surrounding molecules, in turn, were treated using the implementation of ground-state DFT with a plane-wave (PW) basis set available in CASTEP.[42] This combination of model chemistries, which we will refer to as TD-DFT/DFT, leads to the following expression for the system total energy:

$$E_{\text{TD-DFT/DFT}}(\mathbf{S}) = E^{\mathrm{PW}}_{\mathrm{DFT}}(\mathbf{S}) + E^{\mathrm{GTO}}_{\text{TD-DFT}}(\mathbf{C}) - E^{\mathrm{PW}}_{\mathrm{DFT}}(\mathbf{C}) \tag{1.23}$$

where the subscripts and superscripts refer to the electronic structure methods

and the associated basis sets, respectively.

The force vector on the i-th atom in the system is calculated as minus the gradient of the potential energy given by equation 1.23 with respect to the Cartesian coordinates of that atom, resulting in the following expression for the force:

$$\mathbf{F}_i = \begin{cases} -\nabla_i E^{\mathrm{PW}}_{\mathrm{DFT}}(\mathbf{S}) - \nabla_i E^{\mathrm{GTO}}_{\mathrm{TD\text{-}DFT}}(\mathbf{C}) + \nabla_i E^{\mathrm{PW}}_{\mathrm{DFT}}(\mathbf{C}) \text{ if atom } i \text{ belongs} \\ \text{to the photoexcited molecule } \mathbf{C} \\ -\nabla_i E^{\mathrm{PW}}_{\mathrm{DFT}}(\mathbf{S}) \text{ otherwise} \end{cases} \tag{1.24}$$

where $\nabla_i = \dfrac{\partial}{\partial x_i} + \dfrac{\partial}{\partial y_i} + \dfrac{\partial}{\partial z_i}$ represents the gradient with respect to the coordinates of the i-th atom.

The photochemical reactions studied in the present work were modelled by means of running MD trajectories in the microcanonical (NVE) ensemble on the TD-DFT/DFT potential energy surface, where the starting points for these excited-state trajectories were sampled from the canonical (NVT) ground-state ensemble. This simulation setup reflects the assumptions that the photochemical reaction does not involve a substantial change of the unit cell volume, and that the reaction is fast relative to the thermalisation of the system. As discussed in Section 4.3.2 of Chapter 4, the former assumption is known from experiment to be valid in the case of the *cis*-enol $\rightleftarrows$ *trans*-keto photoisomerisation reaction of *N*-salicylidene-2-chloroaniline. In the microcanonical MD simulations on the TD-DFT/DFT potential energy surface, Newton's equations of motion were integrated using the Velocity Verlet algorithm, which is given by the following equations 1.25a-d:

$$\mathbf{v}_i(t + \frac{1}{2}\Delta t) = \mathbf{v}_i(t) + \frac{1}{2}\frac{\mathbf{F}_i(\mathbf{r}(t))}{m_i}\Delta t \tag{1.25a}$$

$$\mathbf{r}_i(t + \Delta t) = \mathbf{r}_i(t) + \mathbf{v}_i(t + \frac{1}{2}\Delta t)\,\Delta t \tag{1.25b}$$

$$\text{Derive } \mathbf{F}_i(\mathbf{r}(t + \Delta t)) \text{ using equation 1.24} \tag{1.25c}$$

$$\mathbf{v}_i(t + \Delta t) = \mathbf{v}_i(t + \frac{1}{2}\Delta t) + \frac{1}{2}\frac{\mathbf{F}_i(\mathbf{r}(t + \Delta t))}{m_i}\Delta t \tag{1.25d}$$

The microcanonical MD trajectories on the TD-DFT/DFT were propagated with

the use of a purpose-made "wrapper" bash script, which created the Gaussian 09 and CASTEP input files, executed these programs, calculated the potential energy and the atomic forces according to equations 1.23 and 1.24, respectively, and integrated Newtons equations of motion according to equations 1.25a-d. The functioning of this wrapper script is depicted in Figure 1.6 on the following page.

The correctness of the dynamics generated using the wrapper script was verified by testing for conservation of total energy and net momentum on the hybrid TD-DFT/DFT potential energy surface given by equation 1.23. In order to reduce the computational cost of running test trajectories over long periods of time, energy and momenum conservation was also verified without hybrid QM/QM coupling, on the entirely ground-state potential energy surface defined by the plane-wave DFT term $E_{\mathrm{DFT}}^{\mathrm{PW}}(\mathbf{S})$ alone. For instance, a microcanonical trajectory was propagated for a period of 500 fs for the $1 \times 1 \times 2$ supercell of *N*-salicylidene-2-chloroaniline equilibrated at a temperature of 280 K, in which all eight molecules were in the electronic ground state (see Section 4.3 of Chapter 4 for a detailed description of the remaining simulation parameters). Throughout that trajectory, total energy was found to be conserved to within $9{\times}10^{-6}$ E_{h}/atom (0.24 meV/atom), and each Cartesian component of the net momentum to within $1{\times}10^{-5}$ a.u./atom. To put these values into context, according to the equipartition theorem at a temperature of $T = 280$ K a freely moving hydrogen atom has an average kinetic energy of $E_{\mathrm{kin}} = \frac{3}{2} k_{\mathrm{B}} T = 1.3{\times}10^{-3}$ E_{h} and a momentum of $p = \sqrt{2 m E_{\mathrm{kin}}} = 2.2$ a.u. Energy and momentum conservation in the microcanonical trajectories was therefore deemed to be satisfactory.

Figure 1.6: A flowchart depicting the functioning of the TD-DFT/DFT wrapper script.

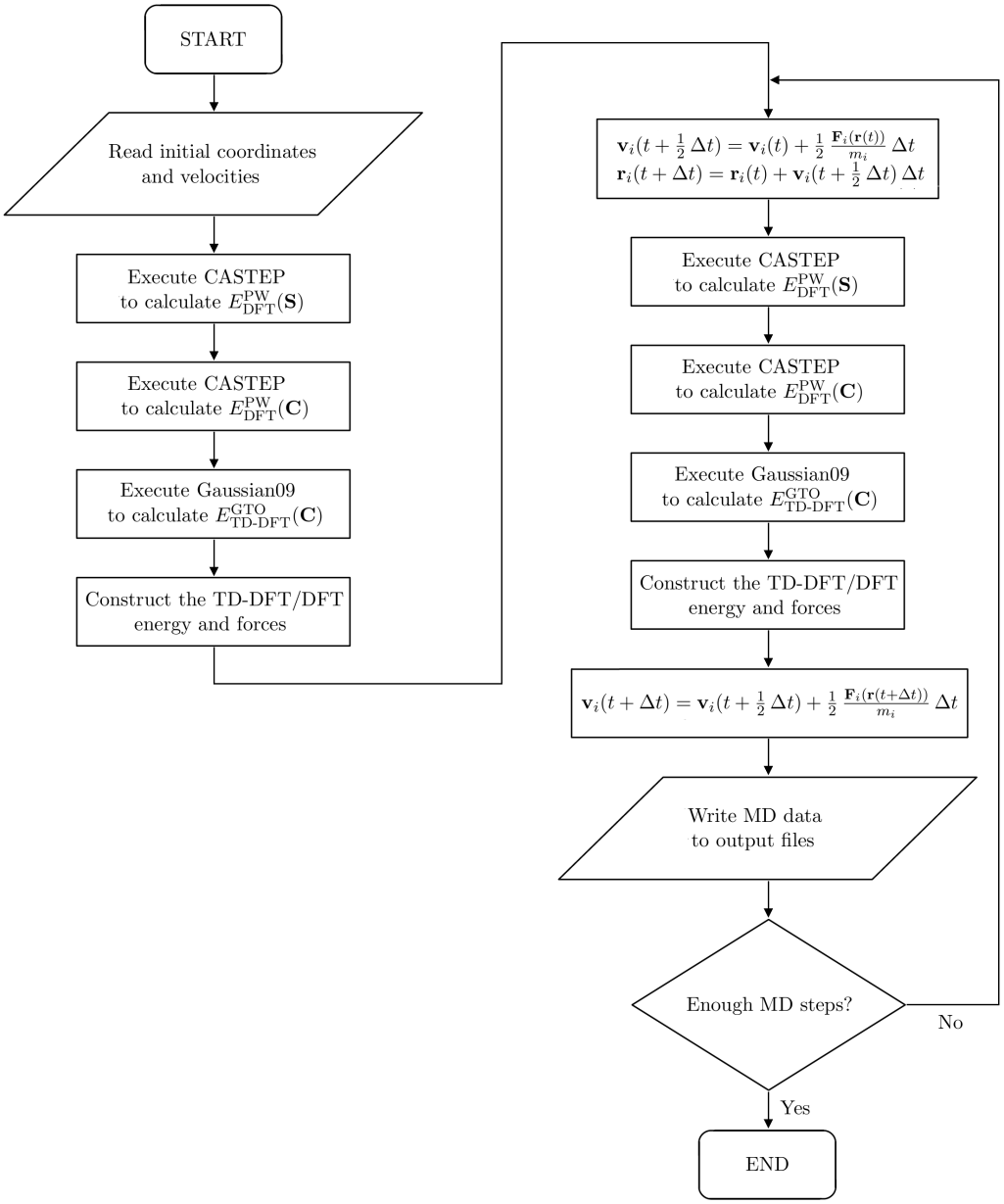

References

[1] P. Gütlich, A. Hauser, H. Spiering, *Angew. Chem. Int. Ed. Engl.*, 1994, **33**, 2024.

[2] M. Irie, S. Kobatake, M. Horichi *Science*, 2001, **291**, 1769.

[3] R. O. Al-Kaysi, C. J. Bardeen, *Adv. Mater.*, 2007, **19**, 1276.

[4] K. Nakatani, J. A. Delaire, *Chem. Mater.*, 1997, **9**, 2682.

[5] S. Park, O.-H. Kwon, S. Kim, S. Park, M.-G. Choi, M. Cha, S. Y. Park, D.-J. Jang, *J. Am. Chem. Soc.*, 2005, **127**, 10070.

[6] J. Narasimha Moorthy, P. Mal, R. Natarajan, P. Venugopalan, *J. Org. Chem.*, 2001, **66**, 7013.

[7] L. R. MacGillivray *J. Org. Chem.*, 2008, **73**, 3311.

[8] F. Toda *Acc. Chem. Res.*, 1995, **28**, 480.

[9] J. R. Scheffer, W. Xia, *Top. Curr. Chem.*, 2005, **254**, 233.

[10] H. E. Zimmerman, I. V. Alabugin, V. N. Smolenskaya, *Tetrahedron*, 2000, **56**, 6821.

[11] M. V. Basilevsky, V. A. Tikhomirov, *Mol. Phys.*, 2008, **106**, 2391.

[12] A. Warshel, M. Levitt, *J. Mol. Biol.*, 1976, **103**, 227.

[13] H. de Waard, A. Amani, J. Kendrick, W. L. J. Hinrichs, H. W. Frijlink, J. Anwar. *J. Phys. Chem. B*, 2010, **114**, 429.

[14] A. Nemkevich, H.-B. Burgi, M. A. Spackman, B. Corry, *Phys. Chem. Chem. Phys.*, 2010, **12**, 14916.

[15] N. L. Allinger, Y. H. Yuh, J. H. Lii, *J. Am. Chem. Soc.*, 1989, **111**, 8551.

[16] J. H. Lii, N. L. Allinger, *J. Am. Chem. Soc.*, 1989, **111**, 8566.

[17] J. H. Lii, N. L. Allinger, *J. Am. Chem. Soc.*, 1989, **111**, 8576.

[18] J. M. Wang, R. M. Wolf, J. W. Caldwell, P. A. Kollman, D. A. Case, J. Comput. Chem., 2004, 25, 11571174.

[19] H. M. Senn, W. Thiel, *Top. Curr. Chem.*, 2007, **268**, 173.

[20] T. Laino, F. Mohamed, A. Laio, M. Parrinello, *J. Chem. Theory Comput.*, 2006, **2**, 1370.

[21] M. Svensson, Stéphane Humbel, R. D. J. Froese, T. Matsubara, S. Sieber, K. Morokuma, *J. Phys. Chem.*, 1996, **100**, 19357.

[22] S. Dapprich, I. Komáromi, K. S. Byun, K. Morokuma, M. J. Frisch, *J. Mol. Struct. (Theochem)*, 1999, **462**, 1.

[23] T. A. Wesołowski, A. Warshel, *J. Phys. Chem.*, 1993, **97**, 8050.

[24] Y. A. Wang, E. A. Carter, in *Theoretical Methods in Condensed Phase Chemistry*, ed. S. D. Schwartz, Kluwer, Dordrecht, 2000, p. 117.

[25] T. A. Wesołowski, J. Weber, *Chem. Phys. Lett.*, 1996, **248**, 71.

[26] T. Klüner, N. Govind, Y. A. Wang, E. A. Carter, *J. Chem. Phys.*, 2002, **116**, 42.

[27] M. Pavanello, J. Neugebauer, *J. Chem. Phys.*, 2011, **135**, 234103.

[28] A. Kovyrshin, J. Neugebauer, *Chem. Phys.*, 2011, **391**, 147.

[29] D. K. Kanan, S. Sharifzadeh, E. A. Carter, *Chem. Phys. Lett.*, 2012, **519**, 18.

[30] H. P. Hratchian, P. V. Parandekar, K. Raghavachari, M. J. Frisch, T. Vreven, *J. Chem. Phys.*, 2008, **128**, 034107.

[31] P. V. Parandekar, H. P. Hratchian, K. Raghavachari, *J. Chem. Phys.*, 2008, **129**, 145101.

[32] N. J. Mayhall, K. Raghavachari, H. P. Hratchian, *J. Chem. Phys.*, 2010, **132**, 114107.

[33] H. P. Hratchian, A. V. Krukau, P. V. Parandekar, M. J. Frisch, K. Raghavachari, *J. Chem. Phys.*, 2011, **135**, 014105.

[34] T. A. Wesołowski, H. Chermette, J. Weber, *J. Chem. Phys.*, 1996, **105**, 9182.

[35] T. A. Wesołowski, J. Weber, *Int. J. Quantum Chem.*, 1997, **61**, 303.

[36] T. A. Wesołowski, *J. Chem. Phys.*, 1997, **106**, 8516.

[37] N. Govind, Y. A. Wang, A. J. R. da Silva, E. A. Carter, *Chem. Phys. Lett.*, 1998, **295**, 129.

[38] Y. A. Bernard, M. Dułak, J. W. Kamiński, T. A Wesołowski, *J. Phys. A: Math. Theor.*, 2008, **41**, 055302.

[39] G. Fradelos, T. A. Wesołowski, *J. Chem. Theory Comput.*, 2011, **7**, 213.

[40] G. Fradelos, T. A. Wesołowski, *J. Phys. Chem. A*, 2011, **115**, 10018.

[41] Gaussian 09, Revision A.02, M. J. Frisch, G. W. Trucks, H. B. Schlegel, G. E. Scuseria, M. A. Robb, J. R. Cheeseman, G. Scalmani, V. Barone, B. Mennucci, G. A. Petersson, H. Nakatsuji, M. Caricato, X. Li, H. P. Hratchian, A. F. Izmaylov, J. Bloino, G. Zheng, J. L. Sonnenberg, M. Hada, M. Ehara, K. Toyota, R. Fukuda, J. Hasegawa, M. Ishida, T. Nakajima, Y. Honda, O. Kitao, H. Nakai, T. Vreven, J. A. Montgomery, Jr., J. E. Peralta, F. Ogliaro, M. Bearpark, J. J. Heyd, E. Brothers, K. N. Kudin, V. N. Staroverov, R. Kobayashi, J. Normand, K. Raghavachari, A. Rendell, J. C. Burant, S. S. Iyengar, J. Tomasi, M. Cossi, N. Rega, J. M. Millam, M. Klene, J. E. Knox, J. B. Cross, V. Bakken, C. Adamo, J. Jaramillo, R. Gomperts, R. E. Stratmann, O. Yazyev, A. J. Austin, R. Cammi, C. Pomelli, J. W. Ochterski, R. L. Martin, K. Morokuma, V. G. Zakrzewski, G. A. Voth, P. Salvador, J. J. Dannenberg, S. Dapprich, A. D. Daniels, Ö. Farkas, J. B. Foresman, J. V. Ortiz, J. Cioslowski, and D. J. Fox, Gaussian, Inc., Wallingford

[42] S. J. Clark, M. D. Segall, C. J. Pickard, P. J. Hasnip, M. J. Probert, K. Refson, M. C. Payne, *Zeitschrift für Kristallographie*, 2005, **220**, 567.

Chapter 2
Validation of computational methods

2.1. Introduction

An important aspect of any computer simulation study of physical phenomena is to attempt to understand the accuracy of the underlying theoretical model, or in other words, how faithfully the simulated system mirrors reality. If, as is almost invariably the case in the field of computational chemistry, the simulation is to make use of approximations which may adversely affect its realism, then the effect thereof on the final results should be recognised and, if possible, quantified. Calculated quantities should be compared to experimental data where possible, or failing that, to the most accurate available theoretical benchmark. Because the quantities that we will concern ourselves with are not accessible experimentally, we adopted the latter approach, and carried out a range of benchmark calculations in order to analyse and quantify the effects of the approximations used in our simulations.

In the case of the MD simulations on the subtractive QM/QM potential energy surface, we may distinguish two categories of approximations: those that are inherent in the two component quantum-mechanical methods, and those that result from the application of the subtractive QM/QM scheme itself. Among the approximations of the first type, the most significant ones are probably the treatment of the dispersion interactions using the semiempirical dispersion correction scheme of Grimme,[1] and the fact that the excited electronic states of the reactive molecules have been described using the time-dependent DFT method. The former problem is considered in the present Chapter, while a discussion of the latter is mostly relegated to Chapters 3 and 4 which deal with the specific photochemical reactions that were modelled in this work.

The approximations due to the use of the subtractive QM/QM scheme have already been introduced in Chapter 1. These include the assumption that the electronic excitation is localised to a single molecule, the fact that the subtractive QM/QM scheme relies on a cancellation of intramolecular forces between the terms $E_{\mathrm{QM1}}(\mathbf{S})$ and $E_{\mathrm{QM1}}(\mathbf{C})$ in equation 1.22 in Chapter 1, and neglect of the polarisation of the photoexcited molecule by the surrounding molecules. The

last-named approximation is addressed in the present Chapter. We did not, however, attempt to test the assumption that in the systems studied in the present work, the relevant electronic excitations can be considered as localised on the individual molecules. We note that, in principle at least, it would be possible to do so by constructing a cluster composed of several molecules, which would serve as a model of the bulk crystal lattice, and calculating its ground- and excited-state electron densities. We would then calculate the electron density differences between the ground state and each of the lowest few excited states, and visually evaluate whether these density differences are localised on individual molecules, or delocalised over multiple molecules. Unfortunately, time-dependent DFT cannot readily be used to carry out such a calculation, because standard functionals do not correctly describe intermolecular interactions, and for large molecules and molecular clusters, they also give rise to spurious low-energy charge-transfer excitations, which are by definition delocalised. On the other hand, correlated wavefunction-based methods scale steeply with increasing system size, making it a very expensive prospect to apply them to a reasonably large molecular cluster. We have therefore accepted without rigorous proof the fundamental assumption that the electronic excitations involved in the photochemical reactions studied in the present work are fully localised on the individual molecules. Nevertheless, given that in the crystals studied in the present work, the intermolecular interactions are relatively weak, we believe that this assumption is realistic.

2.2. Dispersion interactions in DFT calculations

As explained in Section D.6 of Appendix D on DFT methods, in order to correct for the inability of the PBE functional[2,3] to describe the crucial dispersion interaction, all solid-state calculations reported in the present work have made use of the dispersion correction scheme of Grimme. Therein, it is also shown that this scheme is fairly accurate for the important model systems of the benzene dimer in the π-stacked and T-shaped conformations, insofar as the CCSD method coupled with the medium-quality aug-cc-pVDZ basis set can be regarded as a reliable benchmark. Presently, we discuss the application of this dispersion correction scheme to a further five complexes, each of which exemplifies a different type of dispersion interaction that is operative in the molecular crystals studied in the present work: the chloromethane-benzene complex, which features an interaction between the chlorine atom and the π electrons of the benzene aromatic ring, the chloromethane-methane complex bound by a C$-$Cl$\cdots$H$-$C

interaction, the methane dimer bound by a C−H$\cdots$H−C interaction, the benzene-pyrrole complex which features a carbon-nitrogen $\pi\cdots\pi$ interaction, and the benzene-formaldehyde complex which exemplifies an O$\cdots\pi$ interaction. Due to the high computational demands of the CCSD method, all model complexes that we have chosen to serve as a benchmark for the dispersion correction scheme of Grimme were constructed in such a way as to possess high symmetry, which allowed a vast reduction in the cost of the calculations.

We remark here that the CCSD/aug-cc-pVDZ model chemistry is expected to predict dispersion energies with only moderate accuracy. The reasons for this are twofold. Firstly, for the purpose of evaluating dispersion interaction energies, aug-cc-pVDZ should be regarded as only a medium-quality basis set, and it is likely to give rise to significant basis set incompleteness error (BSIE) and basis set superposition error (BSSE). Secondly, triple excitations are known to play an important role in the description of dispersion interactions, and their neglect may lead to significant errors. However, in order to meaningfully address these problems, we would need to improve the basis set size and the treatment of electron correlation, and apply the CCSD(T)/aug-cc-pVTZ or better model chemistry (the CCSD(T) method[4] is an approximation to the full CCSDT method) with counterpoise corrections. Such a calculation is unfortunately beyond our computational capabilities. The CCSD method is nevertheless expected to be more reliable than the alternative: the relatively less expensive second-order Møller-Plesset perturbation method[5] (MP2), which is known to strongly overestimate dispersion interaction energies.[6,7]

Because in order to achieve an accurate description of intermolecular interactions, it is essential to use basis sets augmented with diffuse functions, we have used the aug-cc-pVDZ basis set, which places one *s*-type and three *p*-type diffuse functions on each hydrogen atom, and one *s*-type, three *p*-type and five *d*-type diffuse functions on each second-row atom.

All calculations reported in the present Section were carried out within the computational chemistry software package Gaussian 09.[8] The electronic energy was converged to a tolerance of $1.0 \times 10^{-7}\ E_\mathrm{h}$. In the CCSD calculations, the restricted Hartree-Fock determinant was used as the reference determinant, and the frozen-core approximation was applied.

2.2.1. The chloromethane-benzene complex

Geometries of the benzene and chloromethane molecules were optimised at the PBE/cc-pVDZ level of theory. The chloromethane-benzene complex was subsequently constructed using the isolated-molecule geometries of benzene and chloromethane, with the chlorine atom of the chloromethane molecule positioned directly above the center of the benzene aromatic ring. The resulting complex, illustrated in Figure 2.1(a) on the next page, belongs to the point group C_{3v}. The distance between the chlorine atom and the plane of the benzene molecule, labelled d_3 in Figure 2.1(a), was varied from 2.5 Å to 6.0 Å in steps of 0.1 Å. The single-point energies of the resulting complex geometries were calculated at the PBE/aug-cc-pVDZ level, with and without the semiempirical dispersion correction, and also at the CCSD/aug-cc-pVDZ level. The resulting single-point energies are plotted against the distance d_3 in Figure 2.1(b).

It can be seen in Figure 2.1(b) that the uncorrected PBE curve features a very shallow (0.004 eV) binding minimum at $d_3 = 4.1$ Å, whereas the CCSD method predicts a considerably higher binding energy of 0.054 eV and an equilibrium intermolecular distance of $d_3 = 3.5$ Å. These observations suggest that the interaction between the two molecules is predominantly due to dispersion, which the PBE functional does not describe correctly.

The application of the dispersion correction of Grimme has the expected effect of transforming the uncorrected PBE potential energy curve into a decidedly bonding curve, which is very close to the CCSD curve, and features a minimum corresponding to a binding energy of 0.049 eV at $d_3 = 3.5$ Å that coincides almost exactly with the CCSD minimum.

2.2.2. The chloromethane-methane complex

The chloromethane-methane complex provides an example of a C−Cl$\cdots$H−C dispersion interaction. The constrained potential energy surface scan for this system was carried out as follows.

Geometries of the isolated chloromethane and methane molecules were optimised at the PBE/cc-pVDZ level of theory. Then, the chloromethane-methane complex was constructed with the four atoms engaged in the C−Cl$\cdots$H−C interaction

Figure 2.1: (a) The chloromethane-benzene complex in which the chlorine atom is positioned above the centre of the benzene ring. The point group of the complex is C_{3v}. d_3 is the distance between the chlorine atom and the plane of the benzene ring.

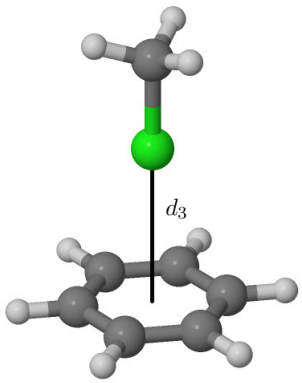

(b) Potential energy curves calculated for the chloromethane-benzene complex at the PBE/aug-cc-pVDZ level of theory, corrected and uncorrected for dispersion, and at the CCSD/aug-cc-pVDZ level. The zero of the energy scale corresponds to the isolated molecules.

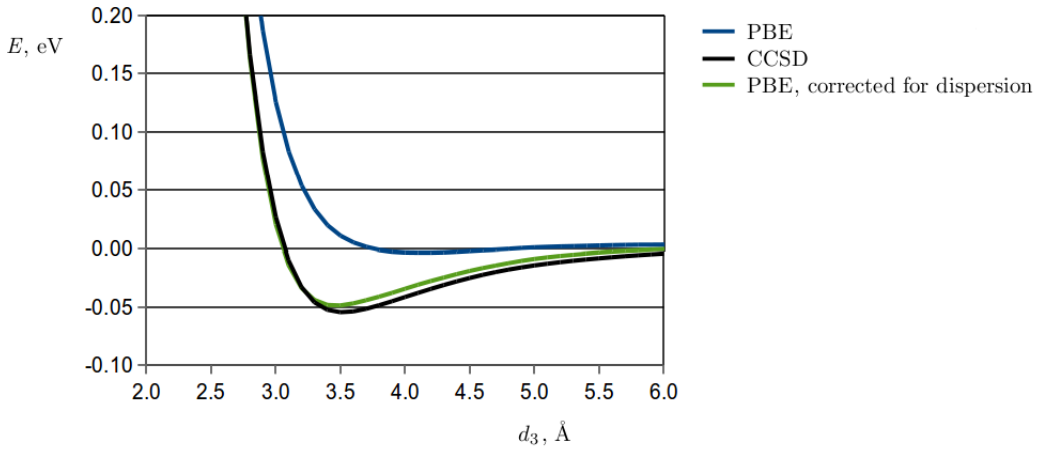

aligned along a straight line. Each molecule was in the isolated-molecule geometry, and the two methyl groups that are not engaged in the dispersion interaction were positioned in a staggered conformation. The complex geometry constructed in this manner is displayed in Figure 2.2(a). The distance between the hydrogen atom of the methane molecule and the chlorine atom of the chloromethane molecule was labelled d_4, and was varied from 2.2 Å to 5.0 Å in steps of 0.1 Å.

Energies of the chloromethane-methane complex were evaluated at the PBE/aug-cc-pVDZ level as implemented in Gaussian 09, corrected and uncorrected

Figure 2.2: (a) The chloromethane-methane complex (point group C_{3v}). d_4 is the distance between the contacting hydrogen and chlorine atoms.

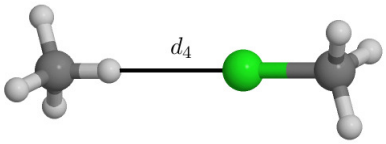

(b) Potential energy curves calculated for the chloromethane-methane complex at the PBE/aug-cc-pVDZ level of theory, corrected and uncorrected for dispersion, and at the CCSD/aug-cc-pVDZ level. The zero of the energy scale corresponds to the isolated molecules.

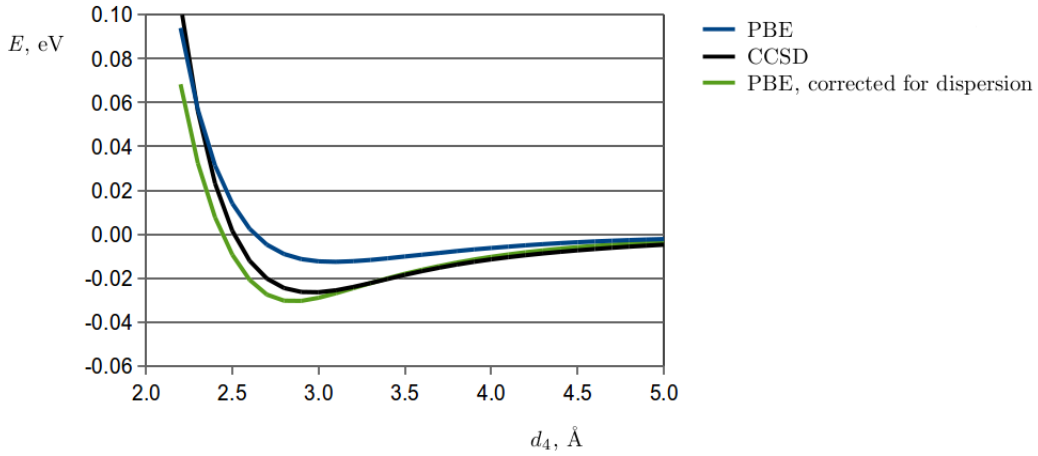

for dispersion, and at the CCSD/aug-cc-pVDZ level. The resulting potential energy curves are plotted in Figure 2.2(b). As might be expected, the uncorrected PBE functional significantly underbinds the complex relative to the CCSD method. The corrected PBE curve, however, is in good agreement with that obtained from the CCSD method. The calculated binding energies are 0.030 eV and 0.026 eV, respectively, from the dispersion-corrected PBE and CCSD calculations, while the equilibrium values of the chlorine-hydrogen distance d_4 are respectively 2.9 Å and 3.0 Å. We may therefore conclude that the PBE functional in conjunction with Grimme's dispersion correction scheme describes for the C−Cl···H−C interaction with good accuracy.

2.2.3. The methane dimer

The third non-covalently bonded that we will discuss is the methane dimer complex bound by a C−H···H−C dispersion interaction. The geometry of the

isolated methane molecule was optimised at the PBE/cc-pVDZ level of theory. The optimum isolated-molecule geometry was subsequently used to construct the dimer illustrated in Figure 2.3(a), the point group of which is D_{3d}. The distance d_5 between the two hydrogen atoms that are in close contact with each other was varied from 1.5 Å to 5.0 Å in steps of 0.1 Å.

As for the previous complex, the energies of the methane dimer were calculated at the PBE/aug-cc-pVDZ level of DFT theory, corrected and uncorrected for dispersion, and at the CCSD/aug-cc-pVDZ level. The potential energy curves obtained in this manner are presented in Figure 2.3(b). It is rather interesting to compare the dispersion-corrected PBE and the CCSD curves, with the former predicting a somewhat shorter equilibrium distance d_5 (2.2 Å) and higher binding energy (0.033 eV) than the latter (2.4 Å and 0.022 eV). What is more, the onset of the repulsive region of the dispersion-corrected PBE curve is also shifted towards shorter distances by around 0.2 Å relative to the CCSD curve. Gruzman and coworkers[9] have previously reported that for simple alkanes, the scheme of Grimme paired with the PBE functional tends to overcorrect for dispersion, and it is possible that the fairly large deviation of the corrected PBE potential energy curve from the CCSD curve is a manifestation of the same effect.

2.2.4. The benzene-pyrrole complex

The benzene-pyrrole complex was constructed so as to serve as a test of π-stacking interactions between a nitrogen atom and a carbon atom. The benzene and pyrrole molecules were optimised in point groups D_{6h} and C_{2v}, respectively, at the PBE/cc-pVDZ level of DFT theory. The benzene-pyrrole complex was subsequently built using the optimal PBE/cc-pVDZ geometries of the two molecules as illustrated in Figure 2.4(a). The two molecules were positioned in parallel planes, such that the nitrogen atom the pyrrole molecule was located directly above one carbon atom of the benzene molecule. The distance between these two contacting atoms, which we labelled d_6, was varied in the range from 2.5 to 6.0 Å in steps of 0.1 Å, and the energies of the resulting complex geometries were calculated at the PBE/aug-cc-pVDZ level of theory, corrected and uncorrected for dispersion, and at the CCSD/aug-cc-pVDZ level.

In Figure 2.4(b), the resulting energy values are plotted as a function of d_6. As expected, the pure PBE functional underestimates the dispersion interaction

Figure 2.3: (a) The methane dimer (point group D_{3d}). d_5 is the distance between the two contacting hydrogen atoms.

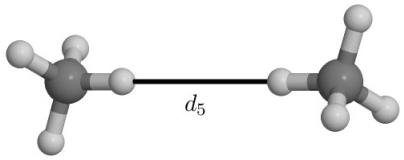

(b) Potential energy curves for the methane dimer calculated at the PBE/aug-cc-pVDZ level of theory, corrected and uncorrected for dispersion, and at the CCSD/aug-cc-pVDZ level. The zero of the energy scale corresponds to the isolated molecules.

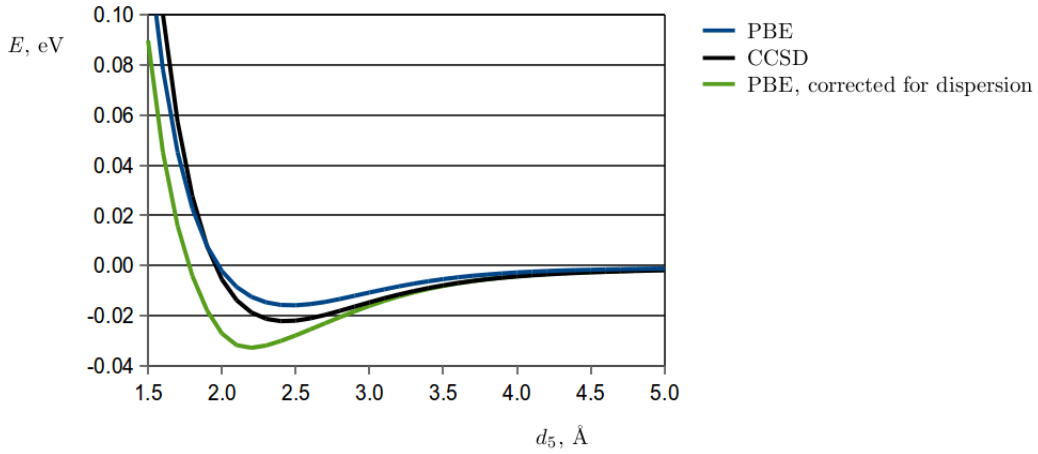

between the contacting nitrogen and carbon atoms, and the PBE curve features a shallow minimum of -0.056 eV at $d_6 = 3.6$ Å. In contrast, on the CCSD curve the minimum has a considerably greater depth of -0.210 eV, and is located at a shorter interatomic distance ($d_6 = 3.2$ Å). The application of the dispersion-correction scheme of Grimme has the desired effect of bringing the PBE curve closter to the CCSD one, with the corrected PBE curve featuring a minimum of -0.177 eV at $d_6 = 3.1$ Å.

2.2.5. The benzene-formaldehyde complex

The final complex that we will consider in the present Chapter, the benzene-formaldehyde complex contains an example of an interaction between the π electron density of an aromatic ring and a ketone oxygen atom. This complex was constructed as follows, from the optimal geometries of the benzene and

Figure 2.4: (a) The benzene-pyrrole complex (point group C_s). d_6 is the distance between the contacting carbon and nitrogen atoms.

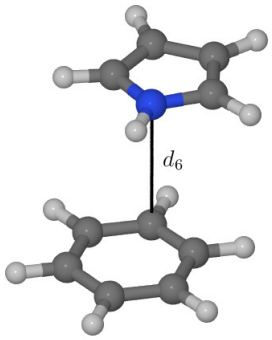

(b) Potential energy curves for the benzene-pyrrole complex calculated at the PBE/aug-cc-pVDZ level of theory, corrected and uncorrected for dispersion, and at the CCSD/aug-cc-pVDZ level. The zero of the energy scale corresponds to the isolated molecules.

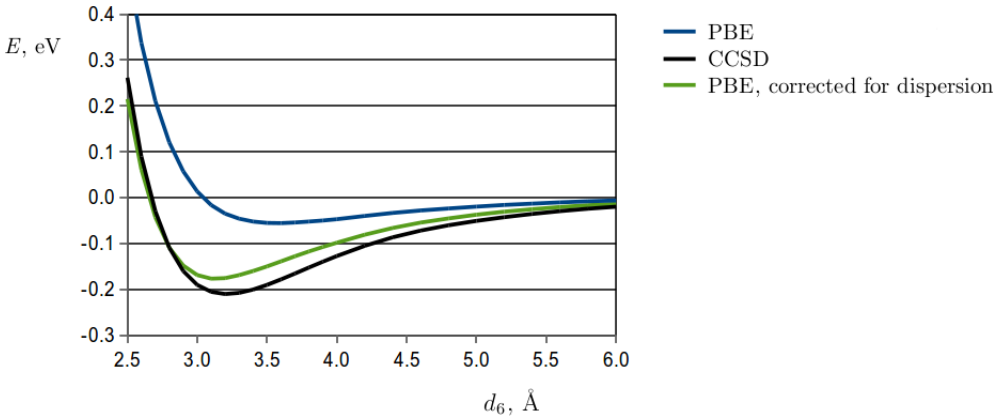

formaldehyde molecules obtained at the PBE/cc-pVDZ level of theory. The C=O bond of the formaldehyde was placed along a line perpendicular to the benzene molecule and passing through one carbon atom of the benzene molecule, such that the resulting complex possessed C_s symmetry. The distance between that carbon atom of the benzene molecule and the oxygen atom of the formaldehyde molecule was labelled d_7 and was varied in the range from 2.5 Å to 6.0 Å in steps of 0.1 Å, and the energies of the resulting complex geometries were calculated at the PBE/aug-cc-pVDZ level of theory, corrected and uncorrected for dispersion, and at the CCSD/aug-cc-pVDZ level.

As can be seen from Figure 2.5(b), where the computed potential energies of the benzene-formaldehyde cluster are plotted against the oxygen-carbon

Figure 2.5: (a) The benzene-formaldehyde complex (point group C_s). d_7 is the distance between the contacting carbon and nitrogen atoms.

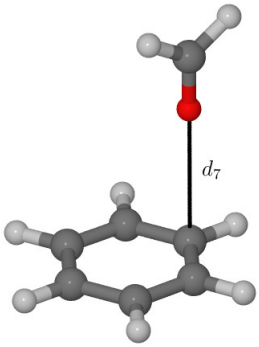

(b) Potential energy curves for the benzene-formaldehyde complex calculated at the PBE/aug-cc-pVDZ level of theory, corrected and uncorrected for dispersion, and at the CCSD/aug-cc-pVDZ level. The zero of the energy scale corresponds to the isolated molecules.

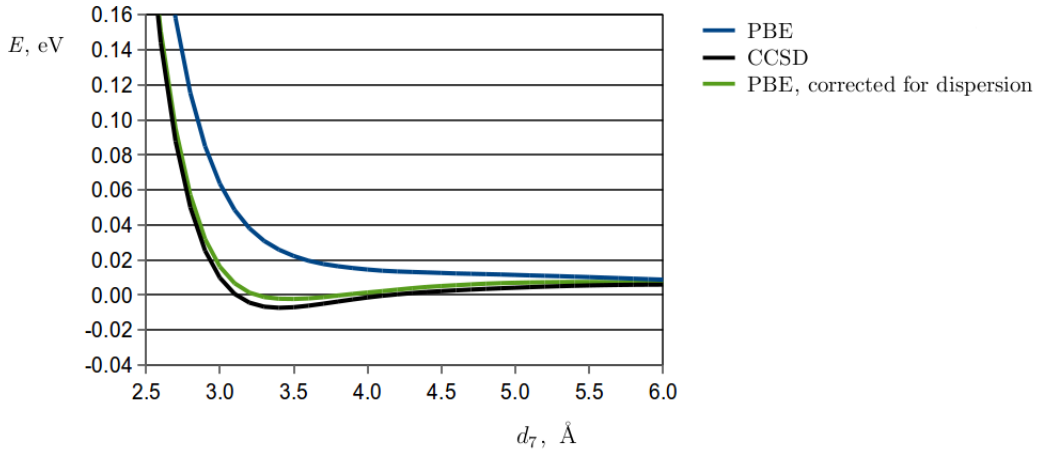

distance d_7, the dispersion interaction in that cluster is weak. The uncorrected PBE functional predicts a purely repulsive potential energy curve which tends very slowly to zero with increasing distance, reflecting the fact that the interaction between the two molecules has a repulsive electrostatic component. The CCSD curve, on the other hand, features a very shallow minimum of -0.007 eV at $d_7 = 3.4$ Å. With the addition of the dispersion correction, the PBE curve becomes very close to the CCSD one, with a minimum of -0.002 eV at $d_7 = 3.5$ Å.

In summary, in the present Chapter and in Appendix D, we have carried out a brief review of the performance of the dispersion-correction scheme of Grimme in combination with the PBE functional when applied to some of

the typical dispersion interactions encountered in the crystals studied in the present work. Overall, these interactions seem to be described with adequate quantitative accuracy. The single exception is the C−H···H−C interaction, which is overestimated for aliphatic species, and therefore it may potentially be also be overestimated for aromatics. In absolute terms, however, this possible error is fairly slight. Furthermore, for the molecular crystals studied in the present work, which consist of aromatic molecules, this interaction is likely to be less important than the C−H···π and $\pi\cdots\pi$ interactions, both of which are described correctly. We therefore believe that the possible overestimation of the C−H···H−C dispersion interaction does not significantly impact the realism of the calculated potential energy surfaces.

2.3. Polarisation of the photoexcited molecule by the bulk lattice

As mentioned in Section 1.3.2 of Chapter 1, one of the approximations inherent in the subtractive QM/QM scheme is that the photoexcited molecule is not allowed to experience electrostatic interactions with the surrounding bulk lattice. In order to quantify the effect of that approximation, we have constructed a simple embedded cluster model of a photoexcited molecule of 7-(2-pyridyl)indole within the bulk lattice, and calculated its polarisation by the nearest few surrounding ground-state molecules.

In the experimental crystal structure of 7PyIn,[10,11] we selected a single molecule of symmetry Type I, which will henceforth be referred to as the "central molecule" (see Figure 3.4 in Chapter 3 for an explanation of the symmetry labels). In addition to the central molecule, we selected all sixteen molecules whose centres of mass are located within 10 Å from the center of mass of the central molecule. From now on, these molecules will be referred to as the "surrounding molecules." Their purpose was to represent the polarising influence of the bulk lattice. The embedded cluster model, shown in Figure 2.6 on the following page, incorporated the central molecule and the sixteen surrounding molecules, while the bulk lattice beyond the selected surrounding molecules was neglected.

Three single point calculations were carried out on this embedded cluster model:

Calculation 1 was designed to provide information on the distribution of

Figure 2.6: The seventeen-molecule embedded cluster model utilised to study the effect of polarisation on the photoexcited 7PyIn molecule. The central molecule is shown using a ball-and-stick representation.

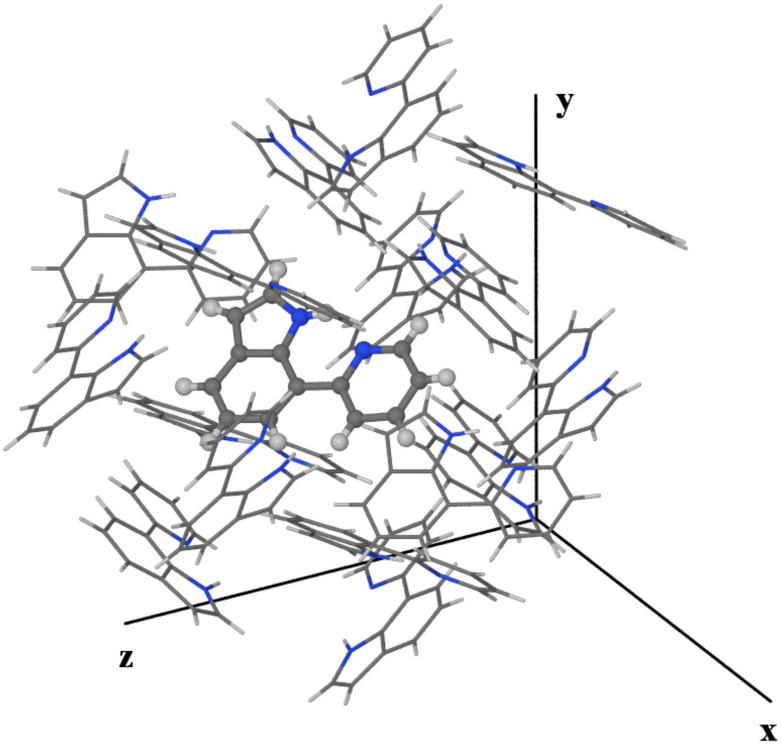

charge within the embedded cluster model. Here, the entire embedded cluster was treated at the quantum-mechanical, ground state PBE0/6-31G(d,p) level of theory as implemented in Gaussian 09.[8] The charges on all atoms were calculated using the Merz-Singh-Kollman[12,13] scheme, which fits atomic charges positioned at the nuclei to reproduce the electrostatic potential at a set of points outside the van der Waals radii of atoms in the system. For reference, in Figure 2.7 we present the atomic charges obtained from the Merz-Singh-Kollman scheme for the isolated molecule of the **1**-*syn* tautomer at the optimal PBE0/6-31G(d,p) geometry. (See Figure 3.1 in Chapter 3 for a listing of the conformers of 7PyIn.)

Calculation 2, here the central molecule was treated using the TD-DFT method using the PBE0 exchange-correlation functional[14] coupled with the 6-31G(d,p) basis set, while the surrounding molecules were replaced by the atomic point charges that had been obtained from the Merz-Singh-Kollman fit carried out in Calculation 1. These point charges were included in the DFT calculation, allowing the electron density of the central molecule to experience the polarising

Figure 2.7: Atomic charges obtained using the Merz-Singh-Kollman scheme for the isolated molecule of the 1-*syn* tautomer of 7PyIn at the PBE0/6-31G(d,p) level.

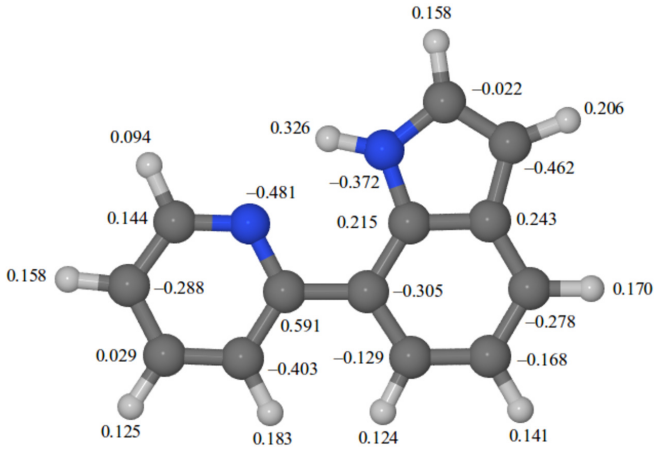

influence of the surrounding molecules. Thus this calculation probed the polarising influence of the surrounding molecules on the central molecule. The three lowest singlet excited states of the central molecule were calculated, as well as the electric dipole moment of the S_1 state. The calculation of the dipole moment of the S_1 state was achieved using the `Density=(Check,Transition=1)` keyword in Gaussian 09; note the resulting dipole moment vector describes only the charge distribution of the central molecule, and does not include the dipole moment of the surrounding system of point charges.

Calculation 3 was performed for the central molecule in the absence of the surrounding charges, and was otherwise identical to Calculation 2. Its purpose was to enable a comparison with the previous calculation, and thereby to allow us to quantify the effects of polarisation of the central molecule by the surrounding charge distribution.

Kohn-Sham orbitals obtained from Calculations 2 and 3 were compared visually. For all orbitals up to HOMO+5, the shapes were found to change only marginally for both calculations, and the ordering of the orbitals was unchanged.

In Table 2.1 on the following page, we compare the excitation energies of the central molecule obtained in Calculations 2 and 3. Also listed for each excitation are the highest coefficients in the configuration interaction expansion as printed by Gaussian 09. Inspection of the data in Table 2.1 shows that the nature

Table 2.1: Excitation energies of the central molecule, obtained in the presence (Calculation 2) and in the absence (Calculation 3) of surrounding point charges. For easier comparison, we include the (signed) differences between quantities calculated in the presence and in the absence of the point charges.

	State	ΔE, eV [a]	Largest coefficients in the configuration interaction expansion [b]
Calculation 2	S_1	3.9984	$51 \rightarrow 52 : 0.69228$
	S_2	4.2346	$50 \rightarrow 52 : 0.66540$ $51 \rightarrow 53 : -0.16676$ $51 \rightarrow 55 : 0.13490$
	S_3	4.4620	$50 \rightarrow 52 : 0.16058$ $51 \rightarrow 53 : 0.67380$
Calculation 3	S_1	4.0152	$51 \rightarrow 52 : 0.69180$
	S_2	4.2545	$50 \rightarrow 52 : 0.66075$ $51 \rightarrow 53 : -0.18120$ $51 \rightarrow 55 : 0.14035$
	S_3	4.4689	$50 \rightarrow 52 : 0.17435$ $51 \rightarrow 53 : 0.66974$
Difference	S_1	-0.0168	$51 \rightarrow 52 : 0.00048$
	S_2	-0.0199	$50 \rightarrow 52 : 0.00465$ $51 \rightarrow 53 : 0.01444$ $51 \rightarrow 55 : -0.00545$
	S_3	-0.0069	$50 \rightarrow 52 : -0.01377$ $51 \rightarrow 53 : -0.00406$

[a] ΔE is the energy of the respective excited state relative to the ground state.
[b] The Kohn-Sham orbitals are numbered according to their eigenvalues, with 51 and 52 corresponding to the HOMO and the LUMO, respectively.

of each of the lowest three singlet excited states of 7PyIn is unchanged by the presence of the point charges generated by the embedded cluster model, and that the excitation energies are affected only slightly (by up to around 0.02 eV).

In order to further explore the effect of polarisation on the central molecule, in Table 2.2 on the next page we compare the dipole moments of the S_1 state of the central molecule obtained from Calculations 2 and 3. It can be seen from Table 2.2 that the dipole moment of the molecule is altered by the presence of the surrounding point charges, but to only a small extent, which indicates that the central molecule in the S_1 state is only weakly polarised by the point charges.

In summary, single-point calculations carried out within the embedded cluster model, whereby the point charges on a set of molecules around the photoexcited

Table 2.2: Electric dipole moment of the central molecule, obtained in the presence (Calculation 2) and in the absence (Calculation 3) of surrounding point charges. For easier comparison, we include the (signed) differences between the magnitude and components of the dipole moment in the presence and in the absence of the point charges.

	$\lvert\mathbf{p}\rvert$, D [a]	p_x, D	p_y, D	p_z, D [b]
Calculation 2	5.6977	−4.1656	−1.0859	3.7326
Calculation 3	5.7871	−4.2769	−1.0576	3.7523
Difference	−0.0894	0.1113	−0.0283	−0.0197

[a] $\lvert\mathbf{p}\rvert$ is the magnitude of the dipole moment of the central molecule, in units of Debye ($1\ \mathrm{D} = 3.33564 \times 10^{-30}\ \mathrm{C} \times \mathrm{m}$)

[b] p_x, p_y and p_z are the projections of the dipole moment vector onto the Cartesian axes; see Figure 2.6 for the orientation of the embedded cluster model relative to the coordinate system.

7PyIn molecule are included in the DFT Hamiltionian, suggest that the photoexcited molecule is not strongly polarised by the surrounding lattice. Although the embedded cluster model provides only an approximation of the true polarising influence of the bulk lattice, since it contains a finite number of molecules whose centres of mass are located within a certain radius of the centre of mass of the photoexcited molecule, and hence it cannot account for long-range polarisation effects, we believe that it does allow for a semi-quantitative characterisation of the importance of polarisation effects in the photochemical reaction of crystalline 7PyIn. We therefore conclude that the polarisation of the photoexcited molecule by the surrounding lattice is of minor importance in the description of the potential energy surface, and that the neglect of this effect, implicit in the subtractive QM/QM scheme, is a justifiable approximation that does not introduce significant error into the simulation results.

References

[1] S. Grimme, *J. Comput. Chem.*, 2006, **27**, 1787.

[2] J. P. Perdew, K. Burke, M. Ernzerhof, *Phys. Rev. Lett.*, 1996, **77**, 3865.

[3] J. P. Perdew, K. Burke, M. Ernzerhof, *Phys. Rev. Lett.*, 1997, **78**, 1396.

[4] K. Raghavachari, G. W. Trucks, J. A. Pople, M. Head-Gordon, *Chem. Phys. Lett.*, 1989, **157**, 479.

[5] C. Møller, M. S. Plesset, *Phys. Rev.*, 1934, **46**, 618.

[6] P. Hobza, K. Müller-Dethlefs, *Non-Covalent Interactions: Theory and Experiment*, Royal Society of Chemistry, Cambridge, 2010, p. 40.

[7] M. Pitoňák, P. Neogrády, J. Černy, S. Grimme, P. Hobza, *ChemPhysChem*, 2009, **10**, 282.

[8] Gaussian 09, Revision A.02, M. J. Frisch, G. W. Trucks, H. B. Schlegel, G. E. Scuseria, M. A. Robb, J. R. Cheeseman, G. Scalmani, V. Barone, B. Mennucci, G. A. Petersson, H. Nakatsuji, M. Caricato, X. Li, H. P. Hratchian, A. F. Izmaylov, J. Bloino, G. Zheng, J. L. Sonnenberg, M. Hada, M. Ehara, K. Toyota, R. Fukuda, J. Hasegawa, M. Ishida, T. Nakajima, Y. Honda, O. Kitao, H. Nakai, T. Vreven, J. A. Montgomery, Jr., J. E. Peralta, F. Ogliaro, M. Bearpark, J. J. Heyd, E. Brothers, K. N. Kudin, V. N. Staroverov, R. Kobayashi, J. Normand, K. Raghavachari, A. Rendell, J. C. Burant, S. S. Iyengar, J. Tomasi, M. Cossi, N. Rega, J. M. Millam, M. Klene, J. E. Knox, J. B. Cross, V. Bakken, C. Adamo, J. Jaramillo, R. Gomperts, R. E. Stratmann, O. Yazyev, A. J. Austin, R. Cammi, C. Pomelli, J. W. Ochterski, R. L. Martin, K. Morokuma, V. G. Zakrzewski, G. A. Voth, P. Salvador, J. J. Dannenberg, S. Dapprich, A. D. Daniels, Ö. Farkas, J. B. Foresman, J. V. Ortiz, J. Cioslowski, and D. J. Fox, Gaussian, Inc., Wallingford CT, 2009.

[9] D. Gruzman, A. Karton, J. M. L. Martin, *J. Phys. Chem. A*, 2009, **113**, 11974.

[10] M. S. Mudadu, A. Singh, R. P. Thummel, *J. Org. Chem.*, 2006, **71**, 7611.

[11] D. A. Fletcher, R. F. McMeeking, D. Parkin, *J. Chem. Inf. Comput. Sci.*, 1996, **36**, 746.

[12] U. C. Singh, P. A. Kollman, *J. Comp. Chem.*, 1984, **5**, 129.

[13] B. H. Besler, K. M. Merz Jr., P. A. Kollman, *J. Comp. Chem.*, 1990, **11**, 431.

[14] C. Adamo, V. Barone, *J. Chem. Phys.*, 1999, **110**, 6158.

Chapter 3
Solid-state photochemical reaction of 7-(2-pyridyl)-indole

3.1. Introduction

The first system to which we have applied the subtractive TD-DFT/DFT method was crystalline 7-(2-pyridyl)-indole (abbreviated 7PyIn). Our motivation in choosing to study this particular compound was the structural simplicity of the 7PyIn molecule, which contains only one bond around which the molecule may undergo torsion, and its photochemistry is therefore relatively uncomplicated. To the best of our knowledge, the photochemical reaction in the crystal form of 7PyIn has not been studied experimentally to date, limiting the scope for the comparison of our simulations to experimental data. Nevertheless, the completion of this study paved the way towards the application of the subtractive TD-DFT/DFT to the more complex and well-studied photochemical reaction of anils (Schiff bases of salicylaldehyde with aniline derivatives), which we discuss in the following Chapter.

3.2. Model system

7PyIn is a member of a broad class of Schiff bases which upon irradiation undergo excited-state intramolecular proton transfer (ESIPT) reactions within a hydrogen bond involved in a six-membered ring. The stable conformations of 7PyIn as predicted by geometry optimisations at the PBE0/6-31G(d,p) level of density functional theory (see Section 3.3.2.1 for a description of these calculations) are listed in Figure 3.1 on the following page. In the ground electronic state, the global potential minimum of 7PyIn is the *syn* conformer (hereafter labelled **1**-*syn*) in which the shuttling proton is at the indolyl group nitrogen. The *anti* conformer (**1**-*anti*) is higher in energy. The *syn* geometry in which the shuttling proton is at the pyridyl group nitrogen (**2**-*syn*) is not a minimum on the ground-state potential energy surface according to calculations performed at both the both MP2[1] and PBE0/6-31G(d,p) levels.

Figure 3.1: Conformers of 7PyIn.

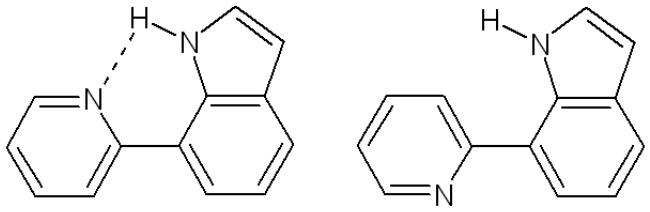

1-*syn*

1-*anti*

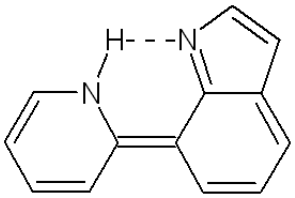

2-*syn*

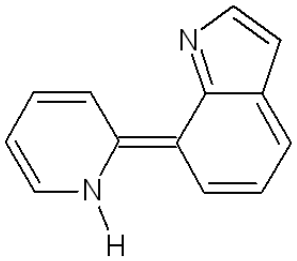

2-*anti*

The lowest singlet excited state (S_1) of 7PyIn is an optically bright π, π^* state,[1] in which the pyridyl group nitrogen is more basic relative to the indolyl group nitrogen. As a result of this change, following photoexcitation to the π, π^* state the proton is transferred from the indolyl group nitrogen to the pyridyl group nitrogen (Figure 3.2). In related Schiff bases, Born-Oppenheimer molecular dynamics[2,3] and wavepacket dynamics[4] simulations point towards ultrafast ESIPT timescales of around 30-50 fs in the isolated molecules.

In gas phase and solution[5] environments, following proton transfer the photoexcited 7PyIn molecule undergoes internal conversion (radiationless decay) to the ground state by passing through a conical intersection (CI) between the S_0 and S_1 states, which is reached through a torsional motion around the carbon-carbon bond connecting the pyridyl and indolyl groups. In the vicinity of the conical intersection, where the pyridyl and indolyl groups are at a near-right angle to one another, the 7PyIn molecule is an almost perfect biradical.[1] The final products of the internal conversion step have not been determined experimentally, but may be expected to consist of a mixture of **1**-*syn* and **2**-*anti*. A sketch of the molecular potential energy surface underlying these processes is given in Figure 3.3 on the next page.

Figure 3.2: The photochemical reaction of 7PyIn.

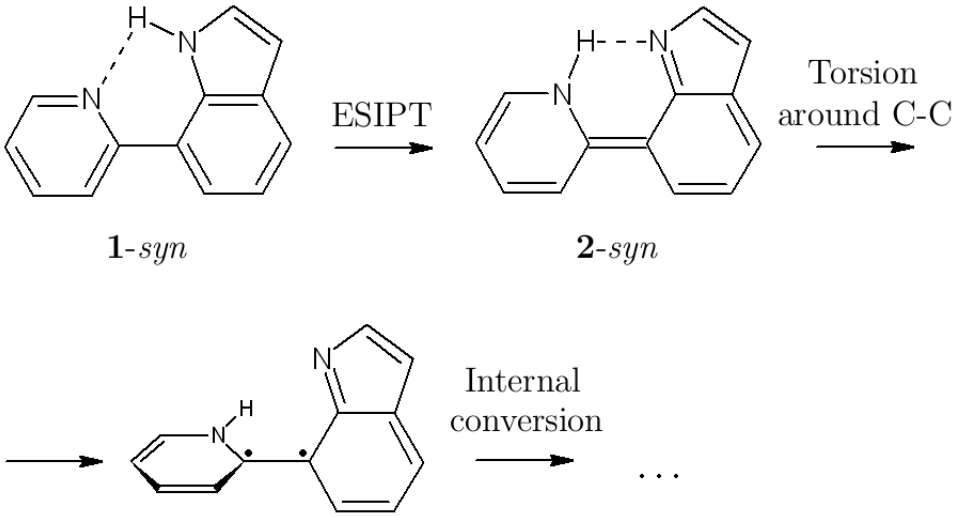

Figure 3.3: A schematic diagram of the potential energy surfaces of the 7PyIn molecule along the proton transfer and torsional reaction coordinates, based the CC2 calculations reported in Ref.[1]

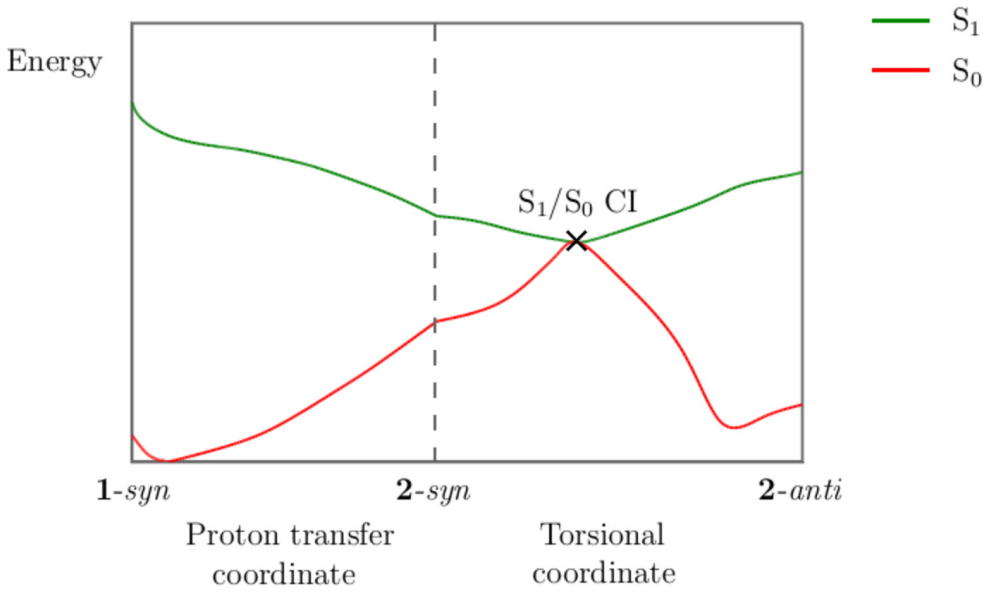

The photoreactivity pattern outlined above, whereby ESIPT is followed by a twist of the molecular skeleton and internal conversion to the ground state, is also characteristic of many other Schiff bases that undergo ESIPT reactions, including *N*-salicylideneaniline, 2-(2'-hydroxyphenyl)benzothiazole and their derivatives. In the molecular crystal forms of some of these compounds, however, the skeletal

twisting is prevented by the close packing of molecules in the crystal lattice. For example, in the crystal structure of 2-(2'-hydroxyphenyl)benzothiazole,[6] molecules are planar and π-stacked, leaving no room for torsion around the carbon-carbon bond connecting the benzothiazole and hydroxyphenyl groups.[7] On the other hand, in one of the known polymorphs of *N*-salicylidene-2-chloroaniline,[8] molecules do not engage in π-stacking interactions, and the salicylidene and chloroaniline moieties are twisted relative to one another. Owing to the less crowded nature of its crystal structure, irradiation of that polymorph yields the *cis*-keto and, through a pedal motion of the chloroaniline moiety, the *trans*-keto isomers, with the photoproducts not appearing as a separate crystal phase.[9] (See Chapter 4 for our TD-DFT/DFT simulations of this reaction.) The different coloration of the *trans*-keto and the original *cis*-enol forms is responsible for the photochromic properties of that polymorph. The general rule governing photoisomerisation through twisting within molecular crystals of Schiff bases is that less crowded lattices with non-planar molecules and an absence of $\pi \cdots \pi$ interactions enable photoisomerisation, while tightly packed structures which exhibit π-stacking prevent it.[9]

The above examples illustrate the interplay between photoreactivity and crystal structure that occurs in ESIPT reactions of Schiff base molecular crystals. Clearly, it is an interesting question whether the QM/QM hybrid method can make any predictions as to whether the crystal structure of 7PyIn permits the photoexcited molecule to twist around the carbon-carbon bond connecting the pyridyl and indolyl groups, and thereby reach the S_1/S_0 CI. Accordingly, in addition to calculating the timescale of the ESIPT reaction, the goal of our simulations was to assess whether that conical intersection is accessible in the molecular crystal phase. To the best of our knowledge, the ESIPT reaction and the possible subsequent radiationless decay process in the crystal form of 7PyIn has not been studied experimentally. In the crystal structure of 7PyIn,[12] as shown in Figure 3.4, there are no π-stacking interactions between molecules, and the density calculated from the crystal cell and contents, at 1.293 g/cm^3, is low. Therefore through comparison with other examples of ESIPT systems,[9,10] we anticipate that the crystal packing should not prevent the photoexcited molecule from undergoing *syn*$\rightarrow$*anti* photoisomerisation.

Figure 3.4: Crystal structure of 7PyIn obtained at $T = 223$ K. The compound crystallises in orthorhombic space group $Pca2_1$[13] with two molecules in the asymmetric unit. $a = 9.7196$ Å, $b = 17.4764$ Å, $c = 11.7484$ Å, $Z = 8$. Layers of symmetry-equivalent molecules are labelled I and II.

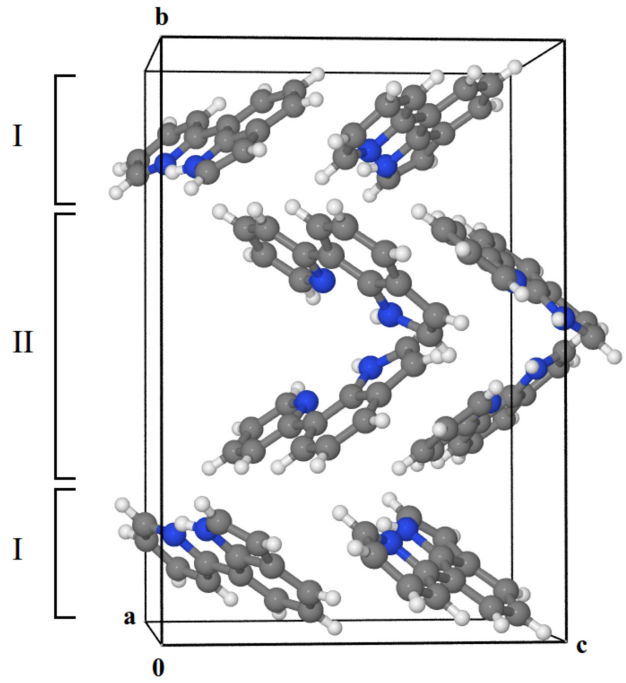

We remark here, however, that existing exchange-correlation functionals, such as the PBE0 functional which we have employed, do not correctly describe non-dynamical electron correlation, and are therefore incapable of correctly describing the vicinity of a CI, where the wavefunction has an intrinsic multiconfigurational character, and they may also incorrectly predict the electron density distribution for a biradicaloid state, such as the 7PyIn molecule near the CI. It will therefore also be essential to critically assess the ability of TD-DFT to provide a correct potential energy surface for the twisting motion of 7PyIn.

In several studies of excited-state *cis-trans* isomerisations through rotations around double bonds,[11] including in ESIPT systems structurally related to 7PyIn,[3,4] results obtained using the TD-DFT method in conjunction with various exchange-correlation functionals were benchmarked against those computed with the use of multiconfigurational methods, which are capable of correctly describing conical intersections as well as biradicals. Encouragingly, in each of the works just cited, TD-DFT was found to correctly predict the existence and rough location of the relevant conical intersection, in that in the vicinity of the CI the energy

separation between the ground state and the first singlet excited state became small. We are also unaware of any report of TD-DFT giving rise to a qualitatively incorrect description of an ESIPT system.

In the case of 7PyIn, as explained in Section 3.4.1, by comparing potential energy surface scans at the TD-DFT and the Complete Active Space SCF (CASSCF) levels, we have obtained results in line with the current literature norms, in that although TD-DFT does appear to qualitatively predict the existence of the relevant CI in 7PyIn, the exact location of the CI and the topology of the potential energy surface around it may be somewhat in error. Despite this, in view of the vastly superior computational efficiency offered by TD-DFT as compared to multiconfigurational methods, as well as its ability to predict ESIPT timescales in agreement with experimental data,[4] in the hybrid QM/QM scheme applied in the present work, we have used the TD-DFT method to describe the photoexcited molecule. The possible error resulting from the use of the TD-DFT method was quantified by comparing with CASSCF calculations, and was borne in mind when interpreting the simulation results.

A point of note is that the asymmetric unit of the 7PyIn crystal consists of two molecules, which form alternating double layers parallel to the *ac* plane (labelled I and II in Figure 3.4). Molecules within each layer type are equivalent by the symmetry of the crystal structure. As the local environments of molecules occupying the two different symmetry sites are different, when conducting molecular dynamics simulations of ESIPT, we have selected molecules to photoexcite from among molecules of both symmetry types.

3.3. Computational methods

3.3.1. Outline of simulation scheme

In the present section we sketch out the computational procedure that was used to study the ESIPT reaction in 7PyIn the crystal lattice, assuming that one molecule out of eight within the unit cell of 7PyIn undergoes photoexcitation.

1. Firstly, geometries of the **1**-*syn* and **1**-*anti* conformers of the 7PyIn isolated molecule were optimised at the DFT level of theory. Vertical excitation energies were calculated using the TD-DFT method.

2. A relaxed potential energy scan along the torsion angle formed by the atoms C1-C2-C3-N2 (henceforth denoted as ϕ, see Figure 3.5(a) in Section 4.1 for atom numbering), which describes rotation around the carbon-carbon bond connecting the pyridyl and indolyl moieties, was carried out for the **2**-*syn* tautomer on the S_1 potential energy surface at the TD-DFT level. Energies of points along the torsional coordinate were subsequently recalculated at the CASSCF level.

3. A unit cell of the 7PyIn crystal, representing the bulk lattice, was thoroughly equilibrated by means of MD simulation in the canonical ensemble on the ground-state potential energy surface.

4. Phase space points (i.e., sets of atomic coordinates and velocities) were sampled from the production run at long time intervals.

5. For each selected phase space point, photoexcitation to the S_1 state of a single molecule of 7PyIn embedded in the crystal lattice was modelled by taking the system from the ground-state DFT potential energy surface to a hybrid QM/QM excited-state potential energy surface in which the photoexcited molecule is treated using the TD-DFT method, while the remaining molecules are described using ground-state DFT.

6. For each such photoexcited system, molecular dynamics was propagated in the microcanonical ensemble on the hybrid QM/QM potential energy surface. The progress of the ESIPT reaction and subsequent skeletal twisting of the photoexcited 7PyIn molecule was monitored by following structural parameters such as the proton transfer coordinate and the donor-acceptor distance.

The various components of the simulation are described in detail in the following subsections.

3.3.2. Simulation setup

3.3.2.1. Isolated-molecule calculations

Geometry optimisations of the isolated 7PyIn molecule were carried out using the PBE0[24] exchange-correlation functional with the 6-31G(d,p) basis set as

implemented in the computational chemistry software package Gaussian 09.[25] The default Berny algorithm using GEDIIS in redundant internal coordinates was used in geometry optimisation. Vertical excitation energies were calculated for both the **1**-*syn* and **2**-*syn* tautomers of 7PyIn. Next, a relaxed potential energy surface (PES) scan along the torsion angle ϕ, which describes rotation around the carbon-carbon bond connecting the pyridyl and indolyl moieties, was conducted for the **2**-*syn* tautomer on the S_1 potential energy surface using the TD-DFT method. At each scan point, the torsion angle ϕ was constrained while all other redundant internal coordinates were optimised.

Single-point CASSCF calculations at geometries derived from the TD-DFT PES scan were carried out within Gaussian 03.[26] All calculations were state-averaged over the two states of interest (S_0 and S_1) with equal weights. For the starting orbitals for the CASSCF calculations, we have used natural orbitals extracted from an unrestricted Hartree-Fock calculation, carried out with the minimal STO-3G basis set, for the planar structure of the **2**-*syn* tautomer obtained from the TD-DFT PES scan. All natural orbitals with occupation numbers in the range from 0.05 to 1.95 were included in the active space of an initial CASSCF calculation, leading to an active space comprising eight electrons distributed in eight orbitals, or an (8,8) active space. All orbitals included in the active space had π-type symmetry. The STO-3G CASSCF wavefunction was subsequently projected onto progressively larger basis sets up to 6-31G(d), which was used in all production CASSCF calculations. This model chemistry is abbreviated SA-2-CASSCF(8,8). The same active space was carried over to single point calculations for all other structures obtained in the PES scan of the **2**-*syn* tautomer.

The geometry with $\phi = 40°$ obtained from the PES scan of the **2**-*syn* tautomer was also used as a starting point for a search for the S_1/S_0 conical intersection involved in the *syn* to *anti* photoisomerisation of 7PyIn. Because prior calculations at the approximate coupled-cluster singles-and-doubles (CC2) level reported in Ref.[1] suggest that this CI occurs at a torsion angle $\phi \approx 90°$, it was anticipated that the active space chosen at the planar geometry ($\phi = 0°$) may no longer be suitable for the CI search. Therefore, for the purpose of locating the S_1/S_0 CI, the CASSCF active space was chosen anew at the $\phi = 40°$ geometry. As before, natural orbitals from an UHF/STO-3G calculation were used as the starting orbitals CASSCF, and all natural orbitals with occupation numbers in the range 0.05 to 1.95 were

included in the active space, now giving rise to an active space comprising 6 electrons distributed among 6 orbitals. This $(6, 6)$ active space contained three predominantly π-type occupied orbitals and three predominantly π-type virtual orbitals. The STO-3G wavefunction was then projected onto progressively larger basis sets, up to the 6-31G(d) basis set which was utilised in the CI search. The model chemistry described above will henceforth be denoted as SA-2-CASSCF(6,6).

3.3.2.2. Solid-state calculations

In the equilibration of the ground-state 7PyIn crystal unit cell in the ground electronic state, the potential energy of the system was evaluated using the Perdew, Burke, Ernzerhof exchange-correlation DFT functional[27] as implemented in the software package CASTEP Academic Release version 5.501.[28] A plane-wave cutoff of 400 eV was applied. The electronic Brillouin zone was sampled by using a Monkhorst-Pack k-point grid with a k-point spacing of at most $0.1\ \text{Å}^{-1}$, achieved using a single k-point at $(\frac{1}{4}\,0\,0)$. The default ultrasoft pseudopotentials were used.[29] This choice of plane-wave cutoff and maximum k-point spacing represents a compromise between computational efficiency and accuracy. As we will demonstrate in Section 4.2, the plane-wave DFT calculation accurately reproduces the experimental crystal structure, and for that reason this compromise was deemed acceptable. Energies and forces were corrected for dispersion interactions using the semiempirical scheme of Grimme.[30] The SCF electronic energy convergence criterion was set to 1.0×10^{-7} eV. The same level of theory was applied in the TD-DFT/DFT simulations of the photoexcited system when evaluating the term $E^{\text{PW}}_{\text{DFT}}(\mathbf{S})$ (see Section 1.3.2 of Chapter 1 for equation 1.23 that defines the subtractive TD-DFT/DFT potential energy surface).

When calculating the term $E^{\text{PW}}_{\text{DFT}}(\mathbf{C})$, the reactive molecule was placed in a cubic supercell of edge length 20 Å, which was found to be large enough that the total energy did not change significantly on increasing the supercell size further. The electronic Brillouin zone was sampled at the Γ-point only. The remaining calculation parameters were identical as in the evaluation of the term $E^{\text{PW}}_{\text{DFT}}(\mathbf{S})$.

The term $E^{\text{GTO}}_{\text{TD-DFT}}(\mathbf{C})$ was evaluated using the PBE0/6-31G(d,p) model chemistry within Gaussian 09,[25] with the molecule $\mathbf{C}$ in the S_1 electronic state.

The ground-state system was equilibrated by propagating Born-Oppenheimer

molecular dynamics in the *NVT* ensemble for 3 ps, following which a production run of 7 ps was carried out. Throughout the equilibration and production periods, the temperature was maintained at 220 K using a chain of five Nosé-Hoover thermostats with a relaxation time of $\tau = 1$ ps. A time step of 1 fs was used throughout the equilibration and production periods. Phase space points were collected from the production run at intervals of 1 ps starting from $t = 3$ ps to serve as starting points for the TD-DFT/DFT simulations of ESIPT, for a total of eight starting points. From each starting point, two trajectories were propagated: one in which the photoexcited molecule was selected from among the symmetry type I molecules, and another in which it was selected from among the symmetry type II molecules, for a total of sixteen trajectories (see Figure 3.4 and accompanying text for an explanation of the symmetry labels I and II).

The ESIPT reaction was modelled by propagating molecular dynamics in the *NVE* ensemble on the subtractive TD-DFT/DFT potential energy surface. Newton's equations of motion were integrated using the Velocity Verlet scheme with a time step of 0.5 fs. On the grounds that previous studies of ESIPT in structurally similar systems have characterised the proton transfer as a ballistic motion of the wave packet, with no significant involvement of proton tunneling,[31,32] we believe that the treatment of the shuttling proton as a classical point particle did not introduce large error into the simulation of the proton transfer reaction. The dynamics was propagated until the system reached the S_1/S_0 conical intersection, which occurred in every simulated trajectory.

3.4. Results and discussion

3.4.1. Energy minima of the isolated molecule

Equilibrium geometries of the **1**-*syn* and **1**-*anti* conformers of 7PyIn are presented in Figure 3.5(a) and (b), respectively. The **1**-*syn* conformer adopts a planar geometry that belongs to the C_s point group. In the **1**-*anti* conformer, the pyridyl and indolyl moieties are twisted relative to one another, with a torsion angle ϕ (the torsion angle formed by the atoms C1-C2-C3-N2, see Figure 3.5(a) for atom numbering) of 148.2°. The **1**-*anti* conformer is higher in energy than the **1**-*syn* by 0.260 eV (25.1 kJ mol^{-1}, energy difference corrected for zero-point vibrational energy). The vertical $S_0 \rightarrow S_1$ excitation energy for the **1**-*syn* conformer was calculated as 3.80 eV.

Figure 3.5: Geometries of the 7PyIn molecule. All distances are given in units of Å.

(a) 1-*syn* conformation optimised at the PBE0/6-31G(d,p) level, ϕ = 0.0°

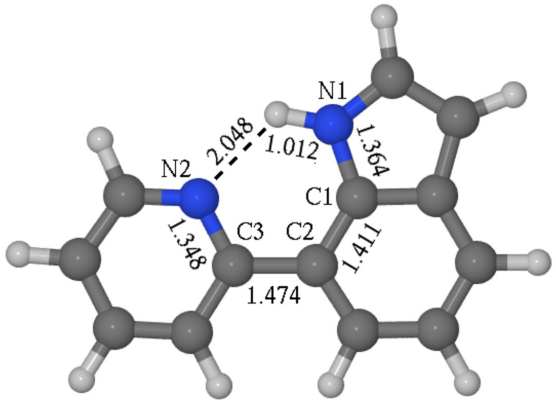

(b) 1-*anti* conformation, optimised at the PBE0/6-31G(d,p) level, ϕ = 148.2°

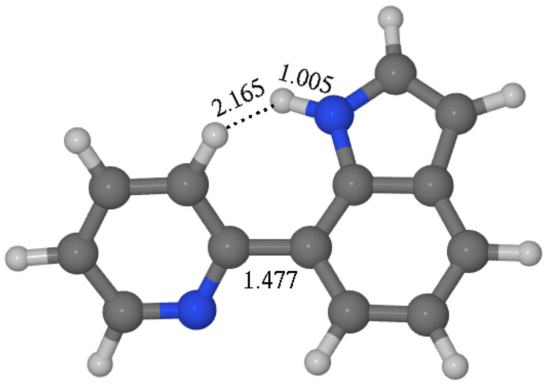

(c) S_1/S_0 conical intersection located at the SA-2-CASSCF(6,6) level, ϕ = 72.3°

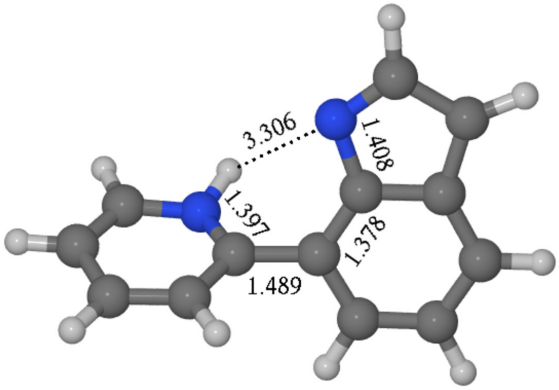

A potential energy surface scan along ϕ on the S_1 surface (calculated at the TD-DFT level) was conducted for the **2**-*syn* tautomer, in which the proton is located at the pyridyl group nitrogen N2. The torsion angle ϕ was varied in the range 0° to 40° in steps of 10°, and all other redundant internal coordinates were reoptimised at each step. The energy at each resulting point on the PES was subsequently recalculated at the SA-2-CASSCF(8,8) level of theory. The potential energy values along the torsional coordinate calculated using the TD-DFT and SA-2-CASSCF(8,8) methods are compared in Figure 3.6 on the following page, which we will now discuss in some detail.

It can be seen from Figure 3.6 that the DFT and the SA-CASSCF(8,8) methods provide a very similar characterisation of the S_0 potential energy surface. Vertical excitation energies of the planar **2**-*syn* conformer calculated at the TD-DFT and SA-CASSCF(8,8) levels are also in good agreement, at 1.536 and 1.458 eV, respectively. However, these two methods paint somewhat different pictures of the topology of the S_1 potential energy surface. At the TD-DFT level, the energy of the S_1 state decreases monotonically with increasing torsion angle ϕ, and the S_0 and S_1 states are very close in energy (0.343 eV apart) at $\phi = 40°$. An attempt to continue the potential energy surface scan to $\phi = 50°$ resulted in failure of the TD-DFT calculation, indicating that the TD-DFT method predicts that the S_1/S_0 conical intersection occurs for a ϕ value just over 40°. In contrast, at the SA-CASSCF(8,8) level the energy of the S_1 state varies more weakly with ϕ, increasing by around 0.08 eV over the range of $\phi = 0°$ to 30° and then decreasing by around 0.01 eV from $\phi = 30°$ to 40°.

The geometry of the S_1/S_0 conical intersection, located at the SA-2-CASSCF(6,6) level, is presented in Figure 3.5(c). At this geometry, the energy gap between S_1 and S_0 states is 0.041 eV (4.0 kJ mol^{-1}), and the torsion angle ϕ takes a value of 72.3°. There remains a vestigial hydrogen bond at the conical intersection geometry, as evidenced by the H-N bond within the pyridyl moiety being slightly bent towards the indolyl group nitrogen.

It is difficult to judge which of the TD-DFT and CASSCF methods provides a more reliable description of the S_1 potential energy surface along the torsional coordinate. Although the CASSCF method is capable of a correct treatment of non-dynamical correlation, due to the fact that we have used a relatively modest active space, the calculated energies include only a small fraction of the

Figure 3.6: Potential energy surfaces of the **2**-*syn* tautomer as a function of the C1-C2-C3-N2 torsion angle (ϕ). The molecular geometries were obtained through a relaxed PES scan on the S_1 surface calculated using the TD-DFT method, in which the torsion angle ϕ was constrained while all other redundant internal coordinates were optimised at each scan point. The DFT S_0 state energy and the SA-CASSCF(8,8) S_1 and S_0 energies were calculated at the geometries extracted from the TD-DFT PES scan. The origin of the energy axis is taken at the ground-state energy of the planar **2**-*syn* tautomer.

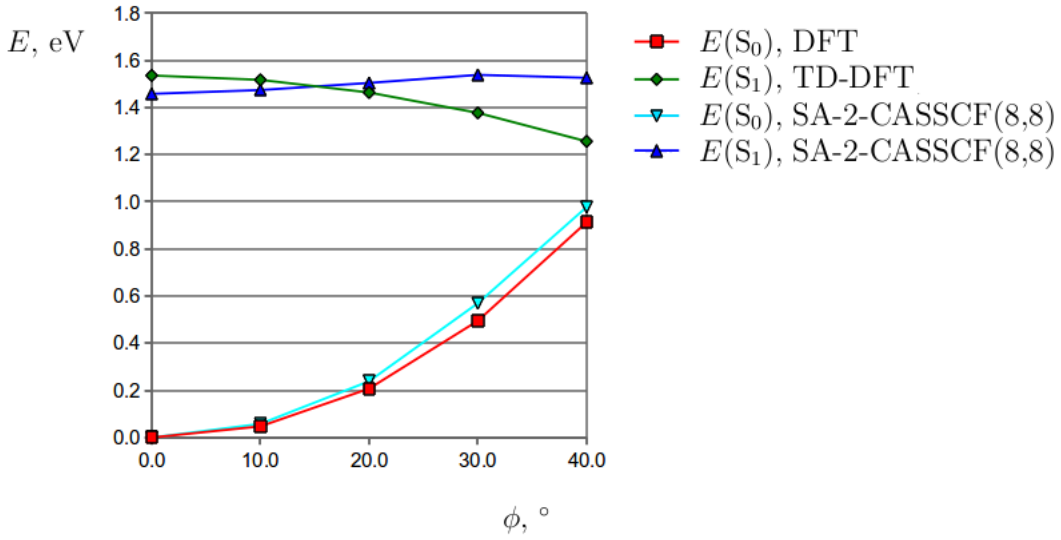

true dynamical correlation energy. Due to these considerations, we do not treat the calculations performed using the CASSCF method as an exact benchmark, but merely use them to identify the possible error introduced by employing the TD-DFT method.

Clearly, at the CASSCF level of theory, the S_1/S_0 conical intersection is located at a substantially higher value of ϕ than that suggested by the TD-DFT calculations. Furthermore, the TD-DFT method predicts a different topology of the S_1 potential energy surface than CASSCF. Because at the TD-DFT level the potential energy of the **2**-*syn* tautomer in the S_1 state decreases with increasing torsion angle ϕ, we might expect that the photoexcited molecule is funneled towards the S_1/S_0 CI by the topology of the TD-DFT potential energy surface. This effect is absent at the CASSCF level, where the S_1 potential energy surface is flatter, which may result in an artificially strong tendency of the photoexcited molecule in the TD-DFT/DFT hybrid simulations to reach the S_1/S_0 CI. The differences between energies of the S_1 state calculated at the TD-DFT and

CASSCF levels are reasonably small, however; up to 0.348 eV for the $\phi = 40°$ structure, relative to the $\phi = 0°$ structure. Also, a survey of trajectories generated on the TD-DFT/DFT potential energy surface, presented in Table 3.1, shows that in some trajectories, upon reaching the S_1/S_0 CI, the photoexcited molecule adopted an absolute value of ϕ of around 60°-70°, which coincides closely with the value of 72.3° predicted for the CI at the SA-2-CASSCF(6,6) level. Hence, we believe that although the TD-DFT method may give rise to an incorrect topology of the potential energy surface near the S_1/S_0 CI, it does provide an adequate description of the torsional motion of the photoexcited molecule in the sense that configurations near the S_1/S_0 CI that are reached by trajectories propagated on the TD-DFT/DFT hybrid potential energy surface are also energetically accessible to the real system.

3.4.2. Crystal Structure of 7PyIn

In order to assess the quality of the simulation of the crystal structure of 7PyIn by the ground-state DFT potential energy surface used in the MD calculations, time-averaged atomic positions were extracted from the production MD run. A superposition of the time-averaged crystal structure of 7PyIn onto the experimentally determined structure is shown in Figure 3.7, where it can be seen that the time-averaged atomic positions coincide very closely with the experimental positions. Hence we infer that the model chemistry used in the MD simulations correctly reproduces the crystal structure at the relevant temperature and density.

3.4.3. Proton transfer and accessibility of the S_1/S_0 conical intersection

The progress of the excited-state trajectories was followed by monitoring a set of structural and energetic parameters, whose definitions we will now provide. The proton transfer coordinate is defined as the difference between the lengths of the breaking N1-H bond and the forming N2-H bond, R(N1-H) − R(N2-H). Proton transfer was considered to have occurred at the point when the system passed through the line of R(N1-H) − R(N2-H) = 0. Although in principle it is possible for the shuttling proton to undergo back transfer from nitrogen N1 to N2, and hence cross through R(N1-H) − R(N2-H) = 0 multiple times, this did not occur in any of the simulated trajectories. The proton donor-acceptor distance in the ESIPT reaction is denoted R(N1-N2). The potential energy of the system with

Figure 3.7: An overlay of the experimental and time-averaged simulated structures of 7PyIn, in light grey and dark grey respectively.

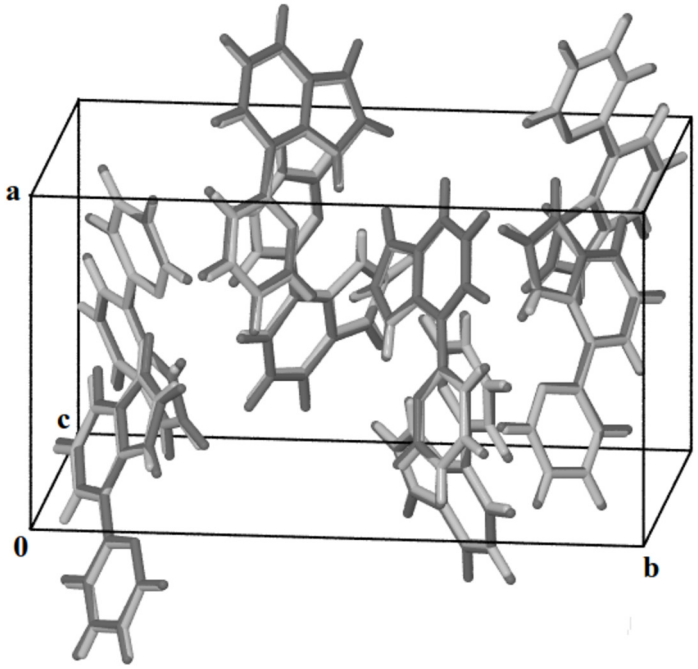

the reactive molecule in the S_1 state is given by equation 3.1. Throughout each trajectory, we also followed the ground-state potential energy of the system, which is defined by:

$$E(S_0) = E^{PW}_{DFT}(\mathbf{S}) + E^{GTO}_{DFT}(\mathbf{C}) - E^{PW}_{DFT}(\mathbf{C}) \tag{3.1}$$

Here $E^{GTO}_{DFT}(\mathbf{C})$ represents the ground-state potential energy of the photoexcited molecule, calculated at the PBE0/6-31G(d,p) level of theory. The system was considered to have reached the S_1/S_0 CI when the potential energy gap between the excited and ground states, $\Delta E = E(S_1) - E(S_0)$, decreased to below the arbitrarily chosen threshold value of 0.1 eV.

The results of all sixteen simulated trajectories are reviewed in Table 3.1 on the next page. Proton transfer occurred in every simulated trajectory, with a mean proton transfer time of 80 fs, indicating a barrierless, or near-barrierless, ESIPT mechanism. In each case, following proton transfer, the photoexcited molecule reached the S_1/S_0 conical intersection, at which point the simulation was terminated because of the inability of TD-DFT to correctly describe the crossing region. We note from the data presented in Table 1 that there is no significant

Table 3.1: Results of simulated trajectories on the TD-DFT/DFT hybrid potential energy surface.

Excited molecule symmetry type [a]	Trajectory	t_{PT}, fs [b]	t_{CI}, fs [b]	$\Delta E(0)$, eV [c]	$\phi(0)$, ° [d]	$\phi(t_{CI})$, ° [d]
I	1	55.5	184.5	3.6764	1.0	−58.0
	2	42.0	174.5	3.6314	14.2	43.6
	3	128.5	386.5	3.8035	−10.5	47.6
	4	55.0	309.0	3.7983	0.6	46.9
	5	90.0	472.5	3.5006	−6.4	38.0
	6	130.0	432.0	3.8134	11.5	54.5
	7	91.0	275.5	3.8254	−7.6	−70.3
	8	142.5	279.0	3.4211	−8.1	41.2
II	1	75.0	374.0	3.6892	−3.4	−49.2
	2	88.0	325.5	3.6444	3.1	54.1
	3	39.5	182.5	3.6872	5.7	42.8
	4	22.0	283.5	3.5532	−8.6	51.9
	5	80.5	335.5	3.6607	14.9	−55.6
	6	108.5	221.0	3.7655	4.9	51.9
	7	91.5	267.0	3.8419	−9.6	40.8
	8	43.5	324.0	3.6108	6.3	−44.2

[a] I and II refer to the choice of the excited molecule from among the two molecules within the asymmetric unit.

[b] t_{PT} and t_{CI} are respectively the time at which proton transfer occurred and the time at which the photoexcited molecule reached the conical intersection, where $t = 0$ corresponds to the photoexcitation time.

[c] $\Delta E(0)$ is the potential energy gap between the states S_1 and S_0 at $t = 0$.

[d] $\phi(0)$ and $\phi(t_{CI})$ are respectively the values of the torsion angle ϕ at the time of the initial photoexcitation, and on reaching the S_1/S_0 CI.

difference in either the mean proton transfer time, or the mean time required for the photoexcited molecule to reach the S_1/S_0 CI, between the two inequivalent molecules within the crystal lattice.

Given that the CI was reached by all simulated trajectories within around 0.5 ps of the initial photoexcitation, it appears that on the hybrid TD-DFT/DFT potential energy surface the twisting motion of the photoexcited 7PyIn molecule within the corresponding crystal lattice is either barrierless, or occurs through a potential barrier that is low relative to the kinetic energy of the photoexcited molecule. Hence, on the TD-DFT/DFT potential energy surface both the

proton transfer and the internal conversion steps are essentially barrierless, and photoexcited molecules are efficiently funneled towards the CI. In the light of the possibly incorrect description of the twisting motion in 7PyIn by the TD-DFT method, as discussed in Section 3.4.1, we conclude that our molecular dynamics simulations on the TD-DFT/DFT potential energy surface predict that in the real system, the S_1/S_0 CI is energetically accessible, but the rate and quantum yield of the internal conversion process may both be lower than the very high rate (under 0.5 ps) and 100% quantum yield our simulations would suggest.

We must also point out that the finding that all photoexcited molecules rapidly reach the S_1/S_0 CI does not, on its own, indicate that *syn* to *anti* isomerisation occurs in the 7PyIn crystal, since molecules which pass through the conical intersection may potentially relax to both the *syn* and *anti* forms. However, from the finding that in some simulated trajectories, on reaching the S_1/S_0 CI the photoexcited molecule had a high absolute value of ϕ (up to $\phi(t_{\mathrm{CI}}) = -70.3°$ in trajectory I-7; see Table 1), we may infer that it is mechanistically possible for photoexcited molecules within the confines of the crystal lattice to undergo a full twist around the C2-C3 bond, and in doing so to relax to the *anti* isomer. In conclusion, it is predicted that a fraction of photoexcited molecules can isomerise to the *anti* form.

In what follows we discuss in detail two representative simulated trajectories. Both these trajectories are also available for viewing in the Electronic Appendix that is attached to this thesis.

3.4.3.1. Trajectory II-5

Trajectory II-5 underwent proton transfer at $t = 80.5$ fs and subsequently reached the S_1/S_0 CI at $t = 335.5$ fs, at which point the simulation was discontinued.

In Figure 3.8(a) on the following page we present a three-dimensional projection of trajectory II-5 onto energy, proton transfer and proton donor-acceptor distance coordinates, which provides a comprehensive mechanistic description of the photochemical reaction. The projection can be roughly divided into a number of segments that correspond to specific events occurring along the trajectory; these are marked as *a* to *e* in Figure 3.8(a). Point *a* is the starting point of the trajectory, and corresponds to the photoexcited molecule in conformation **1**-*syn*.

Figure 3.8: Trajectory II-5

(a) Projection of trajectory II-5 onto energy, proton transfer $(R(\text{N1-H}) - R(\text{N2-H}))$ and proton donor-acceptor distance $(R(\text{N1-N2}))$ coordinates. The potential energy of the photoexcited system, and the ground-state energy calculated at the same geometry, are plotted in green and red, respectively. Label a indicates the starting point of the trajectory, line segment b corresponds to a shortening of the proton donor-acceptor distance, and segment c is the ESIPT step. Segment d corresponds to the relaxation of the molecule following proton transfer, and the lengthening of the proton donor-acceptor distance. Finally, at the point indicated by label e, the reactive molecule reaches an S_1/S_0 conical intersection.

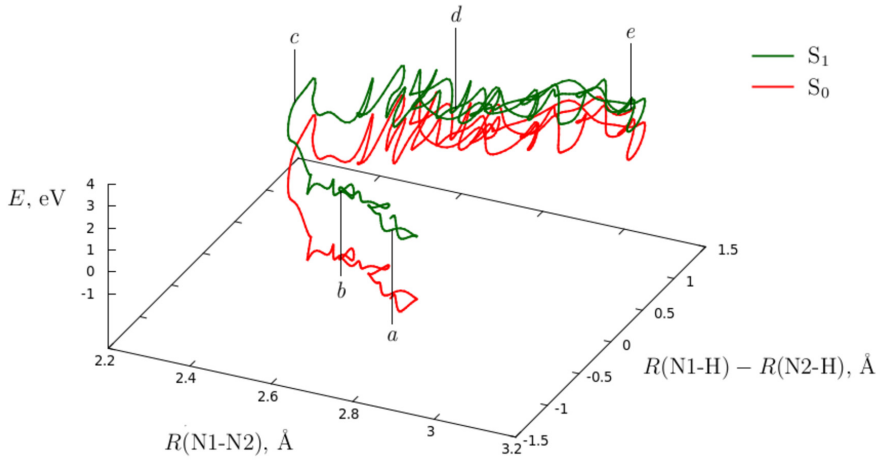

(b) Time evolution of torsion angle ϕ in trajectory II-5.

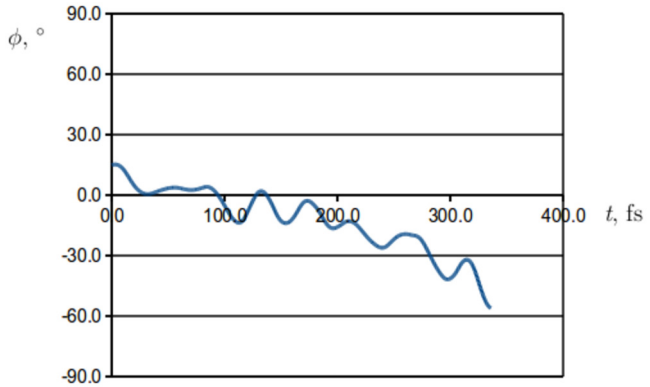

Segment b is largely parallel to the proton donor-acceptor distance coordinate, R(N1-N2), and corresponds to a shortening of the distance between the two nitrogen atoms before the proton transfer step. The next segment c, mostly parallel to the proton transfer coordinate, is the proton transfer step. The potential energy gap between the excited and ground states decreases by around 1.5 eV during the proton transfer step c. Further along the trajectory, segment d corresponds to the relaxation of the molecule on the excited-state potential energy surface following proton transfer. Although segment d as a whole is mostly parallel to the coordinate R(N1-N2), its early part (near the juncture of segments c and d) exhibits strong oscillations along the proton transfer coordinate. These oscillations are caused by the vibrational excitation of the newly formed N2-H bond immediately following proton transfer. It takes around ten oscillation periods for these large-amplitude vibrations to be dampened out.

As seen in Figure 3.8(b), where the torsion angle ϕ is plotted as a function of time, immediately after proton transfer at $t = 80.5$ fs, which occurred at a near-planar geometry, the photoexcited molecule started to undergo twisting motions that modulated the torsion angle ϕ. Through these motions, the pyridyl and indolyl moieties gradually rotated in opposite directions, until the photoexcited molecule reached the S_1/S_0 CI at $t = 335.5$ fs. The point at which the photoexcited molecule reached the S_1/S_0 CI is marked as e in Figure 3.8(a).

The overall sequence of proton donor-acceptor distance shortening (b), followed by proton transfer at a near-planar geometry (c) and relaxation involving a lengthening of the donor-acceptor distance (d), and finally twisting motions ultimately leading to the S_1/S_0 CI (e) is shared by all simulated trajectories.

Finally, we turn our attention to the configuration of the simulated system in trajectory II-5 as it reached the S_1/S_0 CI. In Figure 3.9, the final frame from the trajectory, immediately before the CI is reached, is overlaid on the experimental crystal structure of 7PyIn. From this image we can confirm that the S_1/S_0 CI is reached by the simultaneous twist of the pyridyl and indolyl moieties in opposite directions. A survey of other trajectories that reach the CI shows that the CI can be reached by torsion in either direction (that is to say, by torsion towards both more positive and more negative values of ϕ).

Visual inspection of trajectory II-5 reveals that concurrent with the twisting

Figure 3.9: An overlay of the instantaneous configuration of the system on reaching the S_1/S_0 conical intersection seam in trajectory II-5, and the experimental crystal structure of 7PyIn, drawn in dark grey and light grey, respectively. The photoexcited molecule is labelled $\mathbf{C}$. $\mathbf{M1}$ is a molecule neighbouring $\mathbf{C}$ whose pyridyl moiety undergoes significant displacement from its crystallographic position during the simulated photoreaction. Unit cell axes $\mathbf{a}$, $\mathbf{b}$ and $\mathbf{c}$ shown.

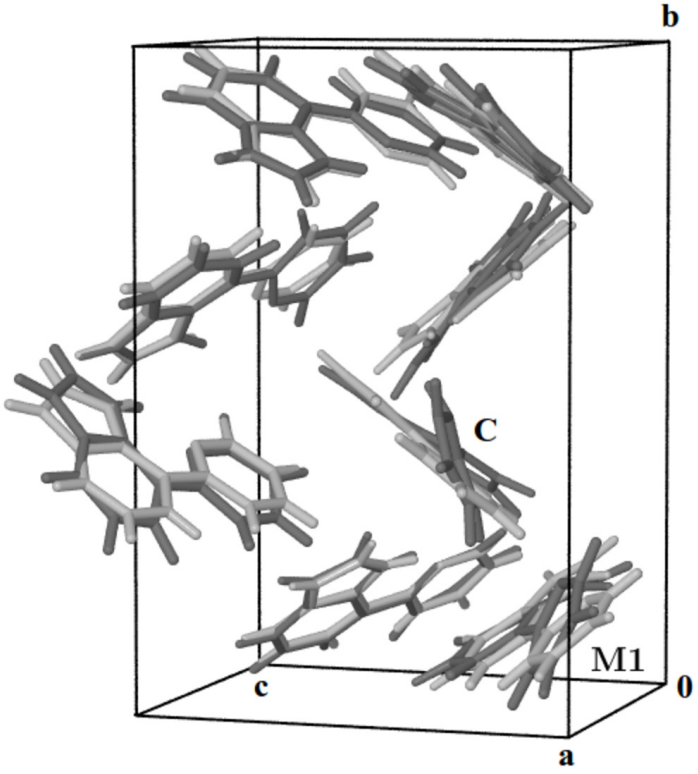

motion of the photoexcited molecule **C**, the indolyl moiety of a neighbouring molecule (labelled **M1** in Figure 3.9) becomes significantly displaced from its crystallographic position, away from molecule **C** (note that molecules **C** and **M1** are neighbours because of the periodic boundary conditions imposed in order to simulate the crystal lattice). The displacements of the other ground-state molecules from their crystallographic positions are not greater in magnitude than typical thermal displacements within the ground-state system. While due to the low number of simulated trajectories it was not possible to rigorously study correlations between the twisting motion of the photoexcited molecule and the movements of the surrounding ground-state molecules, it seems plausible to surmise that in trajectory II-5 the displacement of molecule **M1** is caused by the torsional motion of the photoexcited molecule **C**. Similar instances of molecules

neighbouring **C** becoming displaced from their crystallographic positions while **C** approaches the S_1/S_0 CI were observed in some other trajectories, including trajectory I-1 which will be reviewed in due course.

3.4.3.2. Trajectory I-1

In Trajectory I-1, following proton transfer at $t = 55.5$ fs, the photoexcited molecule underwent torsion around the C2-C3 bond, and the criterion for the system reaching the S_1/S_0 conical intersection was met at $t = 184.5$ fs, at which point the simulation was terminated.

In Figure 3.10(a) on the next page, a projection is shown of the trajectory onto the energy, proton transfer and proton donor-acceptor distance coordinates. Distinct proton donor-acceptor shortening and proton transfer steps of the trajectory can be identified (segments *b* and *c*, respectively). In the relaxation segment *d*, vibrational excitation of the N2-H bond is again visible, although the amplitude of the oscillations is lower and they are dampened out more rapidly than in trajectory II-5. Finally, at point *e*, 184.5 fs after the initial photoexcitation, the photoexcited molecule reached the S_1/S_0 conical intersection. A plot of torsion angle ϕ as a function of time during trajectory I-1 is shown in Figure 3.10(b). Before the termination of trajectory I-1, the photoexcited molecule reached a torsion angle ϕ of $-58.0°$, which represents the second highest absolute value of ϕ on reaching the S_1/S_0 CI from all sixteen simulated trajectories.

In Figure 3.11 we present an overlay of the final frame from the trajectory and the experimental crystal structure of 7PyIn. Analogously to trajectory II-5, in trajectory I-5 one of the molecules neighbouring the photoexcited molecule **C**, labelled **M2** in Figure 3.11, appears to become significantly displaced from its crystallographic position at the same time as **C** undergoes twisting motions and approaches the conical intersection.

Figure 3.10: Trajectory I-1

(a) Projection of trajectory I-1 onto energy, proton transfer $(R(\text{N1-H}) - R(\text{N2-H}))$ and proton donor-acceptor distance $(R(\text{N1-N2}))$ coordinates. The potential energy of the photoexcited system, and the ground-state energy calculated at the same geometry, are plotted in green and red, respectively. Label a points to the starting point of the trajectory, line segment b corresponds to a shortening of the proton donor-acceptor distance before the ESIPT step, which takes place along segment c. Segment d is to the relaxation of the molecule following proton transfer, and the lengthening of the proton donor-acceptor distance. Finally, at the point indicated by label e, the reactive molecule reaches an S_1/S_0 conical intersection.

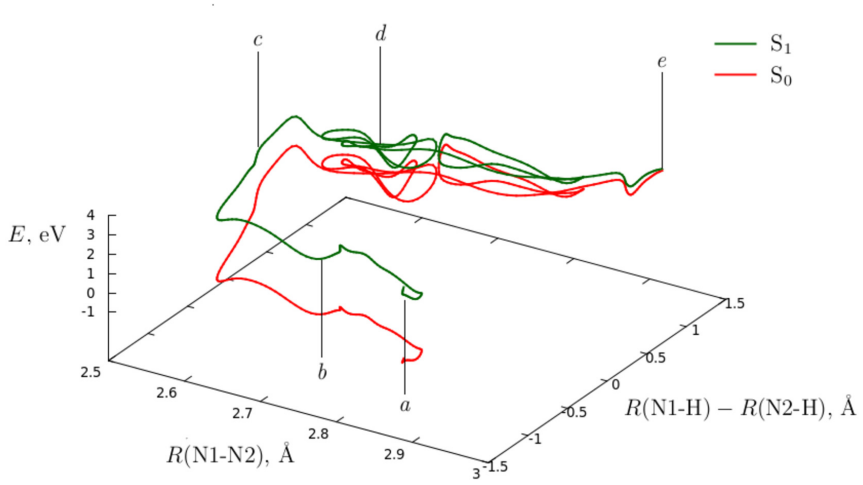

(b) Time evolution of torsion angle ϕ in trajectory I-1.

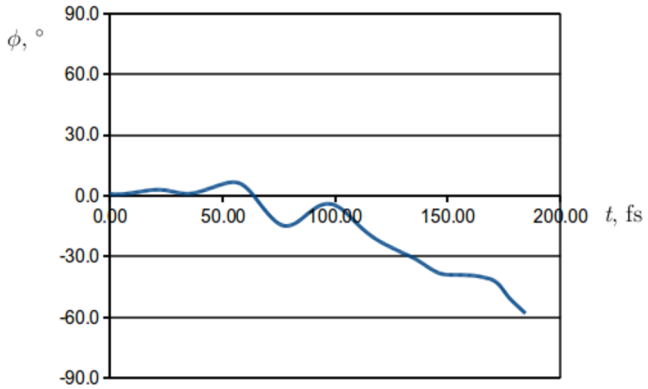

Figure 3.11: An overlay of the instantaneous configuration of the system on reaching the S_1/S_0 conical intersection seam and the experimental crystal structure of 7PyIn, drawn in dark grey and light grey, respectively. The photoexcited molecule is labelled **C**. **M2** is a molecule neighbouring **C** whose indolyl moiety undergoes significant displacement from its crystallographic position during the simulated photoreaction. Unit cell axes **a**, **b** and **c** shown.

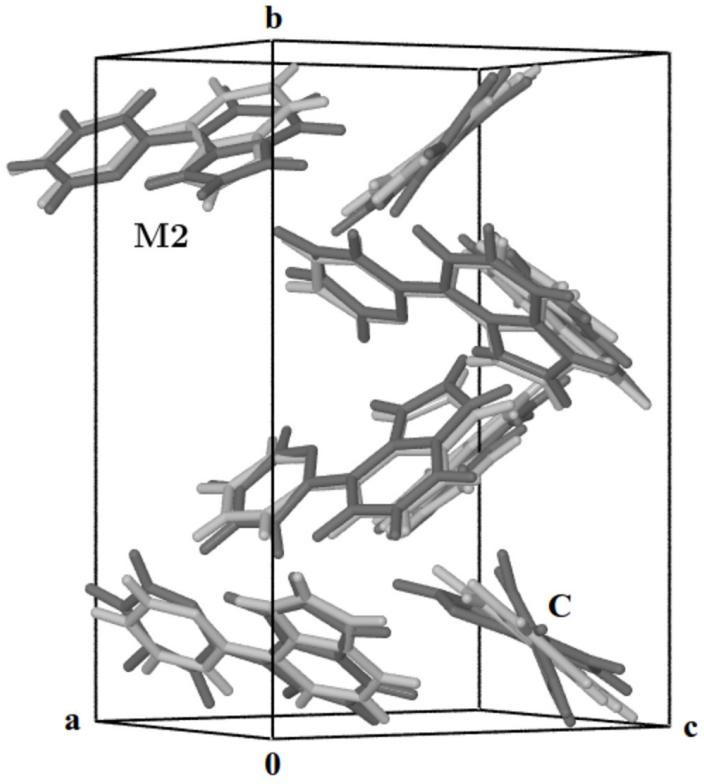

3.5. Conclusions

We have applied the subtractive TD-DFT/DFT method coupled with molecular dynamics to study the photochemical reaction of 7PyIn in the molecular crystal phase. Both the ESIPT step and the subsequent torsional skeletal deformation leading to an S_1/S_0 conical intersection are essentially barrierless. The ESIPT has been simulated to occur within 80 fs, on average, of the initiatory photoexcitation. By reaching the S_1/S_0 conical intersection, the photoexcited molecule is predicted to be able to undergo *syn* to *anti* photoisomerisation.

An unresolved issue is the correctness of the TD-DFT description of the potential energy of the S_1 state of the 7PyIn molecule along the torsional

coordinate (ϕ). While utmost care has been exercised to take into account the possible error due to the use of the TD-DFT method during the analysis of simulated trajectories, the fact remains that the TD-DFT method (or, strictly speaking, the approximate PBE0 exchange-correlation functional) was stretched to the limit when the photoexcited molecule approached the S_1/S_0 conical intersection. This, however, is part of the broader problem of efficient computer simulation of excited states, and as such is beyond the scope of the present work. We wish to underline here that any suitable electronic structure method can be incorporated into the subtractive hybrid QM/QM method for the purpose of describing the photoexcited molecule, and therefore the subtractive hybrid QM/QM method itself is not encumbered by the limitations of TD- DFT.

While at present no experimental data is available to verify the prediction made regarding the occurrence of *syn* to *anti* isomerisation, it is in line with the well-established general relationship between the crystal structure and photoreactivity of a wide range of structurally similar Schiff bases. We hope that the present study will stimulate experimental research into the mechanistic details of ultrafast reactions taking place in the molecular crystal phase.

References

[1] A. L. Sobolewski, W. Domcke, *J. Phys. Chem. A*, 2007, **111**, 11725.

[2] A. J. A. Aquino, F. Plasser, M. Barbatti, H. Lischka, *Croat. Chem. Acta*, 2009, **82**, 105.

[3] M. Barbatti, A. J. A. Aquino, H. Lischka, C. Schriever, S. Lochbrunner, E. Riedle, *Phys. Chem. Chem. Phys.*, 2009, **11**, 1406.

[4] J. M. Ortiz-Sánchez, R. Gelabert, M. Moreno, J. M. Lluch, *J. Chem. Phys.*, 2008, **129**, 214308.

[5] Y. Nosenko, G. Wiosna-Sałyga, M. Kunitski, I. Petkova, A. Singh, W. J. Buma, R. P. Thummel, B. Brutschy, J. Waluk, *Angew. Chem. Int. Ed.*, 2008, **47**, 6037.

[6] P. Sténson, *Acta. Chem. Scand.*, 1970, **24**, 3729.

[7] M. Taneda, Y. Kodama, Y. Eda, H. Koyama, T. Kawato, *Chem. Lett.*, 2007, **36**, 1410.

[8] J. Bregman, L. Leiserowitz, K. Osaki, *J. Chem. Soc.*, 1964, 2086.

[9] E. Hadjoudis, I. M. Mavridis, *Chem. Soc. Rev.*, 2004, **33**, 579.

[10] K. Johmoto, T. Ishida, A. Sekine, H. Uekusa, Y. Ohashi, *Acta Cryst.*, 2012, **B68**, 297.

[11] M. Wanko, M. Garavelli, F. Bernardi, T. A. Niehaus, T. Frauenheim, M. Elstner, *J. Chem. Phys.*, 2004, **120**, 1674.

[12] M. S. Mudadu, A. Singh, R. P. Thummel, *J. Org. Chem.*, 2006, **71**, 7611.

[13] D. A. Fletcher, R. F. McMeeking, D. Parkin,*J. Chem. Inf. Comput. Sci.*, 1996, **36**, 746.

[14] A. Warshel, M. Levitt, *J. Mol. Biol.*, 1976, **103**, 227.

[15] H. M. Senn, W. Thiel, *Top. Curr. Chem.*, 2007, **268**, 173.

[16] N. Bernstein, J. R. Kermode, G. Csányi, *Rep. Prog. Phys.*, 2009, **72**, 026501.

[17] M. J. Bearpark, S. M. Larkin, T. Vreven, *J. Phys. Chem. A*, 2008, **112**, 7286.

[18] P. Altoè, M. Stenta, A. Bottoni, M. Garavelli, *Theor. Chem. Acc.*, 2007, **118**, 219.

[19] H. R. R. Santos, M. J. Ramos, J. A. N. F. Gomes, *Phys. Rev. B*, 2005, **72**, 075445.

[20] C. Tuma, J. Sauer, *Phys. Chem. Chem. Phys.*, 2006, **8**, 3955.

[21] J. Handzlik, *Int. J. Quantum Chem.*, 2007, **107**, 2111.

[22] N. Hansen, T. Brüggemann, A. T. Bell, F. J. Keil, *J. Phys. Chem. C*, 2008, **112**, 15402.

[23] S. Svelle, C. Tuma, X. Rozanska, T. Kerber, J. Sauer, *J. Am. Chem. Soc.*, 2009, **131**, 816.

[24] C. Adamo, V. Barone, *J. Chem. Phys.*, 1999, **110**, 6158.

[25] Gaussian 09, Revision A.02, M. J. Frisch, G. W. Trucks, H. B. Schlegel, G. E. Scuseria, M. A. Robb, J. R. Cheeseman, G. Scalmani, V. Barone, B. Mennucci, G. A. Petersson, H. Nakatsuji, M. Caricato, X. Li,

H. P. Hratchian, A. F. Izmaylov, J. Bloino, G. Zheng, J. L. Sonnenberg, M. Hada, M. Ehara, K. Toyota, R. Fukuda, J. Hasegawa, M. Ishida, T. Nakajima, Y. Honda, O. Kitao, H. Nakai, T. Vreven, J. A. Montgomery, Jr., J. E. Peralta, F. Ogliaro, M. Bearpark, J. J. Heyd, E. Brothers, K. N. Kudin, V. N. Staroverov, R. Kobayashi, J. Normand, K. Raghavachari, A. Rendell, J. C. Burant, S. S. Iyengar, J. Tomasi, M. Cossi, N. Rega, J. M. Millam, M. Klene, J. E. Knox, J. B. Cross, V. Bakken, C. Adamo, J. Jaramillo, R. Gomperts, R. E. Stratmann, O. Yazyev, A. J. Austin, R. Cammi, C. Pomelli, J. W. Ochterski, R. L. Martin, K. Morokuma, V. G. Zakrzewski, G. A. Voth, P. Salvador, J. J. Dannenberg, S. Dapprich, A. D. Daniels, Ö. Farkas, J. B. Foresman, J. V. Ortiz, J. Cioslowski, and D. J. Fox, Gaussian, Inc., Wallingford CT, 2009.

[26] Gaussian 03, Revision E.01, M. J. Frisch, G. W. Trucks, H. B. Schlegel, G. E. Scuseria, M. A. Robb, J. R. Cheeseman, J. A. Montgomery, Jr., T. Vreven, K. N. Kudin, J. C. Burant, J. M. Millam, S. S. Iyengar, J. Tomasi, V. Barone, B. Mennucci, M. Cossi, G. Scalmani, N. Rega, G. A. Petersson, H. Nakatsuji, M. Hada, M. Ehara, K. Toyota, R. Fukuda, J. Hasegawa, M. Ishida, T. Nakajima, Y. Honda, O. Kitao, H. Nakai, M. Klene, X. Li, J. E. Knox, H. P. Hratchian, J. B. Cross, C. Adamo, J. Jaramillo, R. Gomperts, R. E. Stratmann, O. Yazyev, A. J. Austin, R. Cammi, C. Pomelli, J. W. Ochterski, P. Y. Ayala, K. Morokuma, G. A. Voth, P. Salvador, J. J. Dannenberg, V. G. Zakrzewski, S. Dapprich, A. D. Daniels, M. C. Strain, Ö. Farkas, D. K. Malick, A. D. Rabuck, K. Raghavachari, J. B. Foresman, J. V. Ortiz, Q. Cui, A. G. Baboul, S. Clifford, J. Cioslowski, B. B. Stefanov, G. Liu, A. Liashenko, P. Piskorz, I. Komaromi, R. L. Martin, D. J. Fox, T. Keith, M. A. Al-Laham, C. Y. Peng, A. Nanayakkara, M. Challacombe, P. M. W. Gill, B. Johnson, W. Chen, M. W. Wong, C. Gonzalez, and J. A. Pople, Gaussian, Inc., Pittsburgh PA, 2003.

[27] J. P. Perdew, K. Burke, M. Ernzerhof, *Phys. Rev. Lett.*, 1996, **77**, 3865.

[28] S. J. Clark, M. D. Segall, C. J. Pickard, P. J. Hasnip, M. I. J. Probert, K. Refson, M. C. Payne, *Z. Kristallogr.*, 2005, **220**, 567.

[29] Materials Studio CASTEP Online Help. H_00PBE.usp uses 1 valence electron (s state), C_00PBE.usp uses 4 valence electrons (s and p state), N_00PBE.usp uses 5 valence electrons (s and p state).

[30] S. Grimme, *J. Comput. Chem.*, 2006, **27**, 1787.

[31] S. Lochbrunner, A. J. Wurzer, E. Riedle, *J. Phys. Chem. A.*, 2003, **107**, 10580.

[32] C. Schriever, S. Lochbrunner, A. R. Ofial, E. Riedle, *Chem. Phys. Lett.*, 2011, **503**, 61.

Chapter 4
Solid-state photochemical reactions of *N*-salicylidene-2-chloroaniline

4.1. Background

Over a century ago, Senier and coworkers[1,2] discovered that anils (Schiff bases of salicylaldehyde with aniline derivatives) exhibit what in modern terminology is called photochromism: a reversible change in colouration brought about by the absorption of electromagnetic radiation. Since then, anils have enjoyed extensive experimental[3–13] and theoretical[10,11,14–16] attention. Surprisingly, despite the longstanding debate over the mechanism and the structure of the product species of the photochromic process in anil crystals,[5,8] relatively little effort has been made towards understanding the solid-state reaction mechanism using the methods of theoretical chemistry. In particular, to the best of our knowledge, a dynamical simulation of this reaction mechanism in its entirety has not previously been reported. Therefore, we have undertaken to model this mechanism using the subtractive TD-DFT/DFT scheme outlined in Chapter 1. In what follows, the present state of research on the anil photoisomerisation reaction is reviewed briefly so as to provide context for our simulations.

The relevant reactions of anils are shown in Figure 4.1 on the example of the simplest anil, *N*-salicylideneaniline (SA). The lowest-energy form of SA is the colourless *cis*-enol form, which exists in thermal equilibrium with the yellow *cis*-keto form. With increasing temperature, the population of the *cis*-keto form increases, giving rise to a stronger yellow colouration. This temperature-sensitive *cis*-enol $\rightleftarrows$ *cis*-keto equilibrium of anils is an interesting subject in its own right, and is considered in depth in Chapter 5.

If the *cis*-enol form of SA is irradiated with UV light, the red *trans*-keto form is obtained. The reverse reaction is induced by visible light and leads to the *cis*-keto tautomer, which in turn is in thermal equilibrium with the *cis*-enol form. The mechanism of the *cis*-enol to *trans*-keto photoisomerisation in the isolated molecule of SA has been studied using DFT, time-dependent DFT (TD-DFT), CASPT2 and quantum dynamics simulations by Ortiz-Sánchez and coworkers.[16]

Figure 4.1: Thermo- and photochromic reactions of *N*-salicylideneaniline.

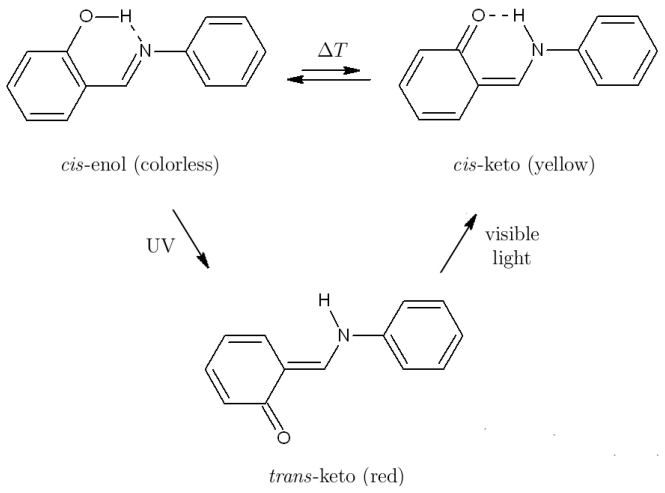

According to this study, the lowest singlet excited state (S_1) of the *cis*-enol form of SA is a π, π^* state in which the aniline group nitrogen is more basic relative to the salicylidene group oxygen. The S_1 surface of the *cis*-enol form was found to have two distinct reaction pathways, which are presented in Figure 4.2 on the next page. Also, the S_1 and S_0 potential energy surfaces calculated by Ortiz-Sánchez *et al.* along both pathways are plotted schematically in Figure 4.3.

In the first pathway, the *cis*-enol molecule in the S_1 state undergoes rapid (with a decay time of 49.6 fs) excited-state intramolecular proton transfer (ESIPT) from the salicylidene group oxygen O1 to the aniline group nitrogen N1 which converts it into the *cis*-keto form. The molecule then undergoes a torsional motion of the salicylidene ring around the C3-C4 bond to reach a conical intersection (henceforth referred to as CI2) between S_0 and S_1. After passing through CI2, the molecule may be converted to either the *trans*-keto form or back to the *cis*-keto form; this internal conversion process was termed IC2 by Ortiz-Sánchez *et al.*

In the second pathway, through a torsional motion around the N1-C3 bond (see Figure 4.2 for atom numbering) the *cis*-enol molecule decays rapidly (with a decay time of 37.7 fs) through another S_0/S_1 conical intersection (which we label CI1), thus undergoing radiationless de-excitation to the ground state. Ortiz-Sánchez *et al.* termed this internal conversion process leading to recovery of the starting enol form in a somewhat deformed geometry as IC1.

Figure 4.2: The two photoreaction pathways of the *cis*-enol form of the isolated *N*-salicylideneaniline (SA) molecule, based on calculations reported in Ref.[16]

(a) The first pathway begins with the photoexcited molecule undergoing intramolecular proton transfer. Through a torsional motion around the C3-C4 bond, the photoexcited molecule subsequently undergoes internal conversion to the ground state (IC2), leading to either the *trans*-keto form or back to the *cis*-keto form.

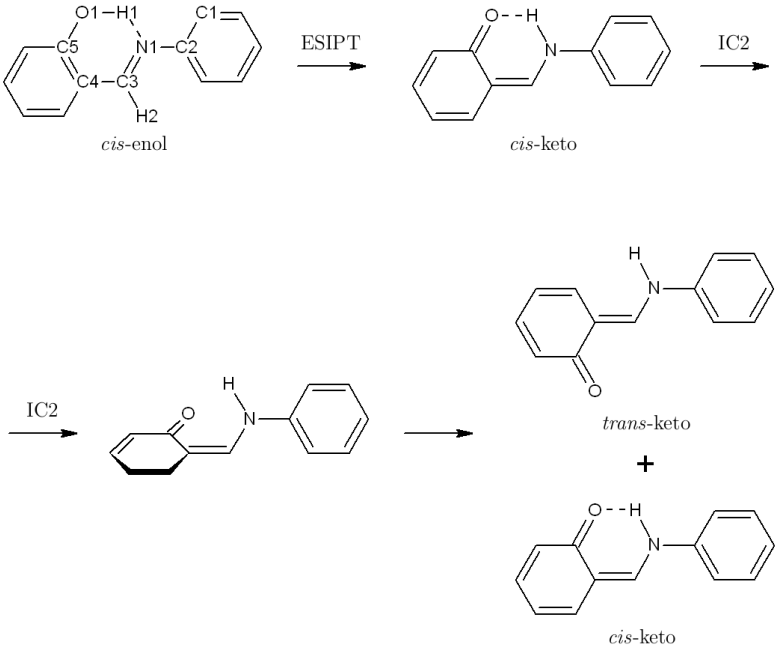

(b) The second pathway involves a torsional motion around the N1-C3 bond, through which the molecule undergoes internal conversion to the ground state (IC1). The final product of this pathway is an enol molecule in a deformed geometry.

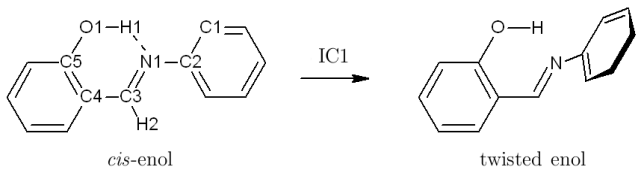

Figure 4.3: Schematic diagram of the S_0 and S_1 potential energy surfaces of the isolated *N*-salicylideneaniline molecule, based on calculations reported in Ref.[16] IC1, ESIPT and IC2 denote reaction coordinates representing the respective photochemical processes. The S_1/S_0 conical intersections involved in the radiationless deactivation processes IC1 and IC2 are labelled CI1 and CI2, respectively.

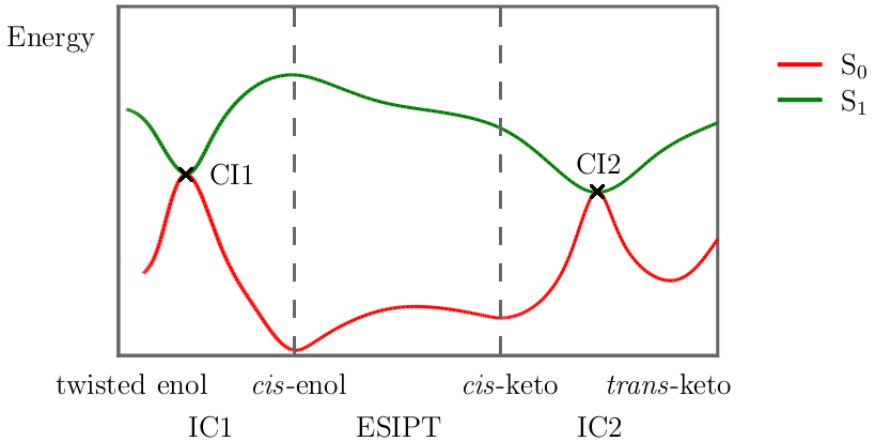

In the solid state, the ability of anils to undergo *cis*-enol to *trans*-keto photoisomerisation depends on the packing of the molecules within the crystal lattice. Extensive crystallographic studies[4,9,12] have shown that in order for an anil crystal to be photochromic, the lattice must be relatively uncrowded, while the constituent molecules must exist in a non-planar conformation and must not engage in intermolecular $\pi \cdots \pi$ interactions. Conversely, tightly-packed structures which exhibit π-stacking are not photochromic. In the case of some non-photochromic structures, the inability of molecules to undergo photoisomerisation can be ascribed to specific close contacts within the crystal lattice.[12]

The crystal structure of the *trans*-keto product of the anil photoisomerisation reaction was obtained for the first time by Harada *et al.*,[5] who also proposed a reaction mechanism (shown schematically in Figure 4.4 on the following page on the example of *N*-salicylidene-2-chloroaniline, which from now on will be abbreviated to SCA) to explain the formation of the *trans*-keto isomer within the confined environment of the crystal lattice. According to this mechanism, following the initial photoexcitation and the subsequent ESIPT step, the *cis*-keto form is converted into the *trans*-keto form through a simultaneous torsion around the C2-N1 and C3-C4 bonds. This torsional motion is often called a "pedal"

Figure 4.4: The solid-state *cis*-enol to *trans*-keto photoisomerisation mechanism of anils proposed by Harada *et al.*,[5] shown on the example of SCA.

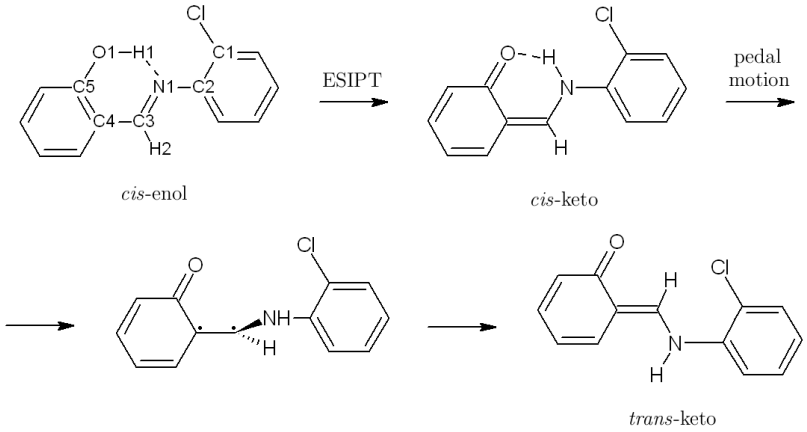

motion, due to its resemblance to the rotating pedals of a bicycle. The argument in favour of this mechanism is that the pedal motion requires less space within the crystal lattice than would be needed by a simple rotation of the salicylidene ring around the C3-C4 bond. The difference in the mechanistic course of the anil photoisomerisation reaction in the isolated molecule and in the solid state provides an example of the directing influence of the bulk crystal structure on the reactivity of the individual component molecules, an effect that is also characteristic of many other photochemical reactions occurring in molecular crystals.[17–20] This, together with the potential technological applications of some anil crystals as optical materials,[21–23] makes this solid-state photoisomerisation reaction an interesting and important subject for theoretical study. In what follows, we describe the choice of the model compound under study in the present work and its crystal structure, before turning our attention to the QM/QM hybrid method that was employed to describe its dynamics.

4.2. Model system

We concerned ourselves with the photochromic polymorph of SCA whose crystal structure was reported by Bregman *et al*,[24] and which has previously been presented as an example of a structure in which the photoisomerisation reaction is permitted by the packing of molecules.[8] Our choice was also motivated in part by the fact that it is one of the smallest anil molecules, with only a single substituent, which is an important consideration because of the steep scaling with system size

Figure 4.5: Crystal structure of SCA obtained at room temperature. The compound crystallises in the orthorhombic space group $P2_12_12_1$ with one molecule in the asymmetric unit. $a = 13.528$ Å, $b = 12.185$ Å, $c = 6.871$ Å, $Z = 4$.

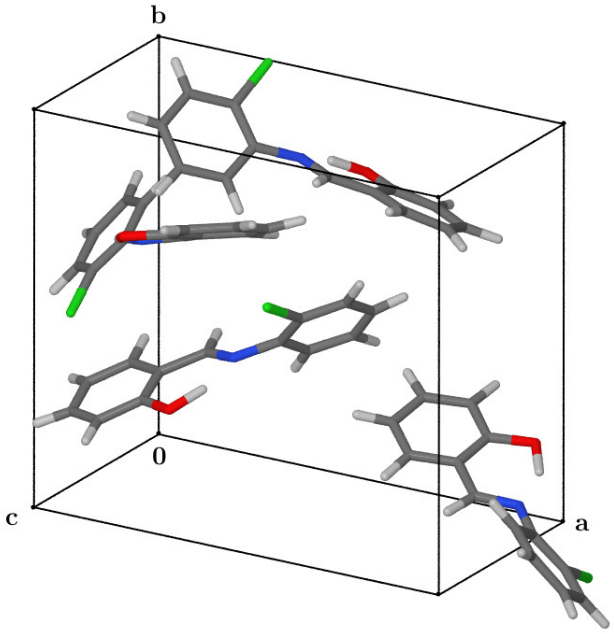

of *ab initio* methods for the description of excited states.

The crystal structure of the photochromic polymorph of SCA is presented in Figure 4.5 above, where it can be seen that the crystal packing does not feature π-stacking interactions between molecules. In the individual molecules, the chlorophenyl aromatic ring is twisted relative to the plane of the salicylidene ring. A least-squares mean plane was fitted to the carbon atoms comprising the chlorophenyl ring, and another to the carbon atoms comprising the salicylidene ring, within the computer program Mercury 3.0.[25] The two planes form a dihedral angle of 51.4°, which lies in the range of dihedral angle values from around 30° to around 50° that is typical of photochromic anils.[12] In order to further assess the crystal packing of SCA, we have carried out a Voronoi-Dirichlet tesselation[26] of the crystal structure using the computer program TOPOS 4.0.[27] This process assigns to each atom (which in this context is considered to be a point positioned at the nucleus) a Voronoi-Dirichlet polyhedron (VDP) that contains all points whose distance to that atom is not greater than the distance to any other atom. In this manner, space is partitioned completely and disjointly into VDPs associated with individual atoms. (The partitioning is not disjoint in the rigorous sense,

Figure 4.6: Atomic VDPs of an SCA molecule in the crystal lattice. Above each view of the VDPs, the SCA molecule is displayed to scale and in the same orientation.

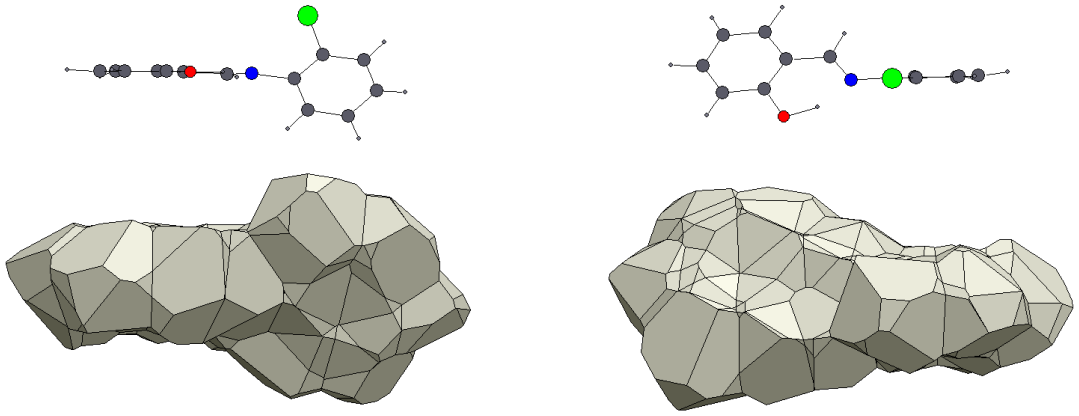

because the surface of each polyhedron is shared with the neighbouring polyhedra, but this fine point can be ignored here.) The VDP of an atom may be roughly interpreted as the region of space taken up by the atom and, by extension, the union of VPDs of atoms comprising a molecule may be regarded as the region of space belonging to that molecule. We must bear in mind, however, that although the Voronoi- Dirichlet tesselation provides a convenient means to analyse the molecular packing, the VDPs are purely geometric constructs that do not reflect the electron density in a crystal, and it would therefore be meaningless to use them to analyse system properties other than the spatial arrangement of atoms.

In Figure 4.6 above, we show two views of the union of atomic VDPs belonging to a single SCA molecule in the crystal lattice. It can be seen that the union of VDPs follows the shape of the molecule quite closely, consisting of two disk-like parts, which correspond to the two aromatic rings, joined at the edge. In particular, no significant bulge or protuberance is visible above or below the aromatic rings, indicating that the crystal structure contains no large voids on either side of the rings. This, in turn, suggests that a photoisomerisation mechanism involving a simple rotation around the C3-C4 bond, as predicted for the isolated anil molecules,[16] is obstructed by intermolecular steric interactions, whereas the mechanism of Harada *et al.*,[5] in which the two aromatic rings are less strongly displaced from their original positions, seems likely to be able to proceed with less steric hindrance.

4.3. Computational methods

4.3.1. Outline of simulation scheme

In the present section we provide a synopsis of the computational scheme that was used to study the photochemical reactions in the SCA crystal.

1. Firstly, geometries of the *cis*-enol, *cis*-keto and *trans*-keto isomers of the isolated SCA molecule were optimised at the DFT level of theory, and $S_0 \rightarrow S_1$ excitation energies were calculated using the TD-DFT method.

2. A $1 \times 1 \times 2$ supercell of the photochromic SCA polymorph, representing the bulk lattice, was thoroughly equilibrated by means of molecular dynamics (MD) simulation in the canonical ensemble on the ground-state potential energy surface.

3. Following equilibration, phase space points (i.e., sets of atomic coordinates and velocities) were sampled from the dynamics of the system at time intervals of 0.5 ps.

4. For each selected phase space point, photoexcitation to the S_1 state of a single molecule of SCA embedded within the crystal lattice was modelled by taking the system from the ground-state DFT potential energy surface to a hybrid QM/QM excited-state potential energy surface, in which the photoexcited molecule is treated using the TD-DFT method while the remaining molecules are described using ground-state DFT.

5. From each starting point generated in this manner, MD was propagated in the microcanonical ensemble on the hybrid QM/QM potential energy surface, thereby constituting a simulation of the photochemical reaction in the SCA crystal. The progress and outcome of the simulated trajectories was characterised by following several structural parameters, such as the proton transfer coordinate, the oxygen-nitrogen distance and the relevant torsion angles of the reactive molecule.

6. In order to test the correctness and accuracy of the TD-DFT method at predicting the S_1 potential energy surface of the SCA molecule, geometries of the photoexcited molecule were extracted from two representative system trajectories, and their energies were recalculated at the second-order approximate coupled cluster singles and doubles method (CC2) level of theory.

7. Having found that the simulated trajectories on the hybrid QM/QM potential energy surface show that the *cis*-enol to *trans*-keto isomerisation reaction in the SCA crystal proceeds through a mechanism involving the pedal motion, the same methodology was applied in order to model the reverse reaction. A $1 \times 1 \times 2$ supercell of the photochromic polymorph was constructed with a single molecule in the *trans*-keto form and the remaining seven molecules in the *cis*-enol form, and the photochemical reaction of the *trans*-keto molecule was simulated by repeating steps **2** to **6** for that system.

The various components of the simulation are described in detail in the following subsections.

4.3.2. Construction of the simulated system

In the photoisomerisation reaction of anils in the solid state, the *trans*-keto isomer does not appear as a separate phase, but instead the *trans*-keto molecules are distributed in the lattice of unreacted *cis*-enol molecules in a disordered fashion.[5,8] As a result, in the case that only a small fraction of molecules undergo photoisomerisation, as is typical under experimental conditions, most reactive molecules are surrounded by nonreactive molecules. In order to reproduce these circumstances in the present theoretical study, simulations of the *cis*-enol to *trans*-keto photoisomerisation (which which we will henceforth call the forward reaction) were carried out in the $1 \times 1 \times 2$ supercell of the photochromic polymorph containing eight *cis*-enol molecules, of which only one was photoexcited. As the eight molecules contained in the supercell are related by symmetry, and therefore start off as equivalent, it does not matter which molecule we select as the photoexcited molecule. In Figure 4.7(a), we present the simulated system with the arbitrarily chosen photoexcited molecule drawn in blue. As in Chapter 1, we will denote the entire simulated system, comprising the photoexcited molecule and the seven nonreactive molecules which represent the surrounding bulk lattice, as **S**, while the photoexcited molecule alone will be referred to as **C**.

Likewise, simulations of the *trans*-keto to *cis*-enol photoisomerisation (the reverse reaction) were also carried out in a $1 \times 1 \times 2$ supercell of the photochromic polymorph, but with one molecule converted into the *trans*-keto isomer. In the experimentally determined structure of the *trans*-keto tautomer of *N*-3,5-di-tert-butylsalicylidene-3-nitroaniline embedded in a lattice consisting

predominantly of *cis*-enol molecules, the *trans*-keto molecule is positioned very similarly to the original *cis*-enol molecule.[5] Hence, the procedure applied in order to "dock" the *trans*-keto molecule into the supercell was as follows. One molecule in the experimental crystal structure was converted from the *cis*-enol into the *trans*-keto form by manually moving the atoms H1, H2, C3 and N1 while preserving the position of the two aromatic rings. The structure obtained in this way was subsequently optimised at the periodic DFT level of theory (see Section 4.3.3.2 of the present Chapter for a detailed description of the parameters of the DFT calculation). The default BFGS optimisation algorithm was applied, with the following convergence criteria: energy tolerance 2.0×10^{-5} eV/atom, maximum force tolerance 5.0×10^{-2} eV/Å, displacement tolerance 1.0×10^{-3} Å. The resulting minimum-energy geometry of the $1 \times 1 \times 2$ supercell containing one *trans*-keto molecule is illustrated in Figure 4.7(b).

Although this is not readily apparent in Figure 4.7, the photoexcited molecule within the $1 \times 1 \times 2$ supercell of the photochromic polymorph of SCA is separated from periodic images of itself by nonreactive ground-state molecules. Namely, the shortest distance between the nuclei of the photoexcited molecule and its periodic images is fairly long, at around 6.3 Å. We therefore believe that $1 \times 1 \times 2$ supercell is large enough so as not to introduce periodic boundary conditions artefacts into the behaviour of the photoexcited molecule.

In the case of *N*-3,5-di-*tert*-butylsalicylidene-3-nitroaniline, the conversion of around 10% of the starting material into the *trans*-keto form resulted in only slight changes in the unit cell dimensions and very slight cell volume expansion (around 0.5%).[5] Therefore, as a simplifying approximation, the dimensions of the simulated $1 \times 1 \times 2$ supercell were taken from the experimental structure[24] and were kept fixed throughout all MD simulations.

Figure 4.7: Construction of the simulated system in the hybrid QM/QM simulations. S denotes the entire system while the photoexcited molecule, drawn in blue, is labelled C.

(a) The $1\times1\times2$ supercell of the photochromic polymorph of SCA used in the MD simulations of the forward reaction, shown at the geometry derived from experiment.[24]

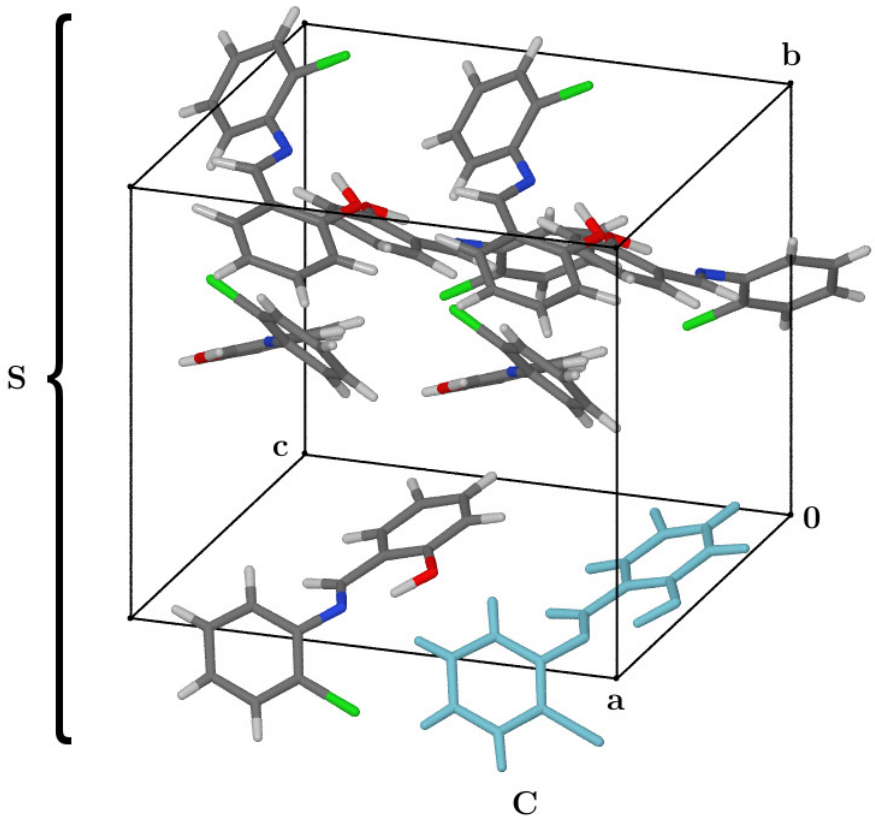

(b) The 1×1×2 supercell containing a single *trans*-keto molecule, used in the MD simulations of the reverse reaction, optimised at the DFT level of theory.

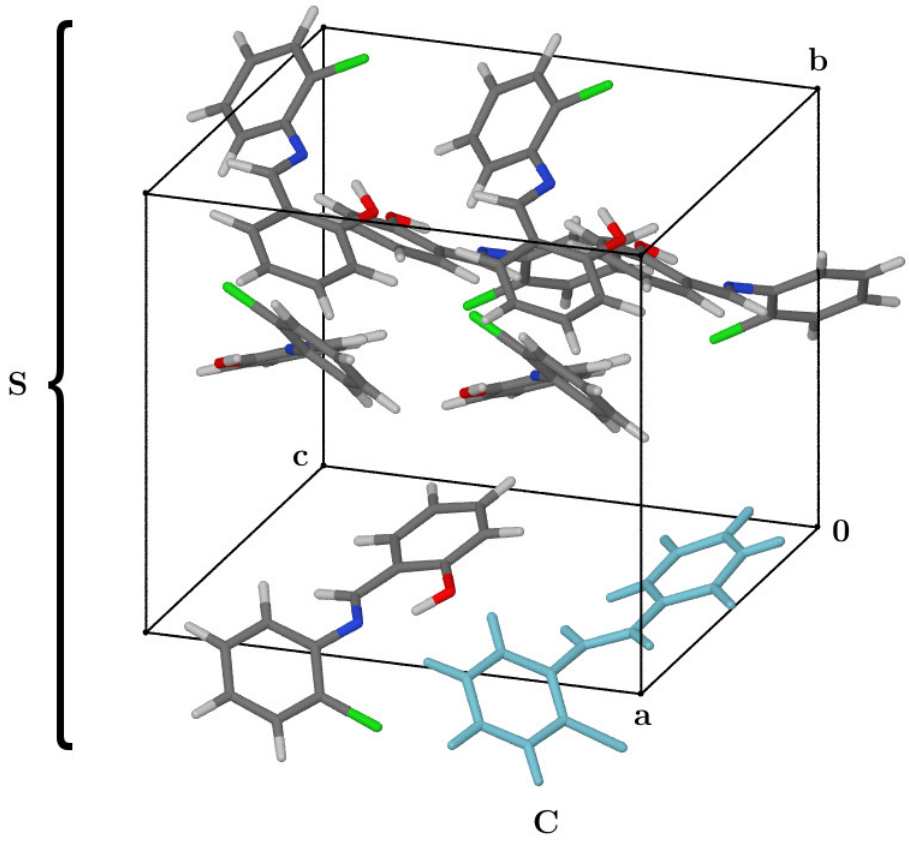

4.3.3. Simulation setup

4.3.3.1. Isolated-molecule calculations

Geometry optimisations of the *cis*-enol, *cis*-keto and *trans*-keto isomers of the isolated SCA molecule were carried out at the DFT level of theory using the PBE0[29] exchange-correlation functional coupled with the 6-31G(d,p) basis set as implemented in the computational chemistry software package Gaussian 09.[30] Vertical $S_0 \rightarrow S_1$ excitation energies were calculated at the optimised geometries using the TD-DFT method. The same level of theory was applied in the calculation of the term $E^{\mathrm{GTO}}_{\text{TD-DFT}}(\mathbf{C})$ in the TD-DFT/DFT simulations.

Our choice of the TD-DFT method for the treatment of the S_1 state of the photoexcited SCA molecule was motivated by the fact that it has previously been demonstrated to predict the topology of the potential energy surface of that state in good agreement with the multireference CASPT2 method,[16] as well as its superior computational efficiency as compared with wavefunction-based excited-state methods. A more in-depth analysis of the applicability of the TD-DFT method to describe the S_1 state is given later on in Section 4.3.4.

4.3.3.2. Solid-state calculations

In the equilibration of the SCA $1 \times 1 \times 2$ supercell in the ground electronic state, the potential energy of the system was evaluated using the exchange-correlation functional of Perdew, Burke and Ernzerhof[31] (the PBE functional) as implemented in the software package CASTEP Academic Release version 5.501.[32] The plane-wave cutoff was set to 450 eV. The electronic Brillouin zone was sampled by using a Monkhorst-Pack k-point grid with a k-point spacing of at most 0.1 Å^{-1}, achieved using a single k-point at the Γ-point (0 0 0). The default ultrasoft pseudopotentials were used.[33] Energies and forces were corrected for dispersion interactions using the semiempirical scheme of Grimme.[34] The SCF convergence threshold was set to 1.0×10^{-7} eV. The same level of theory was applied in the evaluation of the term $E^{\mathrm{PW}}_{\text{DFT}}(\mathbf{S})$ in the TD-DFT/DFT simulations.

When calculating the term $E^{\mathrm{PW}}_{\text{DFT}}(\mathbf{C})$ in the hybrid TD-DFT simulations, the reactive molecule was placed in a cubic cell of edge length 20 Å, which was found to be large enough that the total energy did not change significantly on increasing the cell size further. The electronic Brillouin zone was sampled at

the Γ-point only. The remaining calculation parameters were identical as in the evaluation of the term $E_{\mathrm{DFT}}^{\mathrm{PW}}(\mathbf{S})$.

Lastly, the term $E_{\mathrm{DFT}}^{\mathrm{PW}}(\mathbf{S})$ was evaluated using the TD-DFT method implemented within Gaussian 09[30] at the PBE0/6-31G(d,p) level of theory, with the reactive molecule **C** in the S_1 electronic state.

The system was equilibrated by propagating Born-Oppenheimer molecular dynamics in the canonical (NVT) ensemble for 4 ps, following which a production run was carried out, which lasted 7.5 ps and 3.5 ps for the supercells used in the simulations of the forward and reverse reactions, respectively. Throughout the equilibration and production periods, the temperature was maintained at 280 K using a chain of five Nosé-Hoover thermostats with a relaxation time of $\tau = 1$ ps. A time step of 0.5 fs was used throughout the equilibration and production periods. Phase space points were collected from the production run at intervals of 0.5 ps starting from $t = 4$ ps to serve as starting points for the hybrid QM/QM simulations of the photochemical reaction, for a total of sixteen and eight starting points for the simulations of the forward and reverse reactions, respectively. From each of these starting points, $textBorn - Oppenheimer$ molecular dynamics in the microcanonical (NVE) ensemble was propagated on the hybrid TD-DFT/DFT potential energy surface defined by equation 1.23 from Chapter 1, with the photoexcited molecule in the S_1 electronic state. Newton's equations of motion were integrated using the Velocity Verlet scheme with a time step of 0.5 fs.

On the grounds that previous studies of the ESIPT reaction in the structurally related molecule 2-(2'-hydroxyphenyl)benzothiazole[35,36] have characterised the proton transfer as a ballistic motion of the wave packet, with no significant involvement of proton tunneling, we believe the treatment of the shuttling proton as a classical point particle does not introduce large errors into our simulations of the photochromic polymorph of SCA. The system dynamics was propagated until the photoexcited molecule reached an S_1/S_0 conical intersection, which occurred in every simulated trajectory.

4.3.4. Assessment of the accuracy of the TD-DFT method

As described in Section C.6 of Appendix C, methods such as DFT and TD-DFT are incapable of providing a qualitatively correct description of a

potential energy surface near a conical intersection, where there is strong non-dynamical electron correlation. Their usage may therefore generate simulation artefacts when the photoexcited molecule approaches a conical intersection, as happens in the photochemical reaction of SCA. Moreover, by analogy with the photochemical reactions of the molecules 2-(2'-hydroxyphenyl)benzothiazole[37] and 7-(2'-pyridyl)indole),[38] in both of which the ESIPT reaction is followed by a mutual twist of two aromatic rings, we may expect that during the torsional motions through which the SCA molecule reaches an S_1/S_0 conical intersection, the molecule adopts a strong biradicaloid character. The DFT and TD-DFT methods may also incorrectly predict the charge distribution of a biradicaloid state, which represents another potential source of error in the hybrid TD-DFT/DFT simulations. These factors necessitate a critical evaluation of the ability of the TD-DFT method to describe the photoechemical reaction of SCA.

Fortunately, Ortiz-Sánchez and coworkers[16] have provided evidence that the TD-DFT method provides a qualitatively correct description of the S_1 potential energy surface surface of the *N*-salicylideneaniline (SA) molecule. In the work just cited, the TD-DFT method was found to predict the existence of two S_1/S_0 conical intersections (CI1 and CI2; see Figure 4.3 for the location of these conical intersections on the potential energy surface) involved in the isolated-molecule reaction mechanism, in the sense that near the conical intersection geometries, the energy gap between the S_0 and S_1 states becomes very small. Both these conical intersections were subsequently confirmed to exist, at geometries similar to the TD-DFT-derived geometries, at the multireference second-order perturbation method (CASPT2) level of theory, which includes both dynamical and non-dynamical electron correlation. Therefore, insofar as the results obtained for SA can be extrapolated to its derivative SCA, we believe that the use of the TD-DFT method to describe the S_1 state of the SCA molecule is unlikely to lead to simulation artefacts such as spurious conical intersections.

Nevertheless, despite the demonstrated ability of the TD-DFT method to predict the existence and rough location of the relevant conical intersections of the SA molecule, we took effort to further assess the ability of the TD-DFT to describe the S_1 state of SCA. In order to achieve this, geometries of the photoexcited molecule were extracted from three representative MD trajectories generated on the TD-DFT/DFT potential energy surface (see Sections 4.2.1, 4.2.2 and 4.2.3 for a full discussion of the three selected trajectories). The energies of the ground

and excited states of the photoexcited molecule were subsequently calculated at the second-order approximate coupled-cluster (CC2) level of theory and compared with those computed using the TD-DFT method, which constitutes a *post factum* assessment of the performance of the TD-DFT method employed in the TD-DFT/DFT simulations. While the CC2 method itself, being a single-reference method, does not include non-dynamical electron correlation, in studies of ESIPT systems where it was benchmarked against multiconfigurational methods the CC2 method was found to correctly locate the relevant conical intersections, in that the energy gaps between the S_0 and S_1 states became small in the conical intersection regions.[37,39] The CC2 method is therefore not to be treated as an exact benchmark for the TD-DFT method, but rather it is meant to help identify a possible failure of TD-DFT to correctly describe the S_1 state. We may expect that any strong discrepancy between energies of the S_1 state between the TD-DFT and CC2 methods would indicate that either or both of these methods is yielding inaccurate results.

We remark here that instead of the CC2 method, it clearly would have been more appropriate to use a multireference method, such as CASPT2, to serve as a benchmark for the TD-DFT calculations. However, it is likely that a very extensive active space (larger than ten electrons in ten orbitals) would be necessary to provide an accurate description of the entire potential energy surface of the SA molecule.[16] In the present work, the energy of the photoexcited molecule is calculated along TD-DFT/DFT trajectories in which the photoexcited molecule undergoes large structural changes, thus exploring a sizeable area of the potential energy surface, and therefore due to computational limitations, we did not attempt to apply a multireference method.

The energy of the S_0 state of the reactive SCA molecule were calculated through single-point calculations at the (frozen-core) CC2[40] level of theory as implemented in the open-source computational chemistry software package PSI3.[41] A restricted Hartree-Fock determinant was used as the reference determinant, and the CC2 correlation energy was converged to a tolerance of 1.0×10^{-7} eV. The energy of the S_1 state was subsequently obtained through an equations-of-motion CC2 (EOM-CC2) calculation, whereby the excitation energy was also converged to a tolerance of 1.0×10^{-7} eV. The 6-31G(d) basis set was utilised. Such single-point CC2 calculations were performed along three representative trajectories on the TD-DFT/DFT potential energy surface at intervals of 10 fs, except during the

final 50 fs of each trajectory, when the single-point calculations were performed at intervals of 5 fs. The T_1 diagnostic was monitored along each of three these trajectories, thus providing a measure of the significance of non-dynamical electron correlation in the ground-state of the reactive molecule.

Additionally, in order to ensure that the EOM-CC2 procedure had indeed converged to the S_1 state, and to inspect for possible intersections between the S_1 and S_2 states, in each calculation the S_2 state was also computed. However, no S_2/S_1 conical intersection was found for any of the three trajectories under consideration.

4.4. Results and Discussion

4.4.1. Energy minima of the isolated molecule

Geometries of the *cis*-enol, *cis*-keto and *trans*-keto isomers of SCA optimised at the PBE0/6-31G(d,p) level of theory are shown in Figure 4.8(a), (b) and (c), respectively. In order to be able to monitor the conformational changes of the reactive molecule during simulations on the TD-DFT/DFT potential energy surface, we followed the four torsion angles ϕ(N1-C3-C4-C5), ϕ(C2-N1-C3-C4), ϕ(H2-C3-C4-C5) and ϕ(C1-C2-N1-C3) (see Figure 4.8(a) for atom numbering). The ground-state potential energies, $S_0 \rightarrow S_1$ vertical excitation energies calculated using the TD-DFT method, and values of the four torsion angles which describe the molecular conformation of the isomers of SCA are given in Table 4.1.

As can be read from Table 4.1, the *cis*-enol isomer is the lowest in energy, followed by the *cis*-keto, while the *trans*-keto is much higher in energy. In all three isomers, the hydroxyphenyl moiety and the atoms C2, N1, C3 lie roughly on the same plane, whereas the chlorophenyl moiety is twisted relative to that plane.

Figure 4.8: Equilibrium geometries of the isolated ground-state SCA molecule. Selected distances are given in units of Å.

(a) *cis*-enol form

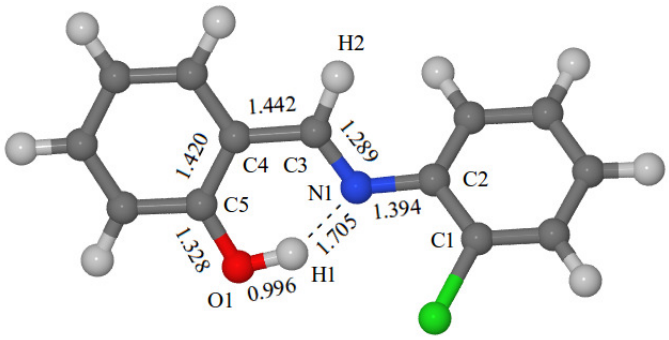

(b) *cis*-keto form

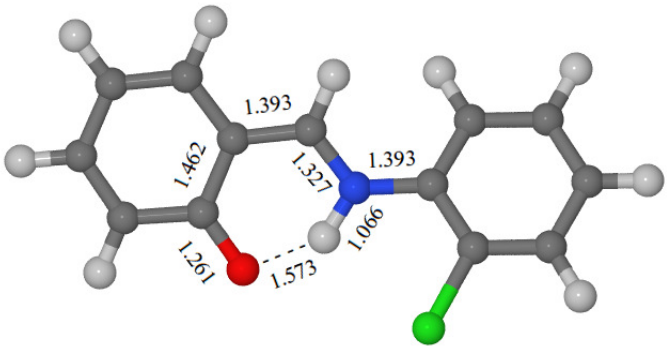

(c) *trans*-keto form

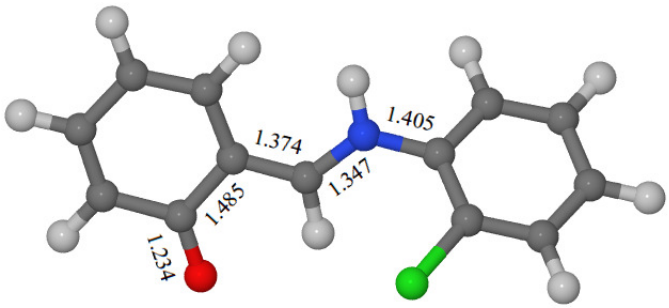

Table 4.1: Summary of geometry optimisations for isomers of the isolated SCA molecule. (See Figure 4.8(a) for atom numbering.)

Conformer:	*cis*-enol	*cis*-keto	*trans*-keto
$E(\mathrm{S}_0)$, eV [a]	0	0.253	0.905
$E(\mathrm{S}_1) - E(\mathrm{S}_0)$, eV	3.70	3.12	2.96
ϕ(N1-C3-C4-C5), °	0.7	−0.2	−176.4
ϕ(C2-N1-C3-C4), °	177.0	177.2	179.7
ϕ(H2-C3-C4-C5), °	−178.3	−178.9	2.1
ϕ(C1-C2-N1-C3), °	144.6	157.5	48.4

[a] the ground-state potential energy values are given relative to the *cis*-enol isomer and include zero-point vibrational energy.

4.4.2. Photochemical reactions of *N*-salicylidene-2-chloroaniline

The mechanistic course of the photochemical reactions in the SCA crystal was followed with the use of several structural parameters whose definitions we will now present. The proton transfer reaction was monitored through the O1-H1 and N1-H1 distances, and proton transfer was considered to have occurred at the point when these distances became equal. Although in principle it is possible for the shuttling proton to undergo back transfer from nitrogen N1 to oxygen O1, and hence cross through R(O1-H1) = R(N1-H1) more than once, this did not happen in any of the simulated trajectories. Additionally, throughout each simulated trajectory we kept track of the proton donor-acceptor distance, R(O1-N1). The skeletal deformations of the reactive SCA molecule were monitored by following the four torsion angles which have already been defined in Section 4.1.

In order to detect when the system approaches a conical intersection between the ground- and excited-state potential energy surfaces, throughout each trajectory we also followed the ground-state potential energy of the system, which is defined by:

$$E(\mathrm{S}_0) = E^{\mathrm{PW}}_{\mathrm{DFT}}(\mathbf{S}) + E^{\mathrm{GTO}}_{\mathrm{DFT}}(\mathbf{C}) - E^{\mathrm{PW}}_{\mathrm{DFT}}(\mathbf{C})$$

where $E^{\mathrm{GTO}}_{\mathrm{DFT}}(\mathbf{C})$ stands for the ground-state potential energy of the photoexcited molecule, calculated at the PBE0/6-31G(d,p) level of theory. The system was considered to have reached an $\mathrm{S}_1/\mathrm{S}_0$ CI when the potential energy gap between the excited and ground states, $\Delta E = E(\mathrm{S}_1) - E(\mathrm{S}_0) = E^{\mathrm{GTO}}_{\mathrm{TD\text{-}DFT}}(\mathbf{C}) - E^{\mathrm{GTO}}_{\mathrm{DFT}}(\mathbf{C})$, decreased to below the arbitrarily chosen threshold of 0.1 eV. Because of the

inability of the TD-DFT method to provide a correct description of the conical intersection region, the simulation was discontinued once the system reached an S_1/S_0 CI, which occurred in every simulated trajectory.

We begin by considering the mechanism of the forward reaction. As will be explained in Sections 4.2.1 and 4.2.2, where two representative trajectories are discussed in detail, the MD trajectories generated on the TD-DFT/DFT potential energy surface revealed two distinct reaction pathways of the photoexcited *cis*-enol molecule. In the first pathway, the molecule undergoes the ESIPT reaction and subsequently reaches an S_1/S_0 conical intersection through a pedal motion of the type predicted by Harada *et al.*[5] The conical intersection reached in the first reaction pathway will from now on be denoted by CIP (short for conical intersection-pedal motion). In the second pathway, the reactive molecule reaches another conical intersection, whose geometry is similar in many respects to the conical intersection CI1 predicted to be involved[16] in the isolated-molecule reaction mechanism.

The results of all sixteen simulated trajectories of the forward reaction are reviewed in Table 4.2 on the next page. Proton transfer occurred in seven trajectories within an average of 25 fs of the initial photoexcitation. Following proton transfer, in each of these trajectories the photoexcited molecule persisted in the *cis*-keto form for a period of time, before reaching CIP on average 420 fs after the initial photoexcitation. In the remaining nine trajectories, proton transfer did not take place, and instead the photoexcited molecule reached CI1 on average 110 fs after the initial photoexcitation. From the fact that CI1 is reached very rapidly, we may deduce that this conical intersection is accessible with little or no potential energy barrier. On the other hand, judging from the fact that following the ESIPT reaction, the molecule always persisted in the *cis*-keto form for a few hundred femtoseconds before undergoing the pedal motion, there probably exists a low potential barrier separating the photoexcited *cis*-keto form from CIP.

Of the eight simulated trajectories of the reverse reaction, which we number $1'$ to $8'$, two did not reach a conical intersection within a time limit of 1.5 ps, and these simulations were therefore discontinued due to computational time concerns. In each of the remaining six trajectories, the reactive molecule which was initially in the *trans*-keto form reached an S_1/S_0 conical intersection by undergoing a pedal motion. Interestingly, this pedal motion was not simply a reversal of the

Table 4.2: Results of simulated trajectories of the forward reaction.

Trajectory	Outcome [a]	t_{PT}, fs [b]	t_{CI1}, fs [b]	t_{CIP}, fs [b]	$\Delta E(t=0)$, eV [c]
1	PT, CIP	24.5	-	313.5	3.636
2	PT, CIP	64.5	-	398.0	3.380
3	CI1	-	120.0	-	3.699
4	PT, CIP	33.0	-	349.0	3.645
5	PT, CIP	10.0	-	589.5	3.351
6	CI1	-	88.0	-	3.307
7	PT, CIP	19.5	-	327.0	3.431
8	CI1	-	88.5	-	3.448
9	CI1	-	120.0	-	3.634
10	CI1	-	105.5	-	3.778
11	PT, CIP	24.5	-	570.0	3.586
12	CI1	-	119.0	-	3.323
13	CI1	-	76.5	-	3.466
14	PT, CIP	5.0	-	361.5	3.347
15	CI1	-	160.5	-	3.424
16	CI1	-	110.0	-	3.558

[a] PT, CI1 and CIP stand for "proton transfer", "reached CI1" and "reached CIP", respectively.
[b] t_{PT} , t_{CI1} and t_{CIP} are respectively the time at which proton transfer took place and the time at which the photoexcited molecule reached CI1 and CIP, where $t = 0$ corresponds to the photoexcitation time.
[c] $\Delta E(t = 0)$ is the energy gap between the ground state and the first singlet excited state at $t = 0$.

pedal motion involved in the forward reaction, but rather proceeded in the same direction as the one involved in the forward reaction. (To use the analogy with the pedals of a bicycle, if the forward reaction is a half-turn of the pedals, then the reverse reaction is another half-turn in the same direction, and not a half-turn in the opposite direction.) In order to distinguish it from the conical intersection geometry CIP reached in some of the trajectories of the forward reaction, we will call the S_1/S_0 conical intersection reached in the trajectories of the reverse reaction CIP′.

Table 4.3 on the next page summarises the results of the simulated trajectories of the reverse reaction. The lower bound for the average time taken by the system to reach CIP′ was calculated as 980 ps.

Table 4.3: Results of simulated trajectories of the reverse reaction.

Trajectory	Outcome [a]	$t_{\mathrm{CIP}'}$, fs [b]	$\Delta E(t=0)$, eV [c]
$1'$	CIP$'$	380.5	2.769
$2'$	CIP$'$	1117.5	2.671
$3'$	CIP$'$	591.0	2.562
$4'$	CIP$'$	665.5	2.958
$5'$	-	-	2.653
$6'$	CIP$'$	829.0	2.701
$7'$	-	-	2.916
$8'$	CIP$'$	1299.0	2.811

[a] CIP$'$ stands for "reached CIP$'$". A dash (-) means that the trajectory did not reach an S_1/S_0 conical intersection within the maximum simulation time of 1.5 ps.
[b] $t_{\mathrm{CIP}'}$ is the time at which the photoexcited molecule reached CIP$'$, where $t = 0$ corresponds to the photoexcitation time.
[c] $\Delta E(t = 0)$ is the energy gap between the ground state and the first singlet excited state at $t = 0$.

In what follows, we examine representative trajectories of the forward reaction, of which one reached CIP and the other CI1, and a single trajectory of the reverse reaction, which reached CIP$'$. To accompany this narrative, in the Electronic Supplement we have provided MPEG animations of these three trajectories, as well as an additional two trajectories that we do not discuss in the text.

4.4.2.1. Trajectory 1 of the forward reaction

In trajectory 1, following ESIPT $t = 24.5$ fs, the reactive molecule underwent a pedal motion conformational change and reached CIP at $t = 313.5$ fs, at which point the simulation was terminated.

In Figure 4.9(a) on the next page, the ESIPT reaction is analysed by projecting the initial 100 fs of trajectory 1 onto a three-dimensional plot of energy, the proton transfer coordinate defined by $R(\text{O1-H1}) - R(\text{N1-H1})$, and the proton donor-acceptor distance coordinate given by $R(\text{O1-N1})$. The energies of both the S_0 and S_1 states are plotted, showing how the energy gap between these two states decreases from 3.636 eV at $t = 0$ to 1.759 eV at $t = 100$ fs.

The projection can be partitioned into segments which correspond to specific events that occur during the initial 100 fs of trajectory 1; these are marked as *a* to *d*. Point *a* is the point at which the initial photoexcitation occurred, and it corresponds to the reactive molecule existing in the *cis*-enol form. Segment *b* is roughly parallel to the proton donor-acceptor distance coordinate, $R(\text{O1-N1})$, and corresponds to a shortening of the distance between the two oxygen and nitrogen atoms before the proton transfer step. The next segment *c*, largely parallel to the proton transfer coordinate, is the proton transfer step which converts the photoexcited molecule from the *cis*-enol to the *cis*-keto form. Further along the trajectory, segment *d* marks the beginning of the period when the molecule persists in the *cis*-keto form, which lasts until around $t = 250$ fs. The proton transfer event is also visible as a crossing of the curves $R(\text{O1-H1})$ and $R(\text{N1-H1})$ in Figure 4.9(b), which describes the variation in the distances O1-H1, N1-H1 and O1-N1 over the entire trajectory 1.

Figure 4.9(c), in turn, shows the time-evolution of the four torsion angles which describe the molecular conformation. In this plot the period of time from $t = 0$ to around 250 fs is largely uneventful, exhibiting some small-amplitude oscillations of the four torsion angles but no marked structural change. At around $t = 250$ fs, however, the torsion angles $\phi(\text{N1-C3-C4-C5})$, $\phi(\text{H2-C3-C4-C5})$ and $\phi(\text{C1-C2-N1-C3})$ simultaneously began to change more rapidly in a manner suggesting a concerted twist around the C2-N1 and C3-C4 bonds. This continued until the molecule reached an S_1/S_0 conical intersection at $t = 313.5$ fs.

Figure 4.9: Trajectory 1.

(a) Projection of the initial 100 fs of trajectory 1 onto energy, the proton transfer $(R(\text{O1-H1}) - R(\text{N1-H1}))$ and proton donor-acceptor $(R(\text{O1-N1}))$ distance coordinates. Label a indicates the starting point of trajectory 1. Line segment b corresponds to the shortening of the nitrogen-oxygen distance which precedes the ESIPT step. Line segment c is the ESIPT step, and finally segment d is the subsequent elongation of the nitrogen-oxygen distance. The zero of the energy scale corresponds to the ground-state energy at the starting point of the trajectory.

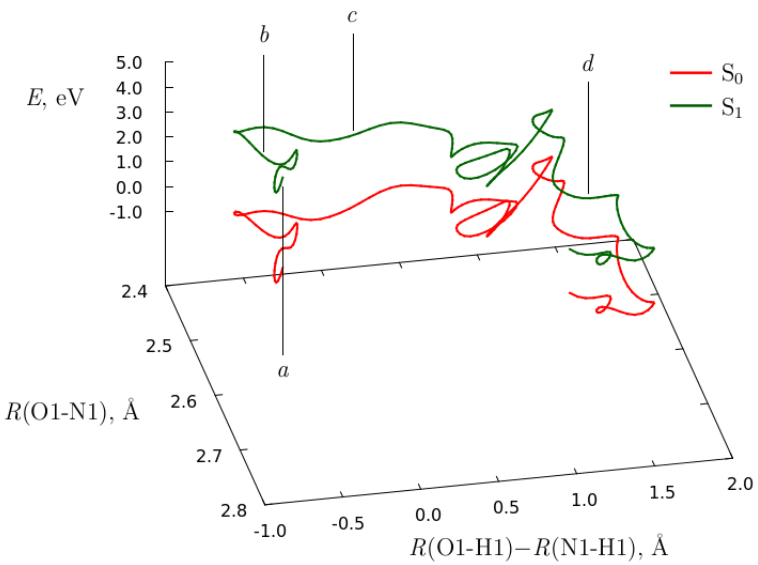

(b) Time-evolution of the O1-H1, N1-H1 and O1-N1 distances.

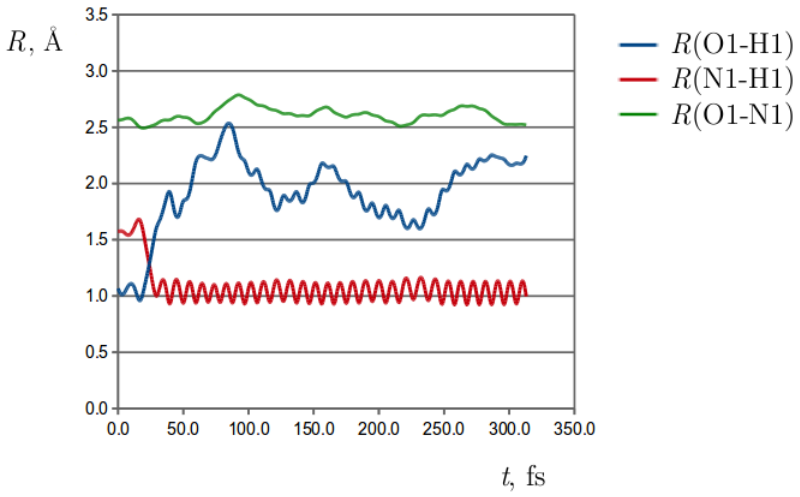

(c) Time-evolution of the four torsion angles which describe the molecular conformation.

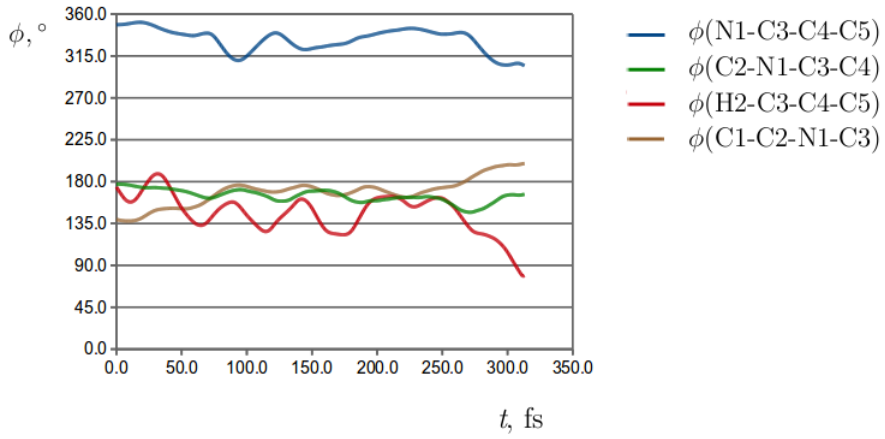

We now turn our attention to the geometry of the system as it reached that conical intersection, which is overlaid on the experimental crystal structure of SCA in Figure 4.10. The salicylidene ring of the photoexcited molecule can be seen to have significantly rotated in its own plane, while the chlorophenyl ring is very close to its crystallographic position. The positions of carbon C3 and nitrogen N1 indicate that the photoexcited molecule is in the process of what can confidently be described as a pedal motion, with C3 being located above its crystallographic position while N1 is beneath its crystallographic position (here, 'above' and 'below' refer, of course, to the orientation of the system as illustrated in Figure 4.10).

From Figure 4.10 we observe that the surrounding ground-state molecules are all fairly close to their crystallographic positions, which suggests that it is not necessary for the surrounding molecules to become displaced away from the photoexcited molecule in order to make room for the pedal motion.

Through a survey of the other simulated trajectories, it was found that in all trajectories in which the photoexcited molecule underwent proton transfer, it subsequently reached an S_1/S_0 conical intersection through a twisting motion similar to the one that took place in trajectory 1. In each case, carbon C3 moved upwards while nitrogen N1 simultaneously moved downwards, and the values of the torsion angles ϕ(N1-C3-C4-C5) and ϕ(H2-C3-C4-C5) decreased, while concurrently the value of ϕ(C1-C2-N1-C3) increased. We therefore conclude

that MD simulations on the TD-DFT/DFT potential energy surface consistently predict that following proton transfer, the photoexcited molecule undergoes a pedal motion, thereby reaching an the S_1/S_0 conical intersection that we denote CIP. Furthermore, the pedal motion is predicted to always proceed in the same direction.

It must be pointed out that this result does not, in itself, prove that by passing through CIP, the reactive molecule undergoes isomerisation to the *trans*-keto form, because after passing through CIP the molecule may also relax back to the *cis*-keto geometry. It seems, however, very unlikely that the *cis*-enol to *trans*-keto photoisomerisation should proceed through a different pathway, because any such pathway would necessarily compete with the very rapid pathway which involves the radiationless de-excitation of the reactive molecule by reaching CIP. Hence, it may be inferred that this reaction proceeds through the mechanism previously proposed through a pedal motion of the type by Harada *et al.*[5] We would like to underline that because all trajectories were propagated by means of non-biased molecular dynamics, the simulations did not rely in any way on our foreknowledge of the pedal-motion mechanism, but represent the natural behaviour of the system.

It is noteworthy that in a recent study by Robert *et al.*[10] of the *cis*-enol to *trans*-keto solid-state photoisomerisation reaction of *N*-salicylideneaminopyridines, which are structurally very similar to anils, the pedal motion was not found to be accompanied by the reactive molecule crossing an S_1/S_0 conical intersection. Instead, the pedal motion was predicted to proceed completely in the S_1 state, thus painting a qualitatively different picture of the reaction mechanism. This non-detection of a conical intersection in the work just cited may possibly be attributed to fact that the energies of the S_1 state were calculated using the CI-Singles method, which has the serious drawback of not including electron correlation effects, and it could therefore conceivably give rise a qualitatively incorrect topology of the S_1 potential energy surface.

Figure 4.10: An overlay of the instantaneous configuration of the system on reaching the S_1/S_0 CI in trajectory 1 and the experimental crystal structure of SCA, drawn in dark grey and light grey, respectively. The photoexcited molecule is labelled C.

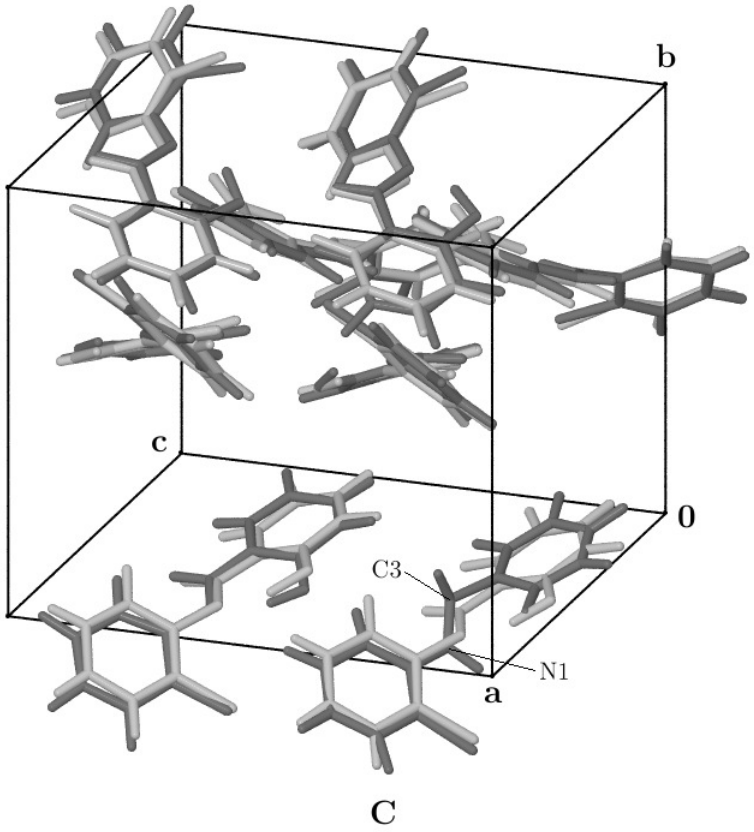

In Figure 4.11(a) on the next page, we plot the energies of the S_0 and S_1 states of the reactive molecule, calculated along trajectory 1 at the DFT, TD-DFT, CC2 and EOM-CC2 levels of theory, as a function of time. Visual inspection of this plot reveals that the agreement between the TD-DFT and EOM-CC2 excited-state energies is reasonably good. Crucially, in the final part of trajectory 1, both the TD-DFT and EOM-CC2 methods predict that the energy gap between the S_0 and S_1 states is progressively decreasing. In particular, at $t = 310$ fs the energy gap calculated at the TD-DFT and EOM-CC2 levels was 0.264 eV and 0.284 eV, respectively. Hence, the EOM-CC2 method predicts the existence of the conical intersection CIP at the same geometry as the TD-DFT method, lending some additional support to the accuracy of the TD-DFT treatment of the reactive SCA molecule.

Figure 4.11: (a) Energies of the S_0 and S_1 states of the photoexcited molecule along trajectory 1, calculated using the DFT, TD-DFT, CC2 and EOM-CC2 methods. The origin of the energy axis is taken at the energy of the S_0 state at $t = 0$.

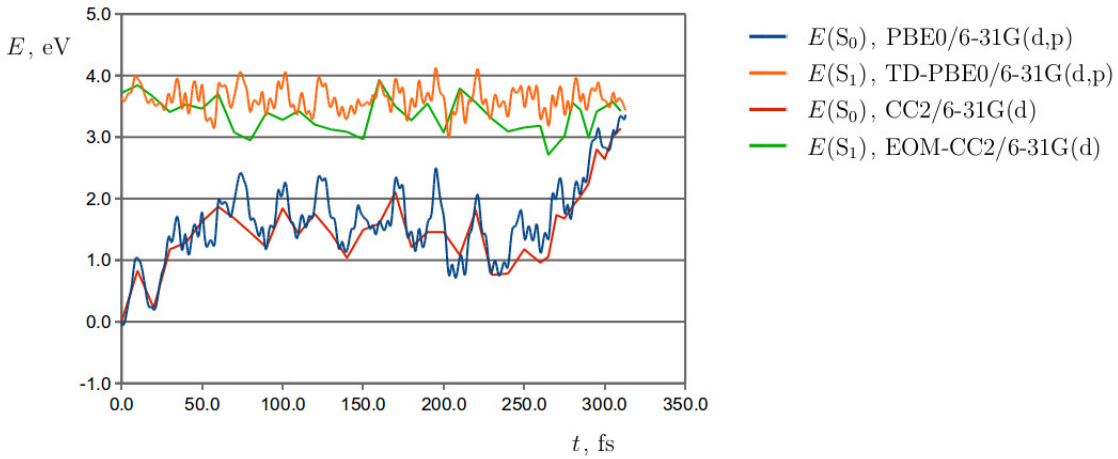

(b) Time-evolution of the T_1 diagnostic of the photoexcited molecule along trajectory 1.

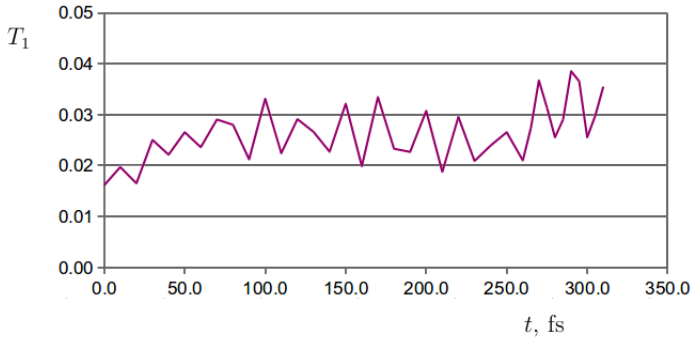

Lastly, in Figure 4.11(b) above we plot the T_1 diagnostic of the ground electronic state of the reactive molecule calculated at the CC2/6-31G(d) level of theory along Trajectory 1. At the onset of Trajectory 1 ($t = 0$), the T_1 diagnostic takes a value of 0.016. From around $t = 0$ fs until around $t = 50$ fs, T_1 increases slightly and then stabilises in the range from 0.02 to 0.03 for the time period from around $t = 50$ fs until around $t = 280$ fs. This early increase of the T_1 diagnostic and its subsequent stabilisation suggests that throughout that period of time, the S_0 state of the reactive molecule may have a biradicaloid character, which may represent a source of error in the description of the S_1 state by both the TD-DFT and EOM-CC2 methods. From around $t = 280$ fs, the energy gap between the S_0 and S_1 states decreases steadily as the molecule approaches a conical intersection, which is reflected by the T_1 diagnostic adopting markedly increased values, up

to 0.039 at $t = 290$ fs. In summary, the time-evolution of the T_1 diagnostic along trajectory 1 supports our contention that the TD-DFT method provides a qualitatively correct picture of this photochemical reaction pathway of SCA.

4.4.2.2. Trajectory 3 of the forward reaction

In trajectory 3, the photoexcited molecule reached CI1 at $t = 120.0$ fs, providing an example of the second reaction pathway of the photochromic polymorph of SCA that leads to the recovery of the starting *cis*-enol form. As evidenced by Figure 4.12(a), where the distances O1-H1, N1-H1 and O1-N1 are plotted as a function of time, proton transfer did not occur during this trajectory. At around $t = 40$ fs the N1-H1 and O1-N1 distances began to elongate, until at around $t = 100$ fs the hydrogen bond of the reactive molecule was nearly ruptured. From around $t = 100$ fs until the end of the trajectory at $t = 120.0$ fs, both of these distances were shortening again, indicating the reformation of the hydrogen bond.

In Figure 4.12(b), we present the time-evolution of the four torsion angles which describe the molecular conformation in the course of trajectory 3. In the period of time from $t = 0$ to around $t = 50$ fs, the photoexcited molecule underwent no significant structural changes, but from around $t = 50$ fs, concurrently with the weakening of the O1-H1$\cdots$N1 hydrogen bond, the value of torsion angle ϕ(C2-N1-C3-C4) began to undergo a marked decrease, revealing that the molecule was undergoing a torsional motion around the N1-C3 bond. The twisting around this bond (compare Figure 4.10(c), where the torsion angle ϕ(C2-N1-C3-C4) remains near 180° throughout the entire trajectory 1) and the nonoccurrence of ESIPT indicate clearly that in trajectory 3, the photochemical reaction proceeded in a qualitatively different manner to that in trajectory 1.

The outcome of trajectory 3 may be explained by referring to Figure 4.13, where the final frame from the trajectory, immediately before the S_1/S_0 conical intersection is reached, is overlaid on the experimental crystal structure of the photochromic polymorph of SCA. The reactive molecule exists in a somewhat deformed *cis*-enol conformation, in which the torsion around the N1-C3 bond has moved both the atoms N1 and C3 to below their crystallographic positions. The occurrence of torsion around the N1-C3 bond leading to an S_1/S_0 conical intersection is reminiscent of the photoreaction pathway IC1 predicted previously[16] for the isolated *N*-salicylideneaniline molecule, which leads to the recovery of

Figure 4.12: Trajectory 3.

(a) Time-evolution of the O1-H1, N1-H1 and O1-N1 distances.

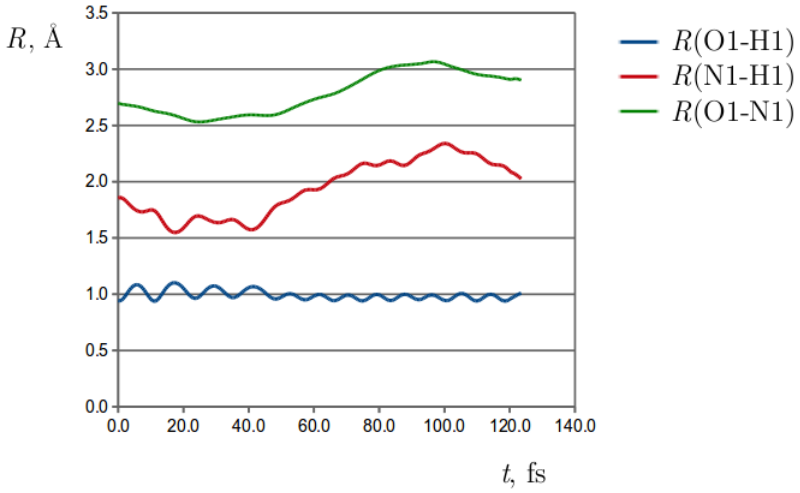

(b) Time-evolution of the four torsion angles which describe the molecular conformation.

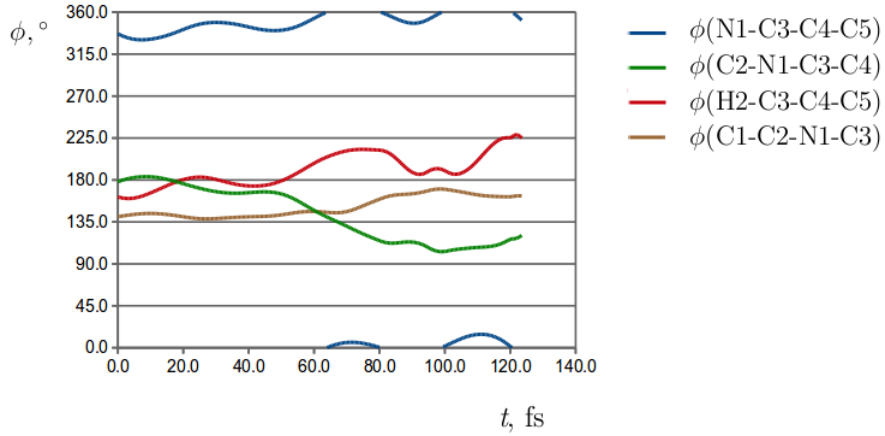

the initial *cis*-enol form. The fact that in the solid-state reaction of SCA, the salicylidene and chlorophenyl rings do not participate in the torsional motion, but instead remain close to their respective crystallographic positions, can be rationalised by noting that (as explained in Section 2) the crystal structure of the photochromic polymorph of SCA does not contain any large voids, and therefore both rings are constrained to remain near their crystallographic positions. On the basis of the above, we identify the motion observed in trajectory 3 with the IC1 pathway of the isolated molecule.

Figure 4.13: An overlay of the instantaneous configuration of the system on reaching the S_1/S_0 CI in trajectory 3 and the experimental crystal structure of SCA, drawn in dark grey and light grey, respectively. The photoexcited molecule is labelled C.

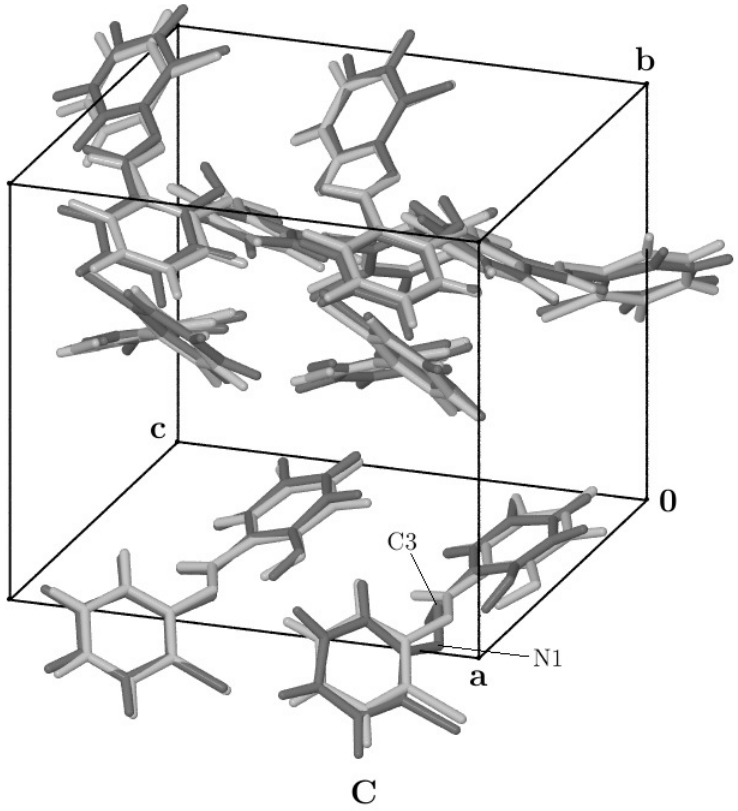

In Figure 4.14(a), the energies of the S_0 and S_1 states of the reactive SCA molecule in trajectory 3, computed using the DFT, TD-DFT, CC2 and EOM-CC2 methods, are plotted as a function of time. Throughout the entire trajectory, the CC2 and EOM-CC2 methods very closely reproduce the energies of the S_0 and S_1 states as calculated using the DFT and TD-DFT methods, respectively. Also, in consistency with the TD-DFT method, the EOM-CC2 method predicts that an S_1/S_0 conical intersection is reached at the end point of trajectory 3.

In Figure 4.14(b), the T_1 diagnostic of the reactive molecule along trajectory 3 is plotted as a function of time. T_1 increases from 0.015 at $t = 0$ to 0.026 at $t = 120.0$ fs, showing an increase with time of the multiconfigurational character of the S_0 state, which is consistent with both the TD-DFT and EOM-CC2 methods predicting that the reactive molecule is nearing a conical intersection.

Figure 4.14: (a) Energies of the S_0 and S_1 states of the photoexcited molecule along trajectory 3, calculated using the DFT, TD-DFT, CC2 and and EOM-CC2 methods. The origin of the energy axis is taken at the energy of the S_0 state at t=0.

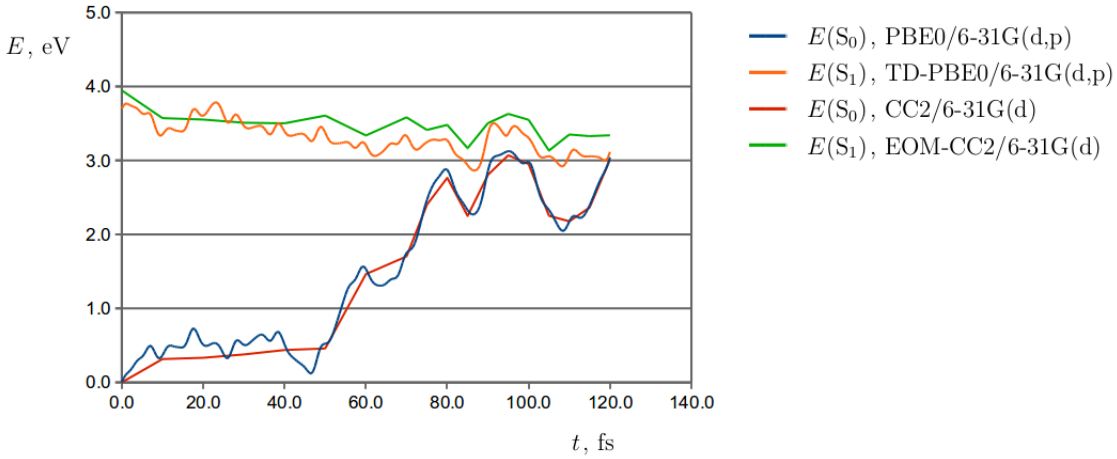

(b) Time-evolution of the T_1 diagnostic of the photoexcited molecule along trajectory 3.

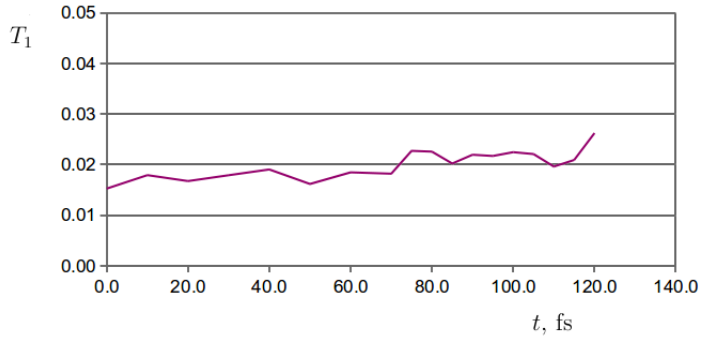

4.4.2.3. Trajectory 3′ of the reverse reaction

In trajectory 3′, following the initial photoexcitation the reactive *trans*-keto molecule persisted with no significant conformational change for around 380 fs before undergoing a pedal motion, which led to it reaching the S_1/S_0 conical intersection geometry which we have termed CIP′.

The time-evolution of the torsion angles ϕ(N1-C3-C4-C5), ϕ(C2-N1-C3-C4), ϕ(H2-C3-C4-C5) and ϕ(C1-C2-N1-C3) along trajectory 3′ is shown in Figure 4.15. From $t = 0$ to around $t = 380$ fs, all four of these torsion angles remained

Figure 4.15: The time-evolution of the four torsion angles which describe the conformation of the reactive molecule in trajectory 3′. (See Figure 4.8(a) for atom numbering.)

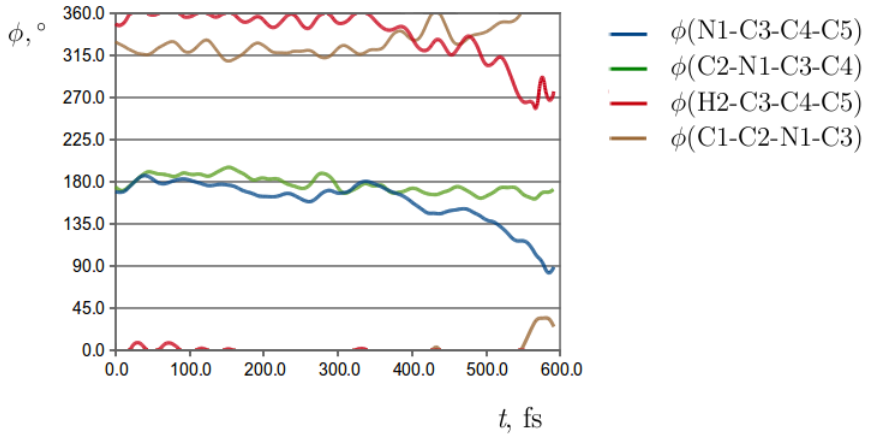

fairly stable, indicating that the reactive molecule underwent no significant conformational changes during this period. At around $t = 380$ fs, however, the molecule began to undergo a pedal motion, which manifested itself as a gradual decrease of the values of the torsion angles ϕ(N1-C3-C4-C5) and ϕ(H2-C3-C4-C5), and an increase in ϕ(C1-C2-N1-C3), until at $t = 591.0$ fs the reactive molecule reached CIP′. The value of ϕ(C2-N1-C3-C4) was close to 180° throughout the entire trajectory, indicating that the atoms C2, N1, C3 and C4 which connect the two aromatic rings of the reactive molecule remained roughly coplanar while the molecule underwent the pedal motion. A survey of the other trajectories of the reverse reaction shows that these features are typical of all trajectories that reached CIP′, and that in every case, the pedal motion proceeded in the same direction.

It is quite notable that in the forward reaction pathway which involves the reactive molecule reaching CIP through a pedal motion, as shown on the example of Figure 4.9(c), the pedal motion also proceeds with a decrease of the values of the torsion angles ϕ(N1-C3-C4-C5) and ϕ(H2-C3-C4-C5), and an increase of the value of ϕ(C1-C2-N1-C3). Thus, we arrive at the surprising conclusion that while the reverse reaction also occurs through a pedal motion, that pedal motion is not a reversal of the one involved in the forward reaction, but proceeds in the same direction. This finding may seem counterintuitive at first, because it might be assumed that the minimum energy pathway for the forward reaction must be the same as the minimum energy pathway for the reverse reaction;

if that were the case for the photoisomerisation reaction for SCA, then the pedal motion involved in the reverse reaction would be a reversion of the one that occurs in the forward reaction. However, the above assumption only holds true for reactions that occur in their entirety on single potential energy surfaces. The photoisomerisation of SCA, on the other hand, takes place not on a single potential energy surface, but on two surfaces, such that during the reaction, the molecule undergoes radiationless de-excitation from one surface to another, which renders that assumption invalid. Accordingly, there does not seem to be a theoretical reason to expect that the pedal motions involved in the forward and reverse photoisomerisations must proceed in opposite directions.

In Figure 4.16, we present the geometry of the system upon reaching the conical intersection CIP′, overlaid on the experimental crystal structure of SCA. The chlorophenyl ring can be seen to be significantly shifted in its own plane relative to its crystallographic position, while the salicylidene ring is slightly tilted away from its crystallographic position. These displacements likely arose both from the fact that the reactive molecule is in the process of undergoing a pedal motion, as well as from the fact that it started out in the *trans*-keto form, which probably does not "fit" perfectly into the bulk crystal lattice composed of *cis*-enol molecules.

The atoms N1 and C3 are above and below, respectively, their crystallographic positions, which again shows that the pedal motion through which CIP′ is reached is not a reversal of the pedal motion involved in the forward reaction mechanism, but proceeds in the same direction.

In Figure 4.17(a), the energies of the S_0 and S_1 states of the reactive SCA molecule, computed using the DFT, TD-DFT, CC2 and EOM-CC2 methods, are plotted as a function of time along trajectory 3′. It can be seen from Figure 4.17 that for both states during this period, the agreement between the DFT and TD-DFT energies on the one hand, and the CC2 energies on the other, is very good except during the final 40 fs of the trajectory, where TD-DFT predicts a significantly smaller energy gap between the S_1 and S_0 states than the EOM-CC2 method. However, in qualitative terms, the TD-DFT and the EOM-CC2 method both clearly predict that the reactive molecule is approaching a conical intersection. We therefore believe that the fairly poor agreement between the energies computed using these two methods is a result of both methods being

Figure 4.16: An overlay of the instantaneous configuration of the system on reaching the S_1/S_0 CI in trajectory 3′ and the experimental crystal structure of SCA, drawn in dark grey and light grey, respectively. The photoexcited molecule is labelled C.

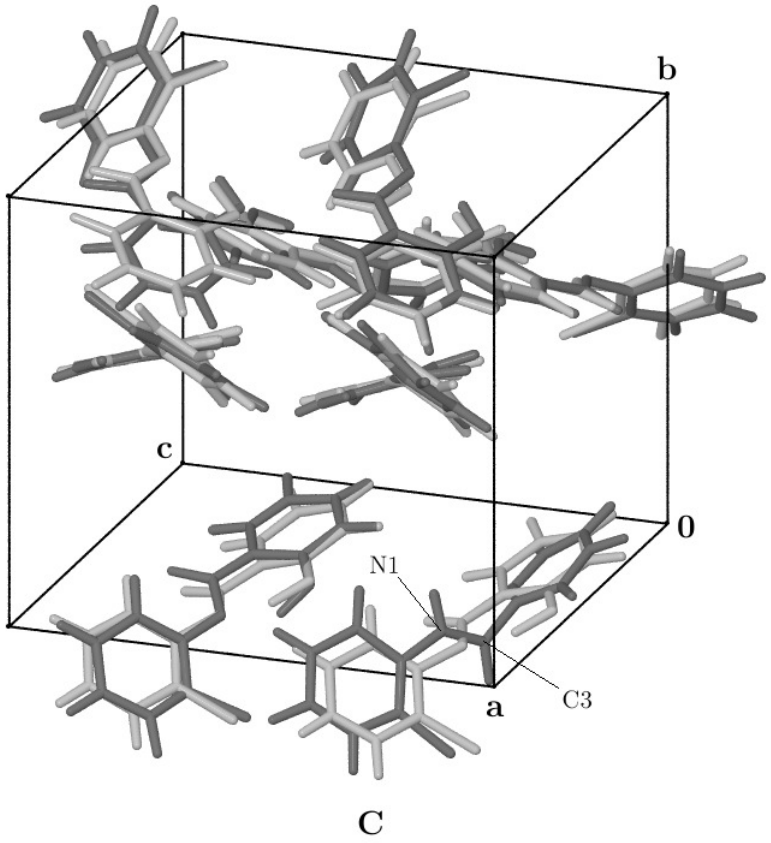

stretched to the limit when applied to a possibly biradicaloid molecule near a conical intersection, and that it does not represent a qualitative failure of either method.

In Figure 4.17(b), on the other hand, we present a plot of the T_1 diagnostic of the reactive molecule as a function of time. At $t = 0$ fs, T_1 took the fairly high value of 0.036, but at later times, until $t = 420$ fs, it remained in the range from 0.02 to 0.03. From around $t = 420$ fs until $t = 550$ fs, the T_1 diagnostic increased markedly, peaking at a value of 0.038 at $t = 545$ fs, which confirms that the molecule was approaching a conical intersection. Surprisingly, in the period from $t = 555$ fs until the termination of the trajectory at $t = 591.0$ fs, T_1 again adopted values below 0.03, despite the fact that the EOM-CC2 method predicted that the energy gap between the S_0 and S_1 states was below 1 eV during that period, and the molecule was clearly in the vicinity of a conical intersection. This

Figure 4.17: (a) Energies of the S_0 and S_1 states of the photoexcited molecule along trajectory 3′, calculated using the DFT, TD-DFT, CC2 and and EOM-CC2 methods. The origin of the energy axis is taken at the energy of the S_0 state at t=0.

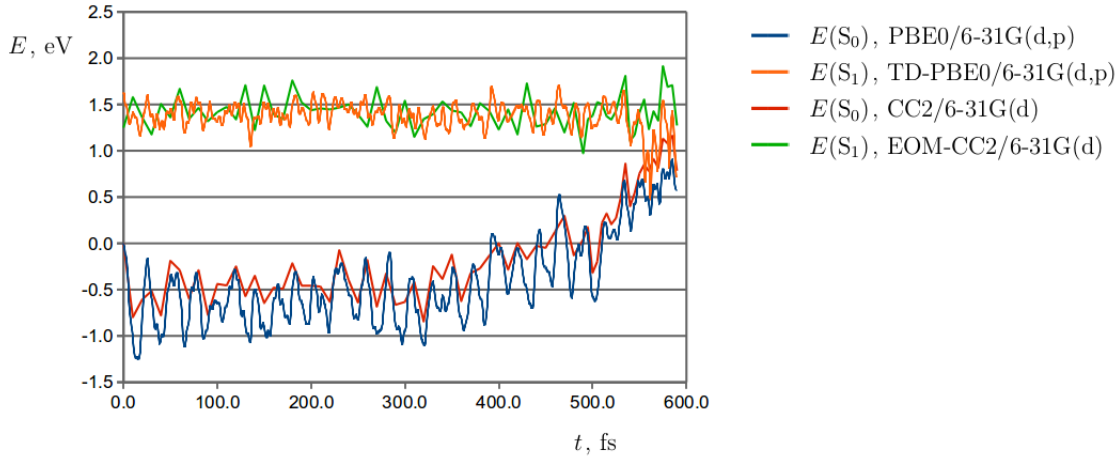

(b) Time-evolution of the T_1 diagnostic of the photoexcited molecule along trajectory 3′.

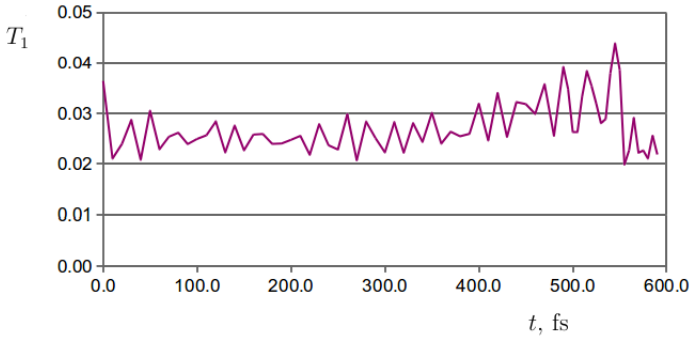

observation suggests that the T_1 diagnostic is not infallible, and that a low value of T_1 does not provide conclusive evidence that the exact wavefunction does not exhibit a multiconfigurational character.

4.5. Conclusions

The photochemical reactions of the photochromic polymorph of the anil *N*-salicylidene-2-chloroaniline were modelled by molecular dynamics simulations employing the hybrid TD-DFT/DFT method to generate the potential energy surface for the solid-state system. It was found that after the initial photoexcitation, the *cis*-enol isomer has two reaction pathways available to it,

which occur with similar probability. The first pathway begins with the ESIPT reaction that converts the photoexcited molecule into the *cis*-keto form. The reactive molecule then persists in the *cis*-keto form, until at an average of 420 fs after the initial photoexcitation event it reaches the conical intersection CIP through a pedal motion (a simultaneous torsion around the C2-N1 and C3-C4 bonds). Because its rapidity precludes the existence of other *cis*-enol to *trans*-keto photoisomerisation pathways, we infer that this pathway must be responsible for the photoisomerisation reaction.

The second reaction pathway of the *cis*-enol isomer is analogous to the IC1 reaction channel which has been characterised previously for the isolated *N*-salicylideneaniline molecule, and proceeds through a torsion around the N1-C3 bond, leading to the recovery of the ground state of the starting *cis*-enol form within an average of 110 fs of the initial photoexcitation.

The *trans*-keto isomer, on the other hand, exhibits only a single reaction pathway. Following the initial photoexcitation, the *trans*-keto molecule remains in a largely unchanged conformation for a period of time ranging from a few hundred femtoseconds to over a picosecond, before undergoing a pedal motion in the same direction as the one which occurs in the *cis*-enol to *trans*-keto photoisomerisation. Through this pedal motion, the molecule reaches an S_1/S_0 conical intersection where it undergoes radiationless de-excitation, and presumably proceeds to relax towards either the *cis*-keto or *trans*-keto form on the ground-state potential energy surface.

To the best of our knowledge this is the first report of a molecular dynamics simulation showing that the anil photoisomerisation reaction in the solid state proceeds through a pedal motion.

References

[1] A. Senier, F. G. Shepheard, *J. Chem. Soc.*, 1943, **95**(1909).

[2] A. Senier, F. G. Shepheard. R. Clarke, *J. Chem. Soc.*, 1952, **101**(1912).

[3] P. F. Barbara, P. M. Rentzepis, L. E. Brus, *J. Am. Chem. Soc.*, 1980, **102**, 2786.

[4] E. Hadjoudis, J. Argyroglou, E. Lambi, I. Moustakali-Mavridis, *Mol. Eng.*, 1991, **1**, 67-74.

[5] J. Harada, H. Uekusa, Y. Ohashi, *J. Am. Chem. Soc.*, 1999, **121**, 5809.

[6] M. Y. Shen, L. Z. Zhao, T. Goto, A. Mordzinski, *J. Lumin.*, 2000, **87-89**, 667.

[7] N. Otsubo, Ch. Okabe, H. Mori, K. Sakota, K. Amimoto, T. Kawato, H. Sekiya, *J. Photochem. Photobiol., A*, 2002, **154**, 33.

[8] E. Hadjoudis, I. M. Mavridis, *Chem. Soc. Rev.*, 2004, **33**, 579.

[9] E. Hadjoudis, A. Rontoyianni, K. Ambroziak, T. Dziembowska, I. M. Mavridis, *J. Photochem. Photobiol., A*, 2004, **162**, 521.

[10] F. Robert, A. D. Naik, B. Tinant, R. Robiette, Y. Garcia, *Chem. Eur. J.*, 2009, **15**, 4327.

[11] F. Robert, A. D. Naik, F. Hidara, B. Tinant, R. Robiette, J. Wouters, Y. Garcia, *Eur. J. Org. Chem.*, 2010, 621.

[12] K. Johmoto, T. Ishida, A. Sekine, H. Uekusa, Y. Ohashi, *Acta Cryst.*, 2012, **B68**, 297.

[13] F. Robert, P.-L. Jacquemin, B. Tinant, Y. Garcia, *Cryst. Eng. Comm.*, 2012, **14**, 4396.

[14] M. Z. Zgierski, A. Grabowska, *J. Chem. Phys.*, 2000, **112**, 6329.

[15] M. Z. Zgierski, A. Grabowska, *J. Chem. Phys.*, 2000, **113**, 7845.

[16] J. M. Ortiz-Sánchez, R. Gelabert, M. Moreno, J. M. Lluch, *J. Chem. Phys.*, 2008, **129**, 214308.

[17] J. N. Moorthy, P. Mal, R. Natarajan, P. Venugopalan, *J. Org. Chem.* 2001, **66**, 7013.

[18] L. R. MacGillivray, *J. Org. Chem.*, 2008, **73**, 3311.

[19] F. Toda, *Acc. Chem. Res.*, 1995, **28**, 480.

[20] J. R. Scheffer, W. Xia, *Top. Curr. Chem.*, 2005, **254**, 233.

[21] K. Nakatani, J. A. Delaire, *Chem. Mater.*, 1997, **9**, 2682.

[22] M. Sliwa, S. Létard, I. Malfant, M. Nierlich, P. G. Lacroix, T. Asahi, H. Masuhara, P. Yu, K. Nakatani, *Chem. Mater.*, 2005, **17**, 4727.

[23] S. Park, O.-H. Kwon, S. Kim, S. Park, M.-G. Choi, M. Cha, S. Y. Park, D.-J. Jang, *J. Am. Chem. Soc.*, 2005, **127**, 10070.

[24] J. Bregman, L. Leiserowitz, K. Osaki, *J. Chem. Soc.*, 1964, 2086.

[25] C. F. Macrae, I. J. Bruno, J. A. Chisholm, P. R. Edgington, P. McCabe, E. Pidcock, L. Rodriguez-Monge, R. Taylor, J. van de Streek, P. A. Wood, *J. Appl. Cryst.*, 2008, **41**, 466.

[26] V. A. Blatov, *Cryst. Rev.*, 2004, **10**, 249.

[27] TOPOS website: http://www.topos.ssu.samara.ru/

[28] H. M. Senn, W. Thiel, *Top. Curr. Chem.*, 2007, **268**, 173.

[29] C. Adamo, V. Barone, *J. Chem. Phys.*, 1999, **110**, 6158.

[30] Gaussian 09, Revision A.02, M. J. Frisch, G. W. Trucks, H. B. Schlegel, G. E. Scuseria, M. A. Robb, J. R. Cheeseman, G. Scalmani, V. Barone, B. Mennucci, G. A. Petersson, H. Nakatsuji, M. Caricato, X. Li, H. P. Hratchian, A. F. Izmaylov, J. Bloino, G. Zheng, J. L. Sonnenberg, M. Hada, M. Ehara, K. Toyota, R. Fukuda, J. Hasegawa, M. Ishida, T. Nakajima, Y. Honda, O. Kitao, H. Nakai, T. Vreven, J. A. Montgomery, Jr., J. E. Peralta, F. Ogliaro, M. Bearpark, J. J. Heyd, E. Brothers, K. N. Kudin, V. N. Staroverov, R. Kobayashi, J. Normand, K. Raghavachari, A. Rendell, J. C. Burant, S. S. Iyengar, J. Tomasi, M. Cossi, N. Rega, J. M. Millam, M. Klene, J. E. Knox, J. B. Cross, V. Bakken, C. Adamo, J. Jaramillo, R. Gomperts, R. E. Stratmann, O. Yazyev, A. J. Austin, R. Cammi, C. Pomelli, J. W. Ochterski, R. L. Martin, K. Morokuma, V. G. Zakrzewski, G. A. Voth, P. Salvador, J. J. Dannenberg, S. Dapprich, A. D. Daniels, Ö. Farkas, J. B. Foresman, J. V. Ortiz, J. Cioslowski, and D. J. Fox, Gaussian, Inc., Wallingford CT, 2009. Ortiz, J. V.; Cioslowski, J.; Fox, D. J. Gaussian, Inc., Wallingford CT, 2009.

[31] J. P. Perdew, K. Burke, M. Ernzerhof, *Phys. Rev. Lett.*, 1996, **77**, 3865.

[32] S. J. Clark, M. D. Segall, C. J. Pickard, P. J. Hasnip, M. J. Probert, K. Refson, M. C. Payne, *Zeitschrift für Kristallographie*, 2005, **220**, 567.

[33] Materials Studio CASTEP Online Help. The pseudopotentials used were H_00PBE.usp, C_00PBE.usp, N_00PBE.usp, O_00PBE.usp and Cl_00PBE.usp

[34] S. Grimme, *J. Comput. Chem.*, 2006, **27**, 1787.

[35] S. Lochbrunner, A. J. Wurzer, E. Riedle, *J. Phys. Chem. A.*, 2003, **107**, 10580.

[36] C. Schriever, S. Lochbrunner, A. R. Ofial, E. Riedle, *Chem. Phys. Lett.*, 2011, **503**, 61.

[37] M. Barbatti, A. J. A. Aquino, H. Lischka, C. Schriever, S. Lochbrunner, E. Riedle, *Phys. Chem. Chem. Phys.*, 2009, **11**, 1406.

[38] A. L. Sobolewski, W. Domcke, *J. Chem. Phys. A*, 2007, **111**, 11725.

[39] L. Łapiński, M. J. Nowak, J. Nowacki, M. F. Rode, A. L. Sobolewski, *ChemPhysChem*, 2009, **10**, 2290.

[40] O. Christiansen, H. Koch, P. Jørgensen, *Chem. Phys. Lett.*, 1995, **243**, 409.

[41] T. D. Crawford, C. D. Sherrill, E. F. Valeev, J. T. Fermann, R. A. King, M. L. Leininger, S. T. Brown, C. L. Janssen, E. T. Seidl, J. P. Kenny, W. D. Allen, *J. Comp. Chem.*, 2007, **28**, 1610.

Chapter 5
Solid-state thermochromism of *N*-salicylidene-2-chloroaniline

5.1. Introduction

In this chapter, we study the thermal, or ground-state, *cis*-enol $\rightleftarrows$ *cis*-keto tautomerisation reaction in the photochromic and non-photochromic polymorphs of *N*-salicylidene-2-chloroaniline (SCA). A comparison of the energetics of tautomerisation in the two polymorphs is of theoretical interest because it contributes towards understanding the origins of the thermochromic properties of anils in the solid state.

5.2. Anil thermochromism in the solid state

Aside from the phenomenon of photochromism, which was discussed in Chapter 4, the anil family of compounds is known for exhibiting thermochromism, which is to say, a reversible change of colour under variation of temperature. Some controversy exists in the literature regarding the physical mechanism of anil thermochromism in the solid state. In accordance with the then widely accepted model of thermochromism, Hadjoudis and Mavridis[1] in their review article have described the properties of photochromism and thermochromism in anil crystals as mutually exclusive, with a few exceptions to the rule. Thermochromism was ascribed to the temperature-sensitive equilibrium between the *cis*-enol and *cis*-keto tautomers, which is illustrated in Figure 5.1 on the following page on the example of the simplest anil, *N*-salicylideneaniline. Specifically, the colour change was believed to arise from the different absorption spectra in the visible range of the two tautomers. The mutual exclusivity of photochromism and thermochromism was rationalised by the conformation of molecules in photochromic and thermochromic crystals. As was explained in the Background section of Chapter 4, the photochromic crystal structures are those in which the planes of the salicylidene and aniline aromatic rings of individual molecules form a dihedral angle that lies in the range from around 30° to around 50°, and the photoexcited molecules are not prevented from undergoing a pedal motion

Figure 5.1: The equilibrium between the *cis*-enol and *cis*-keto tautomers of *N*-salicylideneaniline. The *cis*-keto tautomer is higher in energy than the *cis*-enol. The tautomerisation reaction involves proton transfer between the oxygen and nitrogen atoms.

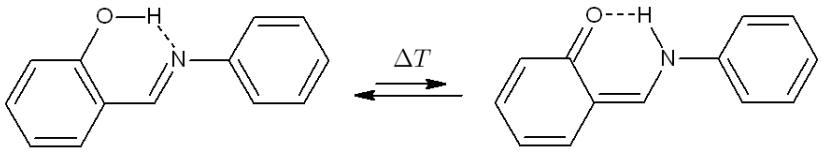

cis-enol (colourless) *cis*-keto (yellow)

by π-stacking or another form of steric hindrance. Thermochromism, on the other hand, was believed to be restricted to those anils which adopt a planar or near-planar conformation in the solid state. It was argued that in a planar anil molecule, the lone electron pair of the imine nitrogen atom does not overlap with the π-type electron density on the aniline ring, which enhances the basicity of the imine nitrogen relative to the non-planar molecules, where such overlap is possible. This, in turn, makes the *cis*-enol and *cis*-keto tautomers of the planar anils closer in energy than those of the non-planar anils, which renders the equilibrium between the *cis*-enol and *cis*-keto tautomers in planar anils sensitive enough to temperature that such crystals are thermochromic.

The model of anil thermochromism outlined above was challenged by the findings of Fujiwara *et al.*,[2] who reported that photochromic crystal forms of *N*-salicylideneaniline and *N*-salicylidene-2-chloroaniline are, in fact, also thermochromic. In particular, it was plainly demonstrated that the crystals of both these compounds are colourless at 77 K and pale yellow at room temperature. The previous mislabelling of these compounds as non-thermochromic[3] was inferred to have been caused by a characteristic absorption band at $\lambda_{\max} \approx 480$ nm of the *cis*-keto tautomers being very weak, which resulted in it not being observed in the absorption spectroscopy measurements that were used to probe for thermochromic properties. It was concluded that in these crystals, the yellow *cis*-keto tautomer is only present in trace amounts, which are nevertheless responsible for the pale yellow colour of the crystals at room temperature. It was also suggested that *N*-salicylideneaniline and *N*-salicylidene-2-chloroaniline are not the only anils to have been wrongly labelled as non-thermochromic, but that anils in general are thermochromic in the solid state, regardless of whether they are photochromic

or not.

Another major revision to the theoretical model of anil thermochromism was introduced by Harada *et al.*,[4] who reported that the temperature-induced colour change cannot be explained on the sole basis of the different absorption spectra in the visible range of the *cis*-enol and *trans*-keto tautomers, but rather, for non-photochromic crystals at low temperatures, the phenomenon of fluorescence comes into play. The complete mechanism of anil thermochromism according to Harada *et al.* is as follows. In non-photochromic crystals near room temperature, fluorescence is negligibly weak, and their colour changes according to the relative population of the *cis*-enol and *cis*-keto forms, which is sensitive to temperature. At low temperatures, however, fluorescence is stronger, and the thermochromic variation in colour is dominated by the temperature dependence of the fluorescence spectrum. The low-temperature colour changes caused by this are much more pronounced than those that occur around room temperature and are due to the shift in chemical equilibrium. Hence, the thermochromic properties of non-photochromic anils cannot be explained without referring to fluorescence.

In photochromic crystals, on the other hand, fluorescence is negligibly weak at all temperatures. In these crystals, the thermochromic colour change is purely a result of the different absorption spectra in the visible range of the *cis*-enol and *trans*-keto tautomers.

If, as concluded by Fujiwara *et al.*,[2] anils in general are thermochromic in the solid state, then the difference in energy between the *cis*-enol and *trans*-keto tautomers of photochromic anils cannot be so large as to preclude the tautomerisation reaction. In the present chapter, we have undertaken to test that conclusion by investigating the thermodynamics of the tautomerisation reaction of a model anil, SCA. SCA is particularly well suited for that purpose because it is known to exist in two polymorphic forms, of which one is photochromic while the other is non-photochromic. By comparing the energy of tautomerisation in the photochromic and non-photochromic polymorphs of the same compound, the effect of the crystal structure on the thermodynamics of the tautomerisation reaction was determined in isolation from other factors that affect the relative energies of the two tautomers, such as the presence of substituents.

In what follows, we consider the crystal structure of the non-photochromic

polymorph of SCA, before turning our attention to the computational methodology applied in the study of the tautomerisation reaction. For a description of the crystal structure of the photochromic polymorph, the Reader is referred to Section 2 of Chapter 4.

5.3. Crystal structure of the non-photochromic polymorph of *N*-salicylidene-2-chloroaniline

The crystal structure of the non-photochromic polymorph of SCA was determined by Johmoto and coworkers[5] using X-ray diffraction analysis. The crystal unit cell is shown in Figure 5.2(a) on the following page. The four molecules contained in the unit cell are all equivalent by symmetry and planar. The π-stacking interactions between molecules cannot be seen in a single unit cell, so in Figure 5.2(b) we present the $3 \times 1 \times 1$ supercell of the non-photochromic polymorph, showing that the molecules are arranged in tilted stacks.

As was done in Section 2 of Chapter 4 for the photochromic polymorph of SCA, the molecular packing in the non-photochromic polymorph was analysed with the help of Voronoi-Dirichlet polyhedra (VDPs). In Figure 5.3, we show a view of the union of atomic VDPs belonging to a single SCA molecule in the lattice of the non-photochromic polymorph. Reflecting the π-stacked arrangement of molecules in the crystal lattice, the VDPs form a slab-like shape around the molecule, and no significant voids can be seen either above or below it.

5.4. Computational details

All calculations for both polymorphs of SCA were performed in a single unit cell at the DFT level of theory using the PBE exchange-correlation functional[6] as implemented in the CASTEP software package version 5.501.[7] The default ultrasoft pseudopotentials were used.[8] A plane-wave cutoff of 500 eV was applied. The electronic Brillouin zone was sampled by using a Monkhorst-Pack k-point grid with a k-point spacing of at most 0.05 Å^{-1}, for a total of 6 and 10 k-points, respectively, for the photochromic and the non-photochromic polymorphs. Energies were corrected for dispersion interactions using the semiempirical scheme of Grimme.[9] Two structures were optimised for each polymorph. In the first structure, which we will henceforth call *cis*-enol@crystal, all four molecules in the

Figure 5.2: (a) Unit cell of the non-photochromic polymorph of SCA determined at room temperature. The compound crystallises in the monoclinic space group $P2_1/c$ with one molecule in the asymmetric unit. $a = 4.6868(1)$ Å, $b = 18.9497(4)$ Å, $c = 12.8231(2)$ Å, $\beta = 105.968(1)^\circ$, $Z = 4$.

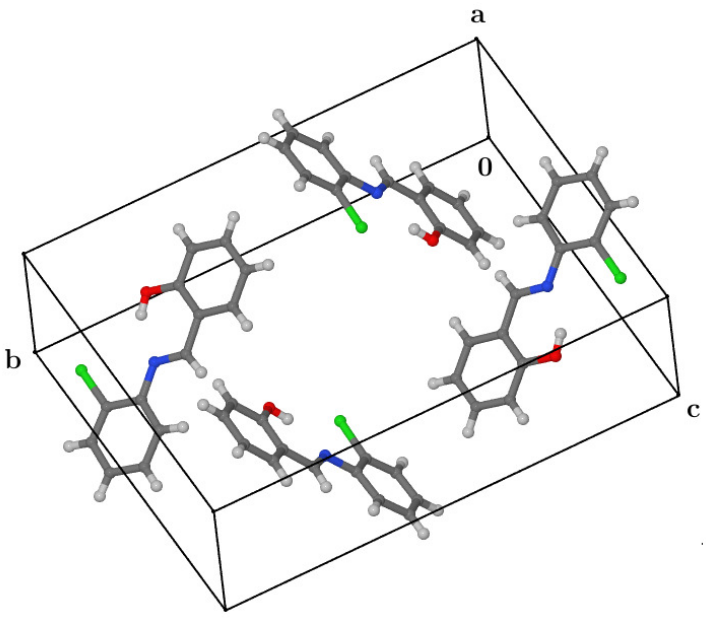

(b) $3\times1\times1$ supercell of the non-photochromic polymorph of SCA, showing how the molecules are π-stacked.

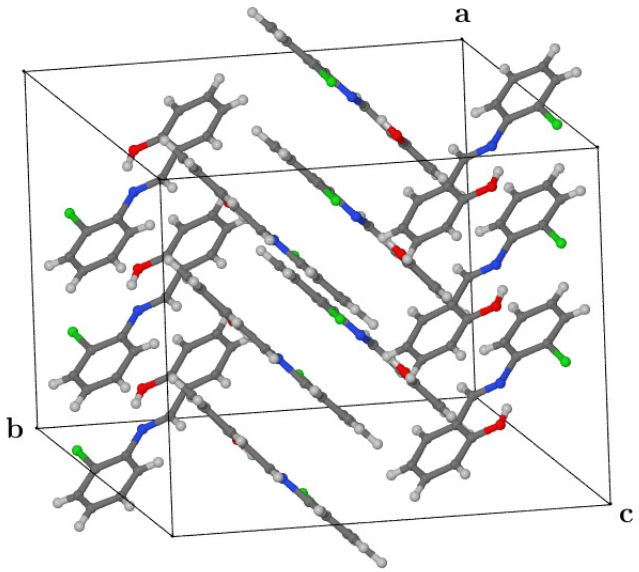

Figure 5.3: Union of atomic VDPs of a molecule within the non-photochromic polymorph of SCA. Next to the VDPs, the SCA molecule is displayed to scale and in the same orientation.

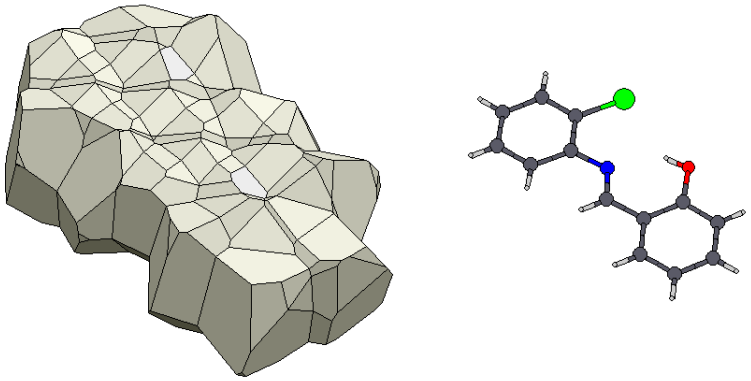

unit cell were in the *cis*-enol tautomeric form. In the second structure, which we will call *cis*-keto@crystal, one molecule was in the *cis*-keto form and the other three were in the *cis*-enol form. Then, the energy difference between these two structures may be identified with the difference in energy between the *cis*-enol and *cis*-keto tautomers of SCA in the solid state. The geometries were optimised using the BFGS algorithm with fixed cell dimensions. The default geometry convergence criteria of CASTEP were applied within energy tolerance 2.0×10^{-5} eV/atom, maximum force tolerance 5.0×10^{-2} eV Å^{-1} and maximum displacement tolerance 1.0×10^{-3} Å.

The potential energy profiles for the tautomerisation reactions in the two polymorphs of SCA were determined using the nudged elastic band (NEB) method[10] for the calculations of minimum energy pathways, the mathematical framework of which is laid out in Appendix A. The elastic band consisted of 11 images, numbered 0 to 10. The 0-th and 10-th images were respectively the optimised structures *cis*-enol@crystal and *cis*-keto@crystal. The intermediate images 1 to 9 were generated through a linear interpolation between the 0-th and 10-th images, using the following formula:

$$\mathbf{R}_i = \mathbf{R}_0 + \frac{i}{10}(\mathbf{R}_{10} - \mathbf{R}_0) \text{ , where } i = 1, 2, \ldots, 9 \tag{5.1}$$

where $\mathbf{R}_i$ is the geometry of the i-th image.

The force constant k of the harmonic springs connecting the successive images was

set to 0.0075 eV Å^{-2}. The geometries of the intermediate images were optimised using the gradient descent algorithm to convergence criteria of maximum force tolerance 2.5×10^{-2} eV Å^{-1} and root-mean-square force tolerance of 5.0×10^{-3} eV Å^{-1}. (Tighter maximum and root-mean-square force tolerances were imposed in the NEB optimisations than in the optimisations of *cis*-enol@crystal and *cis*-keto@crystal to order to balance out the fact that in the NEB optimisations we did not test for the convergence of atomic displacements.)

5.5. Results and discussion

5.5.1. Photochromic polymorph

For the photochromic polymorph of SCA, the structure *cis*-keto@crystal was found to be higher in energy than the *cis*-enol@crystal by 7.2 kJ mol^{-1}, which is compatible with the finding of Fujiwara *et al.*[2] that this polymorph exhibits thermochromism due to the presence of trace amounts of the *cis*-keto tautomer. Indeed, as a first approximation we may neglect the entropy difference between the two tautomers, and calculate the population of the *cis*-keto form as a fraction of the total number of SCA molecules using the simple formula:

$$x(\textit{cis}\text{-keto}) = \frac{\exp(-\Delta E/RT)}{1 + \exp(-\Delta E/RT)} \tag{5.2}$$

where $\Delta E = 7.2$ kJ mol^{-1} is the energy difference between the *cis*-enol and *cis*-keto tautomers. At $T = 77$ K and $T = 298$ K we find $x(\textit{cis}\text{-keto}) = 1.3 \times 10^{-5}$ and $x(\textit{cis}\text{-keto}) = 0.052$, respectively. Thus, the population of the *cis*-keto tautomer is sensitive enough to temperature that it may account for the thermochromic colour change. Even at room temperature, however, the *cis*-keto form remains a trace species, and it is conceivable that it might be difficult to detect using absorption spectroscopy.

The potential energy profile of tautomerisation, calculated using the NEB method, is presented in Figure 5.4, from where it can be seen that the structures *cis*-enol@crystal and *cis*-keto@crystal are separated by a transition state whose structure is approximated by image 6, which lies 9.4 kJ mol^{-1} above the energy of *cis*-enol@crystal. The fact that a potential barrier separates the structures *cis*-enol@crystal and *cis*-keto@crystal confirms that *cis*-keto@crystal is a minimum on the potential energy surface, and hence the photochromic SCA polymorph

Figure 5.4: The minimum energy pathway for *cis*-enol ⇄ *cis*-keto tautomerisation in the photochromic polymorph of SCA. The straight lines connecting the successive data points are a guide to the eye. The energy scale is relative to structure *cis*-enol@crystal (image 0). Image 6 is our best estimate of the transition state structure.

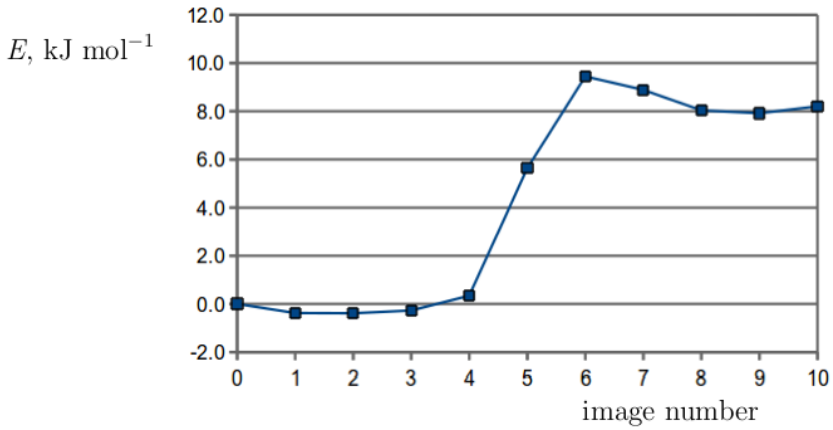

has the capacity for thermochromism due to the *cis*-enol and *cis*-keto tautomers having different absorption spectra. Note that it is also visible that although images 0 (*cis*-enol@crystal) and 10 (*cis*-keto@crystal) are supposed to be energy minima, images 1, 2 and 3 optimised to slightly lower energies than that of image 0, and also images 8 and 9 optimised to slightly lower energies than image 10. This is likely due to the large number (109) of steepest descent steps taken during the NEB optimisation, leading to tighter energy convergence for the intermediate images than was achieved for images 0 and 10.

In Figure 5.5(a), (b) and (c), we show the geometries of the molecule undergoing tautomerisation extracted from image 0 (*cis*-enol@crystal), image 6 (our best estimate for the transition state structure) and image 10 (*cis*-keto@crystal). By comparing the respective bond lengths across Figure 5(a), (b) and (c), it can be seen that during the *cis*-enol to *cis*-keto tautomerisation reaction, the bonds C5-O1 and C3-C4 (see Figure 5.5(a) for atom numbering) shorten and acquire a double bond character, and meanwhile the bonds C4-C5 and C3-N1 elongate, thus becoming single bonds.

Figure 5.5: Geometries of the molecule undergoing tautomerisation extracted from images, 0, 6 and 10. Selected bond lengths are given in units of Å.

(a) image 0 (*cis*-enol@crystal)

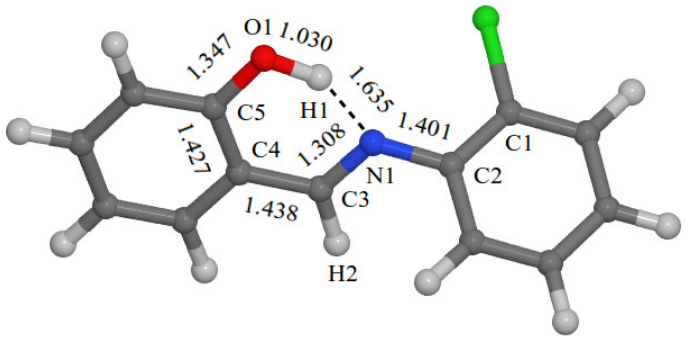

(b) image 6 (estimated transition state structure)

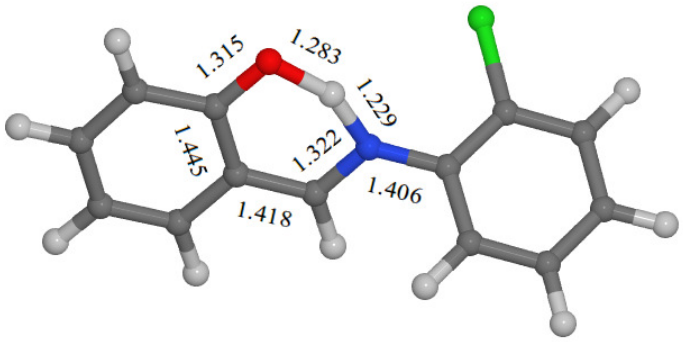

(c) image 10 (*cis*-keto@crystal)

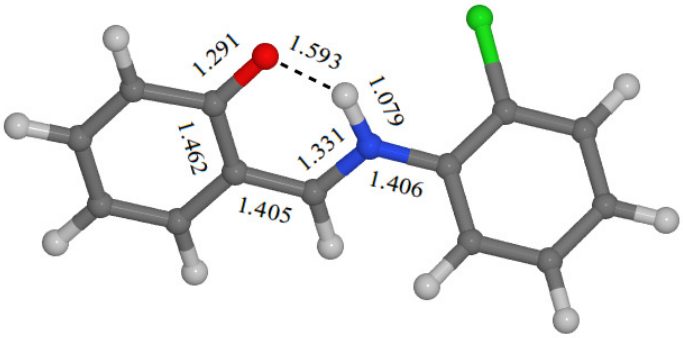

5.5.2. Non-photochromic polymorph

For the non-photochromic polymorph, on the other hand, the structure *cis*-keto@crystal was found to be higher in energy than the *cis*-enol@crystal by only 1.2 kJ mol^{-1}. This small energy difference means that in the non-photochromic polymorph, the change in the population of the *cis*-keto form over a given temperature range will be much greater in absolute terms than in the photochromic polymorph. For example, in the non-photochromic polymorph at $T = 77$ K and $T = 298$ K we find $x(cis\text{-keto}) = 0.13$ and $x(cis\text{-keto}) = 0.38$, respectively, which represents a population increase by 0.25 on going from $T = 77$ K to 298 K, much larger than the corresponding value of the population increase (0.052) calculated for the photochromic polymorph. Hence, the *cis*-enol $\rightleftarrows$ *cis*-keto equilibrium in the non-photochromic polymorph of SCA is much more sensitive to temperature than in the photochromic polymorph. If this finding can be generalised to other anil crystal structures, then we may conclude that although the properties of photochromism and thermochromism are not mutually exclusive, the tautomeric equilibrium in non-photochromic anil crystals is more sensitive to temperature than in photochromic crystals. This, in turn, may explain the previous characterisation[3] of a number of photochromic anils as non-thermochromic.

During the NEB optimisation for the tautomerisation reaction in the non-photochromic polymorph, the maximum force did not converge at first, but instead persistently fluctuated at around 0.035 eV Å^{-1}. This was taken to be a instance of the convergence problem of the type described by Henkelman and Jónsson,[11] whereby the elastic band does not converge to the true MEP either because it comprises a large number of images, or because the force acting along the MEP is large relative to the force along the MEP. Accordingly, as described in Appendix A, we switched to calculating the tangent vectors using the improved method recommended in the work just cited, following which the maximum force did converge. The resulting potential energy profile for the tautomerisation reaction in the non-photochromic polymorph is shown in Figure 5.6. The reaction proceeds through a transition state whose structure is approximated by image 5, the energy of which is 8.6 kJ mol^{-1} relative to image 0 (*cis*-enol@crystal). (Note that the energy of image 6 is marginally lower, by 0.04 kJ mol^{-1}, than that of image 5.)

Figure 5.6: The minimum energy pathway for *cis*-enol $\rightleftarrows$ *cis*-keto tautomerisation in the non-photochromic polymorph of SCA. The straight lines connecting the successive data points are a guide to the eye. The energy scale is relative to *cis*-enol@crystal (image 0). Image 5 is our best estimate of the transition state structure.

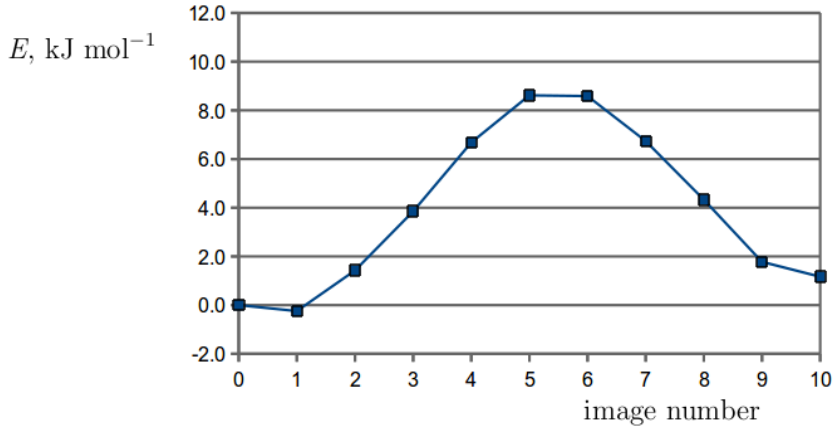

Figure 5.7(a), (b) and (c) shows the geometries of the SCA molecule undergoing tautomerisation extracted from images 0, 5 and 10, respectively. An inspection of the bond lengths reveals that, in the course of the *cis*-enol to *cis*-keto tautomerisation reaction, the C5-O1 and C3-C4 bonds shorten and become double bonds, while the C4-C5 and C3-N1 bonds lengthen and lose their double bond character.

In the non-photochromic polymorph, the molecules are planar, whereas in the photochromic polymorph, the chlorophenyl ring is twisted around the N1-C2 bond relative to the plane containing the salicylidene ring and the six-membered intramolecular hydrogen bond. It may therefore be expected that in the non-photochromic polymorph, improved π orbital overlap should lead to a shorter equilibrium N1-C2 bond length than in the photochromic polymorph. However, a comparison of the geometries of the *cis*-enol (Figures 5(a) and 7(a)) and *cis*-keto (Figures 5(c) and 7(c)) tautomers indicates that this effect is very slight, with the differences in bond lengths not exceeding 0.01 Å.

Figure 5.7: Geometries of the molecule undergoing tautomerisation in the non-photochromic polymorph of SCA, extracted from images 0, 5 and 10. Selected bond lengths are given in units of Å.

(a) image 0 (*cis*-enol@crystal)

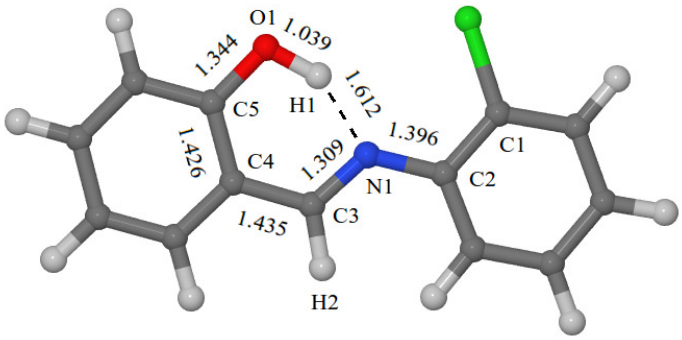

(b) image 5 (estimated transition state structure)

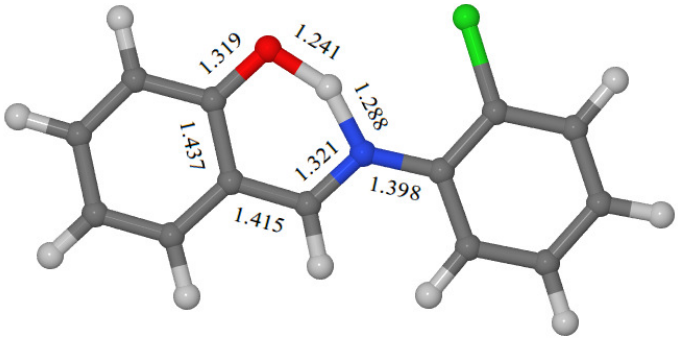

(c) image 10 (*cis*-ketol@crystal)

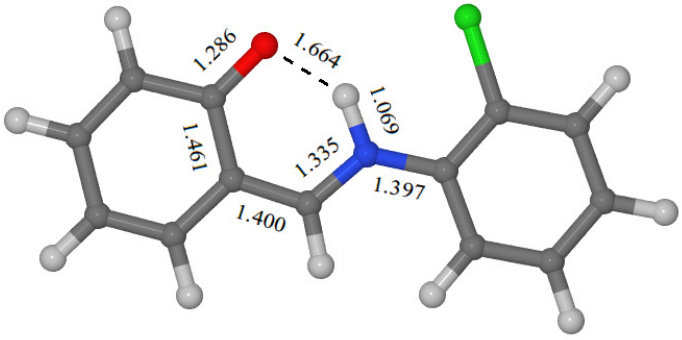

5.6. Conclusions

The *cis*-enol to *cis*-keto tautomerisation energy in the photochromic polymorph of SCA was calculated as 7.2 kJ mol^{-1}. By simple thermodynamic arguments, this value was shown to be low enough for the photochromic polymorph to exhibit thermochromism due to the sensitivity of the tautomeric equilibrium to temperature. In the non-photochromic polymorph, on the other hand, the tautomerisation energy was calculated to be considerably lower (1.2 kJ mol^{-1}), which indicates that the tautomeric equilibrium in that polymorph is more sensitive to temperature than in the photochromic polymorph. The above findings are fully consistent with the empirical model of solid-state anil thermochromism proposed by Fujiwara *et al.*[2]

References

[1] E. Hadjoudis, I. M. Mavridis, *Chem. Soc. Rev.*, 2004, **33**, 579.

[2] T. Fujiwara, J. Harada, K. Ogawa, *J. Phys. Chem. B*, 2004, **108**, 4035.

[3] M. D. Cohen, G. M. Schmidt, S. J. Flavian, *J. Chem. Soc.*, 1964, 2041.

[4] J. Harada, T. Fujiwara, K. Ogawa, *J. Am. Chem. Soc.*, 2007, **129**, 16216.

[5] K. Johmoto, T. Ishida, A. Sekine, H. Uekusa, Y. Ohashi, *Act. Cryst.*, 2012, **B68**, 297.

[6] J. P. Perdew, K. Burke, M. Ernzerhof, *Phys. Rev. Lett.*, 1996, **77**, 3865.

[7] S. J. Clark, M. D. Segall, C. J. Pickard, P. J. Hasnip, M. J. Probert, K. Refson, M. C. Payne, *Zeitschrift für Kristallographie*, 2005, **220**, 567.

[8] Materials Studio CASTEP Online Help. The pseudopotentials used were H_00PBE.usp, C_00PBE.usp, N_00PBE.usp, O_00PBE.usp and Cl_00PBE.usp

[9] S. Grimme, *J. Comput. Chem.*, 2006, **27**, 1787.

[10] H. Jónsson, G. Mills, K. W. Jacobsen, *Nudged Elastic Band Method for Finding Minimum Energy Paths of Transitions*, in *Classical and Quantum Dynamics in Condensed Phase Simulations*, Ed. B. J. Berne, G. Ciccotti and D. F. Coker (World Scientific, 1998), page 385.

[11] G. Henkelman, H. Jónsson, *J. Chem. Phys.*, 2000, **113**, 9978.

Chapter 6
Conclusions and outlook

6.1. Photochemical reactions in molecular crystals

The principal aim of this work has been to model, by means of computer simulation, some selected photochemical reactions that take place in the bulk molecular crystal phase. To this end, we have employed molecular dynamics simulations on potential energy surfaces generated using the subtractive QM/QM hybrid method. In the case of the *cis*-enol $\rightleftarrows$ *trans*-keto photoisomerisation of the anil *N*-salicylidene-2-chloroaniline, this methodology has shown itself to faithfully reproduce the experimentally-determined features of that reaction: its reversibility and the previously postulated mechanism.[1] Owing to its predictive power, and the fact that it does not rely on system-specific parameterisation, it is anticipated that the subtractive QM/QM hybrid method will continue to be applied in simulation studies of reactions taking place in molecular crystals.

At the time of writing, work is underway to utilise this method in order to model the photocyclisation reaction of the dithienylethene derivative 1,2-bis(2,4-dimethyl-5-phenyl-3-thienyl)perfluorocyclopentene, which is illustrated in Figure 6.1 on the following page. Irradiation with UV light of the open-ring form of that compound (labelled **HT** by analogy to hexatriene) in the crystal form converts a fraction of the molecules into to the closed-ring form (labelled **CHD** after cyclohexadiene). The reverse reaction is triggered by visible light. The crystal structure is preserved during these reactions.[2] Our collaborators from the group of Prof. Dwayne Miller at the Institute for Optical Sciences at the University of Toronto, who have studied the dynamics of this photocyclisation reaction using transient absorption spectroscopy[3] and electron diffraction[4] measurements, have expressed interest in the possibility that there may exist side-reaction pathways of photoexcited bf HT that compete with photocyclisation.

We have accordingly undertaken to study this photocyclisation reaction as it happens in the molecular crystal phase with the aim of identifying and determining the quantum yield of any side reactions. Preliminary calculations have shown that the relatively inexpensive second-order approximate coupled cluster singles and doubles (CC2) method[5] is capable of describing the initial stage of the

Figure 6.1: The reversible photocyclisation reaction of the diarylethene derivative 1,2-bis(2,4-dimethyl-5-phenyl-3-thienyl)perfluorocyclopentene.

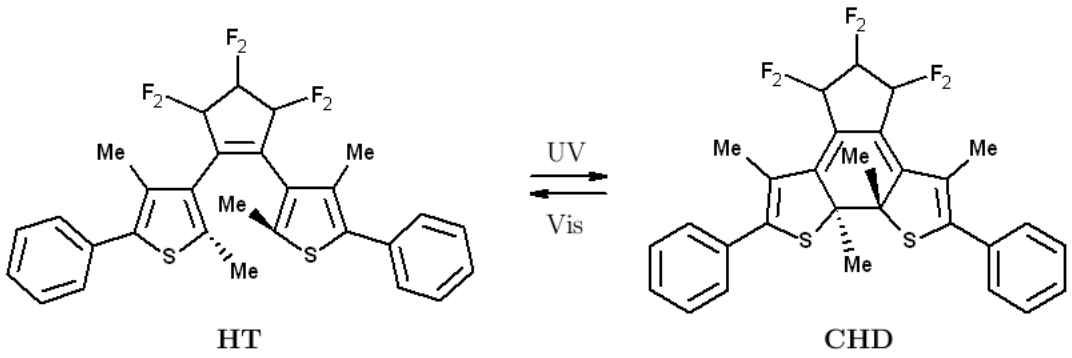

HT **CHD**

photocyclisation reaction, during which the thiophene rings approach closer to each other. In particular, inspection of values of the T_1 diagnostic during the photocyclisation indicates that in the Franck-Condon region, the **HT** molecule is adequately described by a single-reference wavefunction. We therefore believe that the CC2 method is fit for the purpose of describing the dynamics of the molecule at least immediately following photoexcitation.

Due to its large size (59 atoms), it will not be possible to include an entire molecule of 1,2-bis(2,4-dimethyl-5-phenyl-3-thienyl)perfluorocyclopentene in the excited-state CC2 calculation. We will therefore exclude from the CC2 calculation the two phenyl groups and the six fluorine atoms, which do not directly participate in the photocyclisation reaction, and the resulting eight dangling bonds will be capped by hydrogen link atoms. The potential energy expression for the simulated system will therefore take the following form:

$$E_{\mathrm{CC2/DFT}}(\mathbf{S}) = E^{\mathrm{PW}}_{\mathrm{DFT}}(\mathbf{S}) + E^{\mathrm{GTO}}_{\mathrm{CC2}}(\mathbf{C}+\mathbf{L}) - E^{\mathrm{PW}}_{\mathrm{DFT}}(\mathbf{C}+\mathbf{L})$$

where $\mathbf{L}$ denotes the link atoms. This partitioning of the simulated unit cell of 1,2-bis(2,4-dimethyl-5-phenyl-3-thienyl)perfluorocyclopentene into the CC2 and DFT regions is illustrated schematically in Figure 6.2 on the next page.

Figure 6.2: Division of the system into the CC2 and DFT regions. The unit cell of 1,2-bis(2,4-dimethyl-5-phenyl-3-thienyl)perfluorocyclopentene is viewed along the b axis. The hydrogen link atoms are omitted for clarity.

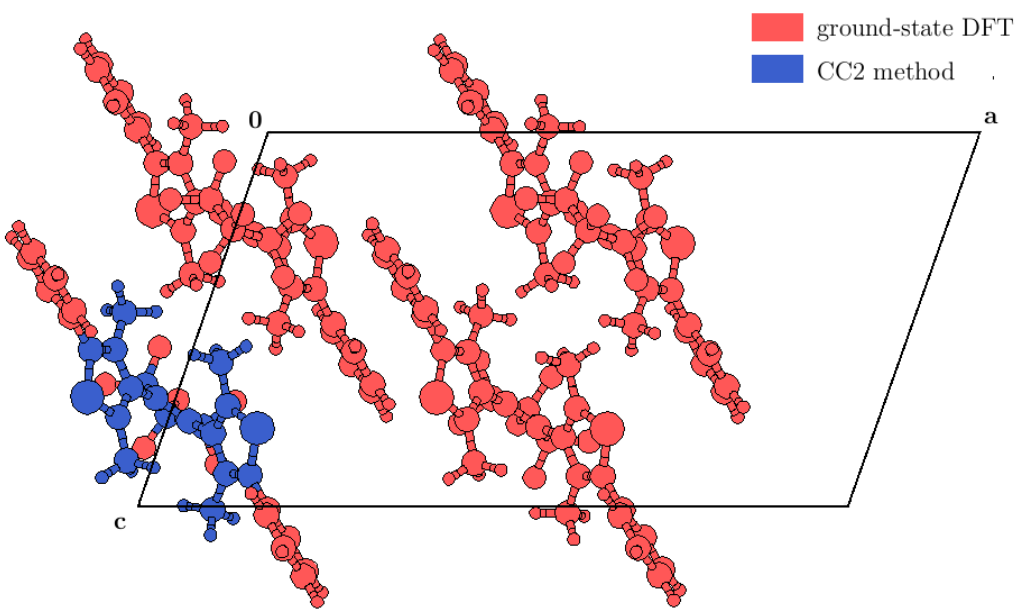

6.2. Methodological developments

As mentioned in Section D.6 of Appendix D, exchange-correlation functionals such as the PBE functional[6,7] fail to account for the dispersion interaction, which is crucial in the modelling of molecular crystals. In the present work the dispersion interaction was included through the correction scheme of Grimme,[8] which takes the form of a Lennard-Jones-like term added *a posteriori* to the potential energy. As demonstrated in Section 2.2 of Chapter 2, the resulting dispersion-corrected PBE functional generally agrees well with high-level *ab initio* calculations. However, the fact that dispersion interactions are included through a molecular mechanics-like correction means the loss of some methodological rigour: the potential energy surface is no longer generated purely using quantum-mechanical methods.

At the cost of an even greater departure from a fully quantum-mechanical model, we might follow the idea of the molecular mechanics-like dispersion correction to its logical conclusion, and construct a simulation scheme in which all intermolecular interactions are treated by means of molecular mechanics. Since

DFT is generally well able to describe intramolecular interactions and related quantities (molecular geometries, vibrational frequencies, the relative energies of conformers), all intramolecular interactions would still be treated using DFT. In effect, a "big" DFT calculation for the unit cell of a molecular crystal, in which dispersion is included through a molecular mechanics-like correction, would be broken up into a series of "small" DFT calculations for the individual constituent molecules, and a series of intermolecular interaction terms calculated through molecular mechanics.

The concept of such a calculation is laid out in equation 6.1 below, and is also presented schematically in Figure 6.3 on the following page.

$$E(\mathbf{S}) = \sum_{a} E^{\text{intra}}_{\text{DFT}}(a) + \sum_{a<b} E^{\text{inter}}_{\text{MM}}(a,b) \tag{6.1}$$

In equation 6.1, each of the terms $E^{\text{intra}}_{\text{DFT}}(a)$ represents the intramolecular DFT energy of the a-th molecule, which is to say, the energy of that molecule calculated using the DFT method as though it was an isolated molecule.

In turn, each of the terms $E^{\text{inter}}_{\text{MM}}(a,b)$ represents the intermolecular interaction between the a-th and b-th molecules, calculated using a molecular mechanics force field. These terms include all intermolecular van der Waals and electrostatic interactions:

$$E^{\text{inter}}_{\text{MM}}(a,b) = \sum_{i}^{\substack{\text{atoms of} \\ \text{molecule } a}} \sum_{j}^{\substack{\text{atoms of} \\ \text{molecule } b}} \left[4\varepsilon \left(\frac{\sigma}{r_{ij}} \right)^{12} - 4\varepsilon \left(\frac{\sigma}{r_{ij}} \right)^{6} + \frac{q_i q_j}{r_{ij}} \right] \tag{6.2}$$

Equation 6.1 can be interpreted as defining a QM/MM partitioning scheme, since it combines a quantum-mechanical (QM) method with molecular mechanics (MM). However, the partitioning defined by equation 6.1 is different in nature to the additive and subtractive QM/MM schemes introduced in Chapter 1, both of which divide the system into QM and MM regions. In contrast, equation 6.1 does not partition the system into regions treated using different methods, but rather the interactions present in the entire system are divided into those that will be treated using a QM method (namely, DFT) and those that will be handled using the MM method.

The potential advantage of the simulation scheme defined by equation 6.1

Figure 6.3: A diagrammatic illustration of the proposed QM/MM partitioning scheme for molecular crystals. The electron densities of the two interacting benzene molecules are coloured differently in order to highlight the fact that they originate from separate isolated-molecule calculations. Some of the interactions between the atoms comprising the two benzene molecules are shown schematically as green arrows.

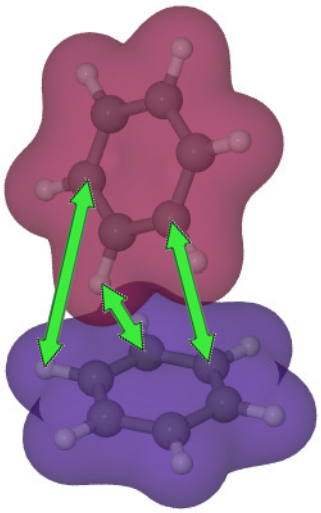

over a dispersion-corrected DFT calculation for the entire system is that the series of isolated-molecule DFT calculations (the terms $E_{\mathrm{DFT}}^{\mathrm{intra}}(a)$ in equation 6.1) may be computationally less expensive to carry out than the DFT calculation for the entire system (although this will clearly depend on the system size and simulation parameters such as the choice of basis set and exchange-correlation functional). Clearly, the computational cost of evaluating the intermolecular interactions at the MM level of theory is very low in comparison to the cost of a DFT calculation for the entire system, so we do not need to take it into account when considering the relative costs of both types of calculation. The drawback is that the intermolecular interaction parameters which appear in equation 6.2 are unknown and must be derived by parameterisation against experimental or theoretical benchmarks. At present, we have no specific plans to attempt to use a potential energy surface (PES) of the type defined by equation 6.1 in production simulations, but nevertheless we believe that such a method of constructing the PES is an interesting idea and may be well-suited to simulations of crystals composed of molecules for which the derivation of the intermolecular interaction parameters does not pose a difficult problem.

6.3. Anil thermochromism in the solid state

Lastly, it is anticipated that the calculations reported in Chapter 5 will form part of a future publication on the thermochromism of anils. In order to broaden the scope of our study, we intend to repeat these calculations for the three known polymorphs of the simplest anil, *N*-salicylideneaniline (SA). Molecules in the α_1 [9] and α_2 [10] polymorphs of SA are non-planar and both these polymorphs are photochromic, while in the β polymorph,[11] the molecules are planar and π-stacked, and consequently it is non-photochromic. At the time of writing, we have thus far optimised the geometries of the structures *cis*-enol@crystal and *cis*-keto@crystal for each of the three polymorphs. The calculated tautomerisation energies are 6.6 kJ mol^{-1}, 4.4 kJ mol^{-1} and 0.0 kJ mol^{-1} for the α_1, α_2 and β polymorphs, respectively.

As expected, the calculated tautomerisation energies are higher in the two photochromic polymorphs than in the non-photochromic polymorph, in which the structures *cis*-enol@crystal and *cis*-keto@crystal are predicted to be very close in energy. These results lend additional support to the model of anil thermochromism postulated by Fujiwara *et al.*[12]

References

[1] J. Harada, H. Uekusa, Y. Ohashi, *J. Am. Chem. Soc.*, 1999, **121**, 5809.

[2] M. Irie, S. Kobatake, M. Horichi, *Science*, 2001, **291**, 1769.

[3] H. Jean-Ruel, R. R. Cooney, M. Gao, C. Lu, M. A. Kochman, C. A. Morrison, R. J. D. Miller, *J. Phys. Chem. A,*, 2011, **115**, 13158.

[4] H. Jean-Ruel, M. Gao, M. A. Kochman, C. Lu, L. C. Liu, R. R. Cooney, C. A. Morrison, R. J. D. Miller, *J. Phys. Chem. B*, 2013.

[5] O. Christiansen, H. Koch, P. Jørgensen, *Chem. Phys. Lett.*, 1995, **243**, 409.

[6] J. P. Perdew, K. Burke, M. Ernzerhof, *Phys. Rev. Lett.*, 1996, **77**, 3865.

[7] J. P. Perdew, K. Burke, M. Ernzerhof, *Phys. Rev. Lett.*, 1997, **78**, 1396.

[8] S. Grimme, *J. Comput. Chem.*, 2006, **27**, 1787.

[9] R. Destro, A. Gavezzotti, M. Simonetta, *Acta Cryst.*, 1978, **B34**, 2867.

[10] F. Arod, M. Gardon, P. Pattison, G. Chapuis, *Acta Cryst.*, 2005, **C61**, o317.

[11] F. Arod, P. Pattison, K. J. Schenk, G. Chapuis, *Cryst. Growth Des.*, 2007, **7**, 1679.

[12] T. Fujiwara, J. Harada, K. Ogawa, *J. Phys. Chem. B*, 2004, **108**, 4035.

Appendix A
The Nudged Elastic Band Method

When modelling a process through which a substrate structure A is converted into a product structure B, we are often interested in the minimum energy path (MEP) connecting A and B. The MEP is defined as a pathway in the configurational space of the system that connects the energy minima A and B through a transition state (a first-order saddle point on the potential energy surface of the system) and runs orthogonally to the equipotential contours of the potential energy surface (PES).[1] In general, on a smooth and continuous PES, any two minima are connected by one or more MEPs. Each MEP passes through at least one transition state, and may also pass through energy minima other than A and B (such minima will then be referred to as intermediates in the reaction $A \rightleftarrows B$). In Figure A.1 on the following page, we illustrate the MEP connecting two minima A and B on an example two- dimensional potential energy surface.

The Nudged Elastic Band (NEB) method[2] is a simple algorithm for finding MEPs, which requires as input the configurations A and B and an initial guess for a MEP connecting them. The NEB method works by constructing an elastic band of $N+1$ images, or replicas of the system in its configuration space, which are denoted by $\mathbf{R}_0$, $\mathbf{R}_1$, $\mathbf{R}_2$, ..., $\mathbf{R}_{N-1}$, $\mathbf{R}_N$. The outermost images $\mathbf{R}_0$ and $\mathbf{R}_N$ are respectively the energy minima A and B. The remaining $N-1$ intermediate images are placed in order along the initial guess for the MEP. The objective of the NEB method is to optimise the positions of the intermediate images to lie along the real MEP. In the optimisation, adjacent images are connected by harmonic springs. The spring force $\mathbf{F}_i^{\mathrm{S}}$ acting on an intermediate image i is given by

$$\mathbf{F}_i^{\mathrm{S}} = k_{i+1}\left(\mathbf{R}_{i+1} - \mathbf{R}_i\right) - k_i\left(\mathbf{R}_i - \mathbf{R}_{i-1}\right) \tag{A.1}$$

where k_i is the force constant of the i-th harmonic spring. In addition to the spring force, on each intermediate image i there acts a real (physical) force given by $-\nabla V(\mathbf{R}_i)$, where $V(\mathbf{R})$ is the potential energy function of the system.

The total force $\mathbf{F}_i^0$ on the i-th image is taken as the sum of the component of the real force perpendicular to the elastic band and the component of the spring

Figure A.1: MEP connecting two potential energy minima A and B, which are separated by a potential energy barrier. The MEP is the blue line, and the black lines are equipotential contours of the potential energy surface. The MEP passes through a transition state, which is labelled TS.

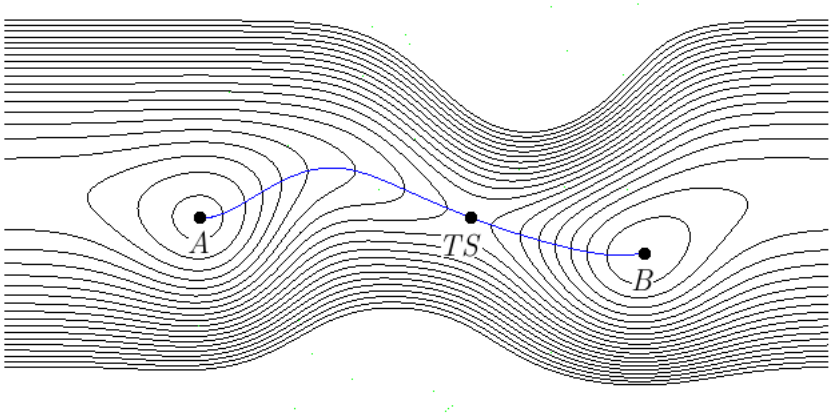

force parallel to the elastic band:

$$\mathbf{F}_i^0 = -\nabla V(\mathbf{R}_i)|_\perp + \left(\mathbf{F}_i^{\mathrm{S}} \cdot \hat{\tau}_i\right) \hat{\tau}_i \tag{A.2}$$

where $\hat{\tau}_i$ is the unit tangent to the band at image i. The unit tangent is not uniquely defined; one possible choice is to calculate the unit tangent vectors as follows:[3]

$$\hat{\tau}_i = \frac{\tau_i}{|\tau_i|} \text{ , where } \tau_i = \frac{\mathbf{R}_{i+1} - \mathbf{R}_i}{|\mathbf{R}_{i+1} - \mathbf{R}_i|} + \frac{\mathbf{R}_i - \mathbf{R}_{i-1}}{|\mathbf{R}_i - \mathbf{R}_{i-1}|} \tag{A.3}$$

and $\left(\mathbf{F}_i^{\mathrm{S}} \cdot \hat{\tau}_i\right) \hat{\tau}_i$ is the component of the spring force parallel to the band. The role of the parallel component of the spring force is to control the spacing of images along the band. It is usual to set all spring constants k_i as equal; then, the parallel component of the spring force ensures that the intermediate images are spaced equally along the MEP.

The component of the physical force perpendicular to the band is given by:

$$\nabla V(\mathbf{R}_i)|_\perp = \nabla V(\mathbf{R}_i) - \left(\nabla V(\mathbf{R}_i) \cdot \hat{\tau}_i\right) \hat{\tau}_i \tag{A.4}$$

Figure A.2: Optimisation of the MEP using the NEB method with $N = 15$, which means the elastic band consisted of $N + 1 = 16$ images. The green lines represent the positions of the intermediate images at successive steepest descent optimisation steps. The red crosses are the final positions of the images comprising the elastic band. The MEP obtained in the optimisation is drawn in blue.

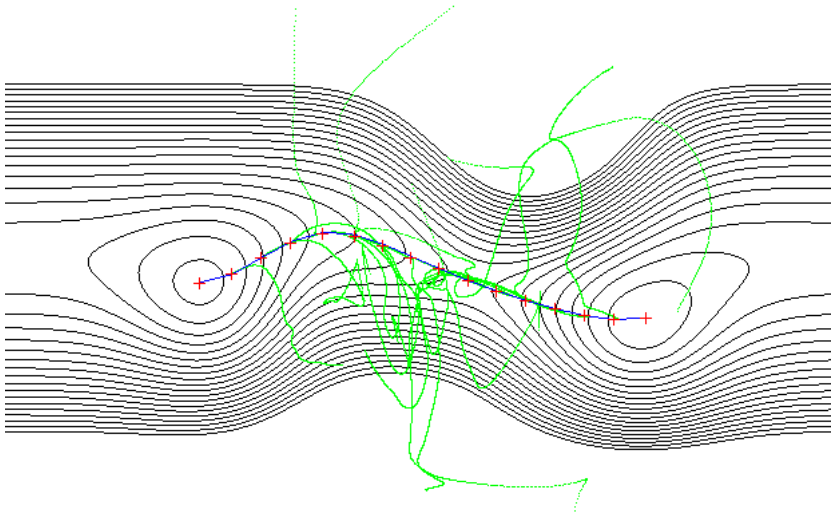

The action of the perpendicular component of the real force causes each image to slide away from high energy regions, towards a point where the perpendicular component of the real force is zero, that is, towards a MEP. The positions of the intermediate images are optimised using any suitable geometry optimisation algorithm, such as steepest descent method or the Newton-Raphson method. The positions of the two outermost images are held fixed throughout the optimisation. In MEP optimisations in polyatomic systems, translations and rotations of the entire system must be eliminated during the optimisation, which may be achieved by constraining six degrees of freedom in each of the intermediate images of the system. For example, in each intermediate image one could fix the Cartesian coordinates of one atom, constrain another atom to only move on a plane, and constrain a third atom to only move along a line.

In Figure A.2 above, we present the application of the NEB method to the model potential energy surface shown in Figure A.1. It can be seen how the NEB method successfully finds the MEP, despite starting from an intentionally bad initial guess (which is to say, in the NEB optimisation shown in Figure A.2, the initial positions of the intermediate images were deliberately scattered far from

the true MEP).

By finding a MEP connecting two minima A and B, the NEB method also locates one or more transition states, which are, by definition, maxima of energy along the MEP. However, because of the discrete nature of the elastic band, a slight complication arises when the NEB method is used to study transition state structures. Following the optimisation of the elastic band, the highest-energy image (which is our best approximation of the transition state structure) will not, in general, coincide exactly with the true transition state, but will be positioned at some distance away from it along the MEP. The energy of that image will therefore be lower than the energy of the transition state. Hence, in the absence of other sources of error, the NEB method always slightly underestimates the transition state energy. This effect disappears in the limit of a continuous elastic band ($N \to \infty$), and it is therefore imperative to use a large number of images in order to minimise the underestimation of the transition state energy.

Another practical issue that arises from the discretisation of the elastic band into a number of images is that during the optimisation of an elastic band, convergence problems may arise in cases where the force parallel to the MEP is large relative to the force perpendicular to the MEP, and/or when the number of images is large.[3] Indeed, as described in Section 5.5.2 of Chapter 5, such an instance of the elastic band failing to converge was encountered during the MEP optimisation for the *cis*-enol $\rightleftarrows$ *cis*-keto tautomerisation reaction in the non-photochromic polymorph of *N*-salicylidene-2-chloroaniline (SCA). The origin of such convergence problems can be traced back to the calculation of the tangent vectors $\hat{\tau}_i$ using equation A.3, and it may be remedied by instead using the following equation to calculate the tangent vectors:[3]

$$\tau_i = \begin{cases} \tau_i^+ & \text{if} \quad V(\mathbf{R}_{i+1}) > V(\mathbf{R}_i) > V(\mathbf{R}_{i-1}) \\ \tau_i^- & \text{if} \quad V(\mathbf{R}_{i-1}) > V(\mathbf{R}_i) > V(\mathbf{R}_{i+1}) \\ \tau_i^+ \, \Delta V_i^{\max} + \tau_i^- \, \Delta V_i^{\min} & \text{if} \quad V(\mathbf{R}_i) > V(\mathbf{R}_{i+1}) > V(\mathbf{R}_{i-1}) \\ & \text{or} \quad V(\mathbf{R}_{i+1}) > V(\mathbf{R}_{i-1}) > V(\mathbf{R}_i) \\ \tau_i^+ \, \Delta V_i^{\min} + \tau_i^- \, \Delta V_i^{\max} & \text{if} \quad V(\mathbf{R}_i) > V(\mathbf{R}_{i-1}) > V(\mathbf{R}_{i+1}) \\ & \text{or} \quad V(\mathbf{R}_{i-1}) > V(\mathbf{R}_{i+1}) > V(\mathbf{R}_i) \end{cases} \tag{A.5}$$

Where $\tau_i^+ = \mathbf{R}_{i+1} - \mathbf{R}_i$, $\tau_i^- = \mathbf{R}_i - \mathbf{R}_{i-1}$, and $V_i^{\max}$ and $V_i^{\min}$ are respectively the

higher and the lower of the two quantities $|V(\mathbf{R}_{i+1})-V(\mathbf{R}_i)|$ and $|V(\mathbf{R}_{i-1})-V(\mathbf{R}_i)|$:

$$\Delta V_i^{\max} = \max(\,|V(\mathbf{R}_{i+1}) - V(\mathbf{R}_i)|\,,\,|V(\mathbf{R}_{i-1}) - V(\mathbf{R}_i)|\,)$$

$$\Delta V_i^{\min} = \min(\,|V(\mathbf{R}_{i+1}) - V(\mathbf{R}_i)|\,,\,|V(\mathbf{R}_{i-1}) - V(\mathbf{R}_i)|\,)$$

The tangent vectors τ_i given by equation A.5 are unnormalised, and must be normalised by setting $\hat{\tau}_i = \tau_i/|\tau_i|$ before they are substituted into equations A.2 and A.4. In the case of the tautomerisation reaction in the non-photochromic polymorph of SCA, by applying equation A.5 in order to calculate the tangents, the convergence problem was successfully eliminated, and the forces converged to within a low tolerance.

A vast advantage of the NEB method is that unlike some other methods for the location of transition states, it uses only the gradient of the potential energy, and does not require the calculation of the Hessian matrix. It also parallelises readily, due to the fact that the vast majority of computational cost lies in independent calculations of real forces acting on the $N-1$ intermediate images, which can be performed in parallel. Owing to these advantages, in the present work the NEB method was applied in the transition state searches for the thermal tautomerisation reactions in the photochromic and non-photochromic polymorphs of SCA.

References

[1] IUPAC Compendium of Chemical Terminology 2008.

[2] H. Jónsson, G. Mills, K. W. Jacobsen, *Nudged Elastic Band Method for Finding Minimum Energy Paths of Transitions*, in *Classical and Quantum Dynamics in Condensed Phase Simulations*, Ed. B. J. Berne, G. Ciccotti and D. F. Coker, 385 (World Scientific, 1998).

[3] G. Henkelman, H. Jónsson, *J. Chem. Phys.*, 2000, **113**, 9978.

Appendix B
The Hartree-Fock method

B.1. Introduction

In this Appendix, we present a concise overview of the Hartree-Fock (HF) method, which is a basic method of solving the time-independent Schrödinger equation for many-electron systems. Due to the inherent limitations of the HF method and the availability of better-performing techniques (notably density functional theory, which is only slightly more demanding in terms of computing time), it is now seldom used in calculations for chemical systems. Nevertheless, it forms the starting point for the so-called post-Hartree-Fock methods which attempt to overcome the limitations of the standalone HF method. In particular, coupled cluster methods, which we have used extensively, usually take as input a reference determinant generated by a prior HF calculation. Furthermore, the HF method is a very convenient backdrop for introducing some concepts which will be useful while discussing the more advanced methods later on.

For the sake of brevity, in this and the following Appendices we will sometimes apply some mathematical concepts with little or no formal introduction. In such cases, however, we will always make reference to more comprehensive literature sources, where the mathematical transformations are fleshed out in more detail.

B.2. Atomic units

As is the practice in most modern texts on *ab initio* calculations, we will use the system of units introduced by D. R. Hartree and known as the atomic units. Within that system of units, the numerical values of the following four fundamental constants are set to be equal to 1:

- The electron mass, m_e, which is considered the atomic unit of mass.
- The electron charge, e, which is likewise considered the atomic unit of charge.
- The reduced Planck's constant, $\hbar = \dfrac{h}{2\pi}$

- Coulomb's constant, $\dfrac{1}{4\pi\epsilon_0}$

Derived units of measurement may be constructed from the above fundamental constants. For example, the Bohr radius defined as $a_0 = \dfrac{4\pi\epsilon_0\hbar^2}{m_e e^2}$ is the atomic unit of distance. Its value is 5.2918×10^{-11} m in SI units, or 0.52918 Å. The atomic unit of energy is the Hartree energy, $E_\mathrm{h} = \dfrac{m_e e^4}{(4\pi\epsilon_0\hbar)^2}$, the value of which is 4.35974×10^{-18} J in SI units, or 27.211 eV.

The introduction of atomic units allows a considerable simplification of the equations that arise in quantum-mechanical electronic structure theory. For instance, in SI units the Hamiltonian operator for a system of a number N of electrons interacting with each other and with N_nuc nuclei takes the form:

$$\hat{H} = -\frac{\hbar^2}{2m_e}\sum_{i=1}^{N}\nabla_i^2 - \frac{e^2}{4\pi\epsilon_0}\sum_{i=1}^{N}\sum_{a=1}^{N_\mathrm{nuc}}\frac{Z_a}{r_{ai}} + \frac{e^2}{4\pi\epsilon_0}\sum_{i<j}\frac{1}{r_{ij}}$$

Once we switch to the atomic units and omit all constants whose values are equal to unity, the mathematical form of the Hamiltonian becomes much more transparent:

$$\hat{H} = -\frac{1}{2}\sum_{i=1}^{N}\nabla_i^2 - \sum_{i=1}^{N}\sum_{a=1}^{N_\mathrm{nuc}}\frac{Z_a}{r_{ai}} + \sum_{i<j}\frac{1}{r_{ij}}$$

B.3. The Slater-Condon rules

Before discussing the HF method proper, we will introduce without proof the mathematical formulae called the Slater-Condon rules.[1]

Within the HF method, the many-electron wavefunction Φ will be written in the form of a Slater determinant involving N orthonormal one-electron wavefunctions ϕ_i, called the spinorbitals.

$$\Phi = \frac{1}{\sqrt{N!}}\begin{vmatrix} \phi_1(1) & \phi_1(2) & \dots & \phi_1(N) \\ \phi_2(1) & \phi_2(2) & \dots & \phi_2(N) \\ \vdots & \vdots & \ddots & \vdots \\ \phi_N(1) & \phi_N(2) & \dots & \phi_N(N) \end{vmatrix} \tag{B.1}$$

The notation $\phi_i(j)$ denotes that the i-th spinorbital is a function of the spatial and spin coordinates of the j-th electron. We will defer a further description of the nature of the spinorbitals and the justification for writing down the many-electron wavefunction in the particular form of B.1 until the next subsection.

On many occasions, we will need to calculate the matrix elements of the type $\langle\Phi|\hat{F}|\Phi\rangle$ and $\langle\Phi|\hat{G}|\Phi\rangle$ of operators $\hat{F}$ and $\hat{G}$ with a Slater determinant Φ :

$$\langle\Phi|\hat{F}|\Phi\rangle = \int\int\cdots\int \Phi^*\,\hat{F}\,\Phi\,\mathrm{d}\tau_1\,\mathrm{d}\tau_2\,\cdots\,\mathrm{d}\tau_N$$

$$\langle\Phi|\hat{G}|\Phi\rangle = \int\int\cdots\int \Phi^*\,\hat{G}\,\Phi\,\mathrm{d}\tau_1\,\mathrm{d}\tau_2\,\cdots\,\mathrm{d}\tau_N$$

where $\int\cdots\mathrm{d}\tau_j$ denotes integration with respect to the spatial and spin coordinates of the j-th electron. The operator $\hat{F}$ will be defined by a sum of one-electron operators $\hat{h}(i)$:

$$\hat{F} = \sum_{i=1}^{N}\hat{h}(i)$$

Each one-electron operator $\hat{h}(i)$ acts on the spinorbitals of the i-th electron: $\phi_1(i)$, $\phi_2(i)$, ... , up to $\phi_N(i)$, but the one-electron operators are otherwise identical.

$\hat{G}$, on the other hand, will be a sum of two-electron operators $\hat{g}(i,j)$:

$$\hat{G} = \sum_{i=1}^{N}\sum_{i<j}^{N}\hat{g}(i,j)$$

As with the one-electron operators, all two-electron operators $\hat{g}(i,j)$ will be identical except for the electron indices i and j.

The Slater-Condon rules tell us how to express the matrix elements of the type $\langle\Phi|\hat{F}|\Phi\rangle$ and $\langle\Phi|\hat{G}|\Phi\rangle$ as matrix elements of the operators $\hat{h}$ and $\hat{g}$ with the spinorbitals ϕ_i. We will introduce the following notation. $\langle i|\hat{h}|j\rangle$ will be the matrix element of the one-electron operator $\hat{h}(1)$ with spinorbitals $\phi_i(1)$ and $\phi_j(1)$:

$$\langle i|\hat{h}|j\rangle = \int \phi_i^*(1)\,\hat{h}(1)\,\phi_j(1)\,\mathrm{d}\tau_1$$

where $\int \cdots \mathrm{d}\tau_1$ denotes the integration over the spatial and the spin coordinates of electron 1. On the other hand, $\langle ij|kl\rangle$ will be the matrix element of the two-electron operator $\hat{g}(1,2)$ with spinorbitals $\phi_i(1)$, $\phi_j(2)$, $\phi_k(1)$ and $\phi_l(2)$:

$$\langle ij|kl\rangle = \int\int \phi_i^*(1)\,\phi_j^*(2)\,\hat{g}(1,2)\,\phi_k(1)\,\phi_l(2)\,\mathrm{d}\tau_1\,\mathrm{d}\tau_2$$

Equipped with this notation, we may now write down the Slater-Condon rules. The **first Slater-Condon rule** deals with the matrix elements $\langle\Phi|\hat{F}|\Phi\rangle$ and $\langle\Phi|\hat{G}|\Phi\rangle$:

$$\langle\Phi|\hat{F}|\Phi\rangle = \sum_{i=1}^{N}\langle i|\hat{h}|i\rangle$$

$$\langle\Phi|\hat{G}|\Phi\rangle = \frac{1}{2}\sum_{i=1}^{N}\sum_{j=1}^{N}\langle ij|ij\rangle - \frac{1}{2}\sum_{i=1}^{N}\sum_{j=1}^{N}\langle ij|ji\rangle$$

Suppose now that from the Slater determinant Φ, we have generated another Slater determinant Φ' by replacing the row containing spinorbital ϕ_k with a row containing another spinorbital ϕ'_k which is orthonormal to all other spinorbitals (including ϕ_k); such a situation will arise in our discussion of the coupled cluster method in Appendix C. Regarding the matrix elements $\langle\Phi|\hat{F}|\Phi'\rangle$ and $\langle\Phi|\hat{G}|\Phi'\rangle$, the **second Slater-Condon rule** states that:

$$\langle\Phi|\hat{F}|\Phi'\rangle = \langle k|\hat{h}|k'\rangle$$

and

$$\langle\Phi|\hat{G}|\Phi'\rangle = \sum_{i=1}^{N}\langle ki|k'i\rangle - \sum_{i=1}^{N}\langle ki|ik'\rangle$$

We can go further, and create from Φ a doubly substituted determinant Φ'' by replacing from two spinorbitals ϕ_k and ϕ_l with new spinorbitals ϕ'_k and ϕ'_l. Again, ϕ'_k and ϕ'_l must be orthogonal to each other and to all other spinorbitals. Then, the **third Slater-Condon rule** tells us that:

$$\langle\Phi|\hat{F}|\Phi''\rangle = 0$$

$$\langle\Phi|\hat{G}|\Phi''\rangle = \langle kl|k'l'\rangle - \langle kl|l'k'\rangle$$

Finally, if we generate a determinant Φ^{3+} by replacing three or more spinorbitals from the original determinant Φ, again making sure that the spinorbitals introduced into Φ''' are orthogonal to each other and to the other spinorbitals, the **fourth Slater-Condon rule** states that the matrix elements $\langle\Phi|\hat{F}|\Phi^{3+}\rangle$ and $\langle\Phi|\hat{G}|\Phi^{3+}\rangle$ will both be zero.

B.4. The variational theorem

We will also make use of the variational theorem, which states that for a given system, the expectation value of the Hamiltonian calculated with any trial wavefunction φ is higher or equal to the energy E_0 of the ground-state wavefunction ψ_0:

$$\frac{\langle\varphi|\hat{H}|\varphi\rangle}{\langle\varphi|\varphi\rangle} \geq \frac{\langle\psi_0|\hat{H}|\psi_0\rangle}{\langle\psi_0|\psi_0\rangle} = E_0 \tag{B.2}$$

The proof is very straightforward. Without loss of generality, we can assume that the trial wavefunction φ is normalised:

$$\langle\varphi|\varphi\rangle = 1$$

Let us denote the expectation value of the Hamiltonian $\hat{H}$ with the normalised trial wavefunction by ϵ :

$$\langle\varphi|\hat{H}|\varphi\rangle = \epsilon \tag{B.3}$$

The Hamiltonian $\hat{H}$ has a set of orthonormal eigenfunctions ψ_n with eigenvalues E_n, which we will index in order of nondecreasing energy:

$$\hat{H}\,\psi_n = E_n\,\psi_n \ \text{, and} \quad E_0 \leq E_1 \leq E_2 \leq E_3 \leq ...$$

Because the eigenfunctions ψ_n form a complete set, the trial function φ may be expressed as a linear combination of these functions with complex coefficients c_n :

$$\varphi = \sum_n c_n\,\psi_n \tag{B.4}$$

By substituting the expansion B.4 into the normalisation condition $\langle\varphi|\varphi\rangle = 1$, we obtain

$$\langle \sum_m c_m \psi_m \mid \sum_n c_n \psi_n \rangle = \sum_m \sum_n c_m^* c_n \langle\psi_m|\psi_n\rangle = 1$$

Since the eigenfunctions ψ_n are orthonormal ($\langle\psi_m|\psi_n\rangle = \delta_{mn}$), we have

$$\sum_n c_n^* c_n = 1 \tag{B.5}$$

If we now also substitute the expansion B.4 into equation B.3, we find

$$\epsilon = \langle \sum_m c_m \psi_m | \hat{H} | \sum_n c_n \psi_n \rangle = \sum_m \sum_n c_m^* c_n \langle\psi_m|\hat{H}|\psi_n\rangle =$$

$$= \sum_m \sum_n c_m^* c_n E_n \langle\psi_m|\psi_n\rangle = \sum_n c_n^* c_n E_n \tag{B.6}$$

Let us subtract E_0 from the left-hand side of the equation B.6, and $E_0 = E_0 \sum_n c_n^* c_n$ (where, according to equation B.5, $\sum_n c_n^* c_n = 1$) from the right-hand side.

$$\epsilon - E_0 = \sum_n c_n^* c_n (E_n - E_0) \tag{B.7}$$

In equation B.7, $c_n^* c_n$ is the square modulus of the coefficient c_n, and must therefore be non-negative. Likewise, because E_0 is the ground-state energy, the difference $E_n - E_0$ is non-negative for any n. It follows that

$$\epsilon - E_0 \geq 0$$

Which proves the variational theorem.

The existence of the variational theorem naturally suggests a criterion for choosing from among many trial wavefunctions the "best" trial wavefunction, which is to say, the one that best approximates the ground-state energy E_0 : it is the one that corresponds to the lowest expectation value of the Hamiltonian. What is more, if we can write down a trial wavefunction $\varphi = \varphi(\mathbf{r}_1, \sigma_1, \mathbf{r}_2, \sigma_2, ...; a_1, a_2, ...)$ that is a function of the electrons' spatial and spin coordinates, and also depends on certain parameters $a_1, a_2, ...$, which could in general be numbers or more complex entities such as functions, then we may search for the best such trial wavefunction

by minimising the expectation value $E = \langle\varphi|\hat{H}|\varphi\rangle/\langle\varphi|\varphi\rangle$ in the space of the parameters $a_1, a_2, \ldots$. We will use precisely this strategy when searching for the best wavefunction within the HF approximation, and again in Appendix D when discussing the density function theory method.

B.5. The single-determinant approximation

We can now proceed to examine the HF method itself. As mentioned in Section 2, the defining feature of the HF method is that the N-electron wavefunction Φ is taken to be the Slater determinant of one-electron wavefunctions ϕ_i, which are referred to as spinorbitals.

$$\Phi = \frac{1}{\sqrt{N!}} \begin{vmatrix} \phi_1(1) & \phi_1(2) & \ldots & \phi_1(N) \\ \phi_2(1) & \phi_2(2) & \ldots & \phi_2(N) \\ \vdots & \vdots & \ddots & \vdots \\ \phi_N(1) & \phi_N(2) & \ldots & \phi_N(N) \end{vmatrix} \tag{B.8}$$

The spinorbitals must satisfy the orthonormality condition

$$\langle i|j\rangle = \delta_{ij} = \begin{cases} 1 \text{ if } i = j \\ 0 \text{ otherwise} \end{cases}$$

The prefactor of $\frac{1}{\sqrt{N!}}$ ensures that the overall wavefunction is normalised.

Each spinorbital contained in the Slater determinant is a function of the spatial position $\mathbf{r}$ of a single electron, most commonly defined by the three Cartesian coordinates (x, y, z), and of that electron's spin coordinate σ, which is discrete and only takes values of $\frac{1}{2}$ and $-\frac{1}{2}$. The shorthand notation $\phi_i(k)$ which appears in the definition of the Slater determinant denotes the i-th spinorbital written as a function of spatial and spin coordinates the k-th electron,

$$\phi_i(\mathbf{r}_k, \sigma_k) = \phi_i(k)$$

The general mathematical form of a spinorbital is

$$\phi_i(\mathbf{r}, \sigma) = \varphi_{i1}(\mathbf{r})\,\alpha(\sigma) + \varphi_{i2}(\mathbf{r})\,\beta(\sigma) \tag{B.9}$$

where $\varphi_{i1}(\mathbf{r})$ and $\varphi_{i2}(\mathbf{r})$ are the spinorbital's spatial components. They, and the spinorbital, may in general adopt complex values, but in most practical implementations of the HF method these functions are restricted to being real-valued.

$\alpha(\sigma)$ and $\beta(\sigma)$ are the basis function in the spin space, and are given by

$$\alpha(\sigma) = \begin{cases} 1 & \text{for} \quad \sigma = \frac{1}{2} \\ 0 & \text{for} \quad \sigma = -\frac{1}{2} \end{cases}$$

$$\beta(\sigma) = \begin{cases} 0 & \text{for} \quad \sigma = \frac{1}{2} \\ 1 & \text{for} \quad \sigma = -\frac{1}{2} \end{cases}$$

Because interchanging any two colums of a matrix has the same effect as multiplying its determinant by -1, a wavefunction written in the form of a Slater determinant inherently satisfies the postulate of quantum mechanics known as the Pauli exclusion principle, which states that the wavefunction must be antisymmetric with respect to the exchange of two identical fermions. A consequence of the Pauli principle is that two electrons with the same spin coordinate cannot occupy the same position in space, and indeed, if write down a Slater determinant in which two electrons (say, j and l) have the same spatial coordinates:

$$\Phi = \frac{1}{\sqrt{N!}} \begin{vmatrix} \phi_1(1) & \dots & \phi_1(j=l) & \dots & \phi_1(j=l) & \dots & \phi_1(N) \\ \phi_2(1) & \dots & \phi_2(j=l) & \dots & \phi_2(j=l) & \dots & \phi_2(N) \\ \vdots & & \vdots & & \vdots & & \vdots \\ \phi_N(1) & \dots & \phi_N(j=l) & \dots & \phi_N(j=l) & \dots & \phi_N(N) \end{vmatrix}$$

then the j-th and l-th columns of the Slater determinant in this determinant are identical, and from the general properties of determinants, the value of a determinant whose two columns or two rows are identical must be zero. Hence, the probability of two electrons of the same spin coordinate to occupy the exact same spatial position is zero. What is more, from the continuity properties of the wavefunction, it follows that the probability of finding two electrons with the same spin coordinate at a short finite distance from each other is very low. Due to its rooting in the Pauli principle, this mutual avoidance of electrons with the same spin coordinate is commonly referred to as the exchange hole, and the underlying quantum mechanical effect as the exchange interaction.

In addition to meeting this fundamental condition, the choice of the Slater

determinant as the functional form of a many-electron wavefunction holds a vast practical advantage: as we shall see in due course, it amounts to the simplification of the many-body problem to an effectively one-body problem.

There is also, however, a price to pay for writing the wavefunction as a Slater determinant. Namely, the exact wavefunction of a many-electron system never takes the form of a single Slater determinant, and therefore in the HF method we are always working with an approximate wavefunction. As a result, from the variational theorem it follows that the HF wavefunction always corresponds to a higher energy than the exact wavefunction. For a given system, there exists a lowest energy that can be obtained with a single-determinant wavefunction; this energy is called the Hartree-Fock limit E_{HF}. The difference between the exact energy and the Hartree-Fock limit defines the correlation energy of the system, E_c:

$$E_c = E_{\mathrm{exact}} - E_{\mathrm{HF}} \tag{B.10}$$

The correlation energy is always negative, and typically takes values of the order of 1% of the exact energy. Its existence, and the fact that the HF method does not deliver an exact solution to the Schrödinger equation, is often described pictorially as originating from the HF method's failure to correctly describe the tendency of electrons to avoid each other due to their mutual Coulombic repulsion.[2,3] This mutual avoidance of electrons due to their electrostatic repulsion is termed electron correlation, and is a separate phenomenon from the exchange interaction, which is a consequence of the Pauli principle. We note, however, that a single Slater determinant *may*, under some conditions, describe this avoidance to a certain extent. A textbook example is the dissociating hydrogen molecule in which, for internuclear distances over a certain threshold value, the lowest-energy UHF determinant does predict a mutual separation of the electrons.[4] We therefore prefer a slightly different interpretation[5] of the correlation energy, which is more in keeping with the definition given by equation B.10: that it is the error in energy which results solely from the approximation of the wavefunction by a single Slater determinant, and that the inadequate description of electron correlation by the HF method is another manifestation of this approximation.

B.6. Derivation of the Fock equations

It is now time for us to bring together the ideas outlined in the previous three Sections. We will derive the Fock equations that define the best spinorbitals, which is to say, the spinorbitals that minimise the expectation value of the Hamiltonian.

The Hamiltonian for a set of N electrons interacting with each other in the external potential of a number N_{nuc} of nuclei is given by

$$\hat{H} = -\frac{1}{2}\sum_{i=1}^{N} \nabla_i^2 - \sum_{i=1}^{N}\sum_{a=1}^{N_{\text{nuc}}} \frac{Z_a}{r_{ai}} + \sum_{i<j} \frac{1}{r_{ij}} \tag{B.11}$$

where the indices i and j run over the electrons and a runs over the nuclei. The first term on the right-hand side of equation B.11 is the kinetic energy operator for the electrons, the second term corresponds to the electrostatic attractions between the electrons and the nuclei, and the third term is the mutual electrostatic repulsion between the electrons. We may collect the first and second terms into a sum over one-electron operators $\hat{h}(i)$

$$-\frac{1}{2}\sum_{i=1}^{N} \nabla_i^2 - \sum_{i=1}^{N}\sum_{a=1}^{N_{\text{nuc}}} \frac{Z_a}{r_{ai}} = \sum_{i=1}^{N} \hat{h}(i) \quad \text{where} \quad \hat{h}(i) = -\frac{1}{2}\nabla_i^2 - \sum_{a=1}^{N_{\text{nuc}}} \frac{Z_a}{r_{ai}}$$

And we may likewise write down the third term as a sum over two-electron operators $\hat{g}(i,j)$

$$\sum_{i<j} \frac{1}{r_{ij}} = \sum_{i<j} \hat{g}(i,j) \quad \text{where} \quad \hat{g}(i,j) = \frac{1}{r_{ij}}$$

The Hamiltonian may then be expressed in the simple form:

$$\hat{H} = \sum_{i=1}^{N} \hat{h}(i) + \sum_{i<j} \hat{g}(i,j) \tag{B.12}$$

Its expectation value is given by

$$E = \langle \Phi | \hat{H} | \Phi \rangle = \int\int \ldots \int \Phi^* \, \hat{H} \, \Phi \, \mathrm{d}\tau_1 \, \mathrm{d}\tau_2 \, \ldots \mathrm{d}\tau_N \tag{B.13}$$

Having separated the Hamiltonian into a sum over one-electron operators $\hat{h}(i)$ and a sum over two-electron operators $\hat{g}(i,j)$, we may rewrite the expression B.13 for

the energy E as:

$$E = \langle\Phi| \sum_{i=1}^{N} \hat{h}(i) |\Phi\rangle + \langle\Phi| \sum_{i<j} \hat{g}(i,j) |\Phi\rangle \tag{B.14}$$

With the expression for E written in this form, we apply the first Slater-Condon rule, thus obtaining an expression for energy which involves the matrix elements of the operators $\hat{h}$ and $\hat{g}$ with the spinorbitals ϕ_i :

$$E = \sum_{i=1}^{N} \langle i|\hat{h}|i\rangle + \frac{1}{2}\sum_{i=1}^{N}\sum_{j=1}^{N} \langle ij|ij\rangle - \frac{1}{2}\sum_{i=1}^{N}\sum_{j=1}^{N} \langle ij|ji\rangle \tag{B.15}$$

Equation B.15 shows explicitly that the expectation value of the Hamiltonian is a functional of the spinorbitals ϕ_i. In the spirit of the variational theorem, we will now search for the spinorbitals that minimise that functional.

Since all spinorbitals ϕ_i must be orthonormal at all times, the minimisation must be carried out subject to the constraints that

$$\langle i|j\rangle = \delta_{ij} \quad \text{for any two spinorbitals } i, j$$

The standard method for searching for stationary points of constrained functions is the method of Lagrange multipliers. In this method, we create a new function (the so-called auxiliary function) by subtracting from the original constrained function all constraint equations multiplied by scalar numbers called the Lagrange multipliers, the values of which are unknown, initially at least. We then minimise the auxiliary function as though the constraints did not apply any more. The exact same strategy applies to functionals.

In our case, the auxiliary functional takes the form:

$$f = E - \sum_{i=1}^{N}\sum_{j=1}^{N} \lambda_{ij}\langle i|j\rangle =$$

$$= \sum_{i=1}^{N} \langle i|\hat{h}|i\rangle + \frac{1}{2}\sum_{i=1}^{N}\sum_{j=1}^{N} \langle ij|ij\rangle - \frac{1}{2}\sum_{i=1}^{N}\sum_{j=1}^{N}\langle ij|ji\rangle - \sum_{i=1}^{N}\sum_{j=1}^{N} \lambda_{ij}\langle i|j\rangle \tag{B.16}$$

The numbers λ_{ij} are the Lagrange multipliers, and they have the dimension of energy. The necessary condition for f being at a minimum is that the variation of f (which is to say, the linear part of the change in the value of f brought about by

a change in the spinorbitals ϕ_i) must be equal to zero:

$$\delta f = 0 \tag{B.17}$$

Now because the spinorbitals are, in general, complex-valued, we could independently vary both the spinorbitals ϕ_i and the complex conjugates ϕ_i^* of the spinorbitals. It is, however, sufficient to vary either only the spinorbitals or their complex conjugates; we will end up with the same final result. We will elect to vary only the complex conjugates of the spinorbitals, obtaining a new set of complex conjugates $\phi_i^{*\prime} = \phi_i^* + \delta\phi_i^*$. The variation in the i-th complex conjugate is then $\delta\phi_i^*$, or δi^* in shorthand notation.

The variation of f can be expanded out as:

$$\delta f = \sum_{i=1}^{N} \langle \delta i|\hat{h}|i\rangle + \frac{1}{2}\sum_{i=1}^{N}\sum_{j=1}^{N} \langle \delta ij|ij\rangle - \frac{1}{2}\sum_{i=1}^{N}\sum_{j=1}^{N} \langle \delta ij|ji\rangle + \frac{1}{2}\sum_{i=1}^{N}\sum_{j=1}^{N} \langle i\delta j|ij\rangle -$$

$$-\frac{1}{2}\sum_{i=1}^{N}\sum_{j=1}^{N} \langle i\delta j|ji\rangle - \sum_{i=1}^{N}\sum_{j=1}^{N} \lambda_{ij}\langle \delta i|j\rangle = 0 \tag{B.18}$$

We would like to convert the above equation B.18 into the form $\langle \delta i|F\rangle = 0$, where F will be some function of the spinorbitals. Because δi^* may be chosen arbitrarily, it will then follow that $F = 0$ for any i. At present, equation B.18 contains the variations δi as well as δj, so we must get rid of the latter.

From the definition of the matrix element $\langle ij|kl\rangle$ it follows that

$$\langle i\delta j|ij\rangle = \langle j\delta i|ji\rangle = \langle \delta ij|ij\rangle \quad \text{and} \quad \langle i\delta j|ji\rangle = \langle j\delta i|ij\rangle = \langle \delta ij|ji\rangle$$

Hence,

$$\delta f = \sum_{i=1}^{N} \langle \delta i|\hat{h}|i\rangle + \sum_{i=1}^{N}\sum_{j=1}^{N} \langle \delta ij|ij\rangle - \sum_{i=1}^{N}\sum_{j=1}^{N} \langle \delta ij|ji\rangle +$$

$$+\sum_{i=1}^{N}\sum_{j=1}^{N} \varepsilon_{ij}\langle \delta i|j\rangle = 0 \tag{B.19}$$

As required, the equation B.19 takes the form $\langle \delta i | F \rangle = 0$. Let us now rewrite it in full integral form:

$$\delta f = \sum_{i=1}^{N} \int \delta\phi_i^*(1)\, \hat{h}\, \phi_i(1)\, \mathrm{d}\tau_1 +$$

$$+ \sum_{i=1}^{N} \sum_{j=1}^{N} \int\int \delta\phi_i^*(1)\, \phi_j^*(2)\, \frac{1}{r_{12}}\, \phi_i(1)\, \phi_j(2)\, \mathrm{d}\tau_1\, \mathrm{d}\tau_2 -$$

$$- \sum_{i=1}^{N} \sum_{j=1}^{N} \int\int \delta\phi_i^*(1)\, \phi_j^*(2)\, \frac{1}{r_{12}}\, \phi_j(1)\, \phi_i(2)\, \mathrm{d}\tau_1\, \mathrm{d}\tau_2 +$$

$$- \sum_{i=1}^{N} \sum_{j=1}^{N} \int\int \lambda_{ij}\, \delta\phi_i^*(1)\, \phi_j(2)\, \mathrm{d}\tau_1\, \mathrm{d}\tau_2 \; = 0 \tag{B.20}$$

As explained previously, from the fact that the choice of the variation δi^* is arbitrary, it follows that for $i = 1, 2, ..., N$

$$\hat{h}\phi_i(1) + \sum_{j=1}^{N} \int \phi_j^*(2)\, \frac{1}{r_{12}}\, \phi_i(1)\, \phi_j(2)\, \mathrm{d}\tau_2 -$$

$$- \sum_{j=1}^{N} \int \phi_j^*(2)\, \frac{1}{r_{12}} \phi_j(1)\, \phi_i(2)\, \mathrm{d}\tau_2 - \sum_{j=1}^{N} \lambda_{ij}\phi_j(1) = 0 \tag{B.21}$$

We would now like to simplify the appearance of this set of equations. In order to do so, let us introduce the Coulomb and exchange operators $\hat{J}$ and $\hat{K}$, which are defined by their action on a generic function $u(\mathbf{r}, \sigma)$:

$$\hat{J}(1)\, u(1) = \sum_{j=1} \hat{J}_j(1)\, u(1) \;\text{ , where }\; \hat{J}_j(1)\, u(1) = \int \phi_j^*(2)\, \frac{1}{r_{12}}\, u(1)\, \phi_j(2)\, \mathrm{d}\tau_2$$

$$\hat{K}(1)\, u(1) = \sum_{j=1} \hat{K}_j(1)\, u(1) \;\text{ , where }\; \hat{K}_j(1)\, u(1) = \int \phi_j^*(2)\, \frac{1}{r_{12}}\, \phi_j(1)\, u(2)\, \mathrm{d}\tau_2$$

The set of equations given by B.21 then becomes:

$$\hat{h}(1)\phi_i(1) + \hat{J}(1)\phi_i(1) - \hat{K}(1)\phi_i(1) = \sum_{j=1}^{N} \lambda_{ij}\phi_j(1) \quad \text{for} \quad i = 1, 2, ..., N \tag{B.22}$$

On the left-hand side of the above equation B.22, there are three operators which act only on the i-th spinorbital, but on the right-hand side, all N spinorbitals appear. It can be shown, however,[6] that without affecting the expectation value

of the Hamiltonian, or indeed any other physical observable, the spinorbitals may be chosen in such a way that the matrix of the Lagrange multipliers λ_{ij} is diagonal (which is to say, only the multipliers with $i = j$ take non-zero values). The special set of spinorbitals which achieve this is called the canonical spinorbitals.

Once the off-diagonal Lagrange multipliers have been eliminated in this manner, we obtain the Fock equations that define the spinorbitals ϕ_i which minimise the expectation value of the Hamiltonian:

$$\boxed{\hat{F}(1)\phi_i(1) = \varepsilon_i\phi_i(1) \quad \text{for} \quad i = 1, 2, ..., N} \tag{B.23}$$

where $\hat{F}(1) = \hat{h}(1) + \hat{J}(1) - \hat{K}(1)$ is the Fock operator, and $\varepsilon_i = \lambda_{ii}$ is the so-called spinorbital energy associated with the i-th spinorbital. N such equations are obtained, one for each spinorbital ϕ_i. Because each of the Coulomb and exchange operators involve all N spinorbitals, and not just the i-th spinorbitals, the Fock equations are not eigenvalue equations, but rather pseudo-eigenvalue equations, and are coupled to one another by the Coulomb and exchange operators.

A connection may be drawn between the spinorbital energies and the total energy of the system. To show it, let us backtrack to equation B.15 which specifies the total energy of the entire system, and write it in a new way:

$$E = \sum_{i=1}^{N} \langle i|\hat{h}|i\rangle + \frac{1}{2}\sum_{i=1}^{N}\sum_{j=1}^{N} \langle ij|ij\rangle - \frac{1}{2}\sum_{i=1}^{N}\sum_{j=1}^{N} \langle ij|ji\rangle =$$

$$= \sum_{i=1}^{N} h_{ii} + \frac{1}{2}\sum_{i=1}^{N}\sum_{j=1}^{N} (J_{ij} - K_{ij}) \tag{B.24}$$

where $h_{ii} = \langle i|\hat{h}|i\rangle$ is a matrix element of $\hat{h}$, $J_{ij} = \langle ij|ij\rangle$ is a Coulomb integral, and $K_{ij} = \langle ij|ji\rangle$ is an exchange integral.

The spinorbital energy ε_i may be calculated by projecting the Fock equation onto the corresponding spinorbital:

$$\varepsilon_i = \langle i|\hat{h}|i\rangle + \langle i|\hat{J}|i\rangle - \langle i|\hat{K}|i\rangle = h_{ii} + \sum_{j=1}^{N} J_{ij} - \sum_{j=1}^{N} K_{ij} \tag{B.25}$$

From a comparison of equations B.24 and B.25, it follows that the total energy can be expressed as:

$$E = \sum_{i=1}^{N} \varepsilon_i - \frac{1}{2} \sum_{i=1}^{N} \sum_{j=1}^{N} J_{ij} + \frac{1}{2} \sum_{i=1}^{N} \sum_{j=1}^{N} K_{ij}$$

We see that the in the HF method, the total energy E is not simply the sum of the spinorbital energies ε_i, but it also involves double sums over the Coulomb and exchange integrals, J_{ij} and K_{ij}.

B.7. The linear combination of atomic orbitals method

As things stand now, the Fock equations in the form given by equation B.23 are not particularly handy for numerical calculations because they do not provide a practically usable prescription to calculate the spinorbitals. To obtain this, we will apply another approximation: the functional form of the spinorbitals will no longer be completely general, but instead each spinorbital ϕ_i will be expressed by a linear combination of one-electron functions $\chi_j(\mathbf{r}, \sigma)$, which will be called basis functions.

$$\phi_i(\mathbf{r}, \sigma) = \sum_{j=1}^{M} c_{ji}\, \chi_j(\mathbf{r}, \sigma) \tag{B.26}$$

c_{ji} is the coefficient of the basis function $\chi_j(\mathbf{r}, \sigma)$ in the spinorbital ϕ_i. At this stage, for the sake of generality and transparent formulae, we specify the basis functions as functions of both the electron position and spin. Collectively, the M basis functions are called the basis set. Because basis set construction is a complex subject in its own right, we discuss it separately in the next Section. For now, suffice it to say that the basis functions are chosen according to the physical structure of the system, usually the positions of the nuclei, and that since they often qualitatively resemble the orbitals of hydrogen-like atoms, the idea of writing the spinorbitals as linear combinations of basis functions is known in the literature as the linear combination of atomic orbitals (LCAO) method.

In order to be able to generate N linearly independent spinorbitals, where N is the number of electrons, we must take at least N linearly independent basis functions (the spinorbitals must be linearly independent, because if they are not, due to the general properties of determinants the Slater determinant becomes zero). In practical calculations, the number M of basis functions is always greater

than the number of electrons ($M > N$). As will become evident in the following discussion, from M basis functions we always generate M spinorbitals, which is more than is necessary to construct the Slater determinant. We therefore need some criterion for which spinorbitals to include in the Slater determinant that represents the wavefunction, and which to exclude. Although this is not guaranteed to lead to the lowest total energy E, it is usual in practice to include in the Slater determinant the N spinorbitals with the lowest energies ε_i, which are then called the occupied spinorbitals. The remaining $M - N$ spinorbitals, called the unoccupied or virtual spinorbitals, are treated as a byproduct of the LCAO method, and are not included in the Slater determinant.

Let us now return to equation B.23 which defines the best spinorbitals. By substituting the expansion B.26 into B.23, we obtain:

$$\sum_{j=1}^{M} c_{ji}\, \hat{F}(1)\, \chi_j(1) = \varepsilon_i \sum_{j=1}^{M} c_{ij}\, \chi_j(1) \tag{B.27}$$

We will now multiply both sides of equation B.27 by the complex conjugate of a basis function $\chi_k(1)$:

$$\sum_{j=1}^{M} c_{ji}\, \chi_k^*(1)\, \hat{F}(1)\, \chi_j(1) = \varepsilon_i \sum_{j=1}^{M} c_{ij}\, \chi_k^*(1)\, \chi_j(1) \tag{B.28}$$

and then integrate the resulting equation B.28 over the spatial and spin coordinates of electron 1. We obtain

$$\sum_{j=1}^{M} F_{kj}\, c_{ji} = \varepsilon_i \sum_{j=1}^{M} S_{kj}\, c_{ji} \tag{B.29}$$

where

$$F_{kj} = \int \chi_k^*(1)\, \hat{F}(1)\, \chi_j(1)\, \mathrm{d}\tau_1 \tag{B.30}$$

$$S_{kj} = \int \chi_k^*(1)\, \chi_j(1)\, \mathrm{d}\tau_1 \tag{B.31}$$

The integrals F_{ij} can be thought of as being the elements of an $M \times M$ square matrix, which we will call the Fock matrix $\mathbf{F}$. Likewise, we can define the coefficients matrix $\mathbf{c}$, the elements of which will be the orbital coefficients c_{ij}, and the overlap martrix $\mathbf{S}$ whose elements will be the overlap integrals S_{ij}. Let us now recall the

rules of matrix multiplication. Given two $M \times M$ matrices $\mathbf{A}$ and $\mathbf{B}$, their product $\mathbf{AB}$ is another $M \times M$ matrix, the elements of which, denoted $(AB)_{ik}$, are given by:

$$(AB)_{ik} = \sum_{j=1}^{M} A_{ij}\, B_{jk}$$

Thus, on the left-hand side of equation B.29, we recognise the element $(Fc)_{ki}$ of the $M \times M$ matrix $\mathbf{Fc}$.

On the right-hand side of B.29, the sum

$$\sum_{j=1}^{M} S_{kj}\, c_{ji}$$

is likewise the element $(Sc)_{ki}$ of the matrix $\mathbf{Sc}$. In equation B.29, that element appears with the energy of the i-th spinorbital, ε_i, in front of it. In order to be able to cast equation B.29 in matrix form, we will therefore define a matrix $\boldsymbol{\varepsilon}$ whose diagonal elements will be the spinorbital ε_i, and the off-diagonal elements will all be zero:

$$\boldsymbol{\varepsilon} = \begin{bmatrix} \varepsilon_1 & 0 & \dots & 0 \\ 0 & \varepsilon_2 & \dots & 0 \\ \vdots & \vdots & \ddots & \vdots \\ 0 & 0 & \dots & \varepsilon_M \end{bmatrix}$$

Equation B.29 may now be rewritten in the very elegant form known as the Roothaan-Hall equation:

$$\boxed{\mathbf{F}\,\mathbf{c} = \mathbf{S}\,\mathbf{c}\,\boldsymbol{\varepsilon}} \tag{B.32}$$

In this form, the Fock equations lend themselves much better to numerical solution. One more mathematical "trick" is necessary for a practical implementation of the HF method: in equation B.30 which defines the elements of the Fock matrix, we would like to express the Fock operator in a way that involves the basis functions χ_i rather than the spinorbitals ϕ_i. As we shall see, this paves the way for a considerable saving of computing time.

By substituting the definition of the Fock operator into B.30, we obtain

$$F_{kj} = \int \chi_k^*(1)\,\hat{h}(1)\,\chi_j(1)\,\mathrm{d}\tau_1 + \sum_{i=1}^{N} \int \chi_k^*(1)\,\hat{J}_i(1)\,\chi_j(1)\,\mathrm{d}\tau_1 -$$

$$-\sum_{i=1}^{N} \int \chi_k^*(1)\,\hat{K}_i(1)\,\chi_j(1)\,\mathrm{d}\tau_1$$

Let us focus first on the term $\hat{J}_i(1)\,\chi_j(1)$.

$$\hat{J}_i(1)\,\chi_j(1) = \int \phi_i^*(2)\,\frac{1}{r_{12}}\,\chi_j(1)\,\phi_i(2)\,\mathrm{d}\tau_2 =$$

$$= \int \left[\sum_{r=1}^{M} c_{ri}^*\,\chi_r^*(2)\right] \frac{1}{r_{12}}\,\chi_j(1) \left[\sum_{s=1}^{M} c_{si}\,\chi_s(2)\right] \mathrm{d}\tau_2 =$$

$$= \sum_{r=1}^{M}\sum_{s=1}^{M} \int c_{ri}^*\,\chi_r^*(2)\,\frac{1}{r_{12}}\,\chi_j(1)\;c_{si}\,\chi_s(2)\,\mathrm{d}\tau_2$$

We may now express the integrals $\int \chi_k^*(1)\,\hat{J}_i(1)\,\chi_j(1)\,\mathrm{d}\tau_1$ in a more convenient form:

$$\int \chi_k^*(1)\,\hat{J}_i(1)\,\chi_j(1)\,\mathrm{d}\tau_1 =$$

$$= \sum_{r=1}^{M}\sum_{s=1}^{M} c_{ri}^*\,c_{si} \int\int \chi_k^*(1)\,\chi_r^*(2)\,\frac{1}{r_{12}}\,\chi_j(1)\;\chi_s(2)\,\mathrm{d}\tau_1\,\mathrm{d}\tau_2 =$$

$$= c_{ri}^*\,c_{si} \sum_{r=1}^{M}\sum_{s=1}^{M} \langle kr|js\rangle_\chi$$

Where the four-centre integrals $\langle ij|kl\rangle_\chi$ are defined as follows:

$$\langle ij|kl\rangle_\chi = \int\; \chi_i^*(1)\,\chi_j^*(2)\,\frac{1}{r_{12}}\,\chi_k(1)\,\chi_l(2)\,\mathrm{d}\tau_1\,\mathrm{d}\tau_2$$

Let us also define the notation $\langle i|\hat{h}|j\rangle_\chi$ as denoting the matrix element of $\hat{h}$ with the basis functions χ_i and χ_j :

$$\langle i|\hat{h}|j\rangle_\chi = \int \chi_i^*(1)\,\hat{h}(1)\,\chi_j^*(1)\,\mathrm{d}\tau_1$$

The element F_{kj} of the Fock matrix may then be written in the following form, which involves only integrals over the basis functions χ_i :

$$F_{kj} = \langle k|\hat{h}|j\rangle_\chi + \sum_{i=1}^{N}\sum_{r=1}^{M}\sum_{s=1}^{M} c_{ri}^{*}\, c_{si}\, \langle kr|js\rangle_\chi - \sum_{i=1}^{N}\sum_{r=1}^{M}\sum_{s=1}^{M} c_{ri}^{*}\, c_{si}\, \langle kr|sj\rangle_\chi \quad \text{(B.33)}$$

It is usual to simplify the form of equation B.33 by defining the $M \times M$ bond-order matrix $\mathbf{P}$, the elements of which are given by:

$$P_{rs} = \sum_{i=1}^{N} c_{ri}^{*}\, c_{si} \quad \text{(B.34)}$$

Note that the sum in B.34 runs over only the occupied orbitals. The substitution of B.34 into equation B.33 leads to the following expression for the elements of the Fock matrix:

$$F_{kj} = \langle k|\hat{h}|j\rangle_\chi + \sum_{r=1}^{M}\sum_{s=1}^{M} P_{rs}\, \langle kr|js\rangle_\chi - \sum_{r=1}^{M}\sum_{s=1}^{M} P_{rs}\, \langle kr|sj\rangle_\chi \quad \text{(B.35)}$$

Inspection of equation B.35 shows that when iteratively solving the Roothaan-Hall equation for the orbital coefficients c_{ij}, we only need to calculate the integrals $\langle i|\hat{h}|j\rangle_\chi$ and $\langle ij|kl\rangle_\chi$ once and store their values in computer memory. The conventional method of solving the Roothaan-Hall equation takes advantage of this fact, and at each iteration, the bond-order matrix $\mathbf{P}$ and the Fock matrix $\mathbf{F}$ are recalculated using equation B.35 and the stored integrals. In this approach, the Roothan-Hall equation is solved through the application of the following iterative algorithm:

1. Calculate the overlap matrix S, all matrix elements $\langle i|\hat{h}|j\rangle_\chi$, and all four-centre integrals $\langle ij|kl\rangle_\chi$.

2. Form an initial guess for the coefficients matrix $\mathbf{c}$, and also an initial guess for which spinorbitals are occupied, and use these to compute the initial density matrix $\mathbf{P}$.

3. From the known $\mathbf{P}$, calculate the Fock matrix $\mathbf{F}$.

4. Solve the Roothaan-Hall equation $\mathbf{F}\,\mathbf{c} = \mathbf{S}\,\mathbf{c}\,\boldsymbol{\varepsilon}$ with the Fock matrix $\mathbf{F}$ fixed in order to obtain a new coefficients matrix $\mathbf{c}$. Consider the N spinorbitals with the lowest energies as occupied, and the remaining $M - N$ spinorbitals as

unoccupied.

5. Compute the new bond-order matrix $\mathbf{P}$ and return to step 3. Repeat this process until at each iteration, the total energy and the spinorbital coefficients change less than some tolerance values.

Because of the self-consistent manner in which the orbitals are optimised, the Hartree-Fock method in conjunction with the LCAO approximation is often referred to as the self-consistent field (SCF) method.

In calculations employing large numbers of basis functions (here, the definition of "large" depends on the hardware specifications), the storage of the numerous four-centre integrals requires large amounts of disk space, and reading and writing them to the disk at each iteration becomes more time-consuming than re-evaluating them at each iteration. For these reasons, in large calculations it is more efficient evaluate the four-centre integrals whenever required, instead of storing them on the disk. This approach forms the basis of the so-called direct SCF methods of solving the Roothan-Hall equation.

B.8. The unrestricted and restricted Hartree-Fock methods

Until now, other than invoking the LCAO approximation, we have placed no constraints whatsoever on the functional form of the spinorbitals ϕ_i. Hence, each spinorbital took the general form given by equation B.9:

$$\phi_i(\mathbf{r}, \sigma) = \varphi_{i1}(\mathbf{r})\,\alpha(\sigma) + \varphi_{i2}(\mathbf{r})\,\beta(\sigma)$$

and, within the LCAO method, the basis functions χ_j were allowed to depend on electron spin as well as on its spatial position:

$$\phi_i(\mathbf{r}, \sigma) = \sum_{j=1}^{M} c_{ji}\,\chi_j(\mathbf{r}, \sigma)$$

This completely unconstrained variant of the HF method is known in the literature as the general Hartree-Fock (GHF) method. In most practical applications of the HF method, however, additional constraints are imposed on the spinorbitals in order to simplify the calculations. The two most widely used variants of the HF

method that take this approach are the unrestricted Hartree-Fock (UHF) and the restricted Hartree-Fock (RHF) methods.

B.8.1. The unrestricted Hartree-Fock method

The "unrestrictedness" of the UHF method is something of a misnomer because, as we shall see, it is less general than the GHF method (but more general than the RHF method). Within the UHF method, which is applicable to systems with both even and odd numbers of electrons, it is assumed that:

- The spatial components of the spinorbitals, $\varphi_{i1}(\mathbf{r})$ and $\varphi_{i2}(\mathbf{r})$, are real-valued.
- There is no mixing of the spin functions $\alpha(\sigma)$ and $\beta(\sigma)$, which means that for each spinorbital $\phi_i(\mathbf{r},\sigma)$, one of the spatial components $\varphi_{i1}(\mathbf{r})$ and $\varphi_{i2}(\mathbf{r})$ must be zero:

$$\phi_i(\mathbf{r},\sigma) = \begin{cases} \varphi_i(\mathbf{r})\,\alpha(\sigma) & \text{or} \\ \varphi_i(\mathbf{r})\,\beta(\sigma) \end{cases}$$

Each UHF spinorbital may therefore be written as a linear combination of basis functions $\overline{\chi}_j$ that are now functions of only the spatial coordinates, multiplied by the appropriate spin function:

$$\phi_i(\mathbf{r},\sigma) = \begin{cases} \displaystyle\sum_{j=1}^{M} c_{ji}\,\overline{\chi}_j(\mathbf{r})\,\alpha(\sigma) & \text{or} \\ \displaystyle\sum_{j=1}^{M} c_{ji}\,\overline{\chi}_j(\mathbf{r})\,\beta(\sigma) \end{cases}$$

Note that both the α and the β spinorbitals are constructed from the same set of basis functions $\overline{\chi}_j$. Hence, whereas in the GHF method we need at least N spin-dependent basis functions to describe a system of N electrons, in the UHF method we only require a minimum of $\frac{1}{2}N$ basis functions if N is even, or $\frac{1}{2}(N+1)$ if N is odd. This observation illustrates how imposing constraints on the functional form of the spinorbitals allows simplifications in the overall HF calculation.

B.8.2. The restricted Hartree-Fock method

The RHF method, applicable only to systems with an even number of electrons, is defined by the following constraints on the form of the spinorbitals:

- The spatial components of the spinorbitals are real-valued.
- There is no mixing of the spin functions $\alpha(\sigma)$ and $\beta(\sigma)$.
- Because the number of α and β spinorbitals is equal, we may number the spinorbitals ϕ_i such that the spinorbitals with odd indices i are the α spinorbitals, and the spinorbitals with even indices are the β spinorbitals. Within the RHF method, every two spinorbitals with indices $2k$ and $2k-1$, where k is an integer in the range from 1 to $\frac{1}{2}N$, are constrained to have the same spatial component $\varphi_k(\mathbf{r})$:

  $$\phi_{2k-1}(\mathbf{r},\sigma) = \varphi_k(\mathbf{r})\,\alpha(\sigma)$$
  $$\phi_{2k}(\mathbf{r},\sigma) \quad = \varphi_k(\mathbf{r})\,\beta(\sigma)$$

  Together, the spinorbitals ϕ_{2k} and ϕ_{2k-1} are said to form a doubly occupied orbital.

Thus, in the RHF method, we only need to generate $\frac{1}{2}N$ spatial spinorbital components $\varphi_k(\mathbf{r})$ in order to describe all N electrons. As in the UHF method, in the RHF method it is natural to use basis functions that are functions of only the spatial coordinates:

$$\phi_{2k-1}(\mathbf{r},\sigma) = \sum_{j=1}^{M} c_{jk}\,\overline{\chi}_j(\mathbf{r})\,\alpha(\sigma)$$

$$\phi_{2k}(\mathbf{r},\sigma) \quad = \sum_{j=1}^{M} c_{jk}\,\overline{\chi}_j(\mathbf{r})\,\beta(\sigma)$$

In the remainder of the present work, when referring to basis functions, we will therefore always mean the basis functions $\overline{\chi}_j(\mathbf{r})$ that depend only on the spatial coordinates.

B.9. Basis sets

In calculations for molecules (as opposed to condensed phases), the basis set is usually built using functions called Gaussian primitives (sometimes called Gaussian-type orbitals, or GTOs), which take the form:

$$g(x, y, z) = N\, x^l\, y^m\, z^n \exp(-\alpha r^2) \tag{B.27}$$

where $r = \sqrt{x^2 + y^2 + z^2}$, and the parameters N and α are called the prefactor and the exponent, respectively. Each primitive is centered at a nucleus, meaning that the Cartesian coordinates in equation B.27 refer to a coordinate system with that nucleus at the origin. When the integral exponents l, m and n are all equal to zero, we have an s-type, or spherically symmetric primitive; when the sum of these numbers is equal to 1, we have a p-type primitive, when it is equal to 2, a d-type primitive, and so on. It deserves pointing out that the number of d-type primitives that result from the definition B.27 is six (the x^2, y^2, z^2, xy, yz and xz primitives), and not five, as might be expected from a comparison to d orbitals of the hydrogen-like atom, which are five in number.

As an illustration of the functional form of the Gaussian primitives, in Figure B.1 on the next page we plot cross-sections through the xy plane of the s-type, p_x-type, d_{xy}-type and d_{x^2}-type primitives. As can be seen from Figure B.1, the individual primitives do not feature the radial nodes that are characteristic of the orbitals of hydrogen-like atoms. Linear combinations of primitives with prefactors of opposing signs may, however, possess radial nodes.

The construction of basis sets from Gaussian primitives is chiefly motivated by computational convenience, rather than any physical argument for using Gaussian functions specifically. In particular, the usage of Gaussian functions allows fast computation of the two-electron integrals that arise in equation B.35. Often, instead of using individual Gaussian primitives as basis functions, it is more convenient to construct each basis function as a linear combination (in basis set terminology: a contraction) of one or more Gaussian primitives of the same type (same l, m and n, but different α) centered on the same atom. This is especially true of basis functions that are meant to describe core electrons. To show why, we will refer to the observation made by E. Steiner[7] and based on a theorem proved by Kato[8] that the electron density $\rho(\mathbf{r})$ (which is defined by equation D.1 in Appendix D) of an any ground or excited electronic state of an atom or molecule

Figure B.1: Cross-sections through the xy plane of selected Gaussian primitives.

(a) An *s*-type primitive
(plotted with $N = 1$ and $\alpha = 1$)

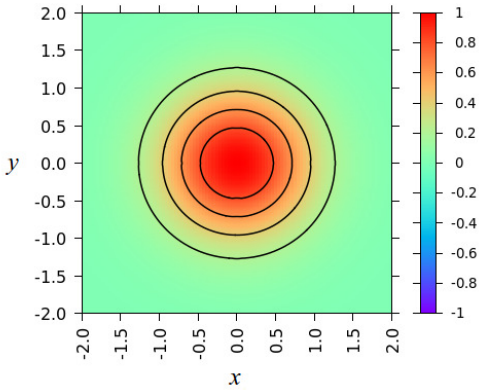

(b) A p_x-type primitive
($N = 2$, $\alpha = 1$)

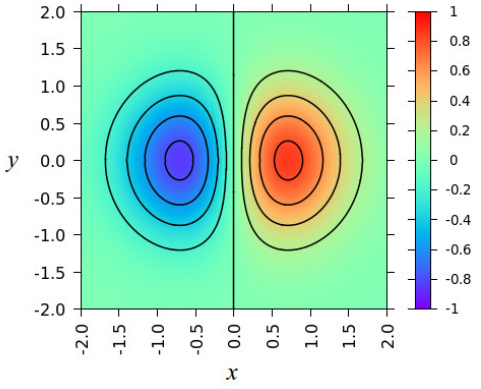

(c) A d_{xy}-type primitive
($N = 7$, $\alpha = 1.5$)

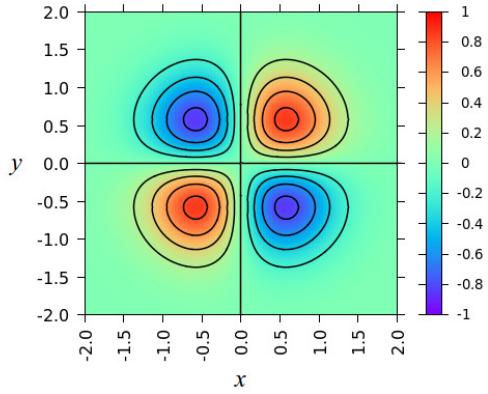

(d) A d_{x^2}-type primitive
($N = 4$, $\alpha = 1.5$)

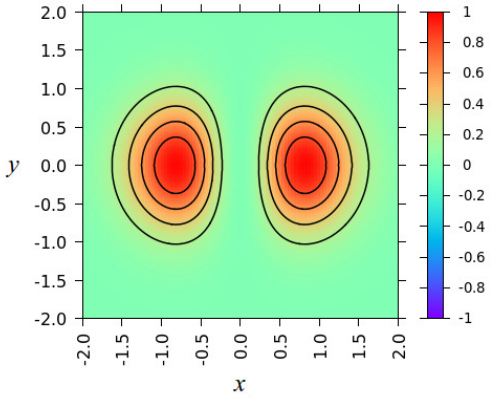

exhibits cusps at the positions of the nuclei. At each such cusp, the spherically averaged derivative of the electron density with respect to the distance r from the nucleus is given by

$$\left(\frac{\partial \rho(\mathbf{r})}{\partial r}\right)_{r=0} = -2\,Z\,\rho(\mathbf{0})$$

where Z is the atomic number and $\rho(\mathbf{0})$ is the electron density at the nucleus. If the electron density at the nucleus is non-zero, then the above condition is satisfied only by an electron density that, in the vicinity of the nucleus, decays as the exponential function:

$$\rho(r) \sim e^{-2Zr}$$

Figure B.2: A linear combination of three (one-dimensional) Gaussian functions, $g(x) = \sum_{i=1}^{3} N_i \, e^{-\alpha_i \, x^2}$, least square-fitted to the exponential function $f(x) = e^{-|x|}$. The quantity $f(x) - g(x)$ is the residual, or fitting error. For the sake of clarity, the curves representing $f(x)$ and $f(x) - g(x)$ have been offset by $+0.2$ and -0.2, respectively.

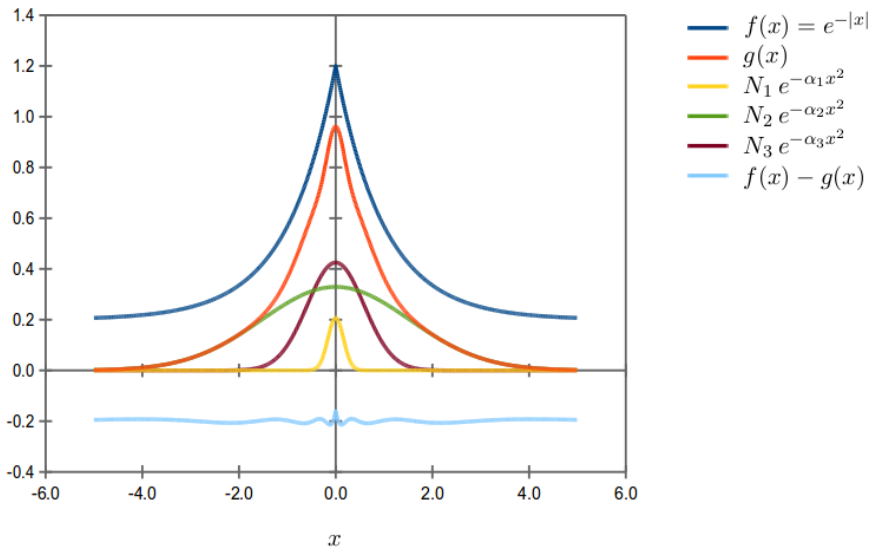

An s-type Gaussian primitive, which behaves as $e^{-\alpha r^2}$, cannot give rise to an electron density which satisfies that condition. A linear combination of Gaussian functions, however, can satisfy it in an approximate manner. In order to show this, in Figure B.2 on the following page we show a least-squares fit of a linear combination of three Gaussian functions to the exponential function $f(x) = e^{-|x|}$, in the range of x from -5 to 5. As seen in Figure B.2, the fit is fairly good. Note, however, that the fitting error is the largest at the cusp (at $x = 0$), which means that at the cusp, the deviations from the desired exponential behaviour are the largest. Accordingly, in good quality basis sets, as many as six Gaussian primitives will be used to construct those basis functions that are meant to describe the core electrons, which are, informally speaking, the closest to the nuclei. On the other hand, the basis functions that describe the valence electrons are not meant to reproduce the electron density cusps that are found at the nuclei, and consequently it is usually sufficient to use from one to three Gaussian primitives to construct a single basis function for the valence electrons. Hence, each basis function is constructed by as a contraction of a few, sometimes only one, Gaussian primitives. (In order to obtain a spin-dependent basis function $\chi_j(\mathbf{r}, \sigma)$, such a basis function would then be multiplied by either of the spin basis functions $\alpha(\sigma)$ and $\beta(\sigma)$.)

In the present work, we have for the most part used the basis sets of Pople and coworkers,[9–12] which are always referred to in the literature by symbols such as "3-21G" or "6-311G(d)" that encode their makeup. Their meaning is as follows.

The number on the left-hand side of the dash (-) is the number of primitives contracted to form each basis function for the inner-shell, or core, electrons. Within the 3-21G basis set, for example, a second-row atom such as carbon has a single basis function for its $1s$ electrons, and this basis function is constructed as a linear combination of three primitives. A third-row atom such as chlorine receives one basis function for the $1s$ electrons, one for the $2s$ electrons, and three for the $2p$ electrons, and each of these basis functions is a contraction of three primitives. Furthermore, all primitives in a given electron shell (here, the primitives of the $2s$ and $2p$ basis functions) share the same exponent. Hydrogen, of course, has no inner electron shells, and it therefore only receives basis functions for valence-shell electrons.

The numbers on the right-hand side of the dash pertain to the basis functions for the valence-shell electrons. Because in quantum chemistry, the accurate description of the valence-shell electrons is much more important than that of the inner-shell electrons, the basis set of Pople and coworkers use multiple sets of contractions for the valence-shell electrons (in basis set parlance, they are split-valence basis sets). Two numbers after the dash indicate that two sets of contractions are used for the valence electrons, and three numbers after the dash indicate that three sets of contractions are used.

To continue with the example of the 3-21G basis set, the fact that there are two numbers ("21") after the dash means that there two sets of contractions (and for this reason, the 3-21 basis set is an example of a so-called double-zeta basis set). In one set of contractions, each basis function is made up of two primitives (the "2" in "21"), and in the other, of only one primitive (the "1" in "21"). Carbon therefore receives a total of eight basis functions for its valence shell: a set of one s-type function and three p-type functions, each a contraction of two primitives, and another set of one s-type function and three p-type functions, each of which is a single primitive. Chlorine, a third-row element, also receives two sets of one s-type and three p-type basis functions for its valence electrons. d-type functions are not included by default for the third-row elements in the Pople's basis sets, and must be added separately as polarisation functions (see below).

To hydrogen, on the other hand, the 3-21G basis set assigns two *s*-type basis functions. One is a linear combination of two primitives, and the other is only a single primitive.

An example of a triple-zeta basis set is the 6-311G basis set, which uses three sets of contractions for the valence shell of each atom.

The "unadorned" basis sets such as 3-21G or 6-311G may also be augmented with further basis functions. Firstly, we may add the so-called diffuse functions, which are basis functions with small exponents that decay slowly on moving away from the nucleus. One "+" symbol, as in 6-31+G, denotes the addition of one *s*-type and three *p*-type diffuse functions on all atoms of the second- and third-row elements (*i.e.*, the heavy atoms). A second "+" symbol (*e.g.* in 6-31++G) means that a single *s*-type diffuse functions is also placed on the hydrogen atoms.

Secondly, the basis set may be expanded with the addition of polarisation functions. For hydrogen, *p*- and *d*- type functions are considered polarisation functions, while for the heavy atoms, the polarisation functions are the *d*- and *f*-type functions. By convention, polarisation functions are listed in brackets at the end of the basis set specification, first the ones placed on the heavy atoms, and then, following a comma, any functions placed on the hydrogens. For instance, in the 6-31G(d) basis set, a set of six *d*-type functions is placed on each heavy atom. In the 6-311G(2d,p) basis set, on the other hand, two sets of six *d*-type functions are placed on each heavy atom, and one set of three *p*-type functions is placed on every hydrogen atom. NB, by default the computational chemistry program Gaussian uses sets of five, instead of six, *d*-type basis functions in some, but not all, basis sets. For example, in the 6-311G(2d,p) basis set, by default Gaussian puts two sets of five *d*-type functions on each heavy atom. In order to request the use of two sets of six *d*-type functions, we must include the "6D" keyword in the job specification.

In production calculations, one would ideally wish to apply a large enough basis set to ensure that the quantities of interest are converged with respect to basis set size, which is to say, that the inclusion of additional basis functions does not significantly change the results. In practice, this is seldom possible due to computational limitations, and hence basis set incompleteness becomes a source

of error in *ab initio* calculations.

The basis set size required to achieve (or approach) basis set convergence depends on the specific quantity being calculated, as well as the electronic structure method used to calculate it. As an illustration of the latter dependency, we have calculated the total energy of the helium atom using a series of basis sets, at the the Hartree-Fock level of theory and at the coupled cluster singles and doubles (CCSD) level. A comprehensive introduction to coupled cluster methods is provided in Appendix C; suffice it to say here that the CCSD method is an electronic structure method that includes electron correlation, and for two-electron systems such as the helium atom provides an exact solution to the electronic Schrödinger equation. In these calculations, we have used the correlation-consistent basis sets of Dunning and coworkers,[13–16] which are designed in such a way as to converge the energy smoothly towards the complete basis set limit. These basis sets are known by their designations of the general form cc-pVXZ, where X = D, T, Q, 5, 6 denotes a double, triple, quadruple, quintuple, sextuple-zeta basis set, respectively. These basis sets include polarisation functions by default. Diffuse functions, on the other hand, are included by adding the prefix "aug-", as in aug-cc-pVTZ.

The calculations were carried out in the electronic structure program Gaussian 09.[17] In the CCSD calculations, the RHF determinant was taken as the reference determinant. The electronic energy was converged to a tolerance of $1.0 \times 10^{-7}\ E_\mathrm{h}$. The basis sets used ranged from aug-cc-pVDZ to aug-cc-pV6Z.

The resulting total energies are given in Table B.1 on the following page, and are also presented in the form of a plot against basis set size in the accompanying Figure B.3. Inspection of Table B.1 and Figure B.3 shows that the CCSD energy (which, in the case of the helium atom, is equivalent to the exact solution within the given basis set) is markedly slower to converge with basis set size than the Hartree-Fock energy. It follows that the correlation energy likewise converges more slowly than the Hartree-Fock energy. This observation is very general and also holds true in calculations that do not recover the total correlation energy within the given basis set.

Table B.1: The energy of a helium atom calculated at the RHF and CCSD levels of theory with the aug-cc-pVXZ basis set series.

Basis set	E(RHF), E_h	E(CCSD), E_h	E_{corr}, E_h [a]
aug-cc-pVDZ	-2.855704	-2.889548	-0.033843
aug-cc-pVTZ	-2.861183	-2.900597	-0.039414
aug-cc-pVQZ	-2.861522	-2.902533	-0.041011
aug-cc-pV5Z	-2.861626	-2.903200	-0.041573
aug-cc-pV6Z	-2.861673	-2.903455	-0.041782

[a] The correlation energy is the difference of the CCSD and RHF energies.

Figure B.3: The energy of a helium atom calculated at the RHF and CCSD levels of theory with the aug-cc-pVXZ basis set series, plotted against basis set size.

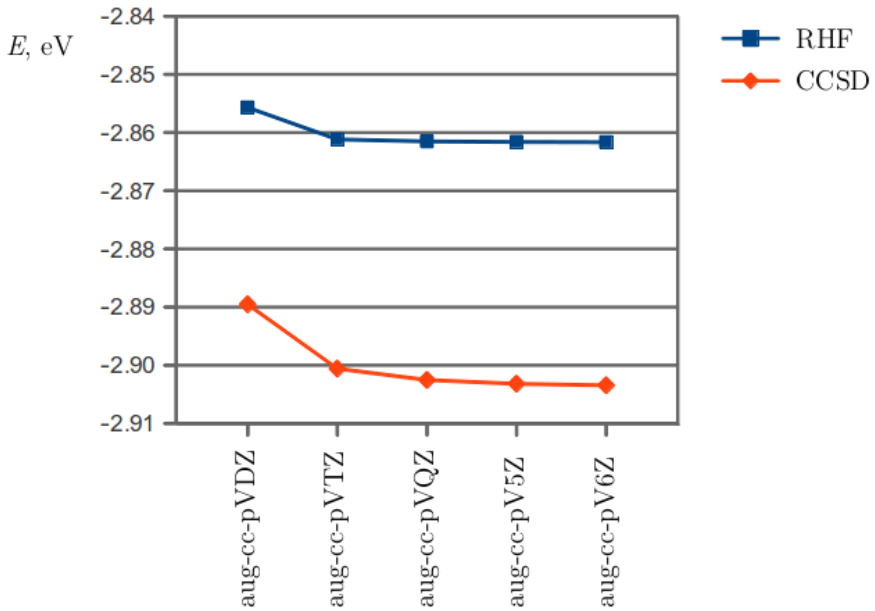

References

[1] L. Piela, *Ideas of Quantum Chemistry*, Elsevier, Amsterdam, 2007, pp. 986-996.

[2] K. I. Ramachandran, G. Deepa, K. Namboori, *Computational Chemistry and Molecular Modeling. Principles and Applications*, Springer-Verlag, Berlin-Heidelberg, 2008, p. 156.

[3] F. Jensen, *Introduction to Computational Chemistry*, John Wiley and Sons, 2nd Ed., 2007, p. 148.

[4] L. Piela, *Ideas of Quantum Chemistry*, Elsevier, Amsterdam, 2007, pp. 369-379.

[5] K. Raghavachari, J. B. Anderson, *J. Phys. Chem.*, 1996, **100**, 12960.

[6] L. Piela, *Ideas of Quantum Chemistry*, Elsevier, Amsterdam, 2007, pp. 338-341.

[7] E. Steiner, *J. Chem. Phys.*, 1963, **39**, 2365.

[8] T. Kato, *Communications on Pure and Applied Mathematics*, 1957, **10**, 151.

[9] W. J. Hehre, R. Ditchfield, J. A. Pople, *J. Chem. Phys.*, 1972, **56**, 2257.

[10] P. C. Hariharan, J. A. Pople, *Theor. Chim. Acta*, 1973, **28**, 213.

[11] J. S. Binkley, J. A. Pople, W. J. Hehre, *J. Am. Chem. Soc.*, 1980, **102**, 939.

[12] M. J. Frisch, J. A. Pople, J. S. Binkley, *J. Chem. Phys.*, 1984, **80**, 3265.

[13] T. H. Dunning, Jr., *J. Chem. Phys.*, 1989, **90**, 1007.

[14] D. E. Woon, T. H. Dunning, Jr., *J. Chem. Phys.*, 1993, **98**, 1358.

[15] D. E. Woon and T. H. Dunning, Jr., *J. Chem. Phys.*, 1994, **100**, 2975.

[16] A. K. Wilson, D. E. Woon, K. A. Peterson, T. H. Dunning, Jr., *J. Chem. Phys.*, 1999, **110**, 7667.

[17] Gaussian 09, Revision A.02, M. J. Frisch, G. W. Trucks, H. B. Schlegel, G. E. Scuseria, M. A. Robb, J. R. Cheeseman, G. Scalmani, V. Barone, B. Mennucci, G. A. Petersson, H. Nakatsuji, M. Caricato, X. Li, H. P. Hratchian, A. F. Izmaylov, J. Bloino, G. Zheng, J. L. Sonnenberg,

M. Hada, M. Ehara, K. Toyota, R. Fukuda, J. Hasegawa, M. Ishida, T. Nakajima, Y. Honda, O. Kitao, H. Nakai, T. Vreven, J. A. Montgomery, Jr., J. E. Peralta, F. Ogliaro, M. Bearpark, J. J. Heyd, E. Brothers, K. N. Kudin, V. N. Staroverov, R. Kobayashi, J. Normand, K. Raghavachari, A. Rendell, J. C. Burant, S. S. Iyengar, J. Tomasi, M. Cossi, N. Rega, J. M. Millam, M. Klene, J. E. Knox, J. B. Cross, V. Bakken, C. Adamo, J. Jaramillo, R. Gomperts, R. E. Stratmann, O. Yazyev, A. J. Austin, R. Cammi, C. Pomelli, J. W. Ochterski, R. L. Martin, K. Morokuma, V. G. Zakrzewski, G. A. Voth, P. Salvador, J. J. Dannenberg, S. Dapprich, A. D. Daniels, Ö. Farkas, J. B. Foresman, J. V. Ortiz, J. Cioslowski, and D. J. Fox, Gaussian, Inc., Wallingford CT, 2009.

Appendix C
Coupled cluster methods

C.1. Introduction

Throughout the present work, we have made extensive use of the second-order approximate coupled cluster singles and doubles method in order to perform wavefunction-based benchmark calculations for density functional theory methods. In the present Appendix, we present an outline of it and some other members of the coupled cluster family. As we shall see, the coupled cluster methods improve on the Hartree-Fock method by including electron correlation effects, and are applicable to excited electronic states as well as the ground state.

C.2. The creation and annihilation operators

Before embarking on a discussion of the coupled cluster methods, we must introduce the creation and annihilation operators which appear in their mathematical formulation. The rigorous definition of these operators, while not overly complex, involves notation which we have not used in the present work, so for the sake of brevity we will opt for a more pragmatic one, and refer the Reader to the textbook by Piela[1] for a more formal treatment.

The creation and annihilation operators will always be encountered acting on some Slater determinant, such as the determinant Φ given below:

$$\Phi = \frac{1}{\sqrt{N!}} \begin{vmatrix} \phi_1(1) & \phi_1(2) & \dots & \phi_1(N) \\ \phi_2(1) & \phi_2(2) & \dots & \phi_2(N) \\ \vdots & \vdots & & \vdots \\ \phi_N(1) & \phi_N(2) & \dots & \phi_N(N) \end{vmatrix}$$

It is assumed that aside from the spinorbitals $\phi_1, \phi_2, ..., \phi_N$ which are occupied in determinant Φ, there exist some so-called unoccupied spinorbitals $\phi_{N+1}, \phi_{N+2}, ..., \phi_M$ that are not found in determinant Φ. Any two spinorbitals are also assumed to satisfy the orthonormality condition $\langle i|j\rangle = \delta_{ij}$.

Suppose now that ϕ_a is a spinorbital occupied in determinant Φ, while ϕ_r

is a spinorbital unoccupied in Φ:

$$\Phi = \frac{1}{\sqrt{N!}} \begin{vmatrix} \phi_1(1) & \phi_1(2) & \dots & \phi_1(N) \\ \vdots & \vdots & & \vdots \\ \phi_a(1) & \phi_a(2) & \dots & \phi_a(N) \\ \vdots & \vdots & & \vdots \\ \phi_N(1) & \phi_N(2) & \dots & \phi_N(N) \end{vmatrix}$$

We could envision an annihilation operator $\hat{a}$ that, pictorially speaking, corresponds to an electron leaving spinorbital ϕ_a. Likewise, let there be a creation operator $\hat{r}^\dagger$ whose action is to place an electron in spinorbital ϕ_r. By themselves, the individual creation and annihilation operators are not particularly useful. However, the product of the creation and annihilation operators, $\hat{r}^\dagger\hat{a}$, which corresponds to an electron being moved (or, in theoretical parlance, excited) from spinorbital ϕ_a to spinorbital ϕ_r, will be very valuable to us. When acting on the determinant Φ, the operator $\hat{r}^\dagger\hat{a}$ will yield a new Slater determinant in which the row containing ϕ_a has been replaced with a row containing ϕ_r:

$$\hat{r}^\dagger\hat{a}\,\Phi = \frac{1}{\sqrt{N!}}\,\hat{r}^\dagger\hat{a} \begin{vmatrix} \phi_1(1) & \phi_1(2) & \dots & \phi_1(N) \\ \vdots & \vdots & & \vdots \\ \phi_a(1) & \phi_a(2) & \dots & \phi_a(N) \\ \vdots & \vdots & & \vdots \\ \phi_N(1) & \phi_N(2) & \dots & \phi_N(N) \end{vmatrix} = \frac{1}{\sqrt{N!}} \begin{vmatrix} \phi_1(1) & \phi_1(2) & \dots & \phi_1(N) \\ \vdots & \vdots & & \vdots \\ \phi_r(1) & \phi_r(2) & \dots & \phi_r(N) \\ \vdots & \vdots & & \vdots \\ \phi_N(1) & \phi_N(2) & \dots & \phi_N(N) \end{vmatrix}$$

All other rows of Φ will be unaffected. (Note that in the resulting determinant $\hat{r}^\dagger\hat{a}\,\Phi$, ϕ_r is considered occupied while ϕ_a is unoccupied. To avoid confusion, we must therefore always specify in which determinant a given spinorbital is occupied or unoccupied.)

Hence, the operator $\hat{r}^\dagger\hat{a}$ corresponds to the excitation of an electron from ϕ_a to ϕ_r. Naturally, we might ask, what happens if we attempt to excite an electron from an unoccupied orbital, or if we try to excite an electron to an orbital that is already occupied? Such moves are legal, but by the definition of the creation and annihilation operators, they always yield zero:

$$\hat{i}^\dagger\hat{j}\,\Phi = 0 \qquad \begin{array}{l} \text{if spinorbital } i \text{ is already occupied in } \Phi, \\ \text{or if spinorbital } j \text{ is unoccupied in } \Phi. \end{array}$$

As a consequence, whereas the creation and annihilation operators always correspond, respectively, to an increase and a decrease of the number of electrons

by one, the creator-annihilator product always leaves the number of electrons unchanged.

We may also consider double, triple, and higher excitations from orbitals which are occupied in Φ to unoccupied orbitals. For example, the operator product $\hat{r}^\dagger \hat{s}^\dagger \hat{a}\hat{b}$ will denote the excitation of two electrons from spinorbitals ϕ_a and ϕ_b to spinorbitals ϕ_r and ϕ_s :

$$\hat{r}^\dagger \hat{s}^\dagger \hat{a}\hat{b}\,\Phi = \frac{1}{\sqrt{N!}}\,\hat{r}^\dagger \hat{s}^\dagger \hat{a}\hat{b} \begin{vmatrix} \phi_1(1) & \phi_1(2) & \dots & \phi_1(N) \\ \vdots & \vdots & & \vdots \\ \phi_a(1) & \phi_a(2) & \dots & \phi_a(N) \\ \vdots & \vdots & & \vdots \\ \phi_b(1) & \phi_b(2) & \dots & \phi_b(N) \\ \vdots & \vdots & & \vdots \\ \phi_N(1) & \phi_N(2) & \dots & \phi_N(N) \end{vmatrix} =$$

$$= \frac{1}{\sqrt{N!}} \begin{vmatrix} \phi_1(1) & \phi_1(2) & \dots & \phi_1(N) \\ \vdots & \vdots & & \vdots \\ \phi_r(1) & \phi_r(2) & \dots & \phi_r(N) \\ \vdots & \vdots & & \vdots \\ \phi_s(1) & \phi_s(2) & \dots & \phi_s(N) \\ \vdots & \vdots & & \vdots \\ \phi_N(1) & \phi_N(2) & \dots & \phi_N(N) \end{vmatrix}$$

As before, any attempt to excite an electron from an unoccupied spinorbital or to an occupied spinorbital will automatically yield zero.

Thus, by employing the appropriate product of creation and annihilation operators, we may generate from determinant Φ a determinant containing any N of the M available spinorbitals.

C.3. The coupled cluster formalism

Recall that in the HF method, the many-electron ground-state wavefunction was expressed in the form of a single Slater determinant:

$$\psi_{\mathrm{HF}} = \frac{1}{\sqrt{N!}} \begin{vmatrix} \phi_1(1) & \phi_1(2) & \dots & \phi_1(N) \\ \phi_2(1) & \phi_2(2) & \dots & \phi_2(N) \\ \vdots & \vdots & & \vdots \\ \phi_N(1) & \phi_N(2) & \dots & \phi_N(N) \end{vmatrix}$$

Writing down the wavefunction as a Slater determinant can be described as an *ansatz*, an educated guess that is rationalised later by its results. It is justified by the fact that with a suitable choice of the spinorbitals ϕ_i, the wavefunction can quite accurately reproduce the total energy and other observables of the real system. However, this choice of the functional form of the wavefunction also means that the lowest absolute energy that can be obtained for a many-electron system using the HF method is higher than the true energy by an amount called the correlation energy. Hence in order to account for this "missing" energy, a new functional form must be chosen for the many-electron wavefunction.

In the coupled cluster method, the ground-state wavefunction is defined by the following *ansatz*. It is presumed that there exists some Slater determinant which gives a reasonably good description of the system's wavefunction. This Slater determinant, which could be the Hartree-Fock determinant, is taken by the coupled cluster method as the reference determinant Φ_0. The exact wavefunction for the system is generated by acting on the reference determinant with the operator $e^{\hat{T}}$, called the wave operator:

$$\psi = e^{\hat{T}}\,\Phi_0 \tag{C.1}$$

$\hat{T}$ itself is called the cluster operator. For practical reasons, instead of imposing the conventional normalisation condition, $\langle\psi|\psi\rangle = 1$, in the coupled cluster method we enforce an *intermediate* normalisation:

$$\langle\psi|\Phi_0\rangle = 1 \tag{C.2}$$

Given the coupled cluster *ansatz* (equation C.1), the challenge becomes to find the cluster operator $\hat{T}$, which will of course be specific to each reference determinant

Φ_0. It is assumed that $\hat{T}$ can be written as a sum of excitation operators $\hat{T}_n$:

$$\hat{T} = \hat{T}_1 + \hat{T}_2 + ... + \hat{T}_{N_{\max}} \tag{C.3}$$

The action of each excitation operator $\hat{T}_n$ is to generate from the reference determinant all possible n-fold excitations by moving electrons from occupied to unoccupied spinorbitals. More formally, the operator for single excitations (or: singles) is defined as:

$$\hat{T}_1 = \sum_a \sum_r t_a^r \, \hat{r}^\dagger \, \hat{a} \tag{C.4}$$

The operator for double excitations (doubles) is defined as:

$$\hat{T}_2 = \frac{1}{4} \sum_a \sum_b \sum_r \sum_s t_{ab}^{rs} \, \hat{s}^\dagger \, \hat{r}^\dagger \, \hat{a} \, \hat{b} \tag{C.5}$$

where the prefactor of $\frac{1}{4}$ in the definition of corrects for the fourfold counting of double excitations in the sum over a, b, r and s. The indices $a, b, ...$ refer to spinorbitals which are occupied in the reference determinant Φ_0, while $r, s, ...$ refer to the unoccupied ones. The higher excitation operators are defined analogously. The scalar numbers t_a^r, t_{ab}^{rs}, ... are called the coupled cluster amplitudes, and it is they which define the cluster operator $\hat{T}$ for a given reference determinant.

Because an attempt to annihilate an electron in an empty spinorbital always gives zero, the highest term $\hat{T}_{N_{\max}}$ that we need to include in the expansion of the cluster operator (equation C.3) is the one with $N_{\max}$ equal to N, the number of electrons in the system. An expansion including all terms up to $\hat{T}_N$ would, in the complete basis set limit, amount to the exact solution of the time-independent nonrelativistic Schrödinger equation. Unfortunately, for most practical systems including all terms up to $\hat{T}_N$ is not computationally feasible, and we must make do with an expansion truncated at $N_{\max} = 1$, 2, or 3, making for the coupled cluster singles (CCS), coupled cluster singles and doubles (CCSD), and coupled cluster singles, doubles and triples (CCSDT) variants of the general coupled cluster method, respectively.

Let us now explain why the wavefunction written in the form C.1 has the capability to include electron correlation. After all, it may seem counterintuitive that by exciting electrons from occupied spinorbitals to virtual spinorbitals

(the energies of which are, by definition, higher or equal to those of the occupied orbitals), we should obtain a wavefunction that corresponds to a lower energy than the reference determinant. Pictorially speaking, double (and higher) excitations may describe electron correlation because when one electron is excited from an occupied spinorbital ϕ_a to a virtual spinorbital ϕ_r while another electron is excited from a different occupied spinorbital ϕ_b to a different virtual spinorbital ϕ_s, there arises a mutual dependency of the spatial distributions of the two electrons, enabling them to avoid each other. The lowering of the total energy due to this mutual avoidance of the two electrons may be large enough to outweigh the energy increase due to exciting electrons to the virtual spinorbitals ϕ_r and ϕ_s, the energies of which are higher than those of ϕ_a and ϕ_b. This line of reasoning is somewhat simplistic, but the conclusion that double and higher excitations may lower the total energy is nevertheless correct.

A linear combination of a Hartree-Fock reference determinant and singly excited determinants, however, cannot on its own yield an energy lower than the HF energy. This statement is known in the literature as Brillouin's theorem; the proof is quite straightforward. Suppose that by solving the Roothan-Hall equation, we have calculated the best spinorbitals that can be obtained with a given basis set, obtaining the HF determinant Φ_{HF}. Let Φ_a^r be a singly excited determinant generated from Φ_{HF} by replacing the occupied spinorbital ϕ_a with the virtual spinorbital ϕ_r. We could generate a trial wavefunction ψ as a linear combination of the determinants Φ_{HF} and Φ_a^r :

$$\psi = c_1\,\Phi_{\mathrm{HF}} + c_2\,\Phi_a^r =$$

$$= \frac{c_1}{\sqrt{N}} \begin{vmatrix} \phi_1(1) & \phi_1(2) & \dots & \phi_1(N) \\ \vdots & \vdots & & \vdots \\ \phi_a(1) & \phi_a(2) & \dots & \phi_a(N) \\ \vdots & \vdots & & \vdots \\ \phi_N(1) & \phi_N(2) & \dots & \phi_N(N) \end{vmatrix} + \frac{c_2}{\sqrt{N}} \begin{vmatrix} \phi_1(1) & \phi_1(2) & \dots & \phi_1(N) \\ \vdots & \vdots & & \vdots \\ \phi_r(1) & \phi_r(2) & \dots & \phi_r(N) \\ \vdots & \vdots & & \vdots \\ \phi_N(1) & \phi_N(2) & \dots & \phi_N(N) \end{vmatrix}$$

The two determinants that appear in the above equation differ by only one row (the one which contains ϕ_a and ϕ_r). Hence, by the general properties of determinants, the sum of these two determinants may be written as a single determinant:

$$\psi = \frac{1}{\sqrt{N}} \begin{vmatrix} \phi_1(1) & \phi_1(2) & \dots & \phi_1(N) \\ \vdots & \vdots & & \vdots \\ c_1\phi_a(1) + c_2\phi_r(1) & c_1\phi_a(2) + c_2\phi_r(2) & \dots & c_1\phi_a(N) + c_2\phi_r(N) \\ \vdots & \vdots & & \vdots \\ \phi_N(1) & \phi_N(2) & \dots & \phi_N(N) \end{vmatrix}$$

This wavefunction cannot correspond to a lower energy than Φ_{HF} because, by definition, Φ_{HF} represents the best single-determinant wavefunction (within the given basis set). It follows that singly excited determinants alone do not introduce any electron correlation. Although doubly excited determinants will already come up in the CCS method (through the term $\hat{T}_1{}^2$ that arises in the expansion of $e^{-\hat{T}}$), the coefficients in front of these determinants will involve the singles amplitudes t_a^r. To achieve a good description of electron correlation we must introduce a set of doubles amplitudes (t_{ab}^{rs}) to control specifically the double excitations, which means that the CCSD method is effectively the lowest level of coupled cluster theory that describes electron correlation.

We now turn our attention to the task of calculating the coupled cluster amplitudes, which we will first do for the CCSD method, and subsequently show that the generalisation to triple and higher excitations is very straightforward. The starting point is the coupled cluster *ansatz* equation:

$$\psi = e^{\hat{T}}\,\Phi_0$$

The wavefunction ψ is to exactly satisfy the Schrödinger equation $\hat{H}\psi = \hat{H}\psi$, therefore we can substitute $\psi = \frac{1}{E}\hat{H}\psi$ into the *ansatz* equation, obtaining:

$$\hat{H}\,\psi = E\,e^{\hat{T}}\,\Phi_0 \tag{C.6}$$

or, equivalently,

$$\hat{H}\,e^{\hat{T}}\,\Phi_0 = E\,e^{\hat{T}}\,\Phi_0 \tag{C.7}$$

We now multiply both sides of C.7 from the left-hand side by $e^{-\hat{T}}$:

$$e^{-\hat{T}}\,\hat{H}\,e^{\hat{T}}\,\Phi_0 = E\,\Phi_0 \tag{C.8}$$

Let us now introduce the following notation: $\hat{r}^\dagger\,\hat{a}\,\Phi_0 = \Phi_a^r$ will be the determinant formed from Φ_0 by replacing occupied spinorbital a with virtual spinorbital r, and $\hat{r}^\dagger\,\hat{s}^\dagger\,\hat{a}\,\hat{b}\,\Phi_0 = \Phi_{ab}^{rs}$ will be determinant formed from Φ_0 by replacing occupied spinorbitals a and b with virtual spinorbitals r and s.

Because all spinorbitals are mutually orthonormal, the determinants Φ_a^r and Φ_{ab}^{rs} are all orthogonal to the reference determinant Φ_0. We may therefore project equations C.8 onto each of the determinants Φ_a^r and Φ_{ab}^{rs} in turn, obtaining the coupled cluster equations:

$$\langle \Phi_a^r \,|\, e^{-\hat{T}}\,\hat{H}\,e^{\hat{T}} \,|\, \Phi_0 \rangle = 0 \qquad \text{for every singly excited determinant } \Phi_a^r \tag{C.9}$$

$$\langle \Phi_{ab}^{rs} \,|\, e^{-\hat{T}}\,\hat{H}\,e^{\hat{T}} \,|\, \Phi_0 \rangle = 0 \qquad \text{for every doubly excited determinant } \Phi_{ab}^{rs} \tag{C.10}$$

The total number of these equations is equal to the number of all coupled cluster amplitudes t_a^r and t_{ab}^{rs}. The amplitudes are, however, "buried" in the operator $e^{-\hat{T}}\,\hat{H}\,e^{\hat{T}}$. Fortunately, $e^{-\hat{T}}\,\hat{H}\,e^{\hat{T}}$ may be expanded out (exactly) into the following commutator expansion:

$$e^{-\hat{T}}\,\hat{H}\,e^{\hat{T}} = \hat{H} + [\hat{H},\hat{T}] + \frac{1}{2!}\big[[\hat{H},\hat{T}],\hat{T}\big] + \frac{1}{3!}\big[\big[[\hat{H},\hat{T}],\hat{T}\big],\hat{T}\big] + \\ + \frac{1}{4!}\big[\big[\big[[\hat{H},\hat{T}],\hat{T}\big],\hat{T}\big],\hat{T}\big] \tag{C.11}$$

The highest power of $\hat{T}$ that appears in the above equation is $\hat{T}^4$. Thus, when the commutator expansion C.11 is substituted into the coupled cluster equations C.9 and C.10, we obtain a set of fourth degree polynomial equations in the coupled cluster amplitudes. In practical applications, these equations are always solved using iterative numerical methods. The extension to triple and higher excitations is achieved by simply writing down further coupled cluster equations for excitations of successively higher rank, *e.g.* for the triples:

$$\langle \Phi_{abc}^{rst} \,|\, e^{-\hat{T}}\,\hat{H}\,e^{\hat{T}} \,|\, \Phi_0 \rangle = 0 \qquad \text{for every triply excited determinant } \Phi_{abc}^{rst}$$

Once the coupled cluster equations C.9 and C.10 have been solved, the energy can be evaluated by projecting equation C.8 onto the reference determinant Φ_0:

$$E = \langle \Phi_0 \,|\, e^{-\hat{T}}\,\hat{H}\,e^{\hat{T}} \,|\, \Phi_0 \rangle \tag{C.12}$$

It deserves pointing out that this expression for energy is not equivalent to the energy which would have been obtained by the minimisation of the expectation value of the Hamiltonian, which is given by

$$E = \frac{\langle \psi \,|\, \hat{H} \,|\, \psi \rangle}{\langle \psi \,|\, \psi \rangle}$$

In other words, the coupled cluster method is not a variational method. The practical rationale for accepting the non-variational approach is that the variational approach is much more computationally demanding, and hence, the vast majority of coupled cluster methodologies take the non-variational approach.

C.4. The second-order approximate coupled cluster singles and doubles method

Koch and coworkers[2] analysed the accuracy of coupled cluster methods within the context of Rayleigh-Schrödinger perturbation theory. The exact Hamiltonian operator $\hat{H}$ defined as follows:

$$\hat{H} = -\frac{1}{2}\sum_{i=1}^{N} \nabla_i^2 - \sum_{i=1}^{N}\sum_{a=1}^{N_{\text{nuc}}} \frac{Z_a}{r_{ai}} + \frac{1}{2}\sum_{i=1}^{N}\sum_{j=1}^{N} \frac{1}{r_{ij}}$$

was partitioned into an N-electron Fock operator $\hat{F}_N$, which is simply the sum of the N one-electron Fock operators, and a fluctuation operator $\hat{U}$ which describes the difference between the electron-electron repulsion energy and the Fock operator:

$$\hat{H} = \hat{F}_N + \hat{U} \quad \text{, where} \quad \hat{F}_N = \sum_{k=1}^{N} \hat{F}(k)$$

where the one-electron Fock operators $\hat{F}(k)$ are defined as per equation B.23 in Appendix B. It follows that the fluctuation operator may be written out as:

$$\hat{U} = \hat{H} - \hat{F}_N = \sum_{i<j} \frac{1}{r_{ij}} - \sum_{j=1}^{N}\sum_{k=1}^{N} \Big[\hat{J}_j(k) - \hat{K}_j(k) \Big]$$

The fluctuation operator $\hat{U}$ was considered as a perturbation to the N-electron Fock operator $\hat{F}_N$ and, as is standard practice in Rayleigh-Schrödinger perturbation theory, the total energy was expanded out as a power series in terms of the magnitude of the perturbation:

$$E = E^{(0)} + E^{(1)} + E^{(2)} + E^{(3)} + ...$$

where $E^{(0)}$ is the eigenvalue of the unperturbed Hamiltonian, $E^{(1)}$ is the first-order correction term, $E^{(2)}$ is the second-order term and so on. It was demonstrated that the CCSD energy is correct through third order in the fluctuation potential, meaning that all terms up to $E^{(3)}$ are included in the CCSD energy. Furthermore, the same group proposed an approximation to the CCSD method,[3] whereby the energy is correct through second order in the perturbation potential. In order to write down the defining equations of this second-order approximate coupled cluster singles and doubles method (known in the literature as the CC2 method), we must first express the original CCSD equations C.9 and C.10 in a slightly different form. Let us introduce the (non-Hermitian and two-electron) $\hat{T}_1$-transformed Hamiltonian operator defined as

$$\widetilde{H} = e^{-\hat{T}_1}\, \hat{H}\, e^{\hat{T}_1} \tag{C.13}$$

Then, equation C.9 becomes

$$\begin{aligned}
&\langle \Phi_a^r \,|\, e^{-\hat{T}_1-\hat{T}_2}\, \hat{H}\, e^{\hat{T}_1+\hat{T}_2} \,|\, \Phi_0 \rangle = \langle \Phi_a^r \,|\, e^{-\hat{T}_2}\, \widetilde{H}\, e^{\hat{T}_2} \,|\, \Phi_0 \rangle = \\
&= \langle \Phi_a^r \,|\, (1 - \hat{T}_2 + \frac{1}{2}\hat{T}_2^{\,2} - ...)\, \widetilde{H}\, (1 + \hat{T}_2 + \frac{1}{2}\hat{T}_2^{\,2} + ...) \,|\, \Phi_0 \rangle = \\
&= \langle \Phi_a^r \,|\, \widetilde{H} + \widetilde{H}\hat{T}_2 + \frac{1}{2}\widetilde{H}\hat{T}_2^{\,2} - \hat{T}_2\widetilde{H} - \hat{T}_2\widetilde{H}\hat{T}_2 - \frac{1}{2}\hat{T}_2\widetilde{H}\hat{T}_2^{\,2} + \\
&+ \frac{1}{2}\hat{T}_2^{\,2}\widetilde{H} + \frac{1}{2}\hat{T}_2^{\,2}\widetilde{H}\hat{T}_2 + \frac{1}{4}\hat{T}_2^{\,2}\widetilde{H}\hat{T}_2^{\,2} + ... \,|\, \Phi_0 \rangle = 0
\end{aligned} \tag{C.14}$$

Almost all of the matrix elements of the type $\langle \Phi_a^r | \cdots | \Phi_0 \rangle$ that appear in the above equation C.14 vanish either because of the fourth Slater-Condon rule, or because the double de-excitation operator $\hat{T}_2^\dagger$ (the adjoint of $\hat{T}_2$) gives zero when acting on Φ_a^r. For example, $\langle \Phi_a^r \,|\, \widetilde{H}\hat{T}_2^{\,2} \,|\, \Phi_0 \rangle = \langle \Phi_a^r \,|\, \widetilde{H} \,|\, \hat{T}_2^{\,2}\Phi_0 \rangle = 0$ because Φ_a^r and every determinant that appears in the term $\hat{T}_2^{\,2}\Phi_0$ differ by three spinorbitals. Likewise, $\langle \Phi_a^r \,|\, \hat{T}_2\widetilde{H}\hat{T}_2 \,|\, \Phi_0 \rangle = \langle \hat{T}_2^\dagger \Phi_a^r \,|\, \widetilde{H}\hat{T}_2 \,|\, \Phi_0 \rangle$ and $\hat{T}_2^\dagger \Phi_a^r = 0$. We are left with the elegant expression

$$\langle \Phi_a^r \,|\, \widetilde{H} + [\widetilde{H}, \hat{T}_2] \,|\, \Phi_0 \rangle = 0 \tag{C.15}$$

Similarly for the double excitations:

$$\langle \Phi_{ab}^{rs} \,|\, \widetilde{H} + [\widetilde{H}, \hat{T}_2] + \frac{1}{2}\big[[\widetilde{H}, \hat{T}_2], \hat{T}_2\big] \,|\, \Phi_0 \rangle = 0 \tag{C.16}$$

The transformation from equations C.9 and C.10 to C.15 and C.16 has involved no approximations, and so C.15 and C.16 also represent an exact formulation of the CCSD method. In the CC2 method, the singles equation C.15 is retained in its original form, while the doubles equation C.16 is approximated by the following expression:

$$\langle \Phi_{ab}^{rs} \,|\, \widetilde{H} + [\hat{F}, \hat{T}_2] \,|\, \Phi_0 \rangle = 0 \tag{C.17}$$

As already mentioned, this approximation is accompanied by a certain loss of accuracy: while in the original CCSD method the energy is correct through third order, in the CC2 method it is only correct through second order (hence the name of the method). The gain is that in the CC2 method, the doubles amplitudes (t_{ab}^{rs}) may be expressed directly in terms of the singles amplitudes (t_a^r) and integrals involving molecular orbitals. Thus, whereas in the CCSD method we must solve the coupled cluster equations iteratively for both the singles and doubles amplitudes, in the CC2 method we need only solve the coupled cluster iteratively for the singles amplitudes, while the doubles amplitudes are calculated non-iteratively.[4] Owing to this simplification, the CC2 method scales more favourably with system size than the CCSD method (as M^5, whereas the CCSD method scales as M^6, M being the number of spinorbitals).

As an illustration of the ability of the CCSD and CC2 methods to describe electron correlation, we have applied these methods to the ground electronic state (the 1^1S state) of the helium atom. Because helium only has two electrons, the CCSD method represents an exact solution of the non-relativistic Schrödinger equation within the approximation of the finite basis set. We have employed the implementation of the CCSD and CC2 methods as provided in the software package PSI3[5] with an RHF reference determinant, coupled with the aug-cc-pV5Z basis set.[6] It is expected through the use of this extensive basis set, the calculation approaches the complete basis set limit, and hence the calculated CCSD wavefunction should be a very good approximation to the exact (adiabatic) wavefunction.

The resulting coupled cluster energies, as well as the energy of the RHF

Table C.1: The energy of the 1^1S state of the helium atom, calculated at the RHF, CCSD and CC2 levels of theory coupled with the aug-cc-pV5Z basis set.

Method	Energy, E_h
RHF	-2.861627
CCSD	-2.903201
E_corr(CCSD)[a]	-0.041574
CC2	-2.898181
E_corr(CC2)[b]	-0.036554

[a] The correlation energy at the CCSD level is given by E(CCSD)$-E$(RHF).
[b] Likewise, the correlation energy at the CC2 level is E(CC2)$-E$(RHF).

reference determinant, are listed in Table C.1 above. The CCSD method predicts a total energy of $-2.903201\ E_\mathrm{h}$, and a correlation energy of $-0.041574\ E_\mathrm{h}$, which is roughly 1% of the RHF energy. The CC2 method, on the other hand, yields a correlation energy of $-0.036554\ E_\mathrm{h}$, meaning that it recovers around 88% of the CCSD correlation energy.

C.5. The equations-of-motion coupled cluster method

The equations-of-motion (EOM) coupled cluster method[7] is an extension of the coupled cluster formalism to excited electronic states. In the present section, we present the derivation of the equations defining this method for the special case of single and double excitations (EOM-CCSD). The derivation for the general case of excitations of any rank (arbitrary N_max in equation C.3) is entirely analogous.

We begin with equation C.1 which is the coupled cluster *ansatz*:

$$\psi_0 = e^{\hat{T}}\Phi_0$$

where, in the special case of single and double excitations, the cluster operator is given by: $\hat{T} = \hat{T}_1 + \hat{T}_2$. The action of the wave operator $e^{\hat{T}}$ is to transform the reference determinant Φ_0 into the correlated ground-state wavefunction ψ_0.

The following *ansatz* is assumed: the wavefunction ψ_k of the k-th excited

state may be obtained by acting on ψ_0 with an operator $\hat{U}_k$:

$$\psi_k = \hat{U}_k \psi_0 \tag{C.18}$$

Now from the coupled cluster *ansatz* itself, it follows that the CCSD ground-state wavefunction ψ_0 may be expressed as a sum over non-excited, singly excited, doubly excited, etc. determinants $(\Phi_0,\, \Phi_a^r,\, \Phi_{ab}^{rs},\, ...)$ with coefficients $c_0,\, c_a^r,\, c_{ab}^{rs},\, ...$:

$$\psi_0 = e^{\hat{T}_1+\hat{T}_2}\,\Phi_0 = \left[1 + (\hat{T}_1+\hat{T}_2) + \frac{1}{2}(\hat{T}_1+\hat{T}_2)^2 + ...\right]\,\Phi_0 =$$

$$= \left[1 + \hat{T}_1 + (\hat{T}_2 + \frac{1}{2}\hat{T}_1^2) + ...\right]\,\Phi_0 = c_0\,\Phi_0 + \sum_a \sum_r c_a^r\,\Phi_a^r +$$

$$+ \sum_{a<b} \sum_{r<s} c_{ab}^{rs}\,\Phi_{ab}^{rs} + ... \tag{C.19}$$

Note that the sum in equation C.19 does not terminate at doubly excited determinants, but goes on to include triply excited, quadruply excited, etc. determinants.

The operator $\hat{U}_k$ acts by modifying the coefficients which stand in front of the various determinants which appear in the expansion C.19. It may be broken down into a sum of operators which deal with excitations of different rank separately:

$$\hat{U}_k = \hat{U}_{k,0} + \hat{U}_{k,1} + \hat{U}_{k,2}$$

The operator $\hat{U}_{k,0}$ simply corresponds to multiplication by a scalar number $\tau_0(k)$.

$$\hat{U}_{k,0} = \tau_0(k)$$

$\hat{U}_{k,1}$ and $\hat{U}_{k,2}$, on the other hand, are defined by sums over all possible single and double excitations, respectively:

$$\hat{U}_{k,1} = \sum_a \sum_r \tau_a^r(k)\,\hat{r}^\dagger\,\hat{a}$$

$$\hat{U}_{k,2} = \sum_a \sum_b \sum_r \sum_s \tau_{ab}^{rs}(k)\,\hat{s}^\dagger\,\hat{r}^\dagger\,\hat{a}\,\hat{b}$$

The scalar numbers $\tau_0(k)$, $\tau_a^r(k)$ and $\tau_{ab}^{rs}(k)$ are the equations-of-motion amplitudes

for the k-th state, whose values must be calculated in order for us to be able to obtain its wavefunction ψ_k. In what follows, we will outline a scheme for achieving this.

The Schrödinger equation for the k-th excited state is:

$$\hat{H}\psi_k = E_k\psi_k \tag{C.20}$$

Into this equation, we will substitute the EOM-CC *ansatz* (equation C.18).

$$\hat{H}\hat{U}_k\psi_0 = E_k\hat{U}_k\psi_0 \tag{C.21}$$

The coupled cluster *ansatz* (equation C.1), in turn, gives us $\psi_0 = e^{\hat{T}}\Phi_0$.

$$\hat{H}\hat{U}_k e^{\hat{T}}\Phi_0 = E_k\hat{U}_k e^{\hat{T}}\Phi_0 \tag{C.22}$$

Because the operators $\hat{U}_k$ and $\hat{T}_n$ both contain only excitations (as opposed to de-excitations), they commute, *i.e.* $\hat{U}_k\hat{T}_n = \hat{T}_n\hat{U}_k$. It follows that the operators $e^{\hat{T}}$ and $\hat{U}_k$ also commute: $\hat{U}_k e^{\hat{T}} = e^{\hat{T}}\hat{U}_k$. After substituting this into both sides of equation C.22, we obtain:

$$\hat{H}e^{\hat{T}}\hat{U}_k\Phi_0 = E_k e^{\hat{T}}\hat{U}_k\Phi_0 \tag{C.23}$$

Let us now act on both sides of equation C.23 with the operator $e^{-\hat{T}}$:

$$e^{-\hat{T}}\hat{H}e^{\hat{T}}\hat{U}_k\Phi_0 = e^{-\hat{T}}E_k e^{\hat{T}}\hat{U}_k\Phi_0 = E_k\hat{U}_k\Phi_0 \tag{C.24}$$

Introducing the $\hat{T}$-transformed Hamiltonian, $\bar{H} = e^{-\hat{T}}\hat{H}e^{\hat{T}}$, we rewrite the above equation as

$$\bar{H}\hat{U}_k\Phi_0 = E_k\hat{U}_k\Phi_0 \tag{C.25}$$

Let us now recall equation C.8:

$$e^{-\hat{T}}\hat{H}e^{\hat{T}}\Phi_0 = E_0\Phi_0$$

Or, taking advantage of the definition of $\bar{H}$,

$$\bar{H}\Phi_0 = E_0\Phi_0 \tag{C.26}$$

If we act on both sides of the above equation C.26 with the operator $\hat{U}_k$, and then subtract this equation from equation C.25, we obtain:

$$\bar{H}\hat{U}_k\Phi_0 - \hat{U}_k\bar{H}\Phi_0 = E_k\hat{U}_k\Phi_0 - E_0\hat{U}_k\Phi_0 \tag{C.27}$$

or, more succinctly,

$$[\bar{H}, \hat{U}_k]\Phi_0 = (E_k - E_0)\hat{U}_k\Phi_0 \tag{C.28}$$

By projecting the above equation C.28 onto each of the determinants Φ_0, Φ_a^r and Φ_{ab}^{rs} in turn, we finally obtain the EOM-CCSD equations, the solution of which yields the target EOM-CCSD amplitudes and the excited-state energy E_k:

$$\langle\Phi_0|[\bar{H}, \hat{U}_k]|\Phi_0\rangle = (E_k - E_0)\langle\Phi_0|\hat{U}_k|\Phi_0\rangle$$

$$\langle\Phi_a^r|[\bar{H}, \hat{U}_k]|\Phi_0\rangle = (E_k - E_0)\langle\Phi_a^r|\hat{U}_k|\Phi_0\rangle$$

$$\langle\Phi_{ab}^{rs}|[\bar{H}, \hat{U}_k]|\Phi_0\rangle = (E_k - E_0)\langle\Phi_{ab}^{rs}|\hat{U}_k|\Phi_0\rangle$$

C.6. Dynamical and non-dynamical electron correlation

Having introduced the coupled cluster methods as an example of a wavefunction-based approach that includes electron correlation, we will now venture on a brief discussion on electron correlation in general. Within the coupled cluster methods, as well as some other correlated wavefunction-based methods such as the multiconfigurational self-consistent-field (MCSCF) method,[8] the correlated wavefunction ψ can be expressed as an expansion into a series of Slater determinants Ψ_i, also sometimes called configurations, with coefficients c_i:

$$\psi = c_0\Psi_0 + c_1\Psi_1 + c_2\Psi_2 + c_3\Psi_3 + ... \tag{C.29}$$

Suppose now that the wavefunction ψ represents a very accurate ground- or excited-state state solution of the Schrödinger equation for a many-electron molecule within the given basis set, obtained by whatever means. We will consider, in qualitative terms, what form the determinant expansion of ψ may take.

In many cases, among the determinants found in the expansion C.29, there

will be a single determinant whose coefficient is near unity. If the wavefunction ψ describes the ground electronic state, then this determinant will closely resemble, up to a unitary transformation, the Hartree-Fock determinant. The coefficients in front of all other determinants will be considerably smaller, although their inclusion in the determinant expansion is nevertheless necessary in order to obtain a description of electron correlation. Such a situation is usually referred to as dynamical electron correlation. Coupled cluster methods with a relatively early truncation of the cluster operator (CCSD, CCSDT and approximations to these methods, such as CC2) are generally well able to describe systems in which only dynamical correlation effects are present, provided that the reference determinant is close to the dominant configuration in the expansion C.29.

There exist molecules, however, where multiple determinants will have appreciably large coefficients, while the coefficients in front of other determinants will be small (but still nonzero). Such systems are said to exhibit non-dynamical (or static) as well as dynamical electron correlation, and they are typically characterised by a near-degeneracy between the energies of the highest occupied and the lowest unoccupied Hartree-Fock spinorbitals. As a consequence, for these systems, the single Hartree-Fock determinant is a very poor approximation of the real wavefunction. Examples include molecules undergoing homolytic bond cleavage and other strong deviations from equilibrium geometry, some molecules containing transition metals, and biradicals. The boundary between purely dynamical correlation on one hand, and non-dynamical in addition to dynamical correlation on the other is not rigorously defined, but this categorisation is nevertheless a very useful one.

Coupled cluster methods with an early truncation (which is to say, after the double or triple excitations operator) of the cluster operator are not, in general, able to correctly describe systems where non-dynamical correlation is important. To see why this should be the case, let us consider what happens when we apply the CCSD method to a system which exhibits strong non-dynamical correlation. We will assume that the non-dynamical correlation manifests itself such that the reference Hartree-Fock determinant Φ_0 is near-degenerate with some singly excited determinant Φ_g^h.

Within the CCSD method, the wave operator is given by

$$e^{\hat{T}_1+\hat{T}_2} = 1 + (\hat{T}_1 + \hat{T}_2) + \frac{1}{2}(\hat{T}_1 + \hat{T}_2)^2 + ... =$$

$$= 1 + \hat{T}_1 + \underbrace{(\hat{T}_2 + \frac{1}{2}\hat{T}_1^2)}_{\substack{\text{double} \\ \text{excitations}}} + \underbrace{(\hat{T}_2\hat{T}_1 + \frac{1}{6}\hat{T}_1^3)}_{\substack{\text{triple} \\ \text{excitations}}} + ...$$

The singles operator $\hat{T}_1$ acting on the reference determinant Φ_0 will generate, among others, the determinant Φ_g^h. Likewise, the sum $\hat{T}_2 + \frac{1}{2}\hat{T}_1^2$ acting on Φ_0 will generate, among others, all determinants of the type Φ_{ga}^{hr} that arise from single substitutions of orbitals in the determinant Φ_g^h. However, a problem arises with the triple excitations, because there is no operator $\hat{T}_3$ that would enable a good description of the coefficients of triply excited determinants, and in particular the determinants of the type Φ_{gab}^{hrs} that arise from double substitutions in Φ_g^h. Hence, the determinants Φ_0 and Φ_g^h are treated on an unequal footing, despite the fact that these determinants are near-degenerate and a correct theory should treat them in a balanced fashion.

Pre-empting the discussion of density functional theory (DFT) in Appendix D, we will mention here that most, if not all, existing exchange-correlation functionals do not correctly describe systems that exhibit non-dynamical correlation. According to Cohen and coworkers,[9] this failure can be traced back to a specific deficiency of the functionals, rather than any shortcoming of DFT itself. Namely, it is incorrectly predicted that the energy of a fractional-spin state is inequal to the energies of the comprising degenerate pure-spin states.

In our hybrid simulations of photochemical reactions in the molecular crystals 7-(2-pyridyl)indole and *N*-salicylidene-2-chloroaniline, the photoexcited molecules were expected to reach conical intersections (*i.e.* points of degeneracy on the molecular potential energy surface) between the ground- and first excited states by undergoing strong torsional deformations from the ground-state geometries. At or near a conical intersection, there exist near-degeneracies of Hartree-Fock spinorbitals, meaning that non-dynamical correlation inevitably comes into play. It is nevertheless often the case that the computationally inexpensive DFT and time-dependent DFT (TD-DFT) methods correctly predict the existence and rough locations of conical intersections, in the sense that the energy gap between the intersecting states becomes small on approaching a conical intersection.

Therefore, we have used the TD-DFT method to describe the potential energy surfaces of the excited 7-(2-pyridyl)indole and *N*-salicylidene-2-chloroaniline molecules. Taking into account the fact that far from the equilibrium ground-state geometry, this method may give rise to significant error, we have carried out additional calculations in order to assess its ability to describe the relevant potential energy surfaces. These calculations are described in the Chapters 3 and 4 which deal with the respective photochemical reactions.

C.7. The T_1 diagnostic

Given that coupled cluster methods with an early truncation of the cluster operator fail to describe non-dynamical correlation, it would clearly be useful to be able to detect when such failures occur. The obvious, but computationally very expensive, solution would be to apply a later truncation of the cluster operator, and to compare the resulting wavefunction with that obtained with an early truncation.

A more practicable method to determine whether a coupled cluster wavefunction has a multiconfigurational character is the T_1 diagnostic proposed by Lee and Taylor.[10] It relies on the observation that the single excitations in the cluster operator account for orbital relaxation: they allow the orbitals to adjust from their Hartree-Fock form. If a large orbital relaxation takes place, then it may be expected that the original Hartree-Fock determinant represents a very poor approximation to the exact, correlated wavefunction. This tends to happen if non-dynamical correlation plays an important role in the exact wavefunction.

Formally, the T_1 diagnostic is a non-negative scalar number defined as the magnitude of the singles amplitudes vector $\mathbf{t}_1$ divided by the square root of the number N_{corr} of correlated electrons:

$$T_1 = \sqrt{\frac{\mathbf{t}_1 \cdot \mathbf{t}_1}{N_{\text{corr}}}} \tag{C.30}$$

The elements of the singles amplitudes vector $\mathbf{t}_1$ are all the singles amplitudes t_a^r. The vector product $\mathbf{t}_1 \cdot \mathbf{t}_1$ may therefore be written out as:

$$\mathbf{t}_1 \cdot \mathbf{t}_1 = \sum_a \sum_r (t_a^r)^2 \tag{C.31}$$

Thus, the value of T_1 increases with an increasing magnitude of the singles excitations, and a high value of T_1 suggests that exact wavefunction exhibits significant non-dynamical correlation.

When the frozen core approximation is applied, N_{corr} is equal to the total number of electrons minus the number of core electrons. The reason for including N_{corr} in the definition C.30 is to ensure that the T_1 diagnostic is size-consistent, in the sense that it is takes equal values for two identical molecules at infinite separation and for a single isolated molecule.

References

[1] L. Piela, *Ideas of Quantum Chemistry*, Elsevier, Amsterdam, 2007, pp. 1023.

[2] H. Koch, O. Christiansen, Poul Jørgensen, A. M. Sanchez de Merás, T. Helgaker, *J. Chem. Phys.*, 1997, **106**, 1808.

[3] O. Christiansen, H. Koch, P. Jørgensen, *Chem. Phys. Lett.*, 1995, **243**, 409.

[4] F. Jensen, *Introduction to Computational Chemistry*, John Wiley and Sons, 2nd Ed., 2007, p. 176.

[5] T. D. Crawford, C. D. Sherrill, E. F. Valeev, J. T. Fermann, R. A. King, M. L. Leininger, S. T. Brown, C. L. Janssen, E. T. Seidl, J. P. Kenny, W. D. Allen, *J. Comp. Chem.*, 2007, **28**, 1610.

[6] D. E. Woon, T. H. Dunning, Jr., *J. Chem. Phys.*, 1994, **100**, 2975.

[7] J. F. Stanton, R. J. Bartlett, *J. Chem. Phys.*, 1993, **98**, 7029.

[8] M. Merchán, L. Serrano-Andrés, in *Theoretical and Computational Chemistry, Vol. 16*, ed. M. Olivucci, Elsevier, New York, 2005, p. 35.

[9] A. J. Cohen, P. Mori-Sánchez, W. Yang, *J. Chem. Phys.*, 2008, **129**, 121104.

[10] T. J. Lee, P. R. Taylor, *Int. J. Quant. Chem. Symp.*, 1989, **23**, 199.

Appendix D
Density functional theory

D.1. Background

As we have witnessed in the preceding Appendices on *ab initio* methods, although the most basic many-electron wavefunction may be written in the form of a single Slater determinant, the inclusion of electron correlation necessitates the use of a more general wavefunction form. In the coupled cluster methods, for instance, the wavefunction is written as a linear combination of many Slater determinants, which are usually generated from a reference Hartree-Fock determinant by substituting some occupied spinorbitals with virtual spinorbitals. The resulting correlated wavefunction is mathematically more complex, and consequently much more challenging to compute than the Hartree-Fock wavefunction.

This Gordian knot can be cut, however, if we turn our attention from the wavefunction to another quantity, the electron density $\rho(\mathbf{r})$ which, as we shall see shortly, provides a description of the electrons that is equivalent to that of the exact wavefunction. The electron density is defined as the integral of the square modulus of the wavefunction over the spin and spatial coordinates of all electrons except one, summed over the spin coordinate of that electron and multiplied by the number of electrons N:

$$\rho(\mathbf{r}) = N \sum_{\sigma_1} \int \int \dots \int \mid \psi(\mathbf{r}_1, \sigma_1, \mathbf{r}_2, \sigma_2, ..., \mathbf{r}_N, \sigma_N) \mid^2 \mathrm{d}\tau_2 \, \mathrm{d}\tau_3 \dots \mathrm{d}\tau_N \qquad \text{(D.1)}$$

$\mathrm{d}\tau_i$ respresents integration over both the spatial and the spin coordinates of the i-th electron, while $\sum_{\sigma_i}$ corresponds to summation over the spin coordinate of that electron. Unlike the wavefunction, which is a function of the spatial and spin coordinates of the N electrons, the electron density is only a function of position in space.

An equivalent definition states that the electron density is given by the expectation value of the density operator $\hat{\rho}(\mathbf{r})$ defined as the sum of the Dirac delta operators, $\delta(\mathbf{r}_i - \mathbf{r})$, for all electrons:

$$\rho(\mathbf{r}) = \langle \psi \,|\, \hat{\rho}(\mathbf{r}) \,|\, \psi \rangle = \langle \psi \,|\, \sum_{i=1}^{N} \delta(\mathbf{r}_i - \mathbf{r}) \,|\, \psi \rangle \tag{D.2}$$

Pictorially speaking, $\rho(\mathbf{r})$ represents the density of the "electron cloud" at a position vector $\mathbf{r}$. The prefactor N in the definition D.1 ensures that the integral of ρ over the entires space is equal to the number of electrons, N :

$$\int \rho(\mathbf{r}) \, \mathrm{d}\mathbf{r} = N \tag{D.3}$$

In the very important special case of the wavefunction ψ given by a single Slater determinant constructed from spinorbitals $\phi_i(\mathbf{r}, \sigma)$, the electron density can be expressed as the following sum over the spinorbitals

$$\rho(\mathbf{r}) = \sum_{i=1}^{N} \sum_{\sigma_1} |\, \phi_i(\mathbf{r}, \sigma_1) \,|^2 \tag{D.4}$$

The area of theoretical modelling which employs the electron density, rather than the wavefunction, as the central quantity is the density functional theory (DFT).

D.2. The two Hohenberg-Kohn theorems

The usefulness of the electron density in quantum chemistry stems from two theorems proved by Hohenberg and Kohn[1] in 1964. The first Hohenberg-Kohn theorem states that for a given system, the ground-state wavefunction ψ_0 and the ground-state density ρ_0 both provide a complete and equivalent description of the ground state. In particular, the external potential $v(\mathbf{r})$ acting on the electrons (which in systems typically encountered in quantum chemistry is simply the Coulombic attraction of the electrons to the nuclei) and the total energy E are both uniquely defined by the ground-state electron density $\rho_0(\mathbf{r})$.

For the special case of a non-degenerate ground state, the proof of the first Hohenberg-Kohn theorem is fairly straightforward and proceeds by assuming the opposite.[1] Let us assume the existence of two different external potentials $v_1(\mathbf{r})$ and $v_2(\mathbf{r})$ that give rise to the exact same ground-state density $\rho_0(\mathbf{r})$. The difference between the corresponding Hamiltonian operators $\hat{H}_1$ and $\hat{H}_2$ is

given by $v_1(\mathbf{r}) - v_2(\mathbf{r})$:

$$\hat{H}_1 - \hat{H}_2 = v_1(\mathbf{r}) - v_2(\mathbf{r})$$

Let us denote the ground-state wavefunctions of the $\hat{H}_1$ and $\hat{H}_2$ as ψ_1 and ψ_2, and the ground-state energies as E_1 and E_2, respectively. By taking advantage of the variational principle (see Section B.3 of Appendix B), we have:

$$E_1 = \langle\psi_1|\hat{H}_1|\psi_1\rangle < \langle\psi_2|\hat{H}_1|\psi_2\rangle = \langle\psi_2|\hat{H}_2|\psi_2\rangle + \langle\psi_2|\hat{H}_1 - \hat{H}_2|\psi_2\rangle =$$

$$= E_2 + \int \rho_0(\mathbf{r})\,[v_1(\mathbf{r}) - v_2(\mathbf{r})]\,\mathrm{d}\mathbf{r} \tag{D.5}$$

Likewise, for E_1 :

$$E_2 < E_1 + \int \rho_0(\mathbf{r})\,[v_2(\mathbf{r}) - v_1(\mathbf{r})]\,\mathrm{d}\mathbf{r} \tag{D.6}$$

If we now add together equations D.5 and D.6, we obtain the contradiction $E_1 + E_2 < E_1 + E_2$. Thus, the initial assumption was false, and we have proven that in the case of a non-degenerate ground state, there is a one-on-one mapping between the external potential $v(\mathbf{r})$ and the ground-state electron density $\rho_0(\mathbf{r})$. Thus, if we know $\rho_0(\mathbf{r})$, then it follows we know $v(\mathbf{r})$ and, according to equation D.3, the total number of electrons comprising the system. We may therefore construct the Hamiltonian operator $\hat{H}$ of the system, and through an exact solution of the Schrödinger equation, we may calculate its energy and all other properties. The ground-state density therefore contains the same information as the exact ground-state wavefunction.

It is straightforward to demonstrate that in the special case where the external potential $v(\mathbf{r})$ is the electrostatic potential of one or more nuclei, we may deduce the ground-state wavefunction from the known exact ground-state electron density. As mentioned in Section 1.9 of Chapter 1, the electron density of any ground or excited state electron density has cusps at the nuclei, and at each such cusp, the spherically averaged derivative of the electron density with respect to the distance r from the nucleus is given by $\left(\frac{\partial\rho(\mathbf{r})}{\partial r}\right)_{r=0} = -2\,Z\,\rho(\mathbf{0})$, where Z is the atomic number. Hence, by inspecting the ground-state electron density, we may determine the positions and atomic numbers of all atoms in the system. What is more, by calculating the integral $N = \int \rho(\mathbf{r})\,\mathrm{d}\mathbf{r}$, we may determine the number of electrons in the system. Having thus found the composition of the system,

we may write down the Hamiltonian operator for the electrons in the electrostatic potential of the nuclei. Knowing the Hamiltonian, in turn, allows us (in principle at least) to obtain the exact ground-state wavefunction by solving the Schrödinger equation. In the general case, to deduce the external potential from the known electron density may be a difficult task, but the principle holds true that the electron density and the wavefunction contain the same information.

The second Hohenberg-Kohn theorem is somewhat analogous to the variational principle which pertains to the wavefunction. It states that for a given number of electrons N and external potential $v(\mathbf{r})$, there exists a functional $E_v^{\mathrm{HK}}[\rho]$ of the electron density which, for an arbitrarily chosen trial electron density ρ, satisfies the following equation:

$$E_v^{\mathrm{HK}}[\rho] \geq E_v^{\mathrm{HK}}[\rho_0] = E_0 \tag{D.7}$$

where ρ_0 is the ground-state density, and E_0 the ground-state energy.

A consequence of the second Hohenberg-Kohn theorem is that the ground state density ρ_0 and the corresponding energy E_0 may be calculated variationally, provided that we know the Hohenberg-Kohn functional $E_v^{\mathrm{HK}}[\rho]$. However, the form of this functional is unknown. It is not specified by the second Hohenberg-Kohn theorem, which merely states that such a functional exists, but does not define its form. We do, however, have at our disposal a number of approximations to $E_v^{\mathrm{HK}}[\rho]$ which, when applied to real-world chemical systems, tend to yield satisfactorily accurate results. In what follows, we will describe the nature of these approximations and how they are applied in computer simulations.

D.3. The Kohn-Sham equations

We now turn our attention to the problem of obtaining the electron density ρ which minimises the Hohenberg-Kohn functional $E_v^{\mathrm{HK}}[\rho]$ for a given number of electrons N and external potential $v(\mathbf{r})$. Because the form of the Hohenberg-Kohn functional is unknown, we cannot directly calculate the ground-state energy E_0 by minimising $E_v^{\mathrm{HK}}[\rho]$ as a functional of the electron density ρ. We must instead take a detour of sorts, and begin our efforts to calculate the ground-state density and its corresponding energy with a wavefunction-based description of a fictitious system of non-interacting electrons.

Let us first consider a system of N "normal" (which is to say, interacting) electrons subject to the external potential generated by a number N_{nuc} of nuclei:

$$v(\mathbf{r}) = -\sum_{a=1}^{N_{\text{nuc}}} \frac{Z_a}{|\mathbf{r} - \mathbf{r}_a|} \tag{D.8}$$

The exact solution of the Schrödinger equation for that system yields the ground-state wavefunction ψ_0 and the ground-state electron density ρ_0.

Let us now imagine that we have switched off the Coulombic repulsion between electrons, so that we are left with a system of N non-interacting electrons, which from now on we will call the auxiliary system. (Note, however, that these imaginary non-interacting electrons are still fermions, so the overall wavefunction must still be antisymmetric with respect to the exchange of any two electrons.) Furthermore, let us assume that the auxiliary system is subject to an as-of-yet unspecified external potential $v_0(\mathbf{r})$ that has been constructed in such a way that it reproduces exactly the ground-state electron density ρ_0 of the original system of N interacting electrons. This assumption does not contravene the first Hohenberg-Kohn theorem, because the original and auxiliary systems differ not only by the form of the external potential, but also by the presence of electron-electron interactions. The form of $v_0(\mathbf{r})$ is unknown at this stage, but we may anticipate that the problem of finding it is no less difficult than the problem of finding ρ_0. Indeed, in what follows we shall see that in order to construct $v_0(\mathbf{r})$, we need to be able to calculate the exact energy of an arbitrary electron density, which in turn entails the knowledge of the Hohenberg-Kohn functional $E_v^{\text{HK}}[\rho]$.

Owing to the fact that the electrons comprising the auxiliary system are non-interacting, we can write down the exact ground-state wavefunction of the auxiliary system in the form of a single Slater determinant. The spinorbitals $\phi_i(\mathbf{r}, \sigma)$ which appear in that determinant, called the Kohn-Sham spinorbitals, must satisfy the following one-electron eigenvalue equation, which is an adaptation of the Fock equation (equation B.23 in Appendix B) to the case of noninteracting electrons subjected to the external potential $v_0(\mathbf{r})$:

$$-\frac{1}{2}{\nabla_1}^2\,\phi_i(\mathbf{r}_1, \sigma_1) + v_0(\mathbf{r}_1)\,\phi_i(\mathbf{r}_1, \sigma_1) = \varepsilon_i\,\phi_i(\mathbf{r}_1, \sigma_1) \tag{D.9}$$

where $\nabla_1{}^2 = \dfrac{\partial^2}{\partial {x_1}^2} + \dfrac{\partial^2}{\partial {y_1}^2} + \dfrac{\partial^2}{\partial {z_1}^2}$

We will use the spinorbitals defined by equation D.9 to write down the expression D.10 for the exact energy of the real system, which is to say, the system with the interacting electrons:

$$E = T_0 + \int v(\mathbf{r})\,\rho(\mathbf{r})\,\mathrm{d}\mathbf{r} + J[\rho] + E_{\mathrm{xc}}[\rho] \tag{D.10}$$

The meaning of the four terms on the right-hand side of equation D.10 is as follows.

- Firstly, $T_0 = -\dfrac{1}{2}\sum_{i=1}^{N}\langle\phi_i|\nabla_1{}^2|\phi_i\rangle$ is the kinetic energy of the auxiliary system of non-interacting electrons. We deliberately calculate the kinetic energy for the auxiliary system, rather than for the real system, and hope that one of the other terms in equation D.10 will later correct for the resulting error in energy.
- Secondly, $\int v(\mathbf{r})\rho(\mathbf{r})\mathrm{d}\mathbf{r}$ is the interaction energy of the electron density with the external potential given by equation D.8.
- The third term, $J[\rho] = \dfrac{1}{2}\int\int \dfrac{\rho(\mathbf{r_1})\rho(\mathbf{r_2})}{|\mathbf{r_1}-\mathbf{r_2}|}\,\mathrm{d}\mathbf{r}_1\,\mathrm{d}\mathbf{r}_2$ is the self-interaction energy of the electron density, calculated as though it was a classical continuous distribution of charge. As such, we know that this term does not allow for the tendency of electrons to avoid each other due to their mutual Coulombic repulsion (the so-called Coulomb hole), nor does it take into account that any two electrons with the same spin coordinate cannot occupy the same position in space (the Fermi, or exchange hole). We nevertheless write down $J[\rho]$ in this manner, hoping that the final term on the right-hand side of equation D.10 will correct for these sources of error.
- Finally, the term $E_{\mathrm{xc}}[\rho]$ contains (by definition) the remainder of the exact energy E. Because a way to calculate this term is not given *a priori*, equation D.10 should be interpreted as the definition of $E_{\mathrm{xc}}[\rho]$, rather than a means to calculate the exact energy. Qualitatively, $E_{\mathrm{xc}}[\rho]$ must contain the energy due to electron exchange and correlation, which is not included in the term $J[\rho]$, as well as a correction for the fact that the kinetic energy term T_0 has been calculated for the auxiliary system of non-interacting electrons, rather than for the real system. Hence, $E_{\mathrm{xc}}[\rho]$ is called the exchange-correlation energy.

At this stage, it may seem that by introducing $E_{\mathrm{xc}}[\rho]$, we have merely increased the complexity of the problem by introducing another quantity (in addition to $v_0(\mathbf{r})$) that we do not know how to calculate. We shall see, however, that $v_0(\mathbf{r})$ and $E_{\mathrm{xc}}[\rho]$ are mathematically related, and that the introduction of $E_{\mathrm{xc}}[\rho]$ does take us closer to a solution of the problem.

Having written down the expression for the exact energy, we may now take advantage of the second Hohenberg-Kohn theorem, and find the set of spinorbitals ϕ_i that minimise the energy subject to the normalisation conditions $\langle\phi_i|\phi_j\rangle = \delta_{ij}$. The minimisation is performed using the Lagrange multipliers method, much in the same way as we have done previously during the derivation of the Fock equations. The details can be found in any quantum chemistry textbook, such as *Ideas of Quantum Chemistry* by Piela.[2] Therefore, here we shall present only the final result: the Kohn-Sham equations for the best spinorbitals.

$$\left[-\frac{1}{2}\nabla^2 + v(\mathbf{r}) + v_{\mathrm{Coul}}(\mathbf{r}) + v_{\mathrm{xc}}(\mathbf{r}) \right] \phi_i(\mathbf{r},\sigma) = \varepsilon_i \phi_i(\mathbf{r},\sigma) \tag{D.11}$$

where the Coulomb operator $v_{\mathrm{Coul}}(\mathbf{r})$ is defined as

$$v_{\mathrm{Coul}}(\mathbf{r}) = \sum_{j=1}^{N} \hat{J}_j(\mathbf{r}) \quad \text{, where} \quad \hat{J}_j(\mathbf{r}_2) = \sum_{\sigma_1} \int \frac{\phi_j^*(\mathbf{r}_1,\sigma_1)\,\phi_j(\mathbf{r}_1,\sigma_1)}{|\mathbf{r}_1 - \mathbf{r}_2|}\,\mathrm{d}\mathbf{r}_1$$

$v_{\mathrm{xc}}(\mathbf{r})$, on the other hand, is the exchange-correlation potential. It is defined as the functional derivative of the exchange-correlation energy with respect to the electron density:

$$v_{\mathrm{xc}}(\mathbf{r}) = \frac{\delta E_{\mathrm{xc}}}{\delta \rho(\mathbf{r})} \tag{D.12}$$

Before further discussing the Kohn-Sham equations, let us embark on a brief digression about functional derivatives. As a simple example, the functional $F[f]$ of a function $f(\mathbf{x})$, where $\mathbf{x}$ denotes one or more variables, could be given as the integral of $f(\mathbf{x})$ over a volume V:

$$F[f] = \int_V f(\mathbf{x})\,\mathrm{d}\mathbf{x}$$

More generally, the functional might be defined as the integral of another function g that may depend on $f(\mathbf{x})$ in a complicated manner. For example, g may be a

function of $\mathbf{x}$, $f(\mathbf{x})$ and $\nabla f(\mathbf{x})$.

$$F[f] = \int_V g(\mathbf{x}, f(\mathbf{x}), \nabla f(\mathbf{x}))\, \mathrm{d}\mathbf{x} \tag{D.13}$$

The functional derivative of $F[f]$ with respect to the function $f(\mathbf{x})$ is denoted $\dfrac{\delta F}{\delta f(\mathbf{x})}$ and defined by the limit:

$$\int_V \frac{\delta F}{\delta f(\mathbf{x})}\, h(\mathbf{x})\, \mathrm{d}\mathbf{x} = \lim_{\epsilon \to 0} \frac{F[f + \epsilon h] - F[f]}{\epsilon} \tag{D.14}$$

where ϵ is a scalar parameter and $h(\mathbf{x})$ an arbitrarily chosen function defined in the same variables as $f(\mathbf{x})$.

From the definition, the functional derivative has the following useful property: when the function f is varied by adding to it another function k, the variation of the functional $F[f]$ may be expressed by the integral

$$\delta F = \int_V \frac{\delta F}{\delta f(\mathbf{x})}\, k(\mathbf{x})\, \mathrm{d}\mathbf{x} \tag{D.15}$$

In the important special case of $F[f]$ given by the integral D.13, $\dfrac{\delta F}{\delta f(\mathbf{x})}$ may be calculated using the following formula:

$$\frac{\delta F}{\delta f(\mathbf{x})} = \frac{\partial g}{\partial f} - \nabla \cdot \frac{\partial g}{\partial \nabla f} = \frac{\partial g}{\partial f} - \nabla \cdot \left[\frac{\partial g}{\partial (\frac{\partial f}{\partial x_1})}, \frac{\partial g}{\partial (\frac{\partial f}{\partial x_2})}, \ldots, \frac{\partial g}{\partial (\frac{\partial f}{\partial x_N})} \right] \tag{D.16}$$

where $x_1, x_2, ..., x_N$ are the components of $\mathbf{x}$.

Returning now to the Kohn-Sham equations, by comparing them with equation D.9 we find that the potential $v_0(\mathbf{r})$ can be expressed as:

$$v_0(\mathbf{r}) = v(\mathbf{r}) + v_{\mathrm{Coul}}(\mathbf{r}) + v_{\mathrm{xc}}(\mathbf{r}) \tag{D.17}$$

Until this point we have tacitly assumed that the spatial distributions of electrons with the α and β spin functions are the same. In the general case, however, they may be different, which is called spin polarisation. We will therefore write down the general form of the Kohn-Sham equations that takes into account the possibility spin-polarised density. The total density $\rho(\mathbf{r})$ is partitioned into α and

β components:

$$\rho(\mathbf{r}) = \rho_\alpha(\mathbf{r}) + \rho_\beta(\mathbf{r})$$

where

$$\rho_\alpha(\mathbf{r}) = N \int \int \ldots \int |\psi(\mathbf{r}_1, \sigma_1, \mathbf{r}_2, \sigma_2, ..., \mathbf{r}_N, \sigma_N)|^2 \, \mathrm{d}\tau_2 \, \mathrm{d}\tau_3 \, \ldots \, \mathrm{d}\tau_N \;\text{ for }\; \sigma_1 = \frac{1}{2}$$

$$\rho_\beta(\mathbf{r}) = N \int \int \ldots \int |\psi(\mathbf{r}_1, \sigma_1, \mathbf{r}_2, \sigma_2, ..., \mathbf{r}_N, \sigma_N)|^2 \, \mathrm{d}\,\tau_2 \, \mathrm{d}\,\tau_3 \, \ldots \, \mathrm{d}\tau_N \;\text{ for }\; \sigma_1 = -\frac{1}{2}$$

In analogy to the UHF method, the spinorbitals are divided into α and β spinorbitals:

$$\phi_i(\mathbf{r}, \sigma) = \varphi_i(\mathbf{r})\, \alpha(\sigma) \quad \text{if } i \text{ is odd}$$

$$\phi_i(\mathbf{r}, \sigma) = \varphi_i(\mathbf{r})\, \beta(\sigma) \quad \text{if } i \text{ is even}$$

Two sets of Kohn-Sham equations result, one for the α spinorbitals and another for the β spinorbitals:

$$\left[-\frac{1}{2}{\nabla_1}^2 + v(\mathbf{r}) + v_{\mathrm{Coul}}(\mathbf{r}) + v_{\mathrm{xc}}^{\alpha}(\mathbf{r}) \right] \phi_i(\mathbf{r}, \sigma) = \varepsilon_i \phi_i(\mathbf{r}, \sigma) \quad \text{if } i \text{ is odd}$$

$$\left[-\frac{1}{2}{\nabla_1}^2 + v(\mathbf{r}) + v_{\mathrm{Coul}}(\mathbf{r}) + v_{\mathrm{xc}}^{\beta}(\mathbf{r}) \right] \phi_i(\mathbf{r}, \sigma) = \varepsilon_i \phi_i(\mathbf{r}, \sigma) \quad \text{if } i \text{ is even}$$

The definition of the Coulomb operator $v_{\mathrm{Coul}}(\mathbf{r})$ is the same as for the Kohn-Sham equations in the form given by D.11. Each of the exchange-correlation operators $v_{\mathrm{xc}}^{\alpha}(\mathbf{r})$ and $v_{\mathrm{xc}}^{\beta}(\mathbf{r})$ will depend on both the α and the β densities.

D.4. Matrix form of the Kohn-Sham equations

The LCAO method introduced in Appendix B in the context of the Hartree-Fock method is equally applicable in DFT methods. In analogy to the Fock operator, we shall define the Kohn-Sham operator $\hat{F}^{\mathrm{KS}}$:

$$\hat{F}^{\mathrm{KS}}\, \phi_i(1) = \begin{cases} [-\frac{1}{2}{\nabla_1}^2 + v(\mathbf{r}) + v_{\mathrm{Coul}}(\mathbf{r}) + v_{\mathrm{xc}}^{\alpha}(\mathbf{r})]\, \phi_i(1) & \text{if } i \text{ is odd} \\ [-\frac{1}{2}{\nabla_1}^2 + v(\mathbf{r}) + v_{\mathrm{Coul}}(\mathbf{r}) + v_{\mathrm{xc}}^{\beta}(\mathbf{r})]\, \phi_i(1) & \text{if } i \text{ is even} \end{cases}$$

Each Kohn-Sham spinorbital will be written as a linear combination of basis functions $\chi_j(\mathbf{r})$:

$$\phi_i(\mathbf{r}) = \sum_{j=1}^{M} c_{ji}\,\chi_j(\mathbf{r})$$

By retracing the derivation of the Roothan-Hall equation given in Appendix B, we may cast the Kohn-Sham equation in the following matrix form:

$$\mathbf{F}^{\mathrm{KS}}\,\mathbf{c} = \mathbf{S}\,\mathbf{c}\,\boldsymbol{\varepsilon} \tag{D.18}$$

where the elements of the matrix $\mathbf{F}^{\mathrm{KS}}$ are given by

$$F_{kj}^{\mathrm{KS}} = \int \chi_k^*(1)\,\hat{F}^{\mathrm{KS}}(1)\,\chi_j(1)\,\mathrm{d}\tau_1$$

and the coefficients matrix $\mathbf{c}$, the overlap matrix $\mathbf{S}$ and the diagonal matrix $\boldsymbol{\varepsilon}$ that contains the Kohn-Sham spinorbital energies are defined as for the Hartree-Fock method.

D.5. The exchange-correlation functional

Although having derived the Kohn-Sham equations for the best spinorbitals, we identified mathematical relationships between the exchange-correlation energy $E_{\mathrm{xc}}[\rho]$, the external potential $v_0(\mathbf{r})$, and the exchange-correlation operator $v_{\mathrm{xc}}(\mathbf{r})$, we have yet to propose a method to calculate any one of these quantities. Unfortunately, a rigorous method to calculate the $E_{\mathrm{xc}}[\rho]$ (or, equivalently, $v_0(\mathbf{r})$ or $v_{\mathrm{xc}}(\mathbf{r})$) is not known, and in practical calculations we must contend with approximations to the true exchange-correlation functional. Such an approximation is substituted for $E_{\mathrm{xc}}[\rho]$ in equation D.10, and likewise using equation D.16 a corresponding approximation to the operator $v_{\mathrm{xc}}(\mathbf{r})$ is generated and substituted into the Kohn-Sham equations D.11.

It is usual to split the exchange-correlation energy $E_{\mathrm{xc}}[\rho]$ into separate exchange ($E_{\mathrm{x}}[\rho]$) and correlation ($E_{\mathrm{c}}[\rho]$) terms:

$$E_{\mathrm{xc}}[\rho] = E_{\mathrm{x}}[\rho] + E_{\mathrm{c}}[\rho] \tag{D.19}$$

Furthermore, as a simplifying approximation, each of the exchange and correlation energies is written as the volume integral of the electron energy and an energy density ε:

$$E_{\mathrm{x}}[\rho] = \int \rho(\mathbf{r})\varepsilon_{\mathrm{x}}(\rho(\mathbf{r}))\mathrm{d}\mathbf{r} \tag{D.20}$$

$$E_{\mathrm{c}}[\rho] = \int \rho(\mathbf{r})\varepsilon_{\mathrm{c}}\left(\rho(\mathbf{r})\right)\mathrm{d}\mathbf{r} \tag{D.21}$$

In what follows, we will briefly discuss a few selected approximations to $E_{\mathrm{x}}[\rho]$ and $E_{\mathrm{c}}[\rho]$ that, over the years, have become landmarks in the landscape of DFT: the local spin density approximation, the gradient-corrected methods, and the hybrid exchange-correlation functionals.

D.5.1. The local spin density approximation

The local spin density approximation (LSDA) is based on the idea that the exchange and correlation energy densities in a real-world system such as a molecule may be approximated by the respective energy densities in a simple model system, the homogeneous electron gas (jellium). The word "local" in the name of the method refers to the fact that in the LSDA approach, the energy densities $\varepsilon_{\mathrm{x}}(\rho(\mathbf{r}))$ and $\varepsilon_{\mathrm{c}}(\rho(\mathbf{r}))$ depend only on the α and β electron densities at position vector $\mathbf{r}$, but not the electron density anywhere else:

$$\varepsilon_{\mathrm{x}}^{\mathrm{LSDA}} = f_{\mathrm{x}}(\rho_\alpha(\mathbf{r}), \rho_\beta(\mathbf{r})) \qquad \varepsilon_{\mathrm{c}}^{\mathrm{LSDA}} = f_{\mathrm{c}}(\rho_\alpha(\mathbf{r}), \rho_\beta(\mathbf{r})) \tag{D.22}$$

The exchange energy density of jellium is known exactly and is given by the simple expression:

$$\varepsilon_{\mathrm{x}}^{\mathrm{LSDA}}(\rho(\mathbf{r})) = -\frac{1}{2}C_{\mathrm{x}}\left[(1+\zeta)^{4/3} + (1-\zeta)^{4/3}\right](\rho_\alpha + \rho_\beta)^{1/3}$$

where $C_{\mathrm{x}} = \frac{3}{4}(\frac{3}{\pi})^{1/3}$ is a constant, and the relative spin polarisation ζ is defined by $\zeta = \dfrac{\rho_\alpha - \rho_\beta}{\rho_\alpha + \rho_\beta}$.

The situation is slightly more complex for the correlation energy, which is known exactly only in the limits of very high and very low electron density. For intermediate densities, accurate values of the correlation energy density have

been calculated by means of quantum Monte Carlo simulations. To this data, analytic functions were fitted by Vosko, Wilk and Nusair,[3] and independently by Perdew and Wang,[4] producing local spin density correlation functionals. As an illustration of the mathematical form of such a correlation functional, we will write down the parameterisation of Perdew and Wang in full. The correlation energy density is given by the expression

$$\varepsilon_{\rm c}(r_{\rm s},\zeta) = \varepsilon_{\rm c}(r_{\rm s},0) + \alpha_{\rm c}(r_{\rm s})\,\frac{f(\zeta)}{f''(0)}\,(1-\zeta^4) + [\varepsilon_{\rm c}(r_{\rm s},1) - \varepsilon(r_{\rm s},0)]\;f(\zeta)\,\zeta^4$$

The function $f(\zeta)$ is given by:

$$f(\zeta) = \frac{(1+\zeta)^{4/3} + (1-\zeta)^{4/3} - 2}{2^{4/3} - 2}$$

$f''(0)$ is the second derivative of $f(\zeta)$ at $\zeta = 0$:

$$f''(0) = \frac{\frac{4}{3}\times\frac{1}{3} + \frac{4}{3}\times\frac{1}{3}}{2^{4/3}-2} = 1.7099209$$

The scalar variable $r_{\rm s} = \left[\dfrac{3}{4\pi\rho(\mathbf{r})}\right]^{1/3}$ is the effective volume containing one electron.

The functions $\varepsilon_{\rm c}(r_{\rm s},0)$, $\varepsilon_{\rm c}(r_{\rm s},1)$ and $-\alpha_{\rm c}(r_{\rm s})$ (note the minus sign in front of $\alpha_{\rm c}(r_{\rm s})$) are each parameterised by the same function g with different values of the parameters A, α_1, and β_1 to β_4, which are given in the table below:

$$g = -2\,A\,(1+\alpha_1\,r_{\rm s})\log\left[1 + \frac{1}{2\,A\,(\,\beta_1\,r_{\rm s}^{1/2} + \beta_2\,r_{\rm s} + \beta_3\,r_{\rm s}^{3/2} + \beta_4\,r_{\rm s}^2\,)}\right]$$

parameter	$\varepsilon_{\rm c}(r_{\rm s},0)$	$\varepsilon_{\rm c}(r_{\rm s},1)$	$-\alpha(r_{\rm s})$
A	0.031091	0.015545	0.016887
α_1	0.21370	0.20548	0.11125
β_1	7.5957	14.1189	10.357
β_2	3.5876	6.1977	3.6231
β_3	1.6382	3.3662	0.88026
β_4	0.49294	0.62517	0.49671

Despite its conceptual elegance, the LSDA approach unfortunately does not achieve the level of accuracy required in chemical applications. Although it predicts molecular geometries in reasonably good agreement with experiment, bond energies and atomisation energies are strongly overestimated. It has,

however, enjoyed much success in the study of solid-state systems such as metals and semiconductors, where the underlying approximation of a uniform electron density is more realistic.

D.5.2. The generalised gradient approximation

The natural starting point for an improvement on the LSDA method is to take into account the inhomogeneity of real-world electron densities. Whereas in the LSDA approach (equation D.22), each of the exchange and correlation energy densities is a function of only the α and β densities at position vector $\mathbf{r}$, within the generalised gradient approximation (GGA) the energy densities also depend on the gradients of the α and β densities:

$$\begin{aligned} \varepsilon_{\mathrm{x}}^{\mathrm{GGA}} &= f_{\mathrm{x}}(\rho_\alpha(\mathbf{r}), \rho_\beta(\mathbf{r}), \nabla\rho_\alpha(\mathbf{r}), \nabla\rho_\beta(\mathbf{r})) \\ \varepsilon_{\mathrm{c}}^{\mathrm{GGA}} &= f_{\mathrm{c}}(\rho_\alpha(\mathbf{r}), \rho_\beta(\mathbf{r}), \nabla\rho_\alpha(\mathbf{r}), \nabla\rho_\beta(\mathbf{r})) \end{aligned} \tag{D.23}$$

A large number of GGA exchange-correlation functionals have been proposed in the literature, constructed in different ways and with varying performance. Here we will discuss only the functional of Perdew, Burke and Ernzerhof[5,6] (the PBE functional), which we have used to describe the ground-state molecules in our hybrid TD-DFT/DFT simulations. The PBE functional is defined as a density and gradient dependent correction to the LSDA functional. The LSDA energy density is multiplied by a function $F(x)$ which depends on the density and its gradient:

$$\varepsilon_{\mathrm{x}}^{\mathrm{PBE}} = \varepsilon_{\mathrm{x}}^{\mathrm{LSDA}} F(x)$$

where $x = \dfrac{|\nabla\rho|}{\rho^{4/3}}$. The LSDA correlation energy density, on the other hand, is modified by the addition of a function $H(t)$

$$\varepsilon_{\mathrm{c}}^{\mathrm{PBE}} = \varepsilon_{\mathrm{c}}^{\mathrm{LSDA}} + H(t)$$

where the variable t is defined by

$$t = \frac{x}{\pi\, 3^{1/3}\, [(1+\zeta)^{2/3} + (1-\zeta)^{2/3}]}$$

The functions $F(x)$ and $H(t)$ have been constructed in such a way so that the resulting exchange-correlation functional reproduces the known behaviour

of the exact exchange-correlation functional under specific conditions, and the only parameters involved in their definitions are fundamental constants. For the homogeneous electron density ($\nabla\rho = \mathbf{0}$, $x = 0$ and $t = 0$), $F(x)$ and $H(t)$ take values of 1 and 0, respectively which means that we recover the LSDA functional, which is exact for the homogeneous density. Thus, the PBE functional may be considered an extension of the design philosophy behind the LSDA functional, whereby the approximate functional is parameterised in order to emulate the known properties of the exact functional.

Some other GGA functionals, such as the HCTH functional,[7] have been developed empirically by fitting to reproduce highly accurate experimental and theoretical *ab initio* benchmarks.

D.5.3. Hybrid exchange-correlation functionals

Another milestone of the development of approximate exchange-correlation functionals is the idea of Becke[8] to introduce into equation D.19 a certain amount of the exact exchange energy, $E_{\mathrm{x}}^{\mathrm{exact}}[\rho]$:

$$E_{\mathrm{xc}}[\rho] = c\, E_{\mathrm{x}}^{\mathrm{exact}}[\rho] + (1-c)\, E_{\mathrm{x}}^{\mathrm{GGA}}[\rho] + E_{\mathrm{c}}^{\mathrm{GGA}}[\rho] \tag{D.24}$$

where $E_{\mathrm{x}}^{\mathrm{DFT}}[\rho]$ and $E_{\mathrm{c}}^{\mathrm{DFT}}[\rho]$ are respectively the exchange and correlation density functionals calculated using a GGA exchange-correlation functional, and c is a weighting coefficient. The exact exchange energy term is the exchange energy of the Slater determinant comprising the Kohn-Sham spinorbitals (see equation B.24 in Appendix B).

$$E_{\mathrm{x}}^{\mathrm{exact}}[\rho] = -\frac{1}{2}\sum_{i=1}^{N}\sum_{j=1}^{N} K_{ij} = -\frac{1}{2}\sum_{i=1}^{N}\sum_{j=1}^{N} \langle ij|ji\rangle \tag{D.25}$$

Exchange-correlation functionals that include exact exchange are normally referred to as hybrid functionals. They are not to be confused with the hybrid QM/MM and QM/QM methods which we have discussed in Chapter 1, which are hybrid methods of an altogether different type.

The insertion of an amount of exact exchange into the equation D.101 is not arbitrary, nor is it simply an attempt to improve the performance of a DFT functional through the addition of another fitting parameter (the coefficient c in

equation D.24). Indeed, there is strong theoretical rationale for the inclusion of exact exchange. Namely, it can be shown[9] that the exact exchange-correlation energy functional, $E_{\mathrm{xc}}[\rho]$, can be expressed in the form of the following equation called the adiabatic connection formula:

$$E_{\mathrm{xc}}[\rho] = \int_0^1 U_{\mathrm{xc}}(\lambda)\,\mathrm{d}\lambda \tag{D.26}$$

where λ is a switching parameter which scales the electron-electron repulsion to $\dfrac{\lambda\, e^2}{r}$. At $\lambda = 0$, the electrons' mutual Coulombic repulsion is switched off completely, and we obtain the auxiliary system of non-interacting electrons subjected to the external potential $v_0(\mathbf{r})$. At $\lambda = 1$, the Coulombic repulsion is included in full. Between $\lambda = 0$ and 1 lies a continuum of systems in which the electron-electron repulsion is scaled by a factor of λ. Each of these intermediate systems is subjected to an external potential $v_\lambda(\mathbf{r})$ such that the ground-state electron densities of all these systems are identical to the ground-state electron density $\rho(\mathbf{r})$ of the fully interacting system.

The integrand $U_{\mathrm{xc}}(\lambda)$ is the potential energy of exchange-correlation at a electron-electron interaction strength λ. It is given by:

$$U_{\mathrm{xc}}(\lambda) = \frac{1}{2}\int\int \frac{P_\lambda(\mathbf{r}_1,\mathbf{r}_2)}{|\mathbf{r}_1-\mathbf{r}_2|}\,\mathrm{d}\mathbf{r}_1\,\mathrm{d}\mathbf{r}_2 - \frac{1}{2}\int\int \frac{\rho(\mathbf{r}_1)\,\rho(\mathbf{r}_2)}{|\mathbf{r}_1-\mathbf{r}_2|}\,\mathrm{d}\mathbf{r}_1\,\mathrm{d}\mathbf{r}_2$$

Here, $P_\lambda(\mathbf{r}_1,\mathbf{r}_2)$ is the electron pair-density, which describes the probability of finding an electron at a point $\mathbf{r}_1$ and another at $\mathbf{r}_2$. It is formally defined as

$$P_\lambda(\mathbf{r}_1,\mathbf{r}_2) = N(N-1)\sum_{\sigma_1}\sum_{\sigma_2}|\psi(\mathbf{r}_1,\sigma_1,\mathbf{r}_2,\sigma_2,...,\mathbf{r}_N,\sigma_N)|^2\,\mathrm{d}\tau_3\,\mathrm{d}\tau_4\ldots\mathrm{d}\tau_N$$

Unlike the electron density, $P_\lambda(\mathbf{r}_1,\mathbf{r}_2)$ varies with λ, hence the subscript.

As stated previously, $\lambda = 0$ corresponds to the system of non-interacting, and therefore non-correlated electrons. The correlation energy of this system is zero, while the exchange energy is equal to the exchange energy of the Slater determinant containing the Kohn-Sham orbitals:

$$E_{\mathrm{x}}^{\mathrm{exact}}[\rho] = -\frac{1}{2}\sum_{i=1}^{N}\sum_{j=1}^{N}\langle ij|ji\rangle$$

Figure D.1: A schematic plot of $U_{\text{xc}}(\lambda)$ within the assumption that it is a linear function of λ. It is immediately visible that $\int_0^1 U_{\text{xc}}(\lambda)\,\mathrm{d}\lambda$ is equal to the area of the shaded region, and must therefore be equal to $\frac{1}{2}U_{\text{xc}}(0) + \frac{1}{2}U_{\text{xc}}(1)$.

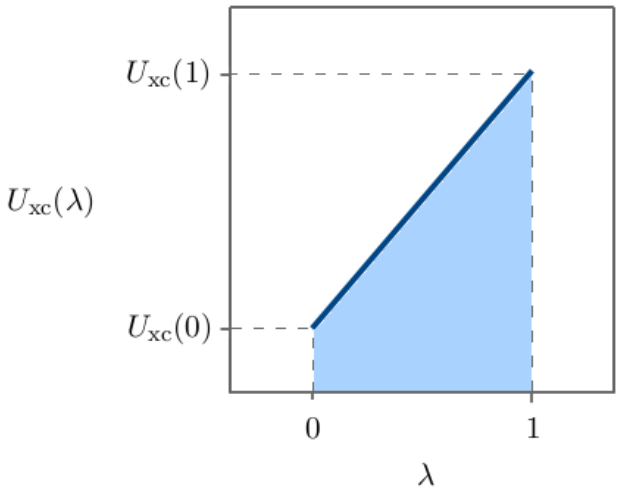

For $\lambda = 1$, on the other hand, the potential energy of exchange-correlation energy may be calculated exactly provided that we know the exact wavefunction (which, of course, we do not, but let us ignore that fact for the moment). Let us assume for the moment that $U_{\text{xc}}(\lambda)$ is a linear function of λ (in reality, it is not). This situation is shown schematically in Figure D.1 above.

$U_{\text{xc}}(\lambda)$ may then be written in the form

$$U_{\text{xc}}(\lambda) = \lambda\, U_{\text{xc}}(1) + (1-\lambda)\, U_{\text{xc}}(0)$$

It follows that

$$E_{\text{xc}}[\rho] = \int_0^1 \left[\lambda\, U_{\text{xc}}(1) + (1-\lambda)\, U_{\text{xc}}(0)\right] \mathrm{d}\lambda = \frac{1}{2}\, U_{\text{xc}}(0) + \frac{1}{2}\, U_{\text{xc}}(1) \qquad \text{(D.27)}$$

As already pointed out, in reality the dependence of $U_{\text{xc}}(\lambda)$ on λ is not linear. Nevertheless, the above equation D.27 does show that the exact exchange-correlation energy E_{xc} contains a contribution from $U_{\text{xc}}(\lambda)$ at $\lambda \approx 0$. Because of their local nature, GGA exchange correlation functionals are incapable of modelling exact exchange. Indeed, in equation D.25 which defines exact exchange, all pairs of spinorbitals ϕ_i and ϕ_j are treated on an equal footing regardless of whether the spinorbitals are spatially close or localised on distant centers, whereas in GGAs the exchange and correlation energies are both calculated

locally. On the grounds of the above, we may anticipate that an admixture of exact exchange could improve the performance of GGA functionals.

Becke demonstrated the correctness of this inference by devising an exchange-correlation functional in the form:

$$E_{\mathrm{xc}}[\rho] = E_{\mathrm{xc}}^{\mathrm{LSDA}}[\rho] + a_0 \left(E_{\mathrm{x}}^{\mathrm{exact}}[\rho] - E_{\mathrm{x}}^{\mathrm{LSDA}}[\rho] \right) + a_x \, \Delta E_{\mathrm{x}}^{\mathrm{B88}}[\rho] + a_c \, \Delta E_{\mathrm{c}}^{\mathrm{PW91}}$$

where $E_{\mathrm{xc}}^{\mathrm{LSDA}}[\rho]$ and $E_{\mathrm{x}}^{\mathrm{LSDA}}[\rho]$ are respectively the LSDA exchange-correlation energy and the LSDA exchange energy. $\Delta E_{\mathrm{x}}^{\mathrm{B88}}[\rho]$ is the correction to the LSDA exchange energy due to Becke,[10] while $\Delta E_{\mathrm{c}}^{\mathrm{PW91}}$ is the correction to the LSDA correlation energy due to Perdew and Wang.[11] Both these corrections are gradient-dependent; the former appears as a term added to the LSDA exchange energy, while the latter is a multiplicative scaling factor for the LSDA correlation energy.

Once the values of the coefficients a_0, a_{x} and a_{c} were obtained through a least-squares fit to experimental data, the resulting functional (now known in the literature as the B3PW91 functional, the "3" denoting the three semiempirical coefficients) reproduced said data significantly better than the parent B88PW91 functional. Sure enough, since Becke's pioneering study many hybrids of GGA exchange-correlation functionals with exact exchange have been developed. For instance, the PBE functional introduced in the previous subsection has been made into the hybrid functional PBE0 by Adamo and Barone.[12] Due to the fact that within the framework of linear response time-dependent density functional theory (see Section D.7), this functional consistently predicts excitation energies of organic molecules in good agreement with experiment,[13–16] and it is also known to predict qualitatively correct excited-state geometries, for small organic molecules at least,[17] we have used this functional to describe the π, π^* excited states of the compounds 7-(2'-pyridyl)indole and *N*-salicylidene-2-chloroaniline.

D.6. Dispersion interactions within density functional theory

As amply evidenced in the literature, GGA and hybrid functionals generally predict molecular equilibrium geometries and potential energy surfaces with fair to good accuracy.[18–22] These successes, however, are tempered by the failure of these types of functionals to accurately describe the relatively weak but often

critically important dispersion interaction. Due to the decisive role of dispersion in controlling the structure and properties of molecular crystals, we must now give consideration to this shortcoming and some practical techniques that attempt to correct for it.

The physical origin of the dispersion interaction is the electron correlation between electron densities at relatively distant (separated by a few Angstroms) atoms, which has the effect of slightly increasing the electron density between such atoms and it consequently creates a weak attractive force between the positively charged nuclei. It is easy to see that since in equations D.23 which define the GGA approach, the exchange and correlation energy densities depend only on the local electron density and its gradient, the long-range correlation effects that are responsible for the dispersion interaction are absent from GGA functionals. It follows that these functionals will fail to provide a realistic description of systems in which dispersion interactions are important, which includes in particular molecular crystals of nonpolar molecules such as we have studied in the present work. The situation is not improved with the introduction of exact exchange in hybrid functionals, since it does nothing to correct for the absence of long-range correlation.

In order to demonstrate the seriousness of the problem, we have conducted a numerical experiment with a classic example of a system held together by dispersion: the benzene dimer in the π-stacked (point group D_{6h}) and T-shaped (C_{2v}) conformations, shown in Figure D.2(a) and (b), respectively. The π-π and C$-$H$\cdots\pi$ interactions that hold together the respective dimers can be considered as a simple model of the dispersion interactions that occur in the crystal forms of 7-(2-pyridyl)-indole and *N*-salicylidene-2-chloroaniline, the molecules of which contain substituted aromatic rings. Hence, conclusions drawn from this system may be generalised to all the molecular crystals studied in the present work.

The following procedure was adopted: first, the geometry of the isolated benzene molecule was optimised at the PBE/cc-pVDZ level of theory as implemented in the program Gaussian 09.[23] A series of π-stacked dimer structures was subsequently constructed, in which the constituent benzene molecules were retained in the equilibrium geometry of the isolated molecule, while the intermolecular distance d_1 was varied in the range from 3.0 to 6.0 Å in steps of 0.1 Å. Likewise, a series of T-shaped structures was also built, where the distance d_2 was varied in the

Figure D.2: The π-stacked and T-shaped conformations of the benzene dimer.

(a) The π-stacked dimer (D_{6h} point group). d_1 is the distance between the parallel planes of the two benzene molecules.

(b) The T-shaped dimer (C_{2v} point group). d_2 is the distance between the plane of the lower molecule and the upper molecule.

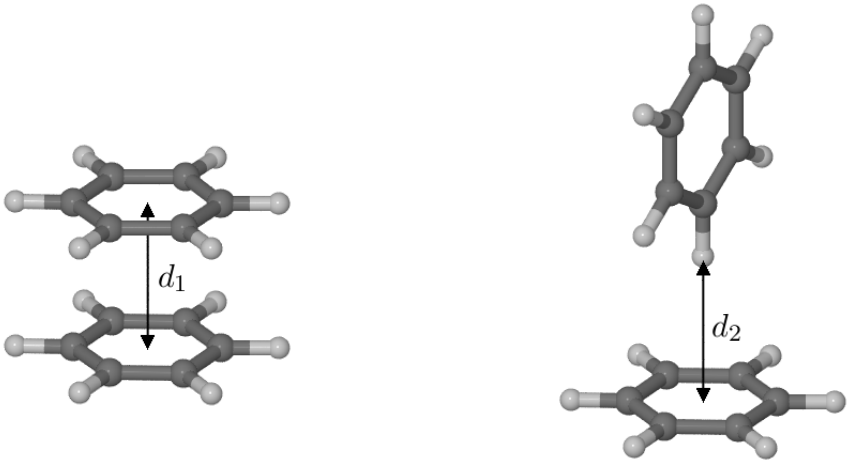

range from 2.0 to 5.5 Å in steps of 0.1 Å. The energies of the dimer structures generated in this manner were evaluated through single-point calculations at the PBE/aug-cc-pVDZ and PBE0/aug-cc-pVDZ levels within Gaussian 09. As a benchmark for the abovementioned DFT functionals, we have employed the CCSD method introduced in Appendix C. When coupled with the aug-cc-pVDZ basis set, which includes diffuse functions, this method may be expected to provide a reasonably accurate description of dispersion. (See, however, the discussion of the accuracy of the CCSD method in Chapter 2.) The single-point energies of the benzene dimer were therefore recalculated at the frozen-core CCSD/aug-cc-pVDZ level implemented in Gaussian 09.

In Figure D.3(a) and (b), respectively, the resulting potential energies of the π-stacked and T-shaped dimer geometries are plotted as functions of the distances d_1 and d_2. For the π-stacked dimer, it can be seen that the PBE and PBE0 functionals yield near-identical purely repulsive curves, in stark contrast to the CCSD method, which features a minimum at $d_1 = 3.8$ Å corresponding to a binding energy of 0.106 eV. Evidently, as far as both the DFT functionals are concerned, π-π interactions do not exist! For the T-shaped dimer, the PBE

Figure D.3: Potential energy curves calculated for the π-stacked and T-shaped benzene dimers using the PBE and PBE0 functionals and the CCSD method. The zero of the energy scale corresponds to two isolated benzene molecules.

(a) The π-stacked dimer.

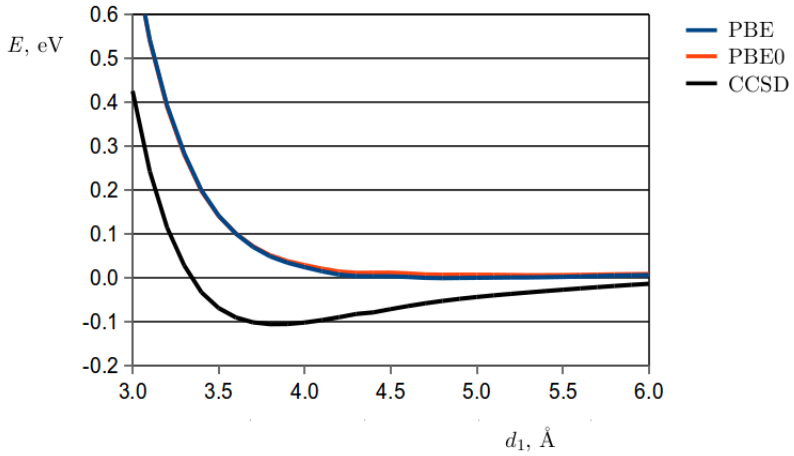

(b) The T-shaped dimer.

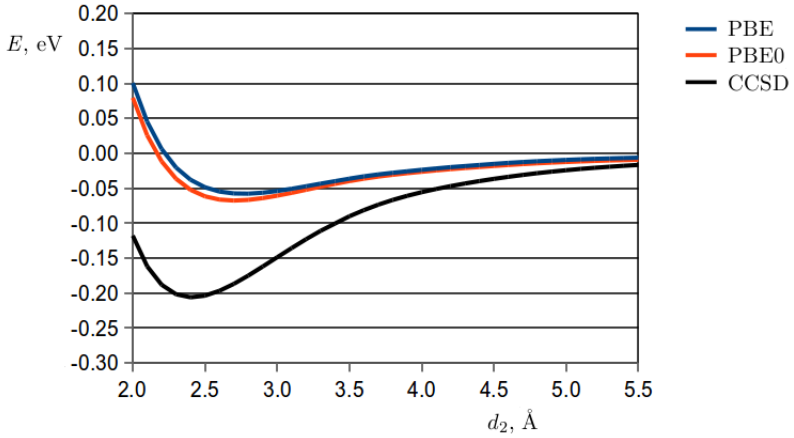

and PBE0 curves are again very close to each other and both feature a minimum corresponding to a binding energy of around 0.058 eV. The CCSD method, however, predicts a significantly higher binding energy of 0.206 eV. Furthermore, the fact that the PBE and PBE0 functionals predict a nonzero binding energy for the T-shaped dimer is likely caused by the partially electrostatic character of the C$-$H$\cdots\pi$ interaction that holds it together, rather than any success of the functionals at describing dispersion interactions.

Clearly, then, dispersion interactions are absent from the picture obtained with GGA functionals. Nevertheless, given that most of the other interactions relevant

in chemistry (such as covalent bonding, electrostatic interactions, and hydrogen bonding) are generally well described by the GGA functionals, and that the electron density changes brought about by dispersion interactions are fairly slight, in order to achieve an accurate description of dispersion-bound systems it seems reasonable to retain the GGA functional in its original form, and only add the dispersion interaction as an *a posteriori* correction to the energy. We will presently discuss two dispersion correction schemes which work in such a manner.

The first was used by Ugliengo and Damin[24] and later by Tuma and Sauer[25] to study molecules physisorbed onto mineral surfaces. The underlying idea was to use the subtractive QM/QM formalism in order to combine a DFT description of the adsorbed molecule and the adsorbent mineral with a treatment of the dispersion interaction between them using the MP2 method, or more generally any correlated wavefunction-based method. Although this approach strays very far from pure density functional theory, it does have the advantage of requiring no empirical parameters to describe the dispersion interaction. Its drawbacks are that the only dispersion interactions included in the calculation are those acting in the region treated using the wavefunction-based method, and that correlated wavefunction-based methods such as the MP2 method and coupled-cluster methods are computationally expensive.

In the second scheme, which is due to Grimme,[26] the dispersion correction takes the form of a Lennard-Jones-like term added to the Kohn-Sham energy of the electron density:

$$E = T_0 + \int v(\mathbf{r})\rho(\mathbf{r})\mathrm{d}\mathbf{r} + J[\rho] + E_{\mathrm{xc}}[\rho] + E_{\mathrm{disp}} \tag{D.28}$$

The dispersion term E_{disp} is a function on the positions of the nuclei, but does not depend in any way on the electron density distribution. It is given by the following sum over all pairs a, b of nuclei:

$$E_{\mathrm{disp}} = -s_6 \sum_{a=1}^{N_{\mathrm{nuc}}-1} \sum_{b=a+1}^{N_{\mathrm{nuc}}} \frac{C_6^{ab}}{{r_{ab}}^6} f(r_{ab}) \tag{D.29}$$

r_{ab} denotes the distance between the nuclei a and b. $f(r)$ is a damping function whose purpose is to "switch off" the correction at short distances.

$$f(r_{ab}) = \frac{1}{1 + \exp\left[-d\left(\frac{r_{ab}}{R_a^0 + R_b^0} - 1\right)\right]} \tag{D.30}$$

The dispersion coefficients C_6^{ab} are empirical parameters whose values have been determined by a least-squares fit to a training set of reaction energies. The van der Waals atomic radii R_a^0, on the other hand, have been estimated based on *ab initio* calculations for isolated atoms. Both sets of parameters are assumed to be transferable without modification across different exchange-correlation functionals and also across different basis sets of high quality (which is to say, triple zeta and better basis sets). The van der Waals radii and the dispersion coefficients for homatomic pairs (e.g. carbon-carbon) for selected elements have been tabulated below:

Element	C_6, J×nm^6×mol^{-1}	R^0, Å
H	0.14	1.001
C	1.75	1.452
N	1.23	1.397
O	0.70	1.342
Cl	5.07	1.639

For heteroatomic pairs (e.g., carbon-nitrogen), the values of the dispersion coefficient are calculated using the standard Lorentz-Berthelot mixing rules:

$$C_6^{\mathrm{CN}} = \sqrt{C_6^{\mathrm{C}}\, C_6^{\mathrm{N}}}$$

where C_6^{C}, C_6^{N} are the homoatomic dispersion coefficients for carbon and nitrogen, respectively.

The number d which appears in the definition of the damping function is another parameter, controlling the form of the damping function. Its value was set by Grimme to 20. Lastly, s_6 is a global scaling factor that controls the magnitude of the dispersion corrections. Values of s_6 were optimised for several popular GGA and hybrid functionals; for the PBE functional, $s_6 = 0.75$.

In Figure D.4, we illustrate the dispersion correction of Grimme on the example of two carbon atoms as a function of the distance between them. The

Figure D.4: The dispersion correction for two carbon atoms, separated by a distance r and described by the PBE functional.

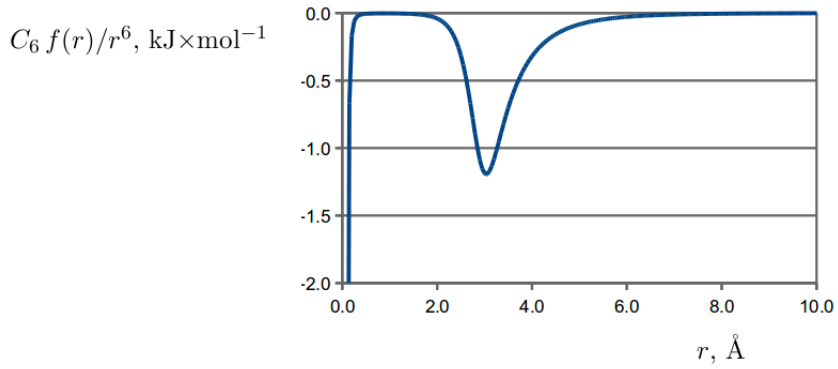

carbons might be isolated atoms, or they might be part of a single molecule, or two separate molecules - the dispersion correction scheme of Grimme does not distinguish between these situations. The dispersion correction curve features a minimum of -1.195 kJ×mol^{-1} at an interatomic distance of 3.04 Å. At longer interatomic distances, the dispersion correction decays approximately as r^{-6}. At shorter distances, on the other hand, it disappears rapidly due to the presence of the damping function $f(r)$, and at distances corresponding to covalent bonding (less than around 2 Å), the dispersion correction is zero. (The dispersion correction diverges to $-\infty$ for internuclear distances less than around 0.2 Å, but such short distances never occur in chemistry, so this behaviour is of no consequence.)

How accurate is Grimme's dispersion correction scheme? To try to answer that question, we applied it to the potential energy curves previously calculated with the use of the PBE functional for the π-stacked and T-shaped benzene dimers. In Figure D.5, the corrected potential energy curves are compared with the CCSD curves. It can be seen from Figure D.5 that for both dimer geometries, the corrected PBE curves are reasonably close to the CCSD curves. The dispersion-corrected dimerisation energies for the π-stacked and the T-shaped dimers are 0.078 and 0.159 eV, respectively, in fairly good agreement with the respective CCSD dimerisation energies of 0.106 and 0.206 eV. This is no small feat, given the simplicity of Grimme's dispersion correction scheme, and the fact that the only parameter tailored specifically to the PBE functional is the global scaling parameter s_6. In Chapter 2, which is devoted to the verification of the computational methodology applied in the present work, we test this dispersion correction scheme on a further three systems, in each case finding that it improves

Figure D.5: Potential energy curves calculated for the π-stacked and T-shaped benzene dimers using the PBE functional corrected and uncorrected for dispersion, and the CCSD method. The zero of the energy scale corresponds to two isolated benzene molecules.

(a) The π-stacked dimer.

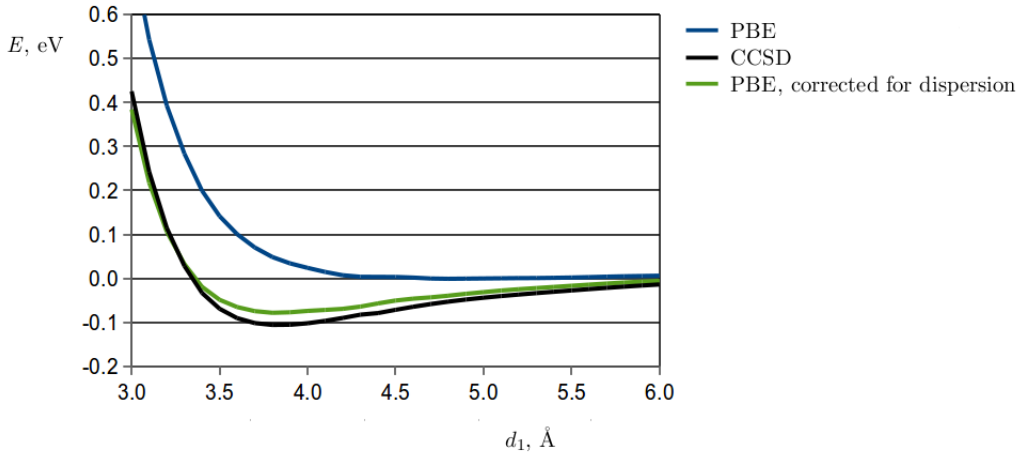

(b) The T-shaped dimer.

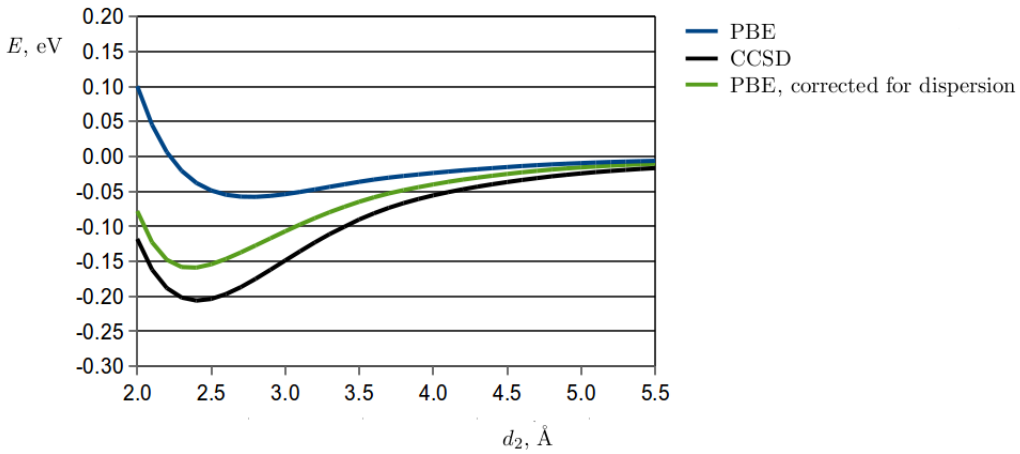

on the basic PBE functional. Having thus verified that the application of the dispersion correction scheme of Grimme to the PBE functional gives rise to a description of π-π and C$-$H$\cdots\pi$ interactions that is in adequate agreement with that obtained with the CCSD method, we have applied Grimme's scheme in all solid-state DFT calculations carried out throughout the present work.

D.7. Time-dependent density functional theory

In the final section of this Appendix on density functional theory, we describe its extension to systems wherein the potential, and hence the electron density, vary in time. We begin by introducing the Runge-Gross theorem and the quantum-mechanical action, which together form the basis of time-dependent density functional theory, in analogy to the two Hohenberg-Kohn theorems which pertain to the time-independent case. We then discuss the application of time-dependent density functional theory (TD-DFT) to the problem of calculating electronic excitation energies of molecules.

D.7.1. The Runge-Gross theorem

Recall the first Hohenberg-Kohn theorem, which states that provided that the ground state of a given system is non-degenerate, there exists a one-to-one mapping between the ground-state electron density and the external potential acting on the electrons. As a consequence, the ground-state electron density provides an equivalent description of the system to the ground-state wavefunction.

Runge and Gross[27] generalised the first Hohenberg-Kohn theorem to the time-dependent case. The Runge-Gross theorem states that when a many-electron system evolving from a fixed initial density is subjected to either of two time-dependent external potentials, $v_1(\mathbf{r},t)$ and $v_2(\mathbf{r},t)$, that differ by more than an additive time-dependent term $c(t)$, they cannot produce the same time-dependent electron density $\rho(\mathbf{r},t)$:

$$v_1(\mathbf{r},t) \neq v_2(\mathbf{r},t) + c(t) \iff \rho_1(\mathbf{r},t) \neq \rho_2(\mathbf{r},t) \tag{D.31}$$

In consequence of the Runge-Gross theorem, the time-dependent potential may, in principle at least, be calculated from a known time-dependent electron density. Having procured the time-dependent potential, we may then solve the time-dependent Schröedinger equation to obtain the time-dependent wavefunction. Hence, the time-dependent electron density and wavefunction provide an equivalent description of the system.

D.7.2. The action integral

The second prerequisite for the construction of a time-dependent density functional theory is a variational principle analogous to the second Hohenberg-Kohn theorem. In the time-independent case, this theorem states that there exists a functional $E_v^{\mathrm{HK}}[\rho]$ of the electron density which, for a given external potential and number of electrons, takes the value of the ground-state energy E_0 if the electron density ρ is the ground-state electron density ρ_0, and higher values for any other electron density. The ground-state electron density may therefore be found by minimising the value of $E_v^{\mathrm{HK}}[\rho]$.

Reflecting the fact that for a system subjected to a time-dependent external potential, the total energy is not conserved in time, a different variational principle is required for the time-dependent case. We may define, however, a quantity which is conserved for any correct time-dependent wavefunction: the action integral given by equation D.32 below.

$$\mathcal{A}[\Psi] = \int_{t_0}^{t_1} \langle\, \Psi(\mathbf{r},t) \,|\, \mathrm{i}\,\frac{\partial}{\partial t} - \hat{H}(\mathbf{r},t) \,|\, \Psi(\mathbf{r},t) \,\rangle \,\mathrm{d}t \tag{D.32}$$

Note that we have explicitly written the action integral as a functional of the wavefunction $\Psi(\mathbf{r},t)$. By comparing the definition of the action integral with the time-dependent Schrödinger equation,

$$\hat{H}(\mathbf{r},t)\,\Psi(\mathbf{r},t) = \mathrm{i}\,\frac{\partial}{\partial t}\,\Psi(\mathbf{r},t)$$

we notice immediately that for a wavefunction $\Psi(\mathbf{r},t)$ that is a solution of the time-dependent Schrödinger equation, $\mathcal{A}[\Psi]$ is zero for any limits of integration t_0 and t_1.

On the basis of the Runge-Gross theorem, the action integral may also be expressed as a functional of the exact electron density:

$$\mathcal{A}[\rho] = \int_{t_0}^{t_1} \langle\, \Psi[\rho](\mathbf{r},t) \,|\, \mathrm{i}\,\frac{\partial}{\partial t} - \hat{H}(\mathbf{r},t) \,|\, \Psi[\rho](\mathbf{r},t) \,\rangle \,\mathrm{d}t \tag{D.33}$$

Furthermore, Runge and Gross proved[27] that for the exact time-dependent electron density $\rho(\mathbf{r},t)$, the functional derivative of $\mathcal{A}$ with respect to $\rho(\mathbf{r},t)$ is zero:

$$\frac{\delta\mathcal{A}}{\delta\rho(\mathbf{r},t)} = 0 \tag{D.34}$$

D.7.3. Time-dependent Kohn-Sham equations

On the basis of the theorem named after them and equation D.34, Runge and Gross extended to the time-dependent case the formalism of Kohn and Sham, whereby one introduces an auxiliary system of non-interacting electrons that generate the same density as the original system of interacting electrons. The time-evolution of the Kohn-Sham spinorbitals can be expressed by a set of N time-dependent Kohn-Sham equations, N being the number of electrons:[28]

$$\left[-\frac{1}{2}\nabla^2 + v_0(\mathbf{r},t)\right]\phi_k(\mathbf{r},t) = \mathrm{i}\frac{\partial}{\partial t}\phi_k(\mathbf{r},t) \tag{D.35}$$

Here it is assumed that there is no spin mixing, and each spinorbital is purely an α or β spinorbital. Therefore the spin variable σ has been dropped from the above equation. Also, to avoid confusion with the imaginary unit (i), the spinorbitals are labelled with an index k instead of i.

The time-dependent electron density is, by construction, equal to the sum of the square moduli of the Kohn-Sham spinorbitals ϕ_k :

$$\rho(\mathbf{r},t) = \sum_{k=1}^{N} |\,\phi_k(\mathbf{r},t)\,|^2 \tag{D.36}$$

The time-dependent Kohn-Sham equations D.35 describe in an exact manner the time-evolution of a many-electron system, but the form of the time-dependent Kohn-Sham potential $v_0(\mathbf{r},t)$ which appears in it is, of course, unknown. As in the time-independent case, it breaks down into a sum of three terms, of which only one is unknown:

$$v_0[\rho](\mathbf{r},t) = v_{\mathrm{External}}(\mathbf{r},t) + v_{\mathrm{Hartree}}[\rho](\mathbf{r},t) + v_{\mathrm{xc}}[\rho](\mathbf{r},t) \tag{D.37}$$

The first term on the right-hand side of equation D.37 is the external potential acting on the electrons, which contains the electrostatic potential of the nuclei as well as the time-dependent external potential that is assumed to act on the electrons. For example, if the time-dependent part of the external potential is the electric field component of electromagnetic radiation, then $v_{\mathrm{External}}(\mathbf{r},t)$ will be given by:

$$v_{\mathrm{External}}(\mathbf{r},t) = E\,f(t)\sin(\omega t)\,\mathbf{r}\cdot\boldsymbol{\alpha} - \sum_{a=1}^{N_{\mathrm{nuc}}}\frac{Z_a}{|\mathbf{r}-\mathbf{r}_a|} \tag{D.38}$$

where $\boldsymbol{\alpha}$ is the polarisation vector of the electromagnetic wave, E the amplitude of its electric field component and ω is its frequency. $f(t)$ is an envelope function that controls the shape of the electromagnetic wave.

The second term on the right-hand side of D.37 is the Hartree term that describes the instantaneous self-interaction energy of the electron density, calculated as though it was a classical continuous distribution of charge.

$$v_{\text{Hartree}}[\rho](\mathbf{r}, t) = \int \frac{\rho(\mathbf{r}, t)}{|\mathbf{r} - \mathbf{r}'|} \, \mathrm{d}\mathbf{r}' \tag{D.39}$$

The third term is the time-dependent exchange-correlation potential which, by definition, contains the quantum-mechanical many-body effects that are absent from the Hartree term, and also corrects for the fact that the kinetic energy is being calculated for the Kohn-Sham spinorbitals which describe the auxiliary system of non-interacting electrons, rather than for the real system. Like its time-independent counterpart, its functional form is unknown. However, some approximate methods to construct $v_{\text{xc}}[\rho](\mathbf{r}, t)$ have been proposed in the literature.[28–30] In the simplest case, we may assume that the time-dependent exchange-correlation potential is completely local in time, and that it may be evaluated as the ground-state (*i.e.*, time-independent) exchange-correlation functional of the instantaneous electron density at time t:

$$v_{\text{xc}}[\rho](\mathbf{r}, t) \approx v_{\text{xc}}[\rho_t](\mathbf{r})$$

This procedure, called the adiabatic approximation, paves the way for the application of the approximate ground-state functionals of the types described in Section D.5 to describe the time-evolution of the electron density. The adiabatic approximation is a fairly severe one, because the ground-state exchange-correlation functional of the instantaneous electron density, $v_{\text{xc}}[\rho_t](\mathbf{r})$, has no "memory" of the electron density at preceding times. Nevertheless, it is realistic enough that through numerical integration, for a finite time period, of equation D.35 with the time-dependent exchange-correlation functional calculated within the adiabatic approximation, optical absorption spectra may be obtained in good agreement with experiment.[31,32]

D.7.4. Kohn-Sham linear response theory

The TD-DFT method outlined in the previous Section, relying as it does on the numerical propagation in time of the Kohn-Sham spinorbitals, represents a very powerful theoretical technique, in the sense that the only fundamental approximation is that some approximate functional is substituted for the unknown exact time-dependent exchange-correlation functional $v_{\mathrm{xc}}(\mathbf{r},t)$. This method is not well suited for typical chemical applications, however, because of the very high computational cost of integrating numerically the time-dependent Kohn-Sham equations for any significant amount of time. More commonly, a more pragmatic approach is adopted, whereby the electronic excitation energies are obtained by considering the linear response of the static ground-state electron density to a small time-dependent perturbation. In the present Section, we take a bird's eye view of this linear-response TD-DFT method.

According to the first Hohenberg-Kohn theorem, all observables, and in particular the excitation energies, are functionals of the ground-state electron density, so in principle it is possible to calculate them directly from the ground-state density. Unfortunately, a rigorous method for doing so is not known, so some approximate scheme must be employed. The way forward is to consider the interaction of the electron density with a time-dependent external potential within the framework of perturbation theory. It is assumed that for $t < t_0$, the many-electron system is subjected to an external potential $v^{(0)}(\mathbf{r})$ that is constant in time. The solution of the time-independent Kohn-Sham equations for this potential yields the ground-state density $\rho^{(0)}(\mathbf{r})$. At time t_0 we "switch on" a time-dependent perturbation, $v^{(1)}(\mathbf{r},t)$, which is assumed to be small relative to the time-independent potential $v^{(0)}(\mathbf{r})$. Hence for $t \geq t_0$, the external potential is

$$v(\mathbf{r},t) = v^{(0)}(\mathbf{r}) + v^{(1)}(\mathbf{r},t) \tag{D.40}$$

The electron density at $t \geq t_0$ may then be expanded into the following perturbative series:

$$\rho(\mathbf{r},t) = \rho(\mathbf{r}) + \rho^{(1)}(\mathbf{r},t) + \rho^{(2)}(\mathbf{r},t) + ... \tag{D.41}$$

where $\rho^{(1)}(\mathbf{r},t)$ is the component of density that scales linearly with $v^{(1)}(\mathbf{r},t)$, $\rho^{(2)}(\mathbf{r},t)$ is the component that scales as the square of $v^{(1)}(\mathbf{r},t)$, and so on. Because the time-dependent perturbation $v^{(1)}(\mathbf{r},t)$ is assumed to be weak, we will

only take into consideration the linear term:

$$\rho(\mathbf{r},t) \approx \rho(\mathbf{r}) + \rho^{(1)}(\mathbf{r},t) \tag{D.42}$$

By performing Fourier transforms of $v^{(1)}(\mathbf{r},t)$ and $\rho^{(1)}(\mathbf{r},t)$, we turn our attention to the behaviour of these functions in the frequency domain, allowing us to investigate the response of the density to a specific frequency ω of the external potential. Our aim will be to calculate the linear density-density response function, $\chi(\mathbf{r},\mathbf{r}',\omega)$, which relates the linear response of the density, $\rho^{(1)}(\mathbf{r},\omega)$, to the external potential $v^{(1)}(\mathbf{r},\omega)$:

$$\rho^{(1)}(\mathbf{r},\omega) = \int \chi(\mathbf{r},\mathbf{r}',\omega)\, v^{(1)}(\mathbf{r}',\omega)\, \mathrm{d}\mathbf{r}' \tag{D.43}$$

The starting point is to impose the condition that the auxiliary system of non-interacting electrons (the Kohn-Sham system) generates the same linear response of the density as the real system:

$$\rho^{(1)}(\mathbf{r},\omega) = \int \chi_{\mathrm{KS}}(\mathbf{r},\mathbf{r}',\omega)\, v_0^{(1)}(\mathbf{r}',\omega)\, \mathrm{d}\mathbf{r}' \tag{D.44}$$

where $v_0^{(1)}(\mathbf{r},\omega)$ is the linear change of the Kohn-Sham potential brought about by the time-dependent external potential $v^{(1)}(\mathbf{r},t)$. We will apply equation D.37 to break down $v_0^{(1)}(\mathbf{r},\omega)$ into a sum of the following three terms:

$$v_0^{(1)}(\mathbf{r},\omega) = v^{(1)}(\mathbf{r},\omega) + v_{\mathrm{Hartree}}^{(1)}(\mathbf{r},\omega) + v_{\mathrm{xc}}^{(1)}(\mathbf{r},\omega) \tag{D.45}$$

The first term on the right-hand side of equation D.45 is the linear change of the external potential, which is simply equal to $v^{(1)}(\mathbf{r},\omega)$.

The second term on the right-hand side of D.45 is the linear change of the Hartree potential. It is given by:

$$v_{\mathrm{Hartree}}^{(1)}[\rho](\mathbf{r},\omega) = \int \frac{\rho^{(1)}(\mathbf{r}',\omega)}{|\mathbf{r}-\mathbf{r}'|}\, \mathrm{d}\mathbf{r}' \tag{D.46}$$

Finally, the third term, $v_{\mathrm{xc}}^{(1)}(\mathbf{r},\omega)$ is the linear change of the exchange-correlation potential. It can be obtained by evaluating the following integral:

$$v_{\mathrm{xc}}^{(1)}(\mathbf{r},\omega) = \int f_{\mathrm{xc}}(\mathbf{r},\mathbf{r}',\omega)\, \rho^{(1)}(\mathbf{r}',\omega)\, \mathrm{d}\mathbf{r}' \tag{D.47}$$

where the quantity $f_{\mathrm{xc}}(\mathbf{r},\mathbf{r}',\omega)$ is the Fourier transform of the exchange-correlation kernel $f_{\mathrm{xc}}(\mathbf{r},t,\mathbf{r}',t')$ which is in turn defined as the functional derivative of the exchange-correlation potential $v_{\mathrm{xc}}(\mathbf{r},t)$ with respect to the electron density:

$$f_{\mathrm{xc}}(\mathbf{r},t,\mathbf{r}',t') = \frac{\delta v_{\mathrm{xc}}(\mathbf{r},t)}{\delta\rho(\mathbf{r}',t')} \tag{D.48}$$

The linear density-density response function of the auxiliary system, $\chi_{\mathrm{KS}}(\mathbf{r},\mathbf{r}',\omega)$, is known exactly and may be expressed as the following double sum over all spinorbitals:

$$\chi_{\mathrm{KS}}(\mathbf{r},\mathbf{r}',\omega) = \lim_{\eta\to 0^+} \sum_{jk} \frac{n_j - n_k}{\omega - (\varepsilon_j - \varepsilon_k) + \mathrm{i}\eta}\, \phi_j(\mathbf{r})\,\phi_j^*(\mathbf{r}')\,\phi_k(\mathbf{r}')\,\phi_k^*(\mathbf{r}) \tag{D.49}$$

Here, n_j is the occupation number of spinorbital ϕ_j in the ground state, and ε_j is the Kohn-Sham eigenvalue of that orbital. η is a positive infinitesimal.

The linear response of the density may therefore be expressed as:

$$\rho^{(1)}(\mathbf{r},\omega) = \int \chi_{\mathrm{KS}}(\mathbf{r},\mathbf{r}',\omega)\, v^{(1)}(\mathbf{r}',\omega)\,\mathrm{d}\mathbf{r}' +$$

$$+ \int\int \chi_{\mathrm{KS}}(\mathbf{r},\mathbf{x},\omega)\left[\frac{1}{|\mathbf{x}-\mathbf{r}'|} + f_{\mathrm{xc}}(\mathbf{x},\mathbf{r}',\omega)\right]\rho^{(1)}(\mathbf{r}',\omega)\,\mathrm{d}\mathbf{x}\,\mathrm{d}\mathbf{r}' \tag{D.50}$$

$$\uparrow$$

$$\rho^{(1)}(\mathbf{r}',\omega) = \int \chi(\mathbf{r}',\mathbf{x}',\omega)\, v^{(1)}(\mathbf{x}',\omega)\,\mathrm{d}\mathbf{x}'$$

By combining equations D.44 and D.50, we obtain the following expression involving both $\chi(\mathbf{r},\mathbf{r}',\omega)$ and $\chi_{\mathrm{KS}}(\mathbf{r},\mathbf{r}',\omega)$:

$$\chi(\mathbf{r},\mathbf{r}',\omega) = \chi_{\mathrm{KS}}(\mathbf{r},\mathbf{r}',\omega) +$$

$$+ \int\int \chi(\mathbf{r},\mathbf{x},\omega)\left[\frac{1}{|\mathbf{x}-\mathbf{x}'|} + f_{\mathrm{xc}}(\mathbf{x},\mathbf{x}',\omega)\right]\chi_{\mathrm{KS}}(\mathbf{x}',\mathbf{r}',\omega)\,\mathrm{d}\mathbf{x}\,\mathrm{d}\mathbf{x}' \tag{D.51}$$

Equation D.51 is an exact expression for the linear density-density response function $\chi(\mathbf{r},\mathbf{r}',\omega)$, but the fact that $\chi(\mathbf{r},\mathbf{r}',\omega)$ appears on both sides of that equation makes the numerical solution of D.51 difficult. Fortunately, a full solution of D.51 turns out not to be necessary for the calculation of excited-state energies.

It can be shown that the exact response function has poles at frequencies which correspond to the excitation energies of the $E_m - E_0$. This becomes evident when we inspect the Lehmann representation[33] of the linear density-density response function, whereby $\chi(\mathbf{r}, \mathbf{r}', \omega)$ is expressed as the following summation over states:

$$\chi(\mathbf{r}, \mathbf{r}', \omega) = \lim_{\eta \to 0^+} \sum_m \left[\frac{\langle \psi_0 | \hat{\rho}(\mathbf{r}) | \psi_m \rangle \langle \psi_m | \hat{\rho}(\mathbf{r}') | \psi_0 \rangle}{\omega - (E_m - E_0) + \mathrm{i}\eta} - \frac{\langle \psi_0 | \hat{\rho}(\mathbf{r}') | \psi_m \rangle \langle \psi_m | \hat{\rho}(\mathbf{r}) | \psi_0 \rangle}{\omega + (E_m - E_0) + \mathrm{i}\eta} \right]$$

Here, $\hat{\rho}(\mathbf{r})$ is the density operator defined by equation D.2, and ψ_m are the eigenfunctions of the unperturbed (time-independent) Hamiltonian with corresponding eigenvalues E_m , ψ_0 being the ground state.

Casida[34] demonstrated that the poles of the response function may be found by solving the eigenvalue equation D.52 that is now named after him:

$$\mathbf{\Omega}\, \mathbf{F}_m = {\omega_m}^2\, \mathbf{F}_m \quad \text{where} \quad \omega_m = E_m - E_0 \tag{D.52}$$

The elements of the Hermitian matrix $\mathbf{\Omega}$ are given by

$$\Omega_{jk\sigma,j'k'\sigma'} = \delta_{jj'}\, \delta_{kk'}\, \delta_{\sigma\sigma'}\, (\varepsilon_{k'\sigma'} - \varepsilon_{j'\sigma'})^2 +$$

$$+ 2\, K_{jk\sigma,j'k'\sigma'} \sqrt{(n_{j\sigma} - n_{k\sigma})\,(n_{j'\sigma'} - n_{k'\sigma'})\,(\varepsilon_{k\sigma} - \varepsilon_{j\sigma})\,(\varepsilon_{k'\sigma'} - \varepsilon_{j'\sigma'})}$$

where

$$K_{jk\sigma,j'k'\sigma'} = \int\int \phi^*_{j\sigma}(\mathbf{r})\, \phi_{k\sigma}(\mathbf{r}) \left[\frac{1}{|\mathbf{r} - \mathbf{r}'|} + f_{\mathrm{xc}}(\mathbf{r}, \mathbf{r}', \omega) \right] \phi_{j'\sigma'}(\mathbf{r}')\, \phi^*_{k'\sigma'}(\mathbf{r}')\; \mathrm{d}\mathbf{r}\, \mathrm{d}\mathbf{r}'$$

In this form, linear response TD-DFT lends itself well to numerical calculations, and has seen extensive use in computational chemistry, to the point that in the literature, TD-DFT has become near-synonymous with linear-response TD-DFT.

Regarding the exchange-correlation kernel $f_{\mathrm{xc}}(\mathbf{r}, t, \mathbf{r}', t')$, it is usual to impose the adiabatic approximation, whereby the exchange-correlation kernel is independent of the frequency ω of the external perturbation. Then, equation D.48 which defines the exchange-correlation kernel in the general case simplifies to:

$$f_{\mathrm{xc}}(\mathbf{r}, t, \mathbf{r}', t') = \delta(t - t')\, \frac{\delta v_{\mathrm{xc}}(\mathbf{r})}{\delta \rho(\mathbf{r}')} = \delta(t - t')\, \frac{\delta^2 E_{\mathrm{xc}}[\rho]}{\delta \rho(\mathbf{r})\, \delta \rho(\mathbf{r}')}$$

In this manner, the adiabatic exchange-correlation kernel may be constructed from any of the approximate exchange-correlation functionals of the type described in Section D.5.

References

[1] P. Hohenberg, W. Kohn, *Phys. Rev. B*, 1964, **136**, 864.

[2] L. Piela, *Ideas of Quantum Chemistry*, Elsevier, Amsterdam, 2007, pp. 584-590.

[3] S. H. Vosko, L. Wilk, M. Nusair, *Can. J. Phys.*, 1980, **58**, 1200.

[4] J P. Perdew, Y. Wang, *Phys. Rev. B*, 1992, **45**, 13244.

[5] J. P. Perdew, K. Burke, M. Ernzerhof, *Phys. Rev. Lett.*, 1996, **77**, 3865.

[6] J. P. Perdew, K. Burke, M. Ernzerhof, *Phys. Rev. Lett.*, 1997, **78**, 1396.

[7] F. A. Hamprecht, A. J. Cohen, D. J. Tozer, N. C. Handy, *J. Chem. Phys.*, 1998, **109**, 6264.

[8] A. D. Becke, *J. Chem. Phys.*, 1993, **98**, 5648.

[9] A. D. Becke, *J. Chem. Phys.*, 1988, **88**, 1053.

[10] A. D. Becke, *Phys. Rev. A*, 1988, **38**, 3098.

[11] J. P. Perdew, in *Electronic Structure of Solids '91*, ed. P. Ziesche and H. Eschrig, Akademie Verlag, Berlin, 1991, p. 11.

[12] C. Adamo, V. Barone, *J. Chem. Phys.*, 1999, **110**, 6158.

[13] C. Adamo, G. E. Scuseria, V. Barone, *J. Chem. Phys.*, 1999, **111**, 2889.

[14] D. Jacquemin, J. Preat, M. Charlot, V. Wathelet, J.-M. André, *J. Chem. Phys.*, 2004, **121**, 1736.

[15] E. A. Perpète, V. Wathelet, J. Preat, C. Lambert, D. Jacquemin, *J. Chem. Theory Comput.*, 2006, **2**, 434.

[16] D. Jacquemin, V. Wathelet, E. A. Perpète, C. Adamo, *J. Chem. Theory Comput.*, 2009, **5**, 2420.

[17] C. A. Guido, D. Jacquemin, C. Adamo, B. Mennucci, *J. Chem. Phys. A*, 2010, **114**, 13402.

[18] C. W. Bauschlicher Jr., *Chem. Phys. Lett.*, 1995, **246**, 40.

[19] J. N. Harvey, *Annu. Rep. Prog. Chem., Sect. C*, 2006, **102**, 203.

[20] S. F. Sousa, P. A. Fernandes, M. J. Ramos, *J. Phys. Chem. A*, 2007, **111**, 10439.

[21] K. E. Riley, B. T. Op't Holt, K. M. Merz , Jr., *J. Chem. Theory Comput.*, 2007, **3**, 407.

[22] M. D. Wodrich, C. Corminboeuf, P. R. Schreiner, A. A. Fokin, P. von Ragué Schleyer, *Org. Lett.*, 2007, **9**, 1851.

[23] Gaussian 09, Revision A.02, M. J. Frisch, G. W. Trucks, H. B. Schlegel, G. E. Scuseria, M. A. Robb, J. R. Cheeseman, G. Scalmani, V. Barone, B. Mennucci, G. A. Petersson, H. Nakatsuji, M. Caricato, X. Li, H. P. Hratchian, A. F. Izmaylov, J. Bloino, G. Zheng, J. L. Sonnenberg, M. Hada, M. Ehara, K. Toyota, R. Fukuda, J. Hasegawa, M. Ishida, T. Nakajima, Y. Honda, O. Kitao, H. Nakai, T. Vreven, J. A. Montgomery, Jr., J. E. Peralta, F. Ogliaro, M. Bearpark, J. J. Heyd, E. Brothers, K. N. Kudin, V. N. Staroverov, R. Kobayashi, J. Normand, K. Raghavachari, A. Rendell, J. C. Burant, S. S. Iyengar, J. Tomasi, M. Cossi, N. Rega, J. M. Millam, M. Klene, J. E. Knox, J. B. Cross, V. Bakken, C. Adamo, J. Jaramillo, R. Gomperts, R. E. Stratmann, O. Yazyev, A. J. Austin, R. Cammi, C. Pomelli, J. W. Ochterski, R. L. Martin, K. Morokuma, V. G. Zakrzewski, G. A. Voth, P. Salvador, J. J. Dannenberg, S. Dapprich, A. D. Daniels, Ö. Farkas, J. B. Foresman, J. V. Ortiz, J. Cioslowski, and D. J. Fox, Gaussian, Inc., Wallingford CT, 2009.

[24] P. Ugliengo, A. Damin, *Chem. Phys. Lett.*, 2002, **366**, 683.

[25] C. Tuma, J. Sauer, *Phys. Chem. Chem. Phys.*, 2006, **8**, 3955.

[26] S. Grimme, *J. Comput. Chem.*, 2006, **27**, 1787.

[27] E. Runge, E. K. U. Gross, *Phys. Rev. Lett.*, 1984, **52**, 997.

[28] M. A. L. Marques, E. K. U. Gross, *Annu. Rev. Phys. Chem.*, 2004, **55**, 427.

[29] J. F. Dobson, M. J. Bünner, E. K. U. Gross, *Phys. Rev. Lett.*, 1997, **79**, 1905.

[30] Y. Kurzweil, R. Baer, *J. Chem. Phys.*, 2004, **121**, 8731.

[31] M. A. L. Marques, A. Castro, G. F. Bertsch, A. Rubio, *Comp. Phys. Comm.*, 2003, **151**, 60.

[32] M. A. L. Marques, X. López, D. Varsano, A. Castro, A. Rubio, *Phys. Rev. Lett.*, 2003, **90**, 258101.

[33] C. A. Ullrich, *Time-Dependent Density-Functional Theory Concepts and Applications*, Oxford University Press, Oxford, 2012, p. 126.

[34] M. E. Casida, in *Recent Applications and Developments of Modern Density Functional Theory*, ed. J. M. Seminario, Elsevier, Amsterdam, 1996, p. 391.

Appendix E
Density functional theory in the solid state

E.1. Introduction

In the preceding Appendix, we discussed the application of density functional theory (DFT) to systems of finite size, such as isolated molecules and molecular dimers. These techniques may, in some cases, be used to study phenomena occurring in the solid state, if the crystal is modelled by a cluster containing a finite number of atoms or molecules.[1–3] This approach seems appropriate for phenomena that are well localised in space, which should ideally allow the simulation to be carried out in a large enough cluster that the quantities of interest are converged with respect to the model size.

Although in the present work we assume that the electronic excitations in the crystals under study are localised on individual molecules, in the course of their photochemical reactions the excited molecules undergo strong geometric deformations, which may cause the surrounding molecules to become displaced from their crystallographic positions, away from the excited molecules. For this reason, we believe that simulations of these reactions cannot be performed within a finite cluster model of manageable size without a detriment to their accuracy. Pictorially speaking, it is likely that in a cluster containing the isolated molecule and a only single layer of surrounding molecules, it would be unrealistically easy for the reactive molecule to "push out" the surrounding molecules while undergoing isomerisation. On the other hand, including more than one layer of surrounding molecules would certainly make the calculation prohibitively expensive.

Due to these considerations, in our hybrid TD-DFT/DFT simulations we have used instead a more sophisticated model of the solid state, in which a unit cell of the crystal containing one photoexcited molecule and several ground-state molecules is repeated periodically and infinitely along the three dimensions of space. The resulting infinite periodic model introduces into the simulation an artifact of another type: namely, the photoexcited molecule contained in the unit cell is repeated periodically throughout the crystal along with the non-reactive ground-state molecules, which means that in the simulated model, the number density of excited molecules is the same as in the original unit cell. In reality the

number density of photoexcited molecules in the crystal at any given time is lower by orders of magnitude. Thus, while in the finite cluster model the packing of the surrounding ground-state molecules around the excited molecules is expected to be too loose, in the infinite periodic model it may potentially be slightly too crowded, especially if (as in the present work) the simulations are carried out under constant-volume conditions. The latter possibility seems, however, less likely to give rise to spurious, unrealistic photoreaction pathways than the former.

In the present Appendix, our focus will be the symmetry properties of this infinite periodic model of the solid state and its description by means of DFT.

E.2. Translational symmetry in the solid state

The defining characteristic of a crystal is the presence of long-range translational symmetry, or in other words, the periodic repetition in space of a structural motif comprising a set of atoms. Accordingly, our discussion of the application of DFT to the solid state will begin with the translational symmetry properties of crystals and their implications for the electronic structure theory of the solid state.

Our model of the solid state will assume that the crystal extends infinitely in all three directions. Its translational symmetry may be fully described by specifying the three linearly independent basis vectors $\mathbf{a}_1$, $\mathbf{a}_2$ and $\mathbf{a}_3$ which have the property that, if an atom is located at position vector $\mathbf{r}_0$, an identical atom will be located at any position vector $\mathbf{r}_0 + n_1\mathbf{a}_1 + n_2\mathbf{a}_2 + n_3\mathbf{a}_3$, where n_1, n_2 and n_3 are arbitrarily chosen integers. The basis vectors are not defined uniquely; for example, if $\mathbf{a}_1$, $\mathbf{a}_2$, $\mathbf{a}_3$ is valid set of basis vectors, then so is $2\mathbf{a}_1$, $\mathbf{a}_2 + \mathbf{a_3}$, $\mathbf{a}_3$. For reasons of computational efficiency, we will usually prefer to choose the basis vectors in such a way that the parallelepiped with sides $\mathbf{a}_1$, $\mathbf{a}_2$ and $\mathbf{a}_3$ has the least possible volume, which is given by $V = \mathbf{a}_1 \cdot (\mathbf{a}_2 \times \mathbf{a}_3)$. This least-volume parallelepiped will have special significance to us, and from now on we will refer to it as our choice of the unit cell of the crystal. An example of a unit cell is shown in Figure E.1 on the following page.

Let us define a set of translation vectors $\mathbf{R}_j$, each of which will be given as a linear combination of the basis vectors $\mathbf{a}_1$, $\mathbf{a}_2$ and $\mathbf{a}_3$ with arbitrary integer

Figure E.1: The unit cell of a crystal. $\mathbf{a}_1$, $\mathbf{a}_2$ and $\mathbf{a}_3$ are the basis vectors, and the vertex denoted by $\mathbf{0}$ is the origin of the unit cell.

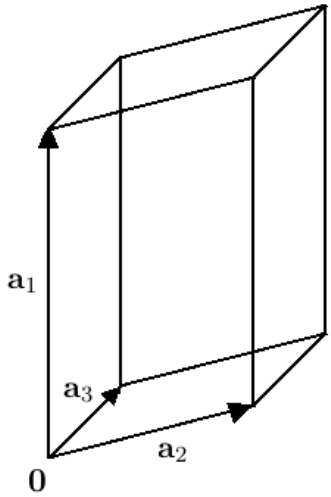

Figure E.2: A two-dimensional primitive lattice. $\mathbf{a}_1$ and $\mathbf{a}_2$ are the basis vectors, and $\mathbf{0}$ denotes the origin of the unit cell. The lattice points are depicted as empty circles. The translation vector $\mathbf{R}_j$ is given by $\mathbf{R}_j = \mathbf{a}_1 - 2\mathbf{a}_2$.

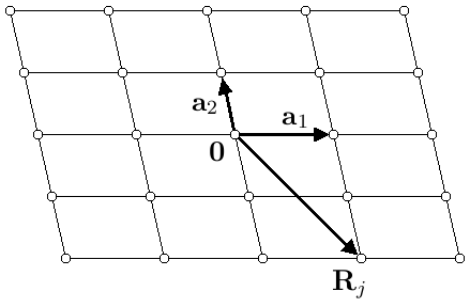

coefficients n_{j1}, n_{j2} and n_{j3}:

$$\mathbf{R}_j = n_{j1}\,\mathbf{a}_1 + n_{j2}\,\mathbf{a}_2 + n_{j3}\,\mathbf{a}_3 \tag{E.1}$$

If we imagine the translation vectors $\mathbf{R}_j$ as starting from the origin $\mathbf{0}$ of the unit cell, then each translation vector will indicate a point that lies at the origin of another unit cell. These points form the so-called primitive lattice of the crystal, which is said to be "primitive" because each unit cell contains exactly one lattice point; in a non-primitive lattice, each unit cell would contain multiple symmetry-equivalent lattice points. The primitive lattice is rather difficult to illustrate in the three-dimensional case, so in Figure E.2 above we show an example of a two-dimensional lattice.

We may also define the translation operator $\hat{T}(\mathbf{R}_j)$ whose action on a function $f(\mathbf{r})$ consists of shifting the function in space by the translation vector $\mathbf{R}_j$:

$$\hat{T}(\mathbf{R}_j)\, f(\mathbf{r}) = f(\mathbf{r} - \mathbf{R}_j) \tag{E.2}$$

Let us now consider an electron subject to the potential $V(\mathbf{r})$ generated by the atoms contained in the primitive lattice. Of course, $V(\mathbf{r})$ has the same translational symmetry as the primitive lattice, which is to say

$$\hat{T}(\mathbf{R}_j)\, V(\mathbf{r}) = V(\mathbf{r} - \mathbf{R}_j) = V(\mathbf{r}) \tag{E.3}$$

for any translation vector $\mathbf{R}_j$. The periodicity of the potential is reflected in the probability density distribution of the electron, which exhibits the same translational symmetry as the primitive lattice. The square moduli of that electron's wavefunction at any two points separated by a translation vector $\mathbf{R}_j$ must therefore be equal:

$$|\,\phi(\mathbf{r} - \mathbf{R}_j)\,|^2 = |\,\phi(\mathbf{r})\,|^2 \tag{E.4}$$

It follows that the one-electron wavefunction $\phi(\mathbf{r})$ must be an eigenfunction of the operator $\hat{T}(\mathbf{R}_j)$ for any choice of translation vector $\mathbf{R}_j$:

$$\hat{T}(\mathbf{R}_j)\,\phi(\mathbf{r}) = \phi(\mathbf{r} - \mathbf{R}_j) = \lambda(\mathbf{R}_j)\,\phi(\mathbf{r}) \tag{E.5}$$

Here, $\lambda(\mathbf{R}_j)$ is the eigenvalue of $\hat{T}(\mathbf{R}_j)$, which depends on $\mathbf{R}_j$ and has a square modulus equal to unity, $|\,\lambda(\mathbf{R}_j)\,|^2 = 1$. From the above, and the general properties of the translation operator, it can be shown that in order for equation E.4 to be satisfied, the eigenvalue of the translation operator must take the form $\lambda(\mathbf{R}_j) = \exp(-\mathrm{i}\mathbf{k}\mathbf{R}_j)$, where $\mathbf{k}$ is a vector, called the wave vector, that is specific to the wavefunction $\phi(\mathbf{r})$ and does not depend on the translation vector $\mathbf{R}_j$. It is straightforward to demonstrate that this form of the eigenvalue is consistent with the fact that the product of any two translation operators $\hat{T}(\mathbf{R}_i)$ and $\hat{T}(\mathbf{R}_j)$ is equal to another translation operator $\hat{T}(\mathbf{R}_i + \mathbf{R}_j)$:

$$\hat{T}(\mathbf{R}_i)\,\hat{T}(\mathbf{R}_j) = \hat{T}(\mathbf{R}_i + \mathbf{R}_j)$$

To show this, we need only perform the following transformations:

$$\hat{T}(\mathbf{R}_i)\,\hat{T}(\mathbf{R}_j)\,\phi(\mathbf{r}) = \hat{T}(\mathbf{R}_i)\exp(-\mathrm{i}\mathbf{k}\mathbf{R}_j)\,\phi(\mathbf{r}) = \exp(-\mathrm{i}\mathbf{k}\mathbf{R}_j)\,\hat{T}(\mathbf{R}_i)\,\phi(\mathbf{r}) =$$
$$= \exp(-\mathrm{i}\mathbf{k}\mathbf{R}_j)\exp(-\mathrm{i}\mathbf{k}\mathbf{R}_i)\,\phi(\mathbf{r}) = \exp[-\mathrm{i}\mathbf{k}\,(\mathbf{R}_i + \mathbf{R}_j)]\,\phi(\mathbf{r}) =$$
$$= \hat{T}(\mathbf{R}_i + \mathbf{R}_j)\,\phi(\mathbf{r})$$

Also, $\lambda(\mathbf{R}_j) = \exp(-\mathrm{i}\mathbf{k}\mathbf{R}_j)$ is consistent with the fact that any two translation operators $\hat{T}(\mathbf{R}_i)$ and $\hat{T}(\mathbf{R}_j)$ commute:

$$\hat{T}(\mathbf{R}_i)\,\hat{T}(\mathbf{R}_j) = \hat{T}(\mathbf{R}_j)\,\hat{T}(\mathbf{R}_i)$$

Indeed,

$$\hat{T}(\mathbf{R}_i)\,\hat{T}(\mathbf{R}_j)\,\phi(\mathbf{r}) = \exp[-\mathrm{i}\mathbf{k}\,(\mathbf{R}_i + \mathbf{R}_j)]\,\phi(\mathbf{r}) = \hat{T}(\mathbf{R}_j)\,\hat{T}(\mathbf{R}_i)\,\phi(\mathbf{r})$$

In summary, the value of the crystal orbital shifted by a translation vector $\mathbf{R}_j$ must meet the following condition:

$$\hat{T}(\mathbf{R}_j)\,\phi(\mathbf{r}) = \phi(\mathbf{r} - \mathbf{R}_j) = \exp(-\mathrm{i}\mathbf{k}\mathbf{R}_j)\,\phi(\mathbf{r}) \tag{E.6}$$

As mentioned above, the wave vector $\mathbf{k}$ is characteristic of the one-electron wavefunction $\phi(\mathbf{r})$. From now on, we will therefore label each one-electron wavefunction with its specific wave vector:

$$\hat{T}(\mathbf{R}_j)\,\phi_{\mathbf{k}}(\mathbf{r}) = \phi_{\mathbf{k}}(\mathbf{r} - \mathbf{R}_j) = \exp(-\mathrm{i}\mathbf{k}\mathbf{R}_j)\,\phi_{\mathbf{k}}(\mathbf{r}) \tag{E.7}$$

The above equation E.7 is widely known as the Bloch theorem, named after Felix Bloch who derived it during his doctoral studies under Werner Heisenberg.[4] One way to ensure that the one-electron wavefunction $\phi_{\mathbf{k}}(\mathbf{r})$ will always conform to the Bloch theorem is to introduce an auxiliary function $u(\mathbf{r})$ which, by construction, has the same translational symmetry as the primitive lattice:

$$\hat{T}(\mathbf{R}_j)\,u(\mathbf{r}) = u(\mathbf{r} - \mathbf{R}_j) = u(\mathbf{r})$$

The one-electron wavefunction $\phi_{\mathbf{k}}(\mathbf{r})$ may then be defined as having the following functional form, called the Bloch function:

$$\phi_{\mathbf{k}}(\mathbf{r}) = u(\mathbf{r})\exp(\mathrm{i}\mathbf{k}\mathbf{r}) \tag{E.8}$$

It is quite easy to show that a Bloch function satisfies Bloch's theorem. Indeed,

$$\hat{T}(\mathbf{R}_j)\,\phi_{\mathbf{k}}(\mathbf{r}) = \hat{T}(\mathbf{R}_j)\,[u(\mathbf{r})\exp(\mathrm{i}\mathbf{k}\mathbf{r})] = u(\mathbf{r}-\mathbf{R}_j)\exp[\mathrm{i}\mathbf{k}(\mathbf{r}-\mathbf{R}_j)] =$$
$$= u(\mathbf{r})\exp(\mathrm{i}\mathbf{k}\mathbf{r})\exp(-\mathrm{i}\mathbf{k}\mathbf{R}_j) = \exp(-\mathrm{i}\mathbf{k}\mathbf{R}_j)\,\phi_{\mathbf{k}}(\mathbf{r})$$

Owing to this property, it is natural to employ Bloch functions as orbitals describing the electron density in a crystal, or crystal orbitals for short. In Section E.3, we will examine the crystal orbitals in greater detail, and demonstrate a practically convenient choice of the auxiliary function $u(\mathbf{r})$.

E.3. The reciprocal lattice

In relation to the primitive lattice defined by the basis vectors $\mathbf{a}_1$, $\mathbf{a}_2$ and $\mathbf{a}_3$ we will define another lattice called the reciprocal lattice. The translation vectors of the reciprocal lattice will be denoted $\mathbf{K}_j$ and will be defined by equation E.9:

$$\mathbf{K}_i = g_{i1}\,\mathbf{b}_1 + g_{i2}\,\mathbf{b}_2 + g_{i3}\,\mathbf{b}_3 \tag{E.9}$$

where g_{i1}, g_{i2} and g_{i3} are arbitrary integers, while $\mathbf{b}_1, \mathbf{b}_2$ and $\mathbf{b}_3$ are the biorthogonal basis vectors, whose magnitudes have a dimension of inverse length and which satisfy the following biorthogonality relations with the basis vectors of the primitive lattice:

$$\mathbf{a}_i \cdot \mathbf{b}_j = 2\,\pi\,\delta_{ij} \qquad \text{for any } i \text{ and } j \tag{E.10}$$

where δ_{ij} is the Kronecker delta. The points indicated by the vectors $\mathbf{K}_j$ from some arbitrarily chosen origin will be called the reciprocal lattice points.

In the three-dimensional case, the biorthogonality relations amount to setting

$$\mathbf{b}_1 = \frac{2\pi\,\mathbf{a}_2 \times \mathbf{a}_3}{V}$$
$$\mathbf{b}_2 = \frac{2\pi\,\mathbf{a}_3 \times \mathbf{a}_1}{V}$$
$$\mathbf{b}_3 = \frac{2\pi\,\mathbf{a}_1 \times \mathbf{a}_2}{V}$$

where V is the unit cell volume. The primitive and reciprocal lattices are difficult to draw in the three-dimensional case, so in Figure E.3 on the following page we present the reciprocal lattice corresponding to the two-dimensional primitive lattice shown previously in Figure E.2. In the two-dimensional case,

Figure E.3: The two-dimensional primitive lattice previously illustrated in Figure E.2 and its corresponding reciprocal lattice. $\mathbf{b}_1$ is perpendicular to $\mathbf{a}_2$, and $\mathbf{b}_2$ is perpendicular to $\mathbf{a}_1$.

(a) The primitive lattice.

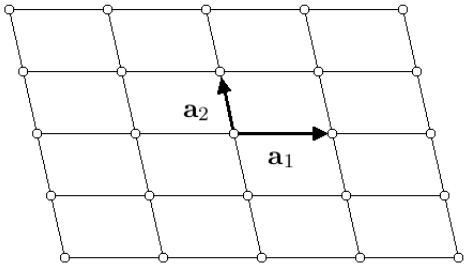

(b) The corresponding reciprocal lattice.

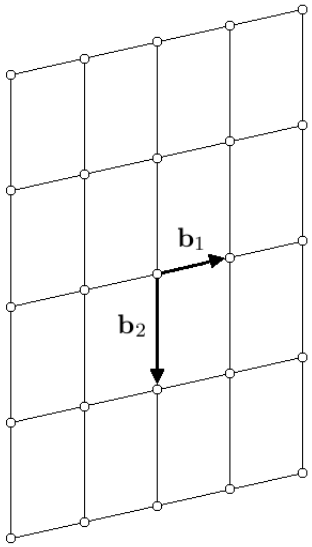

the biorthogonal basis vectors lie in the same plane as the basis vectors of the primitive lattice, and $\mathbf{b}_1$ is perpendicular to $\mathbf{a}_2$ while $\mathbf{b}_2$ is perpendicular to $\mathbf{a}_1$.

We will furthermore define a special area within the reciprocal lattice, which we will call the first Brillouin zone. Let us pick any one of the reciprocal lattice points and denote it as point A. The first Brillouin zone will be defined as the polyhedron that includes all points that are not further from A than from any other reciprocal lattice point. Its faces will lie on the planes which bisect perpendicularly the lines connecting A to the neighbouring reciprocal lattice points. To continue with the example of the two-dimensional reciprocal lattice depicted in Figure E.3(b), in Figure E.4 on the next page we show the construction of the first Brillouin zone in the two-dimensional case.

By construction, the first Brillouin zone has the property that if the point indicated by the wave vector $\mathbf{k}_0$ belongs to the first Brillouin zone, then the point indicated by the wave vector $\mathbf{k}_1 = \mathbf{k}_0 + \mathbf{K}_i$, where $\mathbf{K}_i$ is any nonzero reciprocal lattice vector, does not. Let us now consider the translational symmetry of a Bloch function characterised by the wave vector $\mathbf{k}_1$. Bloch's theorem states that the value of a one-electron wavefunction $\phi_{\mathbf{k}_1}(\mathbf{r})$, characterised by the wave vector $\mathbf{k}_1$ and shifted

Figure E.4: The first Brillouin zone of the two-dimensional case reciprocal lattice shown in Figure E.3(b). The shaded area is the first Brillouin zone, and its edges lie on the the lines, drawn in green, which bisect perpendicularly the lines connecting point A to the neighbouring reciprocal lattice points.

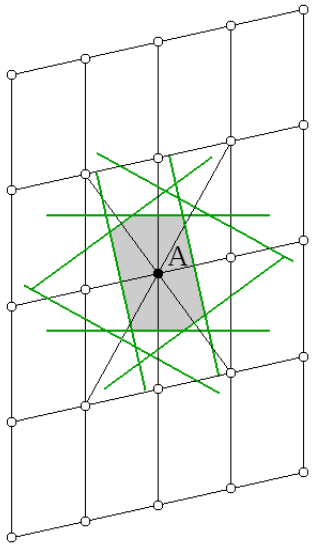

by the translation vector $\mathbf{R}_j$ is equal to:

$$\hat{T}(\mathbf{R}_j)\,\phi_{\mathbf{k}_1}(\mathbf{r}) = \exp(-\mathrm{i}\mathbf{k}_1\cdot\mathbf{R}_j)\,\phi_{\mathbf{k}_1}(\mathbf{r}) = \exp[-\mathrm{i}(\mathbf{k}_0+\mathbf{K}_i)\cdot\mathbf{R}_j]\,\phi_{\mathbf{k}_1}(\mathbf{r}) =$$

$$= \exp(-\mathrm{i}\mathbf{K}_i\cdot\mathbf{R}_j)\exp(-\mathrm{i}\mathbf{k}_0\cdot\mathbf{R}_j)\,\phi_{\mathbf{k}_1}(\mathbf{r}) = \exp(-\mathrm{i}\mathbf{k}_0\cdot\mathbf{R}_j)\,\phi_{\mathbf{k}_1}(\mathbf{r}) \qquad \text{(E.11)}$$

The final part of the above transformation relies on the fact that $\mathbf{K}_i\mathbf{R}_j$ is an integral multiple of 2π:

$$\mathbf{K}_i\cdot\mathbf{R}_j = \sum_{r=1}^{3} g_{ir}\,\mathbf{b}_r\cdot\sum_{s=1}^{3} n_{js}\,\mathbf{a}_s = \sum_{r=1}^{3}\sum_{s=1}^{3} g_{ir}\,n_{js}\,\mathbf{a}_s\cdot\mathbf{b}_r =$$

$$= 2\,\pi\sum_{r=1}^{3}\sum_{s=1}^{3} g_{ir}\,n_{js}\,\delta_{rs}$$

and each of the numbers g_{ir}, n_{js} and δ_{rs} is an integer. Equation E.11 states that the one-electron wavefunctions with wave vectors $\mathbf{k}_0$ and $\mathbf{k}_1$ behave identically under translation, and the wave vector $\mathbf{k}_1$ is therefore equivalent to $\mathbf{k}_0$. It follows that in our description of the electron density of the crystal we will only need those Bloch functions which are identified by wave vectors contained in the first Brillouin zone.

E.4. Plane-wave basis sets

In Section E.1, we showed that by writing down a crystal orbital in the form of a Bloch function, we ensure that it satisfies Bloch's theorem. The auxiliary function $u(\mathbf{r})$ which appears in equation E.8 is required to have the translational symmetry of the primitive lattice, but its form is otherwise unspeficied. In many implementations of DFT in the solid state, such those available in the programs CASTEP[5] and Quantum Espresso,[6] the $u(\mathbf{r})$ of each crystal orbital $\phi_{n,\mathbf{k}}(\mathbf{r})$ is expanded in terms of a series of plane waves $\exp(\mathrm{i}\mathbf{G}\mathbf{r})$ with coefficients $c_{n,\mathbf{k}}(\mathbf{G})$, leading to the following functional form of the crystal orbital:

$$\phi_{n,\mathbf{k}}(\mathbf{r}) = \sum_{\mathbf{G}} c_{n,\mathbf{k}}(\mathbf{G}) \exp\left[\,\mathrm{i}(\mathbf{k}+\mathbf{G})\cdot\mathbf{r}\,\right] \tag{E.12}$$

Here, $\mathbf{G}$ is another wave vector which controls the direction and (figuratively speaking) the frequency of the plane wave. The only permitted values of $\mathbf{G}$ are those which cause the plane wave to have the same translational symmetry as the primitive lattice, *i.e.*

$$\exp\left[\,\mathrm{i}\mathbf{G}(\mathbf{r}+\mathbf{R}_j)\,\right] = \exp(\mathrm{i}\mathbf{G}\mathbf{r}) \quad \text{for any choice of translation vector } \mathbf{R}_j$$

It follows that the only allowed vectors $\mathbf{G}$ are those given by

$$\mathbf{G} = n_1\,\mathbf{b}_1 + n_2\,\mathbf{b}_2 + n_3\,\mathbf{b}_3$$

where n_1, n_2 and n_3 are arbitrary integers.

Thus, each crystal orbital $\phi_{n,\mathbf{k}}(\mathbf{r})$ is expressed as a linear combination of plane waves, which play the role of basis functions. In principle, the set of plane waves $\exp(\mathrm{i}\mathbf{G}\mathbf{r})$ used in the expansion E.12 should be complete, which is to say, infinite. In practice, however, the expansion must be truncated after a finite number of plane waves. The basis set truncation is controlled by a single parameter: the plane-wave cutoff E_{cut}, which has a dimension of energy. For each plane wave appearing in the expansion E.12, we define a kinetic energy value given by:

$$E_{\mathrm{kin}} = \frac{1}{2}\,|\,\mathbf{G}+\mathbf{k}\,|^2 \tag{E.13}$$

which is equal the kinetic energy of a free electron whose wavefunction is a plane wave with wave vector $\mathbf{G} + \mathbf{k}$. Only plane waves with E_{kin} values less or equal to E_{cut} are retained in the expansion E.12.

In comparison with localised basis sets, such as Gaussian-type orbital basis sets which we discussed in Section B.9 of Appendix B, plane-wave basis sets have some important advantages. These include:

- Lack of bias. The plane-wave basis set treats every element of space, and therefore every atom, on an equal footing. In contrast, a poorly designed localised basis set that places few basis functions on some atoms and many on others may induce an unphysical shift of the electron density towards the atoms that have many basis functions centred on them.

- Completeness. In the limit of $E_{\text{cut}} \to \infty$, where all wave vectors $\mathbf{G}$ are included in the expansion E.12, the plane waves form a complete basis set.

- Lack of dependence on the atomic positions. The plane-wave basis set is defined in relation to the dimensions of the unit cell, and does not depend on the positions of atoms. As a consequence of the above, plane-wave basis sets are immune to the basis set superposition error (BSSE) which afflicts simulations carried out with localised basis sets. In calculations of binding energies, BSSE manifests itself as an artificial stabilisation of the bonded complex relative to the component molecules, which may simplistically be described as resulting from the fact that the wavefunction (or electron density) of the bonded complex is calculated in a larger basis set than the wavefunctions of the isolated component molecules. Low-quality localised basis sets are especially susceptible to BSSE. On the other hand, when a plane-wave basis set is applied, the electron densities of the complex and the component molecules are invariably calculated in the same basis, eliminating BSSE.

- Computational efficiency. The functional form of the plane-wave basis set enables the inexpensive calculation of many quantities using fast Fourier transforms.

The last point is, perhaps, the most important. Unlike localised basis sets, which are designed with the explicit goal of describing the electron densities of atoms and molecules, the functional form of the plane-wave basis set is not specifically tailored towards describing electron densities. In this respect, the plane-wave

basis set is at a disadvantage relative to localised basis sets, typically requiring two orders of magnitude more basis functions than localised basis sets, even when pseudopotentials are used to describe the core electrons.[7,8] Fortunately, however, in calculations using a plane-wave basis set a considerable reduction of computational effort may be achieved by transforming some calculated quantities, *e.g.* the kinetic energy and the matrix elements of the Coulomb operator, from the real space to the reciprocal space by means of fast Fourier transforms. This leads to equations that lend themselves much better to efficient numerical calculation than the original equations expressed in the real space. The caveat is that the evaluation of exact exchange, required in the Hartree-Fock method and in DFT calculations with hybrid exchange-correlation functionals, remains relatively expensive with a plane-wave basis set.[9,10] For this reason, although hybrid functionals and in particular the B3LYP functional enjoy widespread usage with localised basis sets, their adoption in the field of solid-state simulation has been thus far been very limited.

E.5. The pseudopotential approximation

Despite the performance gains effected by calculating some quantities in reciprocal space, for even moderately large systems the number of plane waves required for an all-electron DFT calculation would be so high as to make the calculation prohibitively expensive. The reason for this is that in all-electron calculations, whether wavefunction-based or within DFT, the orbitals exhibit rapid oscillations in the vicinity of nuclei. This pertains to both the core orbitals, which are subject to the strong electrostatic potential of a nucleus and are therefore localised very close to the nucleus, and the valence orbitals, which are partially screened from the nucleus by the core electrons, but still vary rapidly in the core region because they must be orthogonal to the core orbitals. Naturally, the description of these rapid variations of the orbitals demands rapidly varying plane waves and therefore a very high plane-wave cutoff.

Outside the core regions, however, the orbitals vary much more smoothly. Furthermore, the shape of the orbitals in the core region is only weakly sensitive to the chemical environment of the atom. The vast majority of plane-wave implementations of DFT take advantage of these facts through the pseudopotential approximation, whereby the core electrons are eliminated from the calculation, and replaced with a one-electron operator, called the pseudopotential, which is

designed to mimic the interaction of the valence electrons with the core electrons while allowing a reduction in the plane-wave cutoff.

Let us recall the Hamiltonian operator for a system of N electrons in the potential of M nuclei:

$$\hat{H} = -\frac{1}{2}\sum_{i=1}^{N}\nabla_i^2 - \sum_{i=1}^{N}\sum_{a=1}^{M}\frac{Z_a}{|\mathbf{r}_a - \mathbf{r}_i|} + \sum_{i=1}^{N-1}\sum_{j=i+1}^{N}\frac{1}{|\mathbf{r}_j - \mathbf{r}_i|} \tag{E.14}$$

Within the pseudopotential approximation, for each a-th atom a number N_a of electrons are considered core electrons and eliminated from the Hamiltonian, leaving $N' = N - \sum_{a=1}^{M} N_a$ valence electrons. The eliminated core electrons are considered as being incorporated into the atomic cores, hence the nuclear charge Z_a of each atom is replaced by a core charge defined as $Q_a = Z_a - N_a$. Finally, the interaction of the valence electrons with the core electrons of each atom is modelled by introducing for each atomic core a pseudopotential operator $\hat{V}_a^{\mathrm{PS}}(\mathbf{r})$:

$$\hat{H} = -\frac{1}{2}\sum_{i=1}^{N'}\nabla_i^2 + \sum_{i=1}^{N'}\sum_{a=1}^{M}\left[-\frac{Q_a}{|\mathbf{r}_a - \mathbf{r}_i|} + \hat{V}_a^{PS}(\mathbf{r})\right] + \sum_{i=1}^{N'-1}\sum_{j=i+1}^{N'}\frac{1}{|\mathbf{r}_j - \mathbf{r}_i|} \tag{E.15}$$

A wavefunction that is an eigenfunction of the Hamiltonian E.15 is often called a pseudo-wavefunction, to distinguish it from the all-electron wavefunction which is an eigenfunction of the all-electron Hamiltonian E.14.

The elimination of the core orbitals means that the valence pseudo-orbitals are not required to be orthogonal to the core orbitals. The pseudopotential may therefore be designed in such a way as to ensure that the pseudo-orbitals are smooth in the core region, allowing a significantly lower plane-wave cutoff than would be required in an all-electron calculation.

Presently, we will briefly review two classes of pseudopotentials widely used in solid-state physics: the norm-conserving pseudopotentials and the ultrasoft pseudopotentials.

E.5.1. Norm-conserving pseudopotentials

The norm-conserving pseudopotentials, originally proposed by Hamann, Schlüter and Chiang[11] in 1979, take their name from the requirement that the pseudo-orbitals and the all-electron orbitals integrate to the same charge within a sphere of radius r_c, called the core radius. Several derivative variants of these original norm-conserving pseudopotentials have since been developed and applied in solid-state simulation.[13–16]

Within the scheme of Hamann, Schlüter and Chiang, the construction of a norm-conserving pseudopotential for an element is based on an all-electron calculation for an isolated atom of that element, which yields the all-electron orbitals $\phi_l^{\mathrm{AE}}(\mathbf{r})$ and the corresponding all-electron eigenvalues $\varepsilon_l^{\mathrm{AE}}$ (the orbitals and eigenvalues are indexed according to their orbital angular momentum quantum number l). The atomic core is then replaced with a trial pseudopotential, which is subsequently optimised so as to satisfy the following four conditions:

1. The eigenvalues of the pseudo-orbitals are to be equal to the eigenvalues of the corresponding all-electron orbitals: $\varepsilon_l^{\mathrm{PS}} = \varepsilon_l^{\mathrm{AE}}$
2. The pseudo-orbitals $\phi_l^{\mathrm{PS}}(\mathbf{r})$ are to have no radial nodes for $r < r_c$.
3. The pseudo-orbitals and the all-electron orbitals must be equal everywhere outside the core radius: $\phi_l^{\mathrm{PS}}(\mathbf{r}) = \phi_l^{\mathrm{AE}}(\mathbf{r})$ for $r \geq r_c$.
4. Lastly, the pseudo-orbitals must adhere to the norm-conservation constraint: $\int_0^{r_c} |\phi_l^{PS}(\mathbf{r})|^2 r^2 \,\mathrm{d}r = \int_0^{r_c} |\phi_l^{AE}(\mathbf{r})|^2 r^2 \,\mathrm{d}r$

When constructing norm-conserving pseudopotentials, there is a tradeoff between the core radius r_c and the properties of the resulting pseudopotential.[12] A higher r_c means that the pseudopotential will "smooth out" the wavefunction in a larger volume of space, allowing a greater reduction in the plane-wave cutoff. However, an increased r_c simultaneously makes the pseudopotential less transferable to atoms in different electronic configurations (and, therefore, in different chemical environments) than the configuration used to generate the pseudopotential.

E.5.2. Ultrasoft pseudopotentials

Vanderbilt[17,18] developed a family of ultrasoft pseudopotentials which enable a greater reduction in the plane-wave cutoff than their norm-conserving counterparts (this quality is the "softness" after which these pseudopotentials are named), at the cost of replacing the norm-conservation constraint with a less physically rigorous constraint, which in turn increases the mathematical complexity of the resulting pseudopotentials. Furthermore, the transferability of ultrafast pseudopotentials tends to be at least as good as that of the norm-conserving pseudopotentials.[18,19]

Molecular dynamics (MD) simulations such as we have carried out in the present work require numerous evaluations of the energy and forces, making it imperative to choose the calculation parameters in such a way as to keep cost of the simulation within acceptable limits. Accordingly, in our MD simulations we have used the PBE exchange-correlation functional in conjunction with the ultrasoft pseudopotentials supplied along with the program CASTEP, version 5.501.

E.6. Kohn-Sham equations in the solid state

With the use of the symmetry properties of the crystal, the set of Kohn-Sham equations for a finite non-periodic system (equation D.11 in Appendix D) may be adapted to the periodic case. In essence, the derivation starts by considering an $g \times g \times g$ supercell, consisting of g^3 primitive cells and possessing cyclic periodic boundary conditions, whereby the points given by $\mathbf{r}$ and $\mathbf{r} + g\mathbf{R}_j$, where $\mathbf{R}_j$ is any translation vector of the primitive lattice, are equivalent. By taking advantage of the translational symmetry properties of the crystal orbitals, and imposing the limit $g \to \infty$, we obtain a set Kohn-Sham equations for a periodic system, which are conveniently expressed in the following matrix form:

$$\mathbf{F}(\mathbf{k})\mathbf{c}(\mathbf{k}) = \mathbf{c}(\mathbf{k})\boldsymbol{\varepsilon}(\mathbf{k}) \tag{E.16}$$

The full mathematical form of these equations is given *e.g.* in References [20] and [21]; for our purposes, it will be sufficient to discuss only their general features. The matrices $\mathbf{F}(\mathbf{k})$, $\mathbf{c}(\mathbf{k})$ and $\boldsymbol{\varepsilon}(\mathbf{k})$ appearing in E.16 each have $H \times H$ dimensions, where H is the number of plane waves comprising the basis set. The elements of the matrix $\mathbf{F}(\mathbf{k})$ are the matrix elements of the Kohn-Sham operator with the plane-wave basis functions. The coefficients matrix $\mathbf{c}(\mathbf{k})$ contains the

coefficients $c_{n,\mathbf{k}}(\mathbf{G})$ which occur in the plane-wave expansion of the n-th crystal orbital. Finally, the diagonal matrix $\boldsymbol{\varepsilon}(\mathbf{k})$ contains the crystal orbital eigenvalues. Owing to the fact that the plane waves are mutually orthonormal, an overlap matrix does not enter E.16.

As indicated by E.16, where it is stressed that each of the matrices $\mathbf{F}(\mathbf{k})$, $\mathbf{c}(\mathbf{k})$ and $\boldsymbol{\varepsilon}(\mathbf{k})$ depends on the wave vector $\mathbf{k}$, a different electronic wavefunction corresponds to each of the infinite number of wave vectors $\mathbf{k}$ contained in the first Brillouin zone. Accordingly, the set of Kohn-Sham equations given by E.16 must, in principle at least, be solved an infinite number of times. Fortunately, within the first Brillouin zone, the variation of the one-electron wavefunctions $\phi_{n,\mathbf{k}}(\mathbf{r})$ and their corresponding eigenvalues $\varepsilon_n(\mathbf{k})$ with the wave vector $\mathbf{k}$ is smooth, which makes it possible to solve E.16 for only a finite set of wave vectors, provided that these wave vectors (in this context called the k-points) are selected so as to representatively sample the first Brillouin zone (the so-called k-point sampling).

In the solid-state calculations carried out in the present work, k-point sampling was carried out by using the Monkhorst-Pack scheme.[22] In this method, the sampling is performed on a $q_p \times q_r \times q_s$ grid of k-points whose positions in reciprocal space are given by:

$$\mathbf{k}_{prs} = u_p \mathbf{b}_1 + u_r \mathbf{b}_2 + u_s \mathbf{b}_3$$

where u_p, u_r and u_s are sequences of numbers defined as follows

$$u_p = \frac{2p - q_p - 1}{2q_p} \quad \text{where} \quad p = 1, 2, 3, ..., q_p$$

and likewise for u_r and u_s. The resulting grid is equally spaced in each of the three lattice directions.

The diagonal elements of the matrix $\boldsymbol{\varepsilon}(\mathbf{k})$ are the eigenvalues $\varepsilon_n(\mathbf{k})$ of the crystal orbitals $\phi_{n,\mathbf{k}}(\mathbf{r})$. Because within the first Brillouin zone, the eigenvalues $\varepsilon_n(\mathbf{k})$ vary continuously with the wave vector $\mathbf{k}$, each eigenvalue $\varepsilon_n(\mathbf{k})$ may be considered as forming the n-th energy band of the solid. The band structure contains information on its electronic and optical properties of the crystal. As an example, we have calculated the band structure of silicon in the diamond (fcc) structure with lattice constant 5.39 Å. The calculation was carried out using the program CASTEP, Academic Release version 5.501. The electron density was

calculated in the primitive cell of the fcc lattice, which contains two silicon atoms. A 10×10×10 Monkhorst-Pack k-point grid was requested, which was automatically reduced to 110 k-points by taking advantage of the point-group symmetry of the crystal. The PBE exchange-correlation functional[23,24] applied, and the plane-wave cutoff was set to 600 eV. The default ultrasoft pseudopotential for silicon was used.

In Figure E.5(a) on the following page, we illustrate the first Brillouin zone of the fcc lattice, which takes the form of a truncated octahedron. A number of points belonging to the first Brillouin zone have special importance due to their high symmetry; for instance, the point labelled Γ lies at the center of the first Brillouin zone, while the points X and L are positioned at the centers of the square and the hexagonal faces of the first Brillouin zone, respectively. We have calculated the energy bands along the following sequence of lines connecting high-symmetry points within the first Brillouin zone:

$$\mathrm{W} \to \Gamma \to \mathrm{X} \to \mathrm{W} \to \mathrm{L} \to \Gamma$$

The resulting band structure plot is presented in Figure E.5(b). There exists a band gap of 0.58 eV between the occupied valence bands and the unoccupied conduction bands, correctly indicating that silicon is a semiconductor. The magnitude of the band gap is, however, strongly underestimated relative to the experimental value of around 1.1 eV.[25] Such strong underestimation of the band gap is typical for LSDA and GGA exchange-correlation functionals.

The band gap is indirect, which means that the highest point of the valence band occurs at a different k-point (namely, Γ) than the lowest point of the conduction band (which is found along the $\Gamma \to \mathrm{X}$ line). This has implications for the optical properties of silicon: in particular, in the process of radiative recombination of an electron in the conduction band and an electron hole in the valence band, which is accompanied by the emission of a photon, the excess momentum of the recombining particles must be dissipated over the lattice vibrations, making the recombination process less efficient than in a direct band gap material. Similarly, the reverse process, which is the excitation of an electron from the valence band to the conduction band through the absorption of a photon, is less efficient in an indirect band gap semidonductor than in one having a direct band gap.

Figure E.5: (a) The first Brillouin zone of the fcc lattice. The biorthogonal basis vectors are drawn in blue. The high symmetry points of the first Brillouin zone are indicated as green dots, and the red lines connecting some of them are a guide to the eye.

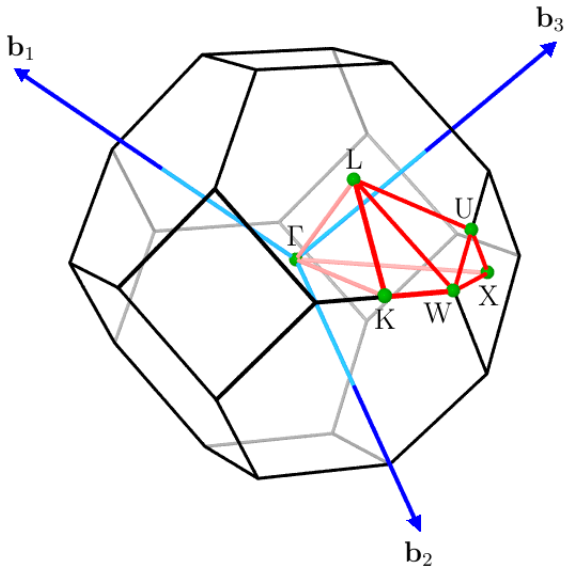

(b) The electronic band structure of silicon in the diamond structure, plotted along selected high symmetry lines of the first Brillouin zone. The zero of the energy scale is set at the valence band maximum.

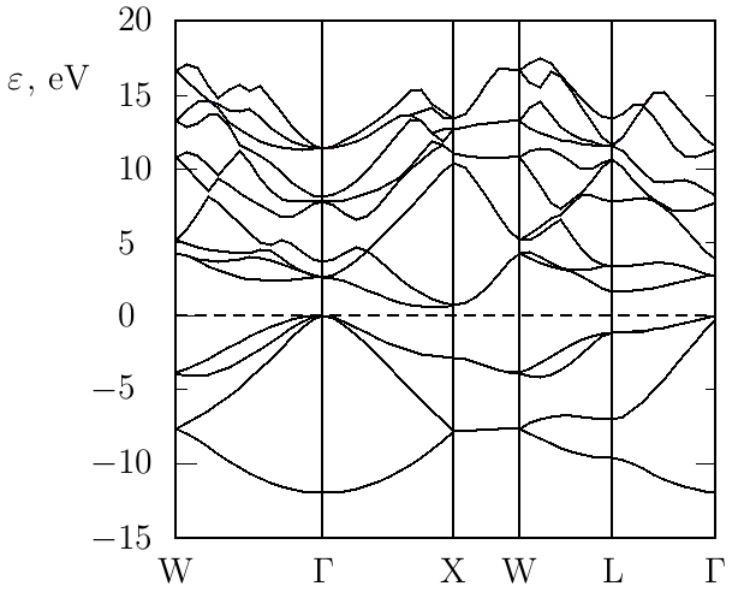

References

[1] C. Janke, R. Jones, S. Öberg, P. R. Briddon, *Phys. Rev. B*, 2007, **75**, 195208.

[2] B. L. Trout, A. K. Chakraborty, A. T. Bell, *J. Phys. Chem.*, 1996, **100**, 4173.

[3] M. Neurock, L. E. Manzer, *Chem. Commun.*, 1996, 1133.

[4] F. Bloch, *Physics Today*, 1976, **29**, 23.

[5] S. J. Clark, M. D. Segall, C. J. Pickard, P. J. Hasnip, M. I. J. Probert, K. Refson, M. C. Payne, *Z. Kristallogr.*, 2005, **220**, 567.

[6] P. Giannozzi, S. Baroni, N. Bonini, M. Calandra, R. Car, C. Cavazzoni, D. Ceresoli, G.L. Chiarotti, m. Cococcioni, I. Dabo, A. Dal Corso, S. Fabris, G. Fratesi, S. de Gironcoli, R. Gebauer, U. Gerstmann, C. Gougoussis, A. Kokalj, M. Lazzeri, L. Martin-Samos, N. Marzari, F. Mauri, R. Mazzarello, S. Paolini, A. Pasquarello, L. Paulatto, C. Sbraccia, S. Scandolo, G. Sclauzero, A. P. Seitsonen, A. Smogunov, P. Umari, R. M. Wentzcovitch, *J. Phys.: Condens. Matter*, 2009, **21**, 395502.

[7] J. Hutter, *J. Chem. Phys.*, 2003, **118**, 3928.

[8] N. L. Doltsinis, D. S. Kosov, *J. Chem. Phys.*, 2005, **122**, 144101.

[9] S. Chawla, G. A. Voth, *J. Chem. Phys.*, 1998, **108**, 4697.

[10] E. J. Bylaska, K. Tsemekhman, S. B. Baden, J. H. Weare, H. Jonsson, *Journal Comp. Chem.*, 2011, **32**, 54.

[11] D. R. Hamann, M. Schlüter, C. Chiang, *Phys. Rev. Lett.*, 1979, **43**, 1494.

[12] A. Filippetti, D. Vanderbilt, W. Zhong, Y. Cai, G. B. Bachelet, *Phys. Rev. B*, 1995, **52**, 11793.

[13] D. Vanderbilt, *Phys. Rev. B*, 1985, **32**, 8412.

[14] D. R. Hamann, *Phys. Rev. B*, 1989, **40**, 2980.

[15] N. Troullier, J. L. Martins, *Phys. Rev. B*, 1991, **43**, 1993.

[16] S. Goedecker, M. Teter, J. Hutter, *Phys. Rev. B*, 1996, **54**, 1703.

[17] D. Vanderbilt, *Phys. Rev. B*, 1990, **41**, 7892.

[18] K. Laasonen, R. Car, C. Lee, D. Vanderbilt, *Phys. Rev. B*, 1991, **43**, 6796.

[19] M. D. Segall, P. J. D. Lindan, M. J. Probert, C. J. Pickard, P. J. Hasnip, S. J. Clark, M. C. Payne, *J. Phys.: Condens. Matter*, 2002, **14**, 2717.

[20] R. A. Evasterov, *Quantum Chemistry of Solids*, Springer-Verlag, Berlin-Heidelberg, 2007, pp. 249-277.

[21] R. M. Martin, *Electronic Structure. Basic Theory and Practical Methods*, Cambridge University Press, Cambridge, 2004, pp. 236-253.

[22] H. J. Monkhorst, J. D. Pack, *Phys. Rev. B*, 1976, **13**, 5188.

[23] J. P. Perdew, K. Burke, M. Ernzerhof, *Phys. Rev. Lett.*, 1996, **77**, 3865.

[24] J. P. Perdew, K. Burke, M. Ernzerhof, *Phys. Rev. Lett.*, 1997, **78**, 1396.

[25] W. Bludau, A. Onton, W. Heinke, *J. Appl. Phys.*, 1974, **45**, 1846.

Appendix F
The electronic appendix

Contents of the electronic appendix:

MKochman_thesis.pdf - This thesis, in PDF format.

7PyIn_trajectory_II-5.mpeg - Trajectory II-5 of the photochemical reaction of 7PyIn, discussed in Section 4.3.1 of Chapter 3. The photoexcited molecule is identified in the image file **Photoexcited_molecule_II-5.png**.

7PyIn_trajectory_I-1.mpeg - Trajectory I-1 of the photochemical reaction of 7PyIn, discussed in Section 4.3.2 of Chapter 3. The photoexcited molecule is identified in the image file **Photoexcited_molecule_I-1.png**.

SCA_Forward_reaction_01.mpeg - Trajectory 1 of the forward reaction of SCA, discussed in Section 4.2.1 of Chapter 4. The projection is the same as in Figure 7(a) on page 75.

SCA_Forward_reaction_02.mpeg - Trajectory 2 of the forward reaction of SCA. The projection is the same as in Figure 7(a) on page 75.

SCA_Forward_reaction_03.mpeg - Trajectory 3 of the forward reaction of SCA, discussed in Section 4.2.2 of Chapter 4. The projection is the same as in Figure 7(a) on page 75.

SCA_Reverse_reaction_03.mpeg - Trajectory 3′ of the reverse reaction of SCA, discussed in Section 4.2.3 of Chapter 4. The projection is the same as in Figure 7(b) on page 76.

SCA_Reverse_reaction_06.mpeg - Trajectory 6′ of the reverse reaction of SCA. The projection is the same as in Figure 7(b) on page 76.

Appendix G
Publications

Femtosecond Dynamics of the Ring Closing Process of Diarylethene: A Case Study of Electrocyclic Reactions in Photochromic Single Crystal
H. Jean-Ruel, R. R. Cooney, M. Gao, C. Lu, M. A. Kochman, C. A. Morrison, R. J. Dwayne Miller, *J. Phys. Chem. A*, 2011, **115**, 13158.

Hybrid QM/QM Simulations of Excited-State Intramolecular Proton Transfer in the Molecular Crystal 7-(2-*Pyridyl*)-*indole*
M. A. Kochman, C. A. Morrison, *J. Chem. Theor. Comput.*, 2013, **9**, 1182.

Hybrid QM/QM simulations of photochemical reactions in the molecular crystal N-*salicylidene*-2-*chloroaniline*
M. A. Kochman, A. Bil, C. A. Morrison, *Phys. Chem. Chem. Phys.*, 2013, **15**, 10803.

Appendix H
Conferences and courses attended

Conferences

Computational Molecular Science 2012
Cirencester, United Kingdom, June 2012
Poster Presentation: *Excited-state intramolecular transfer in molecular crystals of Schiff bases*

Seminar with Research Group of Prof. R. J. Dwayne Miller
Hamburg, Germany, June 2013
Oral Presentation: *Photochemical reactions of molecular crystals*

15th European Symposium on Gas-Phase Electron Diffraction
Frauenchiemsee, Germany, June 2013
Oral Presentation: *The photochemical reaction of* N-*salicylidene*-2-*chloroaniline*

Courses

EPCC Parallel Computing Course
Edinburgh, United Kingdom, March 2011

Computational Biophysics Workshop
Bremen, Germany, October 2011